Spin-Photon Entanglement by Using a Single Optical Transition

Dissertation

zur Erlangung des akademischen Grades

Doktorin der Technischen Wissenschaften

im Rahmen des Studiums

Dr.-Studium der techn. Wissenschaften Technische Physik

eingereicht von

Dipl.-Ing. Sarah Reisenbauer

Matrikelnummer: 00625672, Königsegg 17 2851 Krumbach

an der

Fakultät für Physik der Technischen Universität Wien

Betreuung: Univ.-Prof. Dr. Hannes-Jörg Schmiedmayer, Atominstitut E141
Mitwirkung: Univ.-Ass. Dr. Michael Trupke

Wien, 7.2.2021

_____   _____
(Unterschrift Sarah   (Unterschrift Betreuung)
Reisenbauer)

Acknowledgements

Advances in science are a hugely collaborative and social effort. One couldn't even take something experienced as mundane as a simple pencil in one's hand without the ingenuity of past generations of people, who in today's research we build upon. However, I can thank some important supporters in my scientific journey:

Above all, I am deeply grateful to my co-supervisor Michael Trupke, for everything he has done for me and all his great invaluable support over the years. I started as a Bachelor student in his team and ever since, he held a protective hand over all of us students. He patiently answered all of my questions and can break down the most complex matters in a simple graph on a napkin in the coffee break. I know him as a researcher with huge drive, commitment and brilliant ideas.

I am greatly indebted to my supervisor Jörg Schmiedmayer, from the Technical University of Vienna, who welcomed me in his group and made it possible for me to take part in the doctoral program "Solids for Function". I deeply value the familiar atmosphere in the whole group, his enormous enthusiasm for science and his support for young researchers, the weekly breakfast discussion meetings - all invaluable for a young student to take root.

I had the fortunate luck to get to know another excellent research group during my PhD, hosted by Philip Walther at the University of Vienna, when we moved there. Philip took us in, we were integrated into his group immediately and felt we had found a new home, aided by his legendary annual barbecues.

Colleagues is what lets us PhD students 'survive' hardships, who motivate us in difficult times, who make the many hours in the lab joyful and sweeten our lunch breaks. They give important tips when one doesn't know how to proceed and help when faced

with challenges. They are always there to count on and they know what one talks about. So, thanks to all my colleagues over the years.

Especially, I would like to mention my two team colleagues Rui and Cameron - together we worked countless hours to make all of this possible. Both of you were contagiously motivated and enthusiastic. I always knew we could totally rely on each other. Among many other achievements, Rui optimized allocation of suitable NV centres and Cameron made it possible for us to work with solid immersion lenses. Further, I would like to thank Georg for sharing his deep knowledge of electronics, who constructed some of our experimental hardware and who I could have some nice tech-trash talk with. Daniel, I am glad we 'made' you stay with us longer than you initially planned. It has been a pleasure to work and laugh with you. Thank you, Daniel, Tom and Stefan for proofreading my thesis!

I further want to thank all the people at both universities who provide common services and who care for shared facilities. Especially those, who are not so visible but keep everything running.

Family and friends have been very important anchors to me, likewise my partner Martin and our cats. This thesis reached completion through their loving encouragement.

Also, I would like to acknowledge the heavy use of open software solutions, especially those by the Jupyter, Texmaker, Inkscape und Gimp communities. And finally, I want to thank all my teachers at university and before, who I today have learned to value much more than I might have in the days back then.

Sarah Reisenbauer

Abstract

Spin-photon entanglement provides the basis for numerous applications in quantum technology, including quantum communication and computing. Proposals for photonic quantum computation and quantum networks rely on highly entangled multipartite resource states, and using spin-photon entanglement, quantum emitters can be employed to produce such states. However, previously proposed methods placed stringent requirements on the energy level structure and optical transitions. In this thesis, a protocol to create photonic resource states is presented which significantly reduces the requirements placed on the emitter, thereby making the method suitable for a variety of candidate sources. The improvement is achieved by using only a single optical transition, and by working in the time domain. An unbalanced interferometer is then used to convert the temporal photonic qubit into the polarization basis, which is useful for quantum logic operations and tomography. The thesis details the experimental realization of the main unit of the proposed protocol, which is in principle scalable, on the nitrogen-vacancy centre emitter platform in diamond. Entanglement is shown between the spin of the emitter and a fluorescence photon in the form of a Bell state. Our proposal broadens the palette of emitters suitable for entangled photon state generation and permits to increase the performance of previously available sources. The thesis concludes with an outlook towards multi-photon state creation.

Zusammenfassung

Spin-Photonen Verschränkung stellt die Basis für zahlreiche Anwendungen in den Quantentechnologien dar, wie der Quantenkommunikation und von Quantenberechnungen. Vorschläge zu Quantenberechnungen und Quantennetzwerken benötigen hoch verschränkte photonische Vielteilchen-Ressourcenzustände und Quanten Emitter können verwendet werden um diese herzustellen, wenn Spin-Photonen Verschränkung verwendet wird. Jedoch stellen die bisher vorgeschlagenen Methoden strenge Voraussetzungen an deren Energiezustände und optischen Übergänge. In dieser Dissertation wird ein Protokoll präsentiert, um photonische Ressourcenzustände herzustellen, welches die Voraussetzungen für den Emitter wesentlich lockert, wodurch die Methode für eine Reihe von möglichen Photonenquellen verwendbar ist. Die Verbesserung wird durch Verwendung nur eines einzigen optischen Überganges erreicht und durch einen Wechsel in eine zeitliche Domäne. Ein unausgeglichenes Interferometer konvertiert das temporale photonische Qubit in eine Polarisationsbasis, die für Quantenlogik und Tomografie nützlich ist. Die Dissertation behandelt detailliert die experimentelle Realisierung des Hauptblockes des vorgeschlagenen Protokolls, das prinzipiell skalierbar ist, mit einem Stickstoff-Fehlstellenzentrum in Diamant. Verschränkung zwischen dem Spin des Emitters und einem Fluoreszenz-Photon wird demonstriert, in der Form eines Bell-Zustandes. Unser Vorschlag weitet das Spektrum an Emittern, die geeignet sind um verschränkte photonische Zustände zu generieren und erlaubt eine Steigerung der Leistung für bekannte Quellen. Die Dissertation endet mit einem Ausblick in Richtung von Vielphotonen-Zuständen.

Contents

CONTENTS

<div align="right">

CHAPTER 1

</div>

Introduction

Quantum technology is developing so rapidly, that some even speak of a "second quantum revolution" [78]. Quantum information systems are beginning to surpass their classical counterparts [3, 117], a first inter-city quantum network is being built [18] and in general new quantum technologies are expected to soon become part of everyday life. Prominent examples are technologies for secure communication networks [50, 106], new algorithms for computation [40, 91], and precise sensors [22].

Problem statement and methodology

A substantial research effort is currently directed at the development of sources of large entangled photon states [86, 87, 17, 116], to achieve some of the above introduced goals. A proposal by Lindner and Rudolph [61] put quantum emitters into the spotlight, as viable photonic entanglement generation sources. However, the presented protocol sets stringent requirements on the properties of the emitter - tough to fulfill for real systems. Well researched emitters like quantum dots or the nitrogen-vacancy (NV) centre in general present protocol compatibility, but both have shortcomings too.

This led us to investigate an alternative protocol, that enables to use a lot of the advantageous features of the emitter, while avoiding weaknesses. The alternative protocol relies on generation of spin-photon entanglement between the emitter and its fluorescence photon in two steps instead of a single one, transferring the entanglement into a time basis. By a time-to-polarization conversion (TPC) the photon is recovered in a polarization entangled state, useful for quantum computation or communication applications.

<div align="right">

1

</div>

For the endeavour, an experimental setup was built from scratch at the Technical University of Vienna and University of Vienna and will be reported on in the following chapters. The basis of this work is the experimental demonstration of the core principle of our alternative protocol for imperfect emitters, published in [104]:

Vasconcelos, R., Reisenbauer, S., Salter, C., Wachter, G., Wirtitsch, D., Schmiedmayer, J., Walther, P., and Trupke, M. (2020). Scalable spin-photon entanglement by time-to-polarization conversion. *npj Quantum Information*, 6(1):1-5.

Structure of the Thesis

The thesis is structured as follows:

Chapter 2 starts with a brief introduction to quantum computation and motivates that entanglement can be viewed as a computational resource. Light is shed on the options to create entangled photonic states. A proposal for photonic cluster state production via the aid of a quantum emitter [61] is discussed, which this work is based on. Our ideas of adaption to an imperfect emitter are introduced and positioned within a state-of-the-art context.

Chapter 3 introduces the chosen example emitter for this work, the NV centre. The centre's physics, starting from symmetry arguments, is laid out piece by piece as relevant for later sections of this work.

Chapter 4 accomodates a full description of the experimental setup, the hardware and the routines used and developed for manipulation of NV centres at cryogenic temperatures.

Chapter 5 discusses our aim to work with a single optical transition of a highly crystal strained centre, in the form of the necessary gates for quantum state manipulation, state tomography and newly devised state initialization methods.

Chapter 6 contains the experimental realization of spin-photon entanglement in a time basis followed by TPC. The obtained results are discussed and an outlook for achieving multi-photon states is given.

Chapter 7 treats possible system upgrades and gives an outlook for generating a multi-photon state before concluding.

CHAPTER 2

Scalable Spin-Photon Entanglement - a Universal Resource for Quantum Computation and Communication

2.1 Quantum computing - entanglement as a resource

In the following, a short introduction to quantum computational key concepts relevant for this work is given, followed by a discussion on the role of entanglement in quantum computation, to point at the context of the concepts presented in this thesis.

2.1.1 A brief introduction to quantum computing

While in classical computing the bit serves as fundamental unit of information, in quantum computation the concept of the quantum bit (qubit) has been established as the basic unit of quantum information.[1] A qubit is associated with a specific state, however since that state is described by a linear combination

$$|\psi\rangle = a\,|0\rangle + b\,|1\rangle\,, \tag{2.1}$$

of the computational basis states $|0\rangle$ and $|1\rangle$ with a and b complex numbers, there are not only two states like for classical bits, but infinitely many. Another key difference to

---

[1]The introduction given here follows roughly the one in Nielsen, Chuang: Quantum Computation and Quantum Information, 2010 [73].
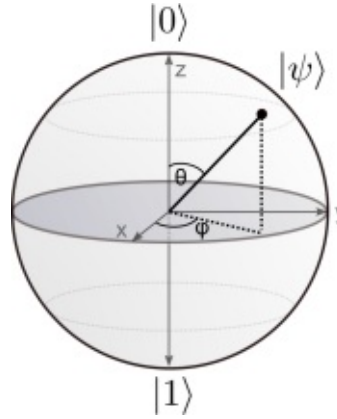
Figure 2.1: *Bloch sphere: A general state $|\psi\rangle$, defined by the angles θ and φ, is representable as a point on the surface of a unit sphere with poles $|0\rangle$ and $|1\rangle$.*

classical bits is the impossibility to measure the exact state of the qubit. On measuring the qubit in the computational basis the state $|0\rangle$ is received with probability $|a|^2$ and the state $|1\rangle$ with probability $|b|^2$, with $|a|^2 + |b|^2 = 1$, due to probability conservation. The qubit can be represented as a unit vector in a complex two-dimensional vector space. A representation of a qubit as

$$|\psi\rangle = \cos(\theta/2)\,|0\rangle + e^{i\varphi}\sin(\theta/2)\,|1\rangle\,, \tag{2.2}$$

with θ and ϕ real numbers, offers a convenient pictorial representation of a qubit on the Bloch sphere, shown in figure 2.1. The values of θ and ϕ define the angles of the vector of the state representation on this unit sphere, which allows to visualize single-qubit manipulations in an intuitive manner.

Scaling up, with two qubits the computational basis formed would include four possible computational basis states, $|00\rangle$, $|01\rangle$, $|10\rangle$ and $|11\rangle$. Again, superposition of these basis states expresses the state vector,

$$|\psi\rangle = a_{00}\,|00\rangle + a_{01}\,|01\rangle + a_{10}\,|10\rangle + a_{11}\,|11\rangle\,, \tag{2.3}$$

where the normalization condition is $\sum_{x \in \{0,1\}} |a_x|^2 = 1$, with the complex probability amplitudes a_x. This hints at the growth of the basis of the vector space for a number of n qubits as 2^n. This exponential scaling of probability amplitudes for large Hilbert spaces cannot be stored on classical computers any more. However, a quantum system naturally handles all of this information and could therefore provide so far unknown computational power.

Gate name	X-gate (X)	Z-gate (Z)	Hadamard (H)
Gate effect	Bit flip	Phase flip	2-axis rotation
Matrix notation	$\begin{bmatrix} 0 & 1 \\ 1 & 0 \end{bmatrix}$	$\begin{bmatrix} 1 & 0 \\ 0 & -1 \end{bmatrix}$	$\frac{1}{\sqrt{2}}\begin{bmatrix} 1 & 1 \\ 1 & -1 \end{bmatrix}$

Table 2.1: *Important single-qubit gates.*

Similarly to classical computation, the distribution and manipulation of information in a quantum computation can be broken down to a description via a quantum circuit with wires and logic gates respectively. In that case, the gates perform unitary actions on a certain number of input qubits. In order to perform arbitrary computations a set of universal operations is needed, like in classical computing. For quantum computations such a set can be constructed from single and two-qubit gates.

The most important single-qubit gates are those which allow to realize arbitrary rotations of the qubit state vector (on the Bloch sphere). The most common single-qubit gates and the corresponding unitary matrices are indicated in table 2.1.

A prominent two-qubit gate is the controlled-NOT or CNOT gate (sometimes CX), which has two inputs - one acting as control qubit and the second as the target qubit. The action of the CNOT on the input state is a bit flip on the target qubit, on the condition, that the control qubit is in the state $|1\rangle$. As an expression for two qubits with the first being the control, the second the target: $|00\rangle \rightarrow |00\rangle$; $|01\rangle \rightarrow |01\rangle$; $|10\rangle \rightarrow |11\rangle$ and $|11\rangle \rightarrow |10\rangle$ or

$$\text{CNOT} |A, B\rangle \rightarrow |A, B \oplus A\rangle, \tag{2.4}$$

where $\oplus$ is addition modulo two. The second common two-qubit gate is the controlled-Z gate (CZ), which is related to the CNOT by [53]

$$\text{CNOT} = \text{H} \cdot \text{CZ} \cdot \text{H}, \tag{2.5}$$

with Hadamard gates acting on the target state. The action of the CZ gate is a phase flip on the target qubit when both the control and the target are $|1\rangle$.

It is shown in Nielsen [73] that single-qubit gates and the CNOT (or CZ) gate are sufficient to perform any unitary operation on a set of qubits, which renders them a universal gate set for quantum computation.
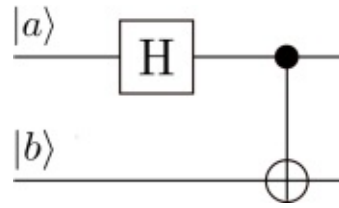
Figure 2.2: *Bell state creation circuit diagram: qubits $|a\rangle$ and $|b\rangle \in \{|0\rangle, |1\rangle\}$; a Hadamard gate is acting on $|a\rangle$ which is in control of the CNOT gate thereafter. CNOT symbol: a black dot marks the control qubit, which is connected by a circled vertical line to the target.*

Input state $|ab\rangle$	Hadamard-gate	CNOT-gate	Output Bell state
$|00\rangle$	$\frac{1}{\sqrt{2}}(|0\rangle + |1\rangle)|0\rangle$	$\frac{1}{\sqrt{2}}(|00\rangle + |11\rangle)$	ϕ^+
$|01\rangle$	$\frac{1}{\sqrt{2}}(|0\rangle + |1\rangle)|1\rangle$	$\frac{1}{\sqrt{2}}(|01\rangle + |10\rangle)$	ψ^+
$|10\rangle$	$\frac{1}{\sqrt{2}}(|0\rangle - |1\rangle)|0\rangle$	$\frac{1}{\sqrt{2}}(|00\rangle - |11\rangle)$	ϕ^-
$|11\rangle$	$\frac{1}{\sqrt{2}}(|0\rangle - |1\rangle)|1\rangle$	$\frac{1}{\sqrt{2}}(|01\rangle - |10\rangle)$	ψ^-

Table 2.2: *Bell state creation: depending on the input states, one of four Bell states is available after the circuit. Columns detailing the action of the Hadamard and CNOT gates on the states are given.*

2.1.2 Entanglement as a resource

Qubits alone are not enough for quantum computation, an overarching power of future quantum technologies lies in the property of entanglement of states. Entanglement in quantum computation plays the role of a whole new type of resource, that doesn't have a classical counterpart [73]. It reflects the property of quantum systems, that makes them impossible to simulate on a classical computer [42]. To enlighten, why entanglement can be interpreted as a resource, the quantum teleportation algorithm is briefly presented. Using the Hadamard and CNOT gates, a type of basic entangled state, called Bell state can be created. As taken from Nielsen [73, p. 16], "this innocuous-looking state is responsible for many surprises in quantum computation".

The illustrated circuit (fig. 2.2) works on the states as indicated in the table 2.2, where the Hadamard gate acts on the first qubit and then this qubit acts as the control for the following CNOT operation, which entangles them, resulting in one of the four Bell states [73].

The four Bell states span a basis for bipartite systems. On measuring the first sub-

6

system in the computational basis, one will attain $|0\rangle$ and $|1\rangle$ with equal probability, since the state does not give us more information. On the other hand, a measurement on the second system will definitely give a certain outcome, depending on the initial Bell state. Even though we don't have knowledge about each subsystem, we have maximal knowledge about the system as a whole [42].

The quantum teleportation algorithm is a simple algorithm that uses such an entangled state as a resource and demonstrates the power of harnessing entanglement in computational procedures. In teleportation, a state is transferred to another site without qubit transmission, only classical communication and entanglement is necessary. Assuming two parties, Alice and Bob, who share an entangled state ϕ^+, the protocol starts with Alice possessing a state $\chi = a|0\rangle + b|1\rangle$, she wants to hand over to Bob. They share a classical communication channel only. Their combined state is

$$|\chi\rangle|\phi_+\rangle = a|0\rangle + b|1\rangle \cdot \frac{1}{\sqrt{2}}(|00\rangle + |11\rangle) = \frac{1}{\sqrt{2}}(a|000\rangle + a|011\rangle + b|111\rangle + b|100\rangle),$$
(2.6)

which can be factored in terms of Bell states as

$$\begin{aligned}
|\chi\rangle|\phi_+\rangle = {} & \frac{1}{2}|\phi_A^+\rangle(a|0\rangle_B + b|1\rangle_B) \\
& + \frac{1}{2}|\phi_A^-\rangle(a|0\rangle_B - b|1\rangle_B) \\
& + \frac{1}{2}|\psi_A^+\rangle(a|1\rangle_B + b|0\rangle_B) \\
& + \frac{1}{2}|\psi_A^-\rangle(a|1\rangle_B - b|0\rangle_B),
\end{aligned}$$
(2.7)

where the qubits of Alice are labelled with A and the one of Bob with B. When Alice measures her two qubits, she communicates her measurement outcomes to Bob classically, so that Bob can recover the state χ on his qubit, by applying one of four possible unitary operations depending on Alice's measurement result. Put in other words, an entangled state is a resource for the transmission of a qubit [42].

Going a step further, teleportation can be used to perform unitary evolution on the target state, induced by measurements, graphically shown in a quantum circuit in figure 2.3a. The state to evolve $|\psi\rangle$ is entangled with an ancilla $|+\rangle$ state $(= \frac{1}{\sqrt{2}}(|0\rangle + |1\rangle))$ by a CZ gate. A Hadamard gate follows and the desired unitary rotation for an angle α around the z-axis, $U_Z(\alpha)$, on the first qubit. Measurement with an observable defined by α, teleports the rotation to the second qubit up to a known factor X^m, depending on
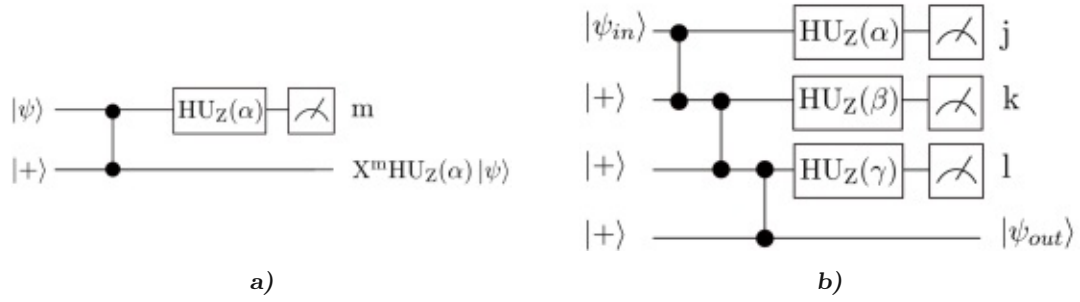
Figure 2.3: *a) Unitary z-rotation by measurement: a CZ-gate (two connected black circles) entangles the input state $|\psi\rangle$ with the ancilla state $|+\rangle$. Performing the rotation and subsequent measurement teleports the rotated input state up to a factor X^m, determined by the measurement outcome m. Note that the circuit compares to the discussed teleportation in that $|+\rangle = H|0\rangle$ and $H \cdot CZ \cdot H = CNOT$. b) General state rotation by measurement: the output state $|\psi_{out}\rangle$ depends on the measurement results j, k and l. On 'feeding' the obtained information forward to the next measurement, the rotated original state can be recovered at the output.*

the measurement result m. Unitary evolution of the state was induced by the measurement [53].

For an arbitrary unitary single-qubit rotation U, three rotations by angles α, β and γ around two axes on the Bloch sphere are required.

$$U = U_Z(\gamma)U_X(\beta)U_Z(\alpha), \tag{2.8}$$

and with $X = HZH$ one can restrict to z-rotations only as

$$U = HHU_Z(\gamma)HU_Z(\beta)HU_Z(\alpha), \tag{2.9}$$

shown as a circuit in figure 2.3b. The input states, entangled with CZ gates, present a type of resource, on which the state is evolved. States produced in this manner are called 'cluster states'. This behaviour of manipulation and measurement on an initially entangled state builds a basis for measurement based quantum computation [53].

Raussendorf et al. [80] showed deterministic universal quantum computation to be possible by teleporting the encoded information through a two-dimensional cluster with single-qubit measurements only.

Cluster states $|C\rangle$ represent a large family of highly entangled states, that obey the eigenvalue equation

$$S_i|C\rangle = \pm|C\rangle, \tag{2.10}$$
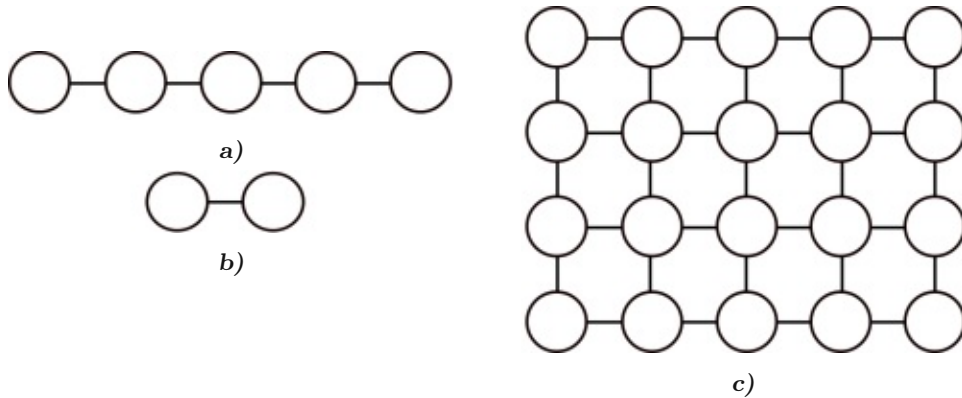
Figure 2.4: *Cluster state representation:* **a)** *a five qubit linear cluster state,* **b)** *a Bell state and* **c)** *a two dimensional cluster suitable for universal computation.*

for a qubit at site i with the commuting operators S_i called stabilizer generators [81]. The stabilizer generator is given by

$$S_i = X_i \otimes_{j=1}^{k} Z_j, \tag{2.11}$$

over all k neighbours of the qubit at i. Cluster states are graphically represented by nodes (physical qubits in state $|+\rangle$) and pairwise connections (CZ-gates between them), as shown in figure 2.4 for a linear cluster state, a Bell state and a two-dimensional cluster state.

2.1.3 Creating and using entangled resource states

"The primary challenge facing optical quantum computation is that of building suitable photon sources." [61, p.1]. Since the generation of a cluster state needs two-qubit interaction, it is problematic to achieve in photonic systems [54]. A lot of research is invested in sources that would be capable of delivering Bell states or even more advanced, linear cluster states. An approach by Browne and Rudolph [15], following earlier proposals of Yoran and Reznik [112] and Nielsen [72], introduced a probabilistic algorithm for generating two-dimensional cluster states using parity gates.

Browne and Rudolph presented a scheme for growing and connecting cluster states probabilistically. They showed that when building up a larger cluster from smaller cluster states or Bell states, the cluster doesn't need to grow at each operation, but on average. The condition imposed on the size m of the newly added cluster being, that it has to

exceed

$$m > \frac{pd_s + (1-p)\,d_f}{p},\tag{2.12}$$

with p being the success probability of the operation and d_s, d_f the number of qubits lost in the success case and failure case of the cluster fusion operation, respectively. Using two types of gates, introduced as fusion gates type I and type II, the scheme avoids the optically hard to implement two-qubit CZ-gates altogether.

On the other hand, instead of working with trial until success, ballistic methods have been presented as a possible alternative [34]. The concept here being, that a cluster state lattice is attempted to be prepared and when some sites fail in the nearest neighbour entangling step, the lattice remains incompletely connected. Percolation theory establishes a threshold probability for these operations, above which the lattice will still be connected "enough", so that it is usable for computation.

A proposal combining both methods mentioned above was put forward by Rudolph in 2017, showing optimism for an integrated-photonic route to large scale quantum computation [86]. He argues that the key challenge for photonic quantum computation is the development of suitable photon sources.

In parallel to these developments in the field of quantum computation, photonic entangled states were adopted as a resource for quantum communication as well [6]. Quantum communication is concerned with secure communication [35], state teleportation [11] and the layout of a quantum network / internet [50, 106].

Photons are excellent information transmission units, but loss in fibres still leads to an exponential decay of signal over tens of kilometres. Quantum repeaters were proposed to recover a polynomial scaling, with the prospect to build up large scale entanglement through the aid of repeater stations [88, 69]. Recently, photonic entangled states, called repeater graph states, were proposed as an efficient resource for the process [6, 17].

2.2 Approaching entangled photons from an imperfect emitter

The aim of the current work falls into the area of developing sources capable of producing photonic entangled resource states - the idea being to manipulate an emitter in order to produce a string of entangled photons, following a proposal by Lindner and Rudolph [61].
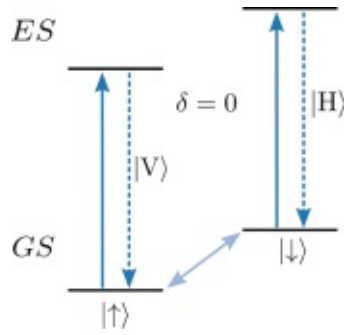
Figure 2.5: *Ideal level scheme for the cluster state generation protocol: two ground state levels (GS) are connected by two degenerate optical transitions ($\delta = 0$, solid arrows) to the excited states (ES). The fluorescence (dashed arrow) is polarized according to the state either horizontally (H) or vertically (V). The ground states may be manipulated to bring them into a superposition state (light blue arrow).*

2.2.1 An emitter based proposal for a photonic cluster state

As motivated in the previous chapter, a device capable of producing resource states for optical quantum technologies would be highly interesting. In 2009, Lindner and Rudolph proposed a new scheme for linear cluster state generation, based on the manipulation of a single emitter [61]. The presentation of the algorithm in the article focuses on an implementation with quantum dots. Nevertheless, it is suitable for other emitters, as long as they fulfil certain criteria:

The emitter needs to have,

1. two ground state levels that can be superimposed,

2. connected by two degenerate optical transitions to excited states,

3. which emit fluorescence photons that have distinct polarizations, determined by the states spin state, and that decay faithfully to the original ground state.

These properties are visualized in figure 2.5.

The protocol as presented here is slightly adapted in notation. It starts with the ground state spin in an equal superposition of basis states $|\uparrow\rangle$ and $|\downarrow\rangle$ as $\frac{1}{\sqrt{2}}(|\uparrow\rangle + |\downarrow\rangle)$. Optical excitation, polarized to equally excite both transitions, leads to subsequent emission of a fluorescence photon with polarization conditional on the initial ground state spin, where $|\downarrow\rangle$ ($|\uparrow\rangle$) leads to emission of a horizontally (H) (vertically (V)) polarized photon, respectively. The process ends up in the same state it started from and the spin
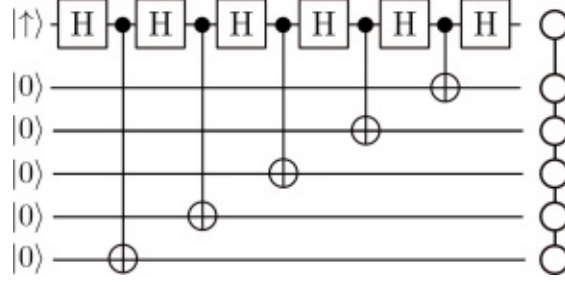
Figure 2.6: *Linear cluster state creation circuit. A spin system starting in $|\uparrow\rangle$ is manipulated with rotations (here Hadamard gates), interlaced with CNOT operations on five photon states initially in $|0\rangle$, producing a six qubit linear cluster state.*

entangled with the emitted photon in the Bell state

$$\frac{1}{\sqrt{2}}\left(|\uparrow\rangle\,|V\rangle + |\downarrow\rangle\,|H\rangle\right). \tag{2.13}$$

Continuing the excitation cycles would produce a Greenberger-Horne-Zeilinger (GHZ)-type state; in order to produce a cluster state, an additional gate is introduced in each step. The spin is rotated (by $\theta = \pi/2$) around the y-axis, which evolves the state to

$$\frac{1}{2}\left[(|\uparrow\rangle + |\downarrow\rangle)\,|V_1\rangle + (-\,|\uparrow\rangle + |\downarrow\rangle)\,|H_1\rangle\right]. \tag{2.14}$$

The second excitation-emission cycle will yield the state

$$\frac{1}{2}\left[(|\uparrow\rangle\,|V_2\rangle + |\downarrow\rangle\,|H_2\rangle)\,|V_1\rangle + (-\,|\uparrow\rangle\,|V_2\rangle + |\downarrow\rangle\,|H_2\rangle)\,|H_1\rangle\right], \tag{2.15}$$

using the qubit encoding $|V\rangle = |0\rangle$, $|H\rangle = -\,|1\rangle$

$$\frac{1}{2}\left[|\uparrow\rangle\,|00\rangle - |\downarrow\rangle\,|10\rangle + |\uparrow\rangle\,|01\rangle + |\downarrow\rangle\,|11\rangle\right]. \tag{2.16}$$

Performing another $\pi/2$-rotation around the y-axis leads to the state

$$\frac{1}{2\sqrt{2}}\left[(|\uparrow\rangle + |\downarrow\rangle)\,|00\rangle - (-\,|\uparrow\rangle + |\downarrow\rangle)\,|10\rangle + (|\uparrow\rangle + |\downarrow\rangle)\,|01\rangle + (-\,|\uparrow\rangle + |\downarrow\rangle)\,|11\rangle\right], \tag{2.17}$$

which is a 3-qubit linear cluster state, becoming visible when encoding $|\uparrow\rangle$ as $|0\rangle$ and $|\downarrow\rangle$ as $|1\rangle$,

$$\frac{1}{2\sqrt{2}}\left[|000\rangle + |100\rangle + |010\rangle - |110\rangle + |001\rangle + |101\rangle - |011\rangle + |111\rangle\right]. \tag{2.18}$$

The process can be continued, whereby each time a photon-qubit is added to the linear cluster. The procedure's circuit representation is shown in figure 2.6.
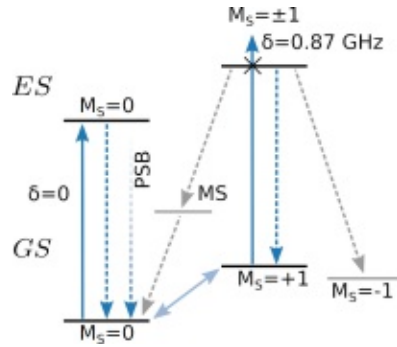
Figure 2.7: *Simplified energy level scheme of our NV centre: two of the three ground states (GS) present may be chosen as qubit space. Excited states (ES) are detuned (δ) and the $M_S = \pm 1$ excited state has a significant decay into a metastable level (MS), which may result in cross decay to the $M_S = 0$ ground state. All excited states exhibit dominant off-resonant fluorescence decay via the phonon sideband (PSB).*

Adaption to the imperfect emitter

The scheme presented above is highly idealized, since it assumes ideal properties of the emitter in fulfilling the requirements. To present day, no emitter perfectly suited to the criteria is known. In our approach we adapt the protocol to be performed with a single NV centre in diamond.

NV centres naturally offer very advantageous features for such an implementation. The centre has been researched since decades and is today a well known photostable single-photon emitter with long coherence times both for its electron and nuclear spin in the range of up to milliseconds and hours respectively [26, 8, 66]. The presence of a long lived nuclear spin opens up new perspectives in the context of the cluster state generation protocol, for example two-dimensional states or cluster states on the nuclear spins altogether [70].

The NV centre has bright optical resonances and features a compatible energy level scheme for the cluster state protocol (fig. 2.7). Methods for fabrication of NV devices, spin state preparation, manipulation and readout have been well established [26, 68].

On the downside, the centre has some challenging properties to tackle - the level scheme is far from ideal for the protocol. The most prominent features in this context being: the necessity to tune the energy levels into resonance without introducing state mixing and the significant probability of cross decay to a non-spin conserving metastable level. Moreover, the decay on resonance via the zero-phonon line (ZPL) happens only about 2 % to 3 % of the time and effective light extraction from the high refractive index
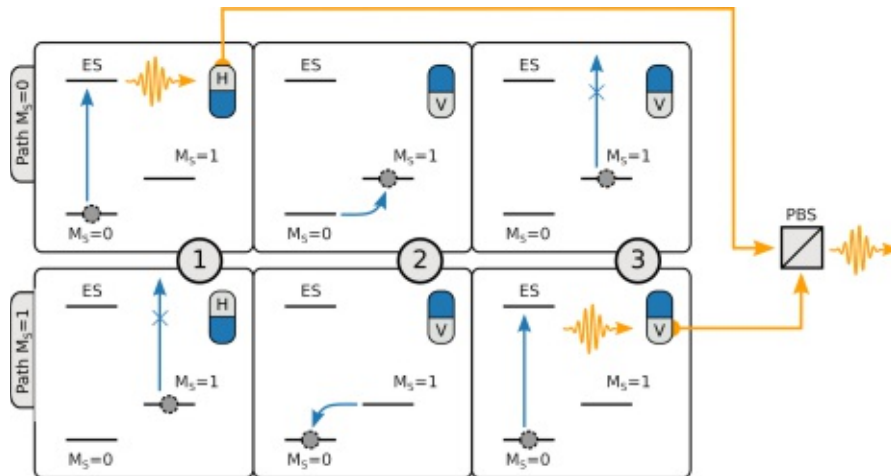
Figure 2.8: *Modified entanglement generation protocol.*

diamond host is a challenge. The centre's optical transition frequencies are prone to drifts, due to susceptibility to electric and magnetic fields as well as temperature changes [26]. In the protocol, initialization and manipulation errors may occur and finite coherence time can further limit the performance.

We propose a modification of the original protocol to overcome some of these hurdles. Based on only a single optical resonance, combined with TPC, the advantageous features of the centre are exploited, while resonance tuning and cross-decaying transitions are avoided. Even though this scheme is designed for use with an NV centre, it is not emitter specific and could be used for other emitters that do not adhere to the original requirements of the Lindner-Rudolph protocol.

A sequential depiction of our protocol is shown in figure 2.8. It starts from an equal superposition of two ground state levels, where only the $M_S = 0$ state is resonant to the optical transition. Two paths according to the respective ground state are enlightened (rows). Optical excitation may produce a fluorescence photon in the first path only (step one), which is routed to a channel with horizontal polarization (H). After flipping the spin with a short microwave pulse in step two, a second round of excitation again generates a photon, this time in the second path, that is routed into a vertically polarized channel (step three). The photonic channels are time-matched with the sequence, so that the created fluorescence photon parts overlap at a polarizing beam splitter (PBS), thereby

performing a conversion from a time- to a polarization-basis, achieving the output state

$$\frac{1}{\sqrt{2}}\left(\left|0\right\rangle\left|V\right\rangle + e^{i\phi}\left|1\right\rangle\left|H\right\rangle\right), \tag{2.19}$$

which is of a ψ^+-Bell-type state and where ϕ is an optional phase. A multi-photon cluster state could then be created by further iteration of this sequence with some additional microwave operations (see chapter 7).

In order to estimate if this approach is feasible and to compare it to other systems, an entangled photons per second estimation is useful: The largest bottleneck is assumed to be the optical setup with a total transmission of less than $1\,\%$. With only about $2\,\%$ of the light being in the ZPL frequency window of usable photons, this yields a detection efficiency on the order of 2×10^{-4}. A duration of the whole cycle of $200\,\mu s$, which is on the upper bound, would result in a repetition frequency of $5\,kHz$, thereby producing one entangled spin-photon pair per second. This rate is low but can be improved and provides realistic conditions for observation in experiment. The estimation incorporates the assumption that initialization and all operations have unit fidelity.

2.2.2 State of the Art

The deterministic and scalable creation of photonic entangled resource states persists to be a challenge [86].

A promising path for generating large entangled photonic states is being followed in spontaneous parametric down-conversion (SPDC) sources [16, 57]. By using the optical non-linearity of a material and by considering certain rules, known as phase matching conditions[2], a pump laser photon may split into two correlated photons. Under type II phase matching, where the photons have opposite polarization, they are each emitted into a cone in the direction of the pump beam propagation. When the cones overlap, at the intersection points, the light is in an entangled state of Bell-type.

By pumping more than one SPDC source with the same pulse, two or more Bell pairs can be fabricated, and using projective measurements, larger photon states can be grown [113, 49, 114]: from a six-photon graph state by Lu et al. in 2007 [63], to a 10-photon GHZ state by Wang et al. in 2016 [105] and a 12-photon source in 2018 [116]. Recently, a four-photon source in an integrated photonic circuit was demonstrated, that would increase stability and scalability tremendously [115].

---

[2]These include temporal overlap, energy conservation and momentum conservation.

However, this type of source for entangled states is inherently probabilistic by the spontaneous nature of the down conversion process involved. Remedies could be temporal or spatial multiplexing and "dumping the pump" approaches, which are being researched [86, 93].

Coupled atom-cavity systems were proposed as deterministic generators of entangled multiqubit states [89] and have been shown to implement a conditional gate on photons [82] through an atom-photon state sensitive phase shift on reflection from an atom-cavity system. The generation of a photonic $\phi^{\pm}$-Bell state was demonstrated, with the outlook to produce a cluster state with single photon manipulations. On the down side, during the lengthy atom state manipulations, photons would need to be stored on the order of μs and single photons need to be operated on conditioned on the atom state measurement outcome. The demonstration used a faint laser pulse as photon source but could be pumped with a deterministic single photon source.

Instead of using a separate photon source, single-photon emitters like quantum dots or NV centres present trigger-able sources of close to indistinguishable photons [1], suited to generate photonic entangled states both for quantum computation and communication [87, 17].

With the publication of the cluster state fabrication protocol by Lindner and Rudolph [61], where a spin acts as an entangling agent on consecutively emitted photons, interest was sparked to investigate possible physical realizations of such an on demand source for large entangled photon states. This work falls into that category.

The intended platform of the proposal is the quantum dot system and in 2016 a publication by Schwartz et al. [90] demonstrated a proof of principle, by assembling a three-qubit photonic cluster state. Nonetheless, the imperfections of the emitter system limited the achieved entangling fidelity.

For the NV centre, where spin-photon entanglement had been shown by Togan et al. [101] already in 2010, proposals to deterministically produce a photonic entangled state have been put forward as well. Rao et al. [79] suggested a periodically pumped lambda scheme, which makes use of the nuclear spin as an entanglement memory connected to the photons. This protocol was deemed unsuitable for our system due to the large experimental overhead required, which included multiple optical, microwave, and radio-frequency drives. Nuclear spin control is furthermore time-consuming within the experimental sequence, and hard to implement under cryogenic conditions.

As the originally proposed Lindner-Rudolph scheme requires two degenerate optical transitions without cross decay, it is challenging to implement with real emitters. Our proposal of the adaption of the protocol for imperfect emitters avoids these shortcomings by using a strong single optical transition. Another aspect of this feature is the compatibility with optical cavity systems in the future, intended to go beyond few photon proof of principle experimental realizations. Another discerning feature of our approach is the (optional) conversion of the entangled photonic state from a temporal basis to a polarization one, useful in quantum computation applications[3].

---

[3]During the preparation of our publication we became aware of efforts to use a single optical transition time-bin approach in a quantum dot [59] and during the review process later work appeared which uses a time-bin approach with NV centres [98].

CHAPTER 3

The Nitrogen Vacancy Centre

The chosen emitter for our devised protocol, presented in the previous chapter, was the NV colour centre in diamond. The selection, due to the many virtues of the centre, is now briefly motivated here in section 3.1, followed by a more thorough introduction to the emitter for various relevant aspects of this work in section 3.2.

3.1 Introduction to the nitrogen-vacancy centre

3.1.1 The nitrogen-vacancy centre in the hall of fame of quantum physics

Under all known point emitters and color centres, the NV centre is probably the most studied one due to its versatile features, allowing experimenters to confide in the extensive available literature for reference. The centre is stable, naturally present in diamond and relatively easy to initialize, manipulate and read out (see chapter 4). Its characteristics fulfil DiVincenzo's criteria [24] for quantum computation and it has proven itself in a range of pioneering experiments in this area: spin-photon entanglement between two such emitters was performed [12], succeeded by a quantum teleportation [75] experiment shortly after. In 2015 a loophole-free Bell test was published by the same group [41] currently setting up a first quantum network, linking four cities in the Netherlands, using NV centres [18]. Even at room temperature (RT) the NV centre shines: it has long spin coherence times of up to milliseconds [8], the electron spin can be coupled to

19

nuclear spins nearby which act as a quantum register [28, 66], or to hyperpolarize the nuclear spins in the crystal [52]. The centre's susceptibility to temperature and fields has been employed for sensing [9, 7, 108] - even thermometry in living cells was shown [55], as well as micro-NMR [64, 36]. Commercial products are starting to become available[1] and electrical circuit integration appears to soon be possible for such [92].

3.1.2   Landmark properties of the nitrogen-vacancy centre

The NV centre comprises by a nitrogen atom next to a lattice vacancy in the diamond crystal, each replacing a carbon atom. It features a spin-1 triplet ground state connected to an excited state manifold via spin-character conserving optical transitions at 637 nm (1.945 eV). Resonant excitation allows to pick certain transitions while off-resonant excitation (e.g. with a green laser) admits an optical pumping cycle, involving intermediate singlet states, which leaves the centre strongly spin-polarized in the $M_s = 0$ ground state, providing a convenient initialization pathway. This off-resonant excitation furthermore has the capability to (de-)ionize the centre so that it can be returned to the naturally occurring negatively charged state (NV$^-$) from a neutrally charged version of the centre (NV^0). Only about 3% of the high fluorescence yield on the order of 10^6 photons per second originate from ZPL transitions, while fluorescence from transitions involving phonons (PSB-transitions) makes up the rest. Experimentally, the PSB portion of the fluorescence can be rendered useful to read the centre's ground state spin [26].

3.1.3   The diamond host

"Practically every publication on research involving diamond materials begins by touting the extreme and unique physical and chemical properties of diamond" [68, p. XV]. Well appreciated for optical endeavours is the wide low temperature band gap of 5.5 eV (226 nm wavelength cut-off) in diamond [68] (see fig. 3.1), since localized ground and excited states of impurities like the NV centre become optically addressable, and at the same time are well isolated from the lattice valence and conduction band. The material's wide spectral transparency window is harnessed in optical experimentation, while the "relatively low phonon population compared with other crystals" preserves quantum coherence [77, p. 5].

---

[1]E.g. http://qzabre.com
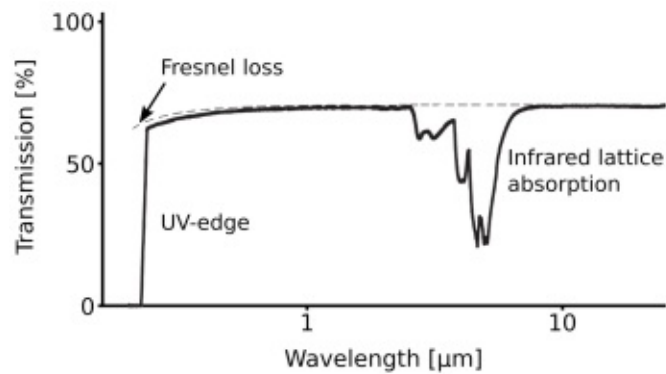
a)

Figure 3.1: *Transmission spectrum of a* 1 mm *thick diamond with cut off at about* 226 nm. *Dashed curve indicates calculated Fresnel loss. Data source [68].*

Diamond has high thermal conductivity, aiding in low temperature settings for fast excitation energy dissipation. Durability and chemical inertness crown the materials profile. Cheap high-grade and custom made crystals have become available through advances in diamond engineering technology [68]. It is furthermore possible to grow crystals which are almost free from unwanted nuclear spins (e.g. ^{13}C), that could degrade coherence times by introducing proximal magnetic field fluctuations.

However, diamond also presents some experimentally challenging properties; notably the high refractive index of 2.4 [68] at 600 to 800 nm wavelength, which leads to high optical transmission losses at interfaces. Material fabrication, shaping and surface polishing is challenging due to the crystals' resistance to deformation, though huge advances have been made in these areas [68]. Finally, crystal imperfections (e.g. like high internal crystal strain) will influence the behaviour of susceptible centres, like the NV centre, strongly (see section 3.2.5).

Quantum technologies have profited enormously from advances in material fabrication by chemical vapour deposition (CVD) diamond growth. This method uses a low pressure plasma to grow layers of diamond with precisely controllable growth parameters and the options of having ultra-pure crystals, doping with other species or using defined amounts of carbon isotopes [68].

21

3.1.4   Nitrogen-vacancy centre creation

NV centres can form naturally in diamond since it is energetically favourable for the vacancies in the crystal lattice to stick to a nitrogen impurity. There are three common artificial methods to create the centres by either introducing vacancies into the lattice of nitrogen containing diamond or by introducing both components: ion implantation with nitrogen or other atoms, irradiation of diamond containing nitrogen with electrons or positrons and nitrogen doping during CVD crystal growth. The process is often followed up on with high temperature annealing (T>650 °C), which causes vacancies to become mobile in the lattice [77].

3.2   The physics of nitrogen-vacancy centres

Structural understanding leads to insights into the physics of the centre. The method employed is a group theoretical analysis, which is a quite mathematical approach that yields surprisingly deep insight from symmetry arguments alone. In this section, starting from group theory, NV centre states and their ordering are derived. Light is shed on effects from perturbations, on optical transitions and on optical pumping dynamics.

3.2.1   Group theory approach to orbitals

As introduced above, the centre consists of a nitrogen atom neighboured by a lattice vacancy of the diamond crystal. The nitrogen to vacancy axis can have eight different orientations in the crystal. It is the axis of highest symmetry in the defect and will be important in the following description of the defects electronic structure. The diamond lattice carbon atoms are bounded through covalent bonds to their neighbours. A vacancy containing defect breaks the regular crystal symmetry and leaves the neighbouring atoms with dangling bonds as shown in figure 3.2a. These dangling bonds consist of one sp^3-hybridized orbital filled with a single electron of the three carbon atoms each (ρ_{1-3}) and one sp^3-hybridized orbital ρ_n with two electrons from the nitrogen atom in a tetrahedral configuration. We choose the z-axis to lie in the symmetry axis of the centre. Then we find that certain symmetry operations on the centre around this axis are possible that leave the centre physically unchanged, e.g. rotations around the z-axis. Since the Hamiltonian needs to be invariant under such operations, an operation described by R
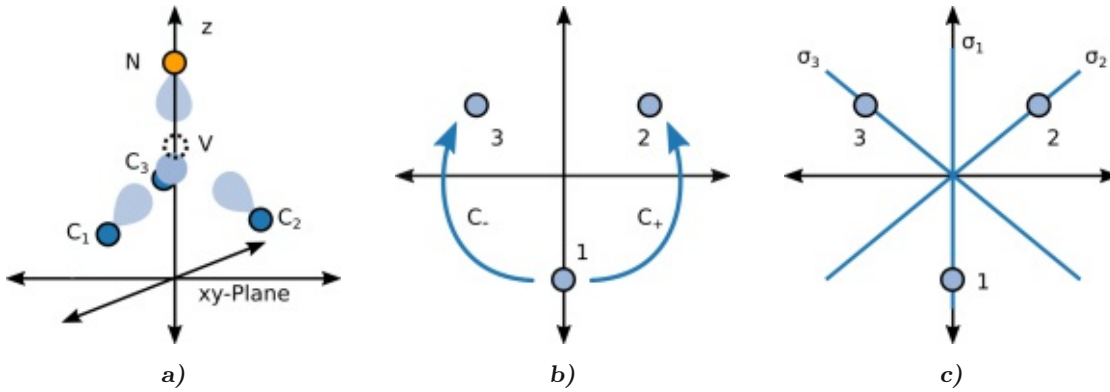
Figure 3.2: *NV centre structure and symmetry operations:* **a)** *structure with symmetry axis along z-direction. N - nitrogen atom, V - vacancy, C_{1-3} carbon atoms. Dangling bond orbitals shaded in light blue.* **b)** *View along symmetry axis with carbon atoms labelled 1-3. Clockwise C_- and anticlockwise C_+ rotation by an angle of $\frac{2\pi}{3}$ and* **c)** *three reflection planes σ_{1-3} leave the centre physically unchanged.*

needs to commute with the Hamiltonian H of the NV centre when acting on a state ψ as

$$\mathrm{RH}\psi = \mathrm{HR}\psi = \mathrm{E}\psi, \tag{3.1}$$

with E being the energy of the state [99]. This insight is useful in that it allows a group theoretical approach to find eigenstates of the system [67]. To work these out, we need to know about the exact symmetries of the centre.

As for rotational symmetry, the centre can be turned along the z-axis by an angle of $\frac{2\pi}{3}$ to replace the position of carbon atoms with a neighbouring one, which gives two possible orientations for the rotation, that are inverse operations of each other (fig. 3.2b). Additionally, the centre offers three possible planes for reflection that leave the centre physically unchanged: each plane of reflection is spanned by the symmetry axis and contains one of the three carbon atoms as shown in figure 3.2c. The action of the reflection is a swap of the carbon atoms not being located in the reflection plane.

Mathematically, these operations are represented by a group consisting of six 2×2-matrices (table 3.1), as it is sufficient for rotations and reflections to operate in the xy-plane. E refers to the identity operation present in every group by definition, C_+ and C_- are the rotation operations and σ_{1-3} are the reflection matrices. This is exactly a representation of the C_{3v} point group, where C_n indicates the existence of a cyclic n-fold rotation axis and v the existence of reflection planes [99].[2] For the C_{3v} point

---

[2]See appendix A for a complete C_{3v} group definition.

23

C_{3v}	E	C_+	C_-	σ_1	σ_2	σ_3
A_1	1	1	1	1	1	1
A_2	1	1	1	-1	-1	-1
E	$\begin{bmatrix} 1 & 0 \\ 0 & 1 \end{bmatrix}$	$\begin{bmatrix} -\frac{1}{2} & -\frac{\sqrt{3}}{2} \\ +\frac{\sqrt{3}}{2} & -\frac{1}{2} \end{bmatrix}$	$\begin{bmatrix} -\frac{1}{2} & +\frac{\sqrt{3}}{2} \\ -\frac{\sqrt{3}}{2} & -\frac{1}{2} \end{bmatrix}$	$\begin{bmatrix} -1 & 0 \\ 0 & +1 \end{bmatrix}$	$\begin{bmatrix} +\frac{1}{2} & +\frac{\sqrt{3}}{2} \\ +\frac{\sqrt{3}}{2} & -\frac{1}{2} \end{bmatrix}$	$\begin{bmatrix} +\frac{1}{2} & -\frac{\sqrt{3}}{2} \\ -\frac{\sqrt{3}}{2} & -\frac{1}{2} \end{bmatrix}$

Table 3.1: *A mathematical representation for the C_{3v} point group.*

defect there are three irreducible representations (IRs): one of them is represented by the above introduced matrices for the group operations and has dimensionality two, therefore labelled as E. Further, there are two one-dimensional representations defined by the unit element and the determinant of group elements, labelled A_1 and A_2 respectively.

A short derivation for four suitable eigenfunctions of the C_{3v} group from single atomic orbitals is given in appendix A. They are labelled: a_C, a_N, e_x and e_y.

3.2.2 Ordering of states

Coulomb interaction

Maze et al. [67] use a simple model of electron-ion Coulomb interaction to model the ordering of the derived single electron orbitals. This interaction leads to a mixing of the levels

$$
\begin{aligned}
a_1(1) &= \alpha a_C + \beta a_N, \\
a_1(2) &= \beta a_C + \alpha a_N, \\
e_x &= \frac{1}{\sqrt{6}} \left(2\rho_1 - \rho_2 - \rho_3 \right), \\
e_y &= \frac{1}{\sqrt{2}} \left(\rho_3 - \rho_2 \right),
\end{aligned}
\tag{3.2}
$$

with ordering of energy levels shown in figure 3.3. The ordering of the energy levels was confirmed by ab initio density functional theory calculations [32].

With the symmetry and the degeneracy of orbitals set, we turn to the dynamics originating from filling the centre with six electrons. The spin behaviour is set through the number of electrons in the system, which is even in NV$^-$. In the electronic ground state, there are four electrons in the a-levels and two in the e-levels, while in the excited
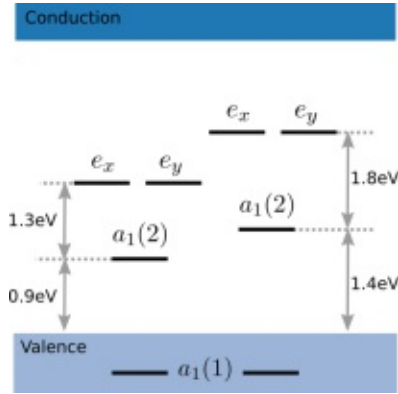
Figure 3.3: *Calculated coulomb and spin-ordering of energy levels with respect to the valence band edge [32].*

Configuration	State	Name
Ground states		
$e^2(T)$	$\|e_x e_y - e_y e_x\rangle \otimes \begin{cases} \|\beta\beta\rangle \\ \|\alpha\beta + \beta\alpha\rangle \\ \|\alpha\alpha\rangle \end{cases}$	$\left.\begin{array}{l} {}^3A_{2-} \\ {}^3A_{20} \\ {}^3A_{2+} \end{array}\right\} \Rightarrow {}^3A_2$
Singlet states		
$e^2(S)$	$\left.\begin{array}{l} \|e_x e_x - e_y e_y\rangle \\ \|e_x e_y + e_y e_x\rangle \\ \|e_x e_x + e_y e_y\rangle \end{array}\right\} \otimes \|\alpha\beta - \beta\alpha\rangle$	${}^1E_1$ ${}^1E_2$ ${}^1A_1$
Excited states		
$ea(T)$	$\|E_-\rangle \otimes \|\alpha\alpha\rangle - \|E_+\rangle \otimes \|\beta\beta\rangle$ $\|E_-\rangle \otimes \|\alpha\alpha\rangle + \|E_+\rangle \otimes \|\beta\beta\rangle$ $\|E_-\rangle \otimes \|\beta\beta\rangle - \|E_+\rangle \otimes \|\alpha\alpha\rangle$ $\|E_-\rangle \otimes \|\beta\beta\rangle + \|E_+\rangle \otimes \|\alpha\alpha\rangle$ $\|Y\rangle \otimes \|\alpha\beta + \beta\alpha\rangle$ $\|X\rangle \otimes \|\alpha\beta + \beta\alpha\rangle$	$\left.\begin{array}{l} A_1 \\ A_2 \\ E_1 \\ E_2 \\ E_y \\ E_x \end{array}\right\} \Rightarrow {}^3E$

Table 3.2: *Hole configurations and namings for selected states discussed throughout the thesis: e symbols a hole in either e_x or e_y while a in $a_1(2)$; T - triplet (S=1), S - singlet (S=0); $E_\pm = \|ae_\pm - e_\pm a\rangle$ where $e_\pm = \mp(e_x \pm ie_y)$; $\|X\rangle = \frac{1}{2}(\|E_-\rangle - \|E_+\rangle)$; $\|Y\rangle = \frac{i}{2}(\|E_-\rangle + \|E_+\rangle)$; α and β indicate the spin parts [67].*
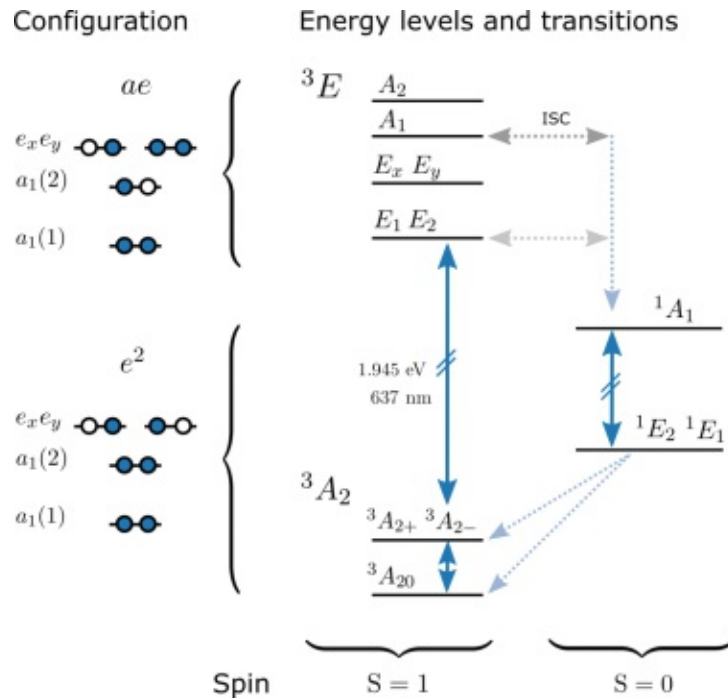
Figure 3.4: *Ordering of energy levels due to Coulomb and magnetic interactions. Solid blue arrows indicate allowed transitions, dotted light blue arrows are vibronic transitions. Transition between singlet states is in the infrared, ground state transition at 2.88 GHz. The excited state A_1 level can undergo intersystem crossing (ISC) through spin-orbit coupling to $S = 0$, which may be followed by a vibronic decay to the $^1A_1$ singlet state [38]. Since the E_1 and E_2 states couple via phonons to A_1 they too have this decay channel, although at lower rate.*

state, one electron from the ground state is lifted into an e-level. Considering, all levels can be filled with eight electrons at maximum the description can be done from a two-hole perspective as well, which simplifies matters and is used in the following. The ground state then is an e^2-configuration and the excited state is of ae-form. Again, group theory can be employed for deriving two-hole state functions as summarized in table 3.2, giving rise to singlet (S) and triplet (T) states [67].

Coulomb interaction energetically splits triplet and singlet states on the order of eV and the triplets themselves are split by spin-orbit and spin-spin interactions on a GHz-scale. Figure 3.4 summarizes the ordering of energy levels from table 3.2. Upon optical excitation, the ground state e^2-configuration changes to ae, indicated schematically on the left side of the figure. The figure also includes the most important pathways for photonic, spin, and vibronic dynamics.

Magnetic interactions

The magnetic moments of electrons lead to magnetic interactions with other magnetic moments and magnetic fields. In general, these can be classified as contact interactions and dipole-dipole interactions.

The most straightforward interaction of an electron spin with a magnetic field is described by the Zeeman Hamiltonian [43]

$$H_Z = \mu_B \mathbf{B} \mathbf{g} \mathbf{S}, \tag{3.3}$$

with μ_B the Bohr magneton, $\mathbf{B}$ the magnetic field transposed vector, $\mathbf{g}$ the g-factor tensor and $\mathbf{S}$ the spin operator $1/2[\hat{\sigma}_x, \hat{\sigma}_y, \hat{\sigma}_z]$, with $\hat{\sigma}_i$ the Pauli matrices. In general the g-factor is a tensor, but due to the NV centre's symmetry axis it can be diagonalized and yields an effective g-factor consisting of axial and transversal components [107],

$$H_Z = \mu_B \left[g_\perp \left(B_x \hat{S}_x + B_y \hat{S}_y \right) + g_\parallel B_z \hat{S}_z \right]. \tag{3.4}$$

A general expression of magnetic interactions between two magnetic dipoles (or dipole and field) contains the dipole strengths, their distance and field orientation with respect to each other and, when close enough, an overlap integral. The classical magnetic field produced by a dipole is given as

$$\mathbf{B}(\mathbf{r}) = \frac{\mu_0}{4\pi r^3} [3\hat{\mathbf{r}} (\mathbf{m} \cdot \hat{\mathbf{r}}) - \mathbf{m}], \tag{3.5}$$

where μ_0 is the vacuum permeability, r is the distance, $\hat{\mathbf{r}}$ is the unit distance vector and $\mathbf{m}$ is the magnetic moment [5]. The anisotropic interaction can then be expressed similarly to a Zeeman-term as a magnetic moment of one dipole coupling to the field produced by the other as

$$H = -\mathbf{m_1} \mathbf{B_2} = A \cdot \mathbf{S_1} \mathbf{B_2} = \frac{\mu_0 g^2 \mu_B^2}{4\pi r^3} [\mathbf{S_1} \cdot \mathbf{S_2} - 3 (\mathbf{S_1} \cdot \hat{\mathbf{r}}) (\mathbf{S_2} \cdot \hat{\mathbf{r}})], \tag{3.6}$$

where $\mathbf{S_i}$ are the respective spin operators and A is a constant [5].

An optional isotropic contact term is proportional to the overlap integral of the involved states [107].

In the following, the specific interactions for spin-orbit coupling, spin-spin coupling and hyperfine coupling are treated in more detail in relation to the NV centre.

Spin-orbit interaction. The relativistic motion of electrons in the electrostatic potential of the nuclei leads to a magnetic field experienced in the rest frame of the electron [21]

$$\mathbf{B} \propto \mathbf{v} \times \mathbf{E} \propto \mathbf{p} \times \boldsymbol{\nabla}\phi, \tag{3.7}$$

with $\mathbf{v}$ being the electrons velocity, $\mathbf{E}$ the electric field of the nuclei, $\mathbf{p}$ the momentum and ϕ the potential of the nuclei. This field, originating from the orbital motion, interacts with the electrons' spin magnetic moment, resulting in the spin-orbit interaction. Spin-orbit interaction erases the degeneracy of states with orbital angular momentum and enables transitions between states with different spin. Rewriting the expression of the magnetic field and inserting it into the single electron spin-orbit Hamiltonian yields [67]

$$\mathrm{H_{SO}} = \frac{\hbar q}{2c^2 m_e^2} \left(\boldsymbol{\nabla}\phi \times \mathbf{p}\right) \cdot \mathbf{S}, \tag{3.8}$$

with $\hbar$ the reduced Planck's constant, q the elementary charge, m_e the electron mass and c the speed of light. Since

$$\mathbf{p} \times \boldsymbol{\nabla}\phi \propto \left(L_x, L_y, L_z\right), \tag{3.9}$$

with $\mathbf{L}$ the orbital angular momentum, transforms as an axial vector according to (E, E, A_2) [60], which is the same for the spin vector, the expectation values of the orbital angular momentum operators can be sorted in two classes $\langle L_x\rangle = \langle L_y\rangle$, $\langle L_z\rangle$ and the interaction can be expressed in the form

$$\mathrm{H_{SO}} = \lambda_{xy}\left(\hat{L}_x\hat{S}_x + \hat{L}_y\hat{S}_y\right) + \lambda_z\hat{L}_z\hat{S}_z = \lambda_\perp\left(\hat{S}_+\hat{L}_- + \hat{S}_-\hat{L}_+\right)/2 + \lambda_\parallel\hat{L}_z\hat{S}_z, \tag{3.10}$$

split into an axial and a transversal part. Not all matrix elements might exist - for the NV centre the interaction only splits the ^3E excited state between levels (A_2, A_1) and (E_x, E_y) as well as (E_1, E_2) and (E_x, E_y). Furthermore, spin-orbit interaction has the property of linking states between triplets and singlets via ISC, through non-radiative transitions as indicated in figure 3.4 [67].

Spin-spin interaction. Due to the non-spherical symmetries of the NV centre's orbitals, the spin-spin dipolar interaction does not vanish [67] and is present in ground and excited states of the centre. The anisotropic spin-spin interaction between two spins $\mathbf{S_1}$ and $\mathbf{S_2}$ enters as

$$\mathrm{H_{SS}} = \frac{\mu_0 \mathrm{g}^2\mu_B^2}{4\pi r^3}[\mathbf{S_1}\cdot\mathbf{S_2} - 3\left(\mathbf{S_1}\cdot\hat{\mathbf{r}}\right)\left(\mathbf{S_2}\cdot\hat{\mathbf{r}}\right)] \tag{3.11}$$

in the Hamiltonian (see eq. 3.6). The expression can be separated in spatial and spin terms. In the ground state triplet the $M_S = 0$ and $M_S = \pm 1$ states are split, since the Hamiltonian can be expressed in terms of a spin-projection dependent energy splitting as

$$\mathrm{H_{SS}} = D \left(\hat{S}_z^2 - \frac{S^2}{3} \right) + E \left(\hat{S}_x^2 - \hat{S}_y^2 \right), \tag{3.12}$$

with D and E the fine structure splitting constants [107].

Hyperfine interaction. The nuclear magnetic moment interacts with the electron spin in the form of isotropic and anisotropic interactions. The anisotropic parts correspond to a dipole-dipole interaction with the electron spin orbit and the electron magnetic moment. For the isotropic part, which is dominant in the NV centre, a contact term has to be considered. The most common nuclear spin is the ^{14}N spin-1 present naturally, but couplings to ^{15}N and ^{13}C spins are common. The hyperfine Hamiltonian is given as

$$\mathrm{H_{HF}} \propto \hat{A}\mathbf{SI} \propto \left(\hat{A}_{contact}^{ij} + \hat{A}_{dipole}^{ij} \right) \mathbf{SI}, \tag{3.13}$$

with $\mathbf{I}$ the nuclear spin operator vector and the hyperfine tensor

$$\hat{A}^{ij} = \frac{1}{2S} \int d^3 r n_s(\mathbf{r}) \gamma_N \gamma \hbar^2 \left[\left(\frac{8\pi}{3} \delta(r) \right) + \left(\frac{3x_i x_j}{r^5} - \frac{\delta_{ij}}{r^3} \right) \right], \tag{3.14}$$

where $n_s(\mathbf{r})$ is the spin density of spin state S and γ (γ_N) are the electron (nuclear) gyromagnetic factor, respectively. The first term in $\hat{A}^{ij}$ is the contact term, the second the dipole-dipole interaction [32].

The hyperfine coupling contact term and dipole terms vary for different orbital symmetries. An s-orbital-like spin distribution will have higher spin density at the nucleus, leading to a larger contact contribution than, for example, a p-like orbital state which has a node at the nuclear position. For the dipole-dipole term, the situation is reversed [32]. If there is axial symmetry in the hyperfine interaction, due to the nuclear spin being situated on the symmetry axis, the hyperfine tensor will be diagonal with components $A^{xx} = A^{yy} = A_\perp$ and $A^{zz} = A_\parallel$ [43].

29
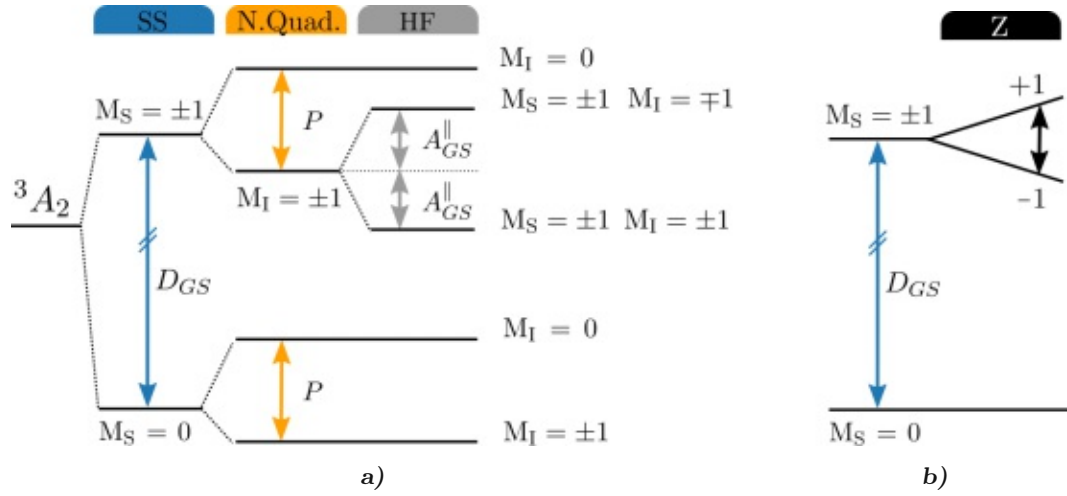
Figure 3.5: *a) Ground state $^3A_2$ energy levels: SS is the spin-spin interaction, N.Quad. the nuclear quadrupole interaction and HF the axial hyperfine coupling. The coupling constants (divided by h) are: $D_{GS} = 2.88\,\text{GHz}$, $P = -4.95\,\text{MHz}$ and $A_{GS}^{\parallel} = -2.16\,\text{MHz}$. b) Zeeman splitting of levels in axial B-field for electron spin state with magnitude $2.802\,\text{MHz}\,\text{G}^{-1}$ in frequency units.*

3.2.3 Ground state fine and hyperfine structure

The unperturbed low temperature (LT) ground state Hamiltonian of the centre is the $^3A_2$ orbital-singlet, spin-triplet state, given by [26, 76]

$$\text{H}_{\text{GS}} = D_{GS}\left[\hat{S}_z^2 - S\left(S+1\right)/3\right] + P\left[\hat{I}_z^2 - I\left(I+1\right)/3\right] + A_{GS}^{\perp}\left(\hat{S}_+\hat{I}_- + \hat{S}_-\hat{I}_+\right) + A_{GS}^{\parallel}\hat{S}_z\hat{I}_z, \tag{3.15}$$

wherein $\hat{S}_i$ and $\hat{I}_i$ are the usual spin-1 operators for $i = x, y, z$ and S, I are the spin quantum number and the nuclear spin quantum number respectively. The different terms and constants in equation 3.15 are now discussed.

The fine structure zero-field splitting in the ground state, described by the first term, is attributed to the electron spin-spin interaction, with a zero-field splitting constant D_{GS}/h of $2.88\,\text{GHz}$ at low temperature. As illustrated in figure 3.5a, this spin-spin interaction leads to two levels, with the higher energy one being degenerate for $M_S = \pm 1$. A magnetic dipole transition connects the levels, so that D_{GS} is accessible in electron paramagnetic resonance.

The second term expresses the nuclear quadrupole interaction of the ^{14}N nuclear spin-1, with P/h being the nuclear electric quadrupole parameter of magnitude $-4.95\,\text{MHz}$. The splitting effect, depending on the nuclear spin state, is shown in the figure.

The third and fourth term in equation 3.15 relate to the interaction of the electron

spin with a nearby nuclear spin. Of course this would always occur with the nuclear spin of the nitrogen atom, but could be extended to other nearby nuclear spins by adding more such coupling terms. The hyperfine coupling constant can be expressed in the form of a part which acts in axial direction of the NV centre and a transversal part, due to the centre's symmetry. For the most abundant ^{14}N nuclear spin the axial hyperfine interaction $A_{GS}^{\parallel}/h$ was established as $-2.16\,\mathrm{MHz}$ and the transversal component $A_{GS}^{\perp}$ is quite similar with $-2.62\,\mathrm{MHz}$ [76]. The axial part splits energy levels with $\mathrm{M_S} = \pm 1$ and $\mathrm{M_I} = \pm 1$, as indicated in figure 3.5a and thereby leads to the final ordering of hyperfine levels. The transversal hyperfine interaction may produce electron-spin nuclear-spin flip-flops.

The ground state is sensitive to magnetic fields, coming into the Hamiltonian as Zeeman terms [26, 76]

$$\mathrm{H_Z} = \mu_B \mathrm{g}\mathbf{SB} + \mu_N \mathrm{g_N}\mathbf{IB}, \tag{3.16}$$

with $\mathrm{g} = \mathrm{g}^{\parallel} = \mathrm{g}^{\perp}$ the electron g-factor of 2.0028 [10], μ_N the nuclear magneton and $\mathrm{g_N}$ the nuclear g-factor. The behaviour is shown for an axial magnetic field in 3.5b for the electron spin part, whereby levels remain pure but shift in energy by $2.802\,\mathrm{MHz\,G^{-1}}$ [76]. For the nuclear spin the shift is only $0.308\,\mathrm{kHz\,G^{-1}}$. Transversal magnetic field components may mix the spin.

The ground state is sensitive to a lesser extent to electric fields and crystal strain. This insensitivity results from the antisymmetric combination of the e_x and e_y orbitals (see table 3.2) [67].

3.2.4 Excited state fine and hyperfine structure

The effective LT fine structure Hamiltonian for the ^3E optically excited state orbital-doublet, spin-triplet manifold is [26]

$$\begin{aligned}
\mathrm{H_{ES}} = \Big[& \hat{I}_2 \otimes D_{ES}^{\parallel} \Big[\hat{S}_z^2 - S\left(S+1\right)/3 \Big] \\
& - \lambda_{ES}^{\parallel} \hat{\sigma}_y \otimes \hat{S}_z + D_{ES}^{\perp} \Big[\hat{\sigma}_z \otimes \left(\hat{S}_y^2 - \hat{S}_x^2 \right) - \hat{\sigma}_x \otimes \left(\hat{S}_y \hat{S}_x + \hat{S}_x \hat{S}_y \right) \Big] \\
& + \lambda_{ES}^{\perp} \Big[\hat{\sigma}_z \otimes \left(\hat{S}_x \hat{S}_z + \hat{S}_z \hat{S}_x \right) - \hat{\sigma}_x \otimes \left(\hat{S}_y \hat{S}_z + \hat{S}_z \hat{S}_y \right) \Big] \Big] \otimes \hat{I}_3, \tag{3.17}
\end{aligned}$$

with $\hat{I}_d$ the identity operator of dimension d, in the notation of spin-orbit $\otimes$ electron spin $\otimes$ nuclear spin states, where the $\hat{\sigma}_i$ are the Pauli-matrices for the basis of orbital states $|X\rangle$, $|Y\rangle$ to produce the action of fine structure orbital operators. The Hamiltonian
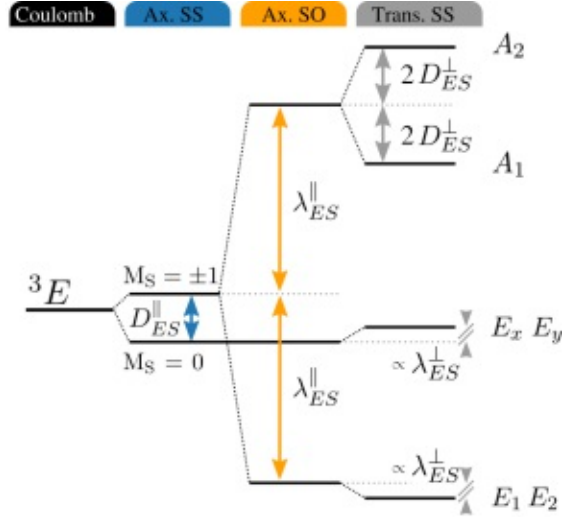
Figure 3.6: *Excited state ^3E energy levels: 'Ax. SS' is the axial spin-spin, 'Ax. SO' the axial spin-orbit interaction and 'Trans. SS' the transversal spin-spin coupling. The coupling constants (divided by h) are: $D_{ES}^{\parallel} = 1.44\,\text{GHz}$, $\lambda_{ES}^{\parallel} = 5.33\,\text{GHz}$, $D_{ES}^{\perp} = 1.541/2\,\text{GHz}$ and $\lambda_{ES}^{\perp} = 0.154/2\,\text{GHz}$ [10]. The effect of $\lambda_{ES}^{\perp}$ is exaggerated in the figure.*

has contributions of spin-spin and spin-orbit interaction, with the D_{ES} terms describing spin-spin interaction and $\lambda_{ES}^{\parallel}$ being attributed as having spin-orbit origin. According to reference Doherty et al. [26], $\lambda_{ES}^{\perp}$ has spin-spin roots but may also have a spin-orbit influence. The energetic ordering of the six energy levels, introduced in the previous section, due to these contributions as well as the magnitude of coupling rates is indicated in figure 3.6, where the lower two levels are degenerate each. $E_{x,y}$ are $M_S = 0$ states, the other four have contributions from $M_S = 1$ and $M_S = -1$.

The LT hyperfine and quadrupole coupling Hamiltonian, given by [37]

$$\text{H}_{\text{ES}}^{\text{HF}} = \hat{I}_2 \otimes \hat{I}_3 \otimes \left[P \hat{I_z}^2 + A_{ES}^{\perp} \left(\hat{S}_+ \hat{I}_- + \hat{S}_- \hat{I}_+ \right) + A_{ES}^{\parallel} \hat{S}_z \hat{I}_z \right], \tag{3.18}$$

is in structure similar to the ground state one, but the coupling to the nitrogen nuclear spin is stronger as reflected by $A_{ES}^{\parallel}/h$ being about $40\,\text{MHz}$ [95] and $A_{ES}^{\perp}/h$ about $23\,\text{MHz}$ [76], which is connected to a shift of unpaired electron spin density in the direction of the nitrogen atom [37]. Further nuclear spins in the vicinity of the centre would couple with additional hyperfine terms, as already mentioned in the ground state Hamiltonian discussion. The quadrupolar shift P is assumed to be the same as in the ground state [76].

Figure 3.7: *Axial magnetic field acting on the excited state levels: initial levels having both $M_S = 1$ and $M_S = -1$ chara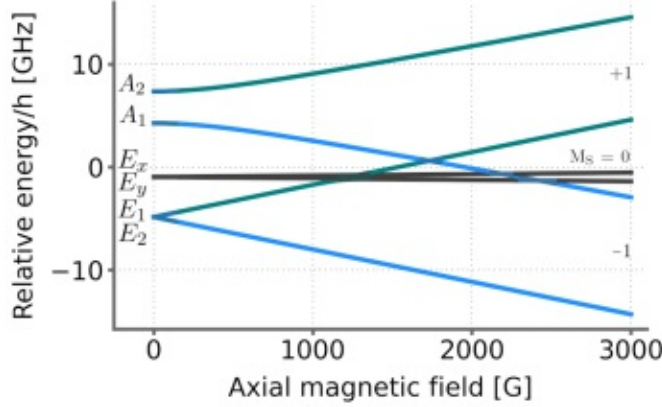cter transition to pure spin states. Levels in green have spin eigenvalue $M_S = 1$, blue ones have $M_S = -1$ and black ones $M_S = 0$. On contact, states show avoided crossings.*

3.2.5 Excited state magnetic field, electric field and crystal strain sensitivity

The NV centre, due to its symmetry, is susceptible to changes in magnetic field **B**, electric field **E**, and crystal strain $\boldsymbol{\delta}$, qualifying the centre as an excellent sensor but requiring stable experimental conditions. The low temperature B- and E-field/strain Hamiltonians for the excited state are [26]:

$$H_B = \left[\mu_B B_z \left(g_{ES}^{\parallel} \left(\hat{I}_2 \otimes \hat{S}_z \right) + l_{ES}^{\parallel} \left(\hat{\sigma}_y \otimes \hat{I}_3 \right) \right) + \mu_B g_{ES}^{\perp} \left(\hat{I}_2 \otimes \left(\hat{S}_x B_x + \hat{S}_y B_y \right) \right) \right]$$
$$\otimes \left[g_N \mu_N \mathbf{B} \hat{\mathbf{I}} \right],$$
$$H_{E,\delta} = \left[d_{ES}^{\parallel} \left(\hat{I}_2 \otimes (E_z + \delta_z) \hat{I}_3 \right) + d_{ES}^{\perp} \left((E_x + \delta_x) \hat{\sigma}_z - (E_y + \delta_y) \hat{\sigma}_x \right) \otimes \hat{I}_3 \right] \otimes \hat{I}_3,$$

which present a similar magnetic field dependence to the ground states, but the symmetry of the excited states leads to a slight difference in the axial and transverse component of the g-factor tensor, with $g_{ES}^{\parallel}$ being 2.15 and $g_{ES}^{\perp}$ being about 2.01 [10]. An additional term related to an axial diamagnetic shift acting on the orbital states with the orbital magnetic moment $l_{ES}^{\parallel}$ is present. Figure 3.7 shows the response of the excited states to an axial magnetic field. A transversal magnetic field strongly mixes spin states.

The DC electric field Stark shift and crystal strain actions manifest similar on the centre as a piezoelectric effect [67] and can be treated combined where $d_{ES}^{\parallel}$ and $d_{ES}^{\perp}$ are the axial and transversal components of the electric dipole moment.

	A_1	A_2	E_x	E_y	E_1	E_2
${}^3A_{2-}$	σ_-	σ_-			σ_+	σ_+
${}^3A_{20}$			$\hat{y}$	$\hat{x}$		
${}^3A_{2+}$	σ_+	σ_+			σ_-	σ_-

Table 3.3: *Optical transition selection rules: linear polarization represented as $\hat{x}$,$\hat{y}$. $\sigma_\pm = \hat{x} \pm i\hat{y}$ represents circularly polarized transitions [67].*

The effects of crystal strain. Strain effects can be modelled using group theory again, as they potentially change the symmetry of the crystal field by moving the lattice atoms through physical stress, electric fields or temperature. In the excited state, axial strain leads to a global shift of the transition energy of the ground and excited states, causing inhomogeneous broadening of the optical resonances.

Transversal strain lifts the degeneracy of the e_x and e_y orbitals, so that they split and mix, causing shifts in the relative energies of the levels as shown in figure 3.8a. If the transversal strain interaction exceeds the spin-orbit coupling of about 5.5 GHz, the spin decouples from the orbital momentum and total angular momentum ceases to be a good quantum number. In this high strain regime, two energetically separated triplets or "branches" appear in the excited state manifold [67]. The upper branch stays faithful in its spin character even at high strain (fig. 3.8c) while the lower branch shows two avoided crossings where the $M_S = 0$ state swaps to being the state lowest in energy (fig. 3.8d).

Since the effect of an electric field on the centre is similar to strain, electric fields permit energy level tuning operations. An axial field changes the transition frequency while a transverse field can restore or deform the C_{3v} symmetry of the defect [67].

3.2.6   637 nm transitions

Low temperature ground to excited state transitions present a strongly spin-conserving character but cross decay might nevertheless occur as indicated in figure 3.8b.

Allowed dipole moments between the excited and ground states can be extracted using group theoretical arguments [67]. The non-vanishing transition matrix elements
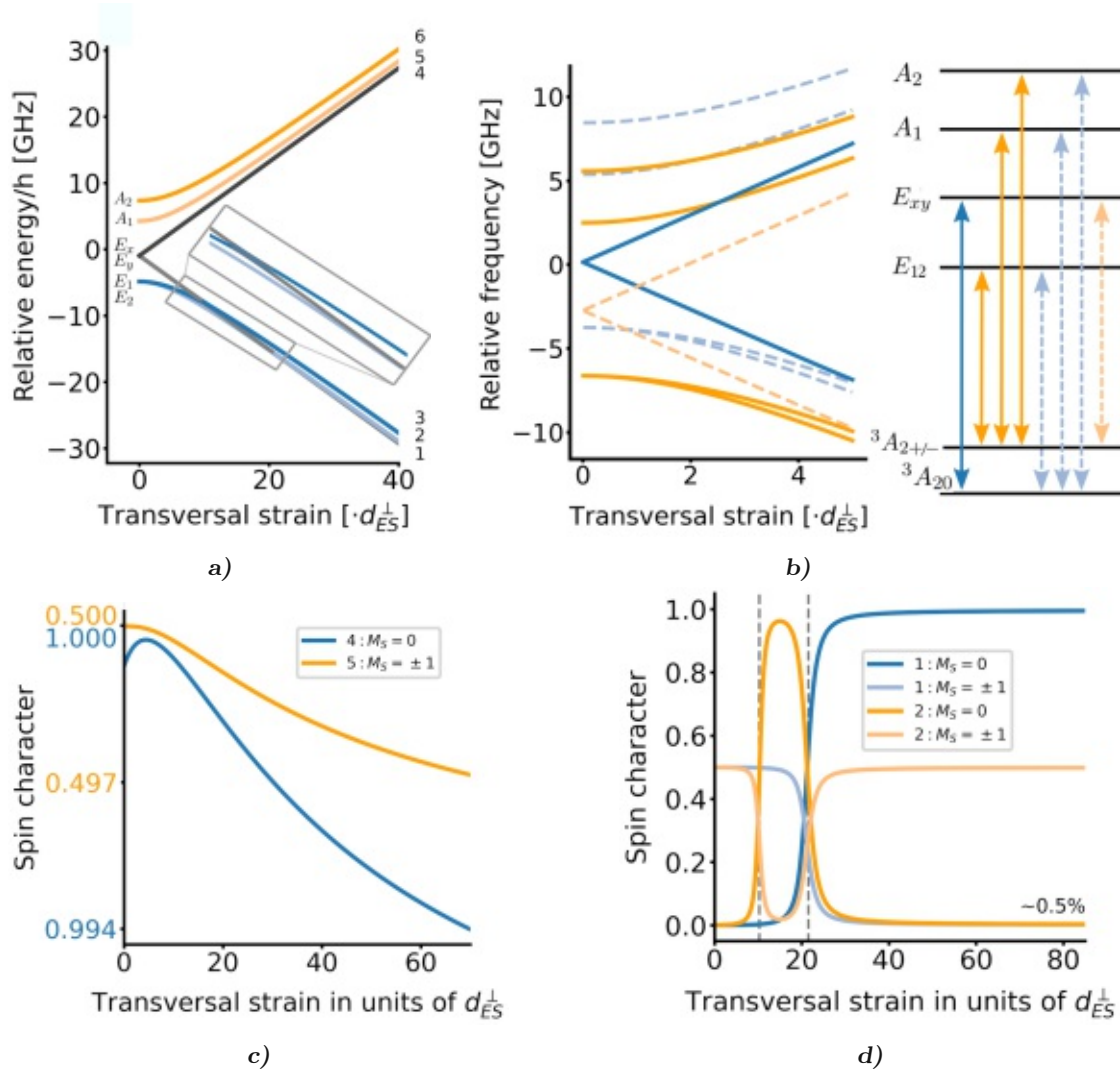
Figure 3.8: *Crystal strain effects on the ^3E excited state and on transition frequencies:* **a)** *transversal strain (in units of $d_{ES}^{\perp}$) action on the energies of optically excited states (in frequency units). Strain indicated on x-scale was equally split in x- and y-direction. Inset shows double avoided level crossing in the lower branch.* **b)** *relative change of transition frequencies in dependence of strain. Level scheme to the right serves as a legend to the plot, containing possible spin-allowed (solid arrows) and forbidden (dashed arrows) resonances between ground and excited state with respective color encoding. Zero on the y-scale is set to $M_S = 0$ transitions (blue).* **c)** *spin character change of the fourth and fifth level from figure a) (indicated on the right edge) due to strain. For both almost no change is present, which is typical for the upper branch levels.* **d)** *spin character change of the first and second level from figure a) due to strain. Vertical dashed lines indicate positions of avoided crossings where the spin character changes drastically.*

35
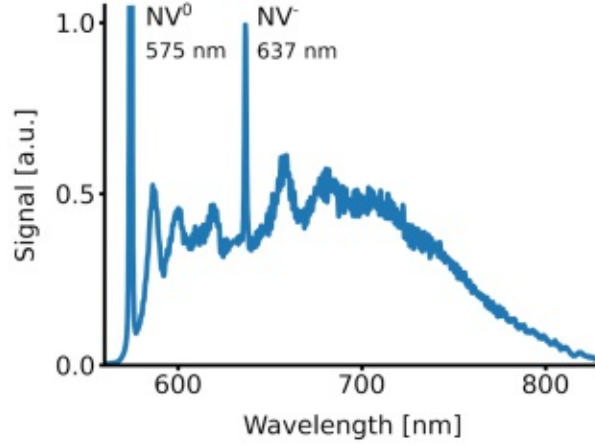
Figure 3.9: *NV ensemble fluorescence spectrum: spectrum taken at $88\,\mathrm{K}$ under off-resonant $532\,\mathrm{nm}$ excitation. Narrow peaks originate from ZPL emission of the uncharged and negatively charged centre. To the right of both ZPL peaks, a broad PSB emission profile is apparent.*

are

$$\langle a|\hat{x} \cdot r|e_x\rangle\,, \tag{3.19}$$

$$\langle a|\hat{y} \cdot r|e_y\rangle\,, \tag{3.20}$$

since $\hat{x}$ and $\hat{y}$ transform as irreducible representation E, and $E \times E$ can be reduced to $A_1 + A_2 + E$, yielding two orthogonal dipoles in the x- and y-directions. Owing to the orbital angular momentum in the unperturbed excited state, some transitions yield circularly polarized light, as summarized in table 3.3, due to total angular momentum conservation and the ground state not having orbital angular momentum.

In the high transverse strain regime circular polarized transitions get a linearly polarized character [67]. Lastly, the high strain induces mixing in the lower branch leading to spin-flips [26].

3.2.7 Phonon coupling and optical pumping dynamics

The intricate vibronic structure of the NV leads to a fluorescence spectrum of the centre, shown in figure 3.9 for an ensemble, dominated by a wide PSB, due to Franck-Condon coupling of electronic and vibrational states of the lattice [26]. Nevertheless, at low temperature the linewidth of the ZPL in the spectrum of the NV centre narrows to $13\,\mathrm{MHz}$ in the limit of the spontaneous decay lifetime [77].

36
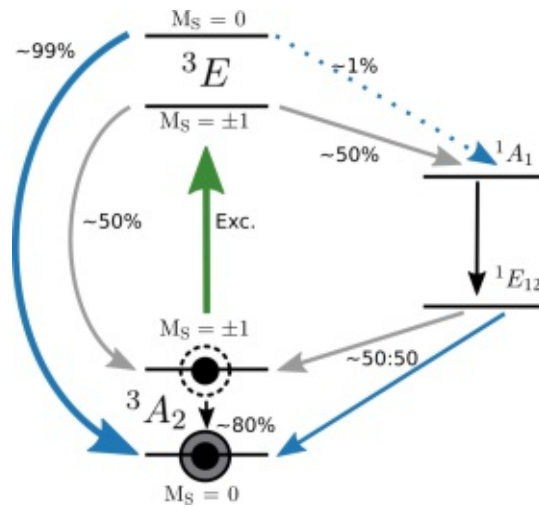
Figure 3.10: *Simplified optical spin-polarization mechanism: decay rates from excited state after off-resonant excitation (green arrow in centre) vary for different states. While $M_S = 0$ proportion remains with high percentage in the original state after decay, the A_1 (together with E_1 and E_2 through phononic coupling to A_1) state likely transitions via transversal spin-orbit coupled intersystem-crossing to the singlet states [39]. Consequently, by bleeding out of $M_S = \pm 1$ population, spin population is redistributed with accumulation in the $M_S = 0$ state.*

Upon off-resonant optical excitation, the centre is found to exhibit spin polarisation into the $M_S = 0$ ground state (see figure 3.10). This effect is promoted by the ISC mechanism in the excited state, coupled with phononic transitions. The responsible pathways could be determined by symmetry arguments and confirmed with lifetime measurements [39]. It was found that the states A_2, E_x, E_y show weak spin-orbit coupled ISC, conserving the $M_S = 0$ population in the excited state. Contrarily, the state A_1 has the highest ISC rate and therefore the shortest lifetime. The $E_{1,2}$ states couple to A_1 and therefore are prone to ISC as well. All of these states have spin projections of $M_S = \pm 1$, leading to predominant depletion of $M_S = \pm 1$ population through ISC to the $^1A_1$ singlet state. The singlet state further decays via radiative and non-radiative transitions to the $^3A_2$ ground state with about equal parts of $M_S = 0$ and $M_S = \pm 1$ re-population [39]. Spin polarizations with an average of 80 % are reported in the literature through this experimentally simple mechanism [26].

More detailed aspects of optical and spin dynamics can be found in chapters 4 and 5.

CHAPTER 4

Manipulation of NV Centres at Cryogenic Temperature

This chapter investigates all the requirements and routines necessary for our proposed scalable spin-photon entangling scheme, which was introduced in chapter 2. In the course of this thesis, a suitable experimental setup had to be constructed from scratch and all the necessary methods needed to be established. The proposed protocol has stringent experimental preconditions that needed to be met. On the NV centre side it mainly depended upon

1. a single, environmentally well-isolated NV centre, with

2. a microwave interface for manipulation of the electron-spin qubit space in the NV centre ground state, and

3. an optical interface to address resonant ZPL transitions.

The constructed setup, instrumentation, and methods for fulfilling these conditions are presented.

The chapter begins with a discussion of the diamond material used, followed by the allocation of suitable NV centres and diamond engineering to improve the optical performance. An overview of the confocal microscope setup is given and the necessity of a cryogenic environment for the NV centre is motivated (4.1). Section 4.2 is concerned with hardware instrumentation, experimental control and data acquisition. Thereafter,

section 4.3 treats NV centre ground state spin manipulation technique and experiments done to perform high fidelity operations and to characterize the centres spin coherence time. Finally, in the last section (4.4) the centre is optically characterized and coherent optical manipulation methods are established.

4.1 Confocal microscopy

4.1.1 Diamond material

The diamond sample used for most of the work presented herein was produced by Diam2Tech, is of type IIa and was fabricated by plasma enhanced CVD. It has dimensions of 4 mm times 1.8 mm and a height of 0.4 mm. The surface has [111]-orientation by choice, so that one of the four possible NV centre axes in the crystal lies normal to the diamond surface, while the NV centre dipoles are oriented parallel to the surface plane and dipole emission in surface direction is maximal, improving fluorescence collection. The natural nitrogen concentration in the sample was specified to be lower than 1 ppb, leading to well isolated naturally occurring NV centres. No implantation or annealing procedures took place after the growth.

4.1.2 Single centre confocal microscopy

As almost ideal point sources, NV centres are well addressable in optical fluorescence confocal microscopy, which offers increased imaging contrast by removing two major sources of background light: collection from non-focal spot positions and reduction of detected scattered light. This is achieved by the use of a pinhole in the image plane. In fluorescence confocal microscopy, excitation light and fluorescence detection are focused in the same region of the specimen. A single objective lens for excitation and collection suffices when the microscope is used in a reflection/transmission setup as shown in figure 4.1. The size of the pinhole determines the achievable resolution and the number of collected photons. The diameter should be on the order of the diameter of the Airy disk, which contains 86 % of the light emitted by a point source. A confocal microscope of the type shown in figure 4.1, where the same objective lens is used in excitation and fluorescence collection, potentially (depending on the pinhole size) has a minimal confocal
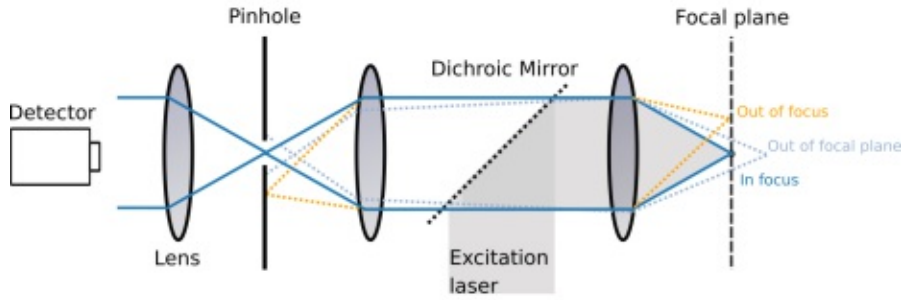
Figure 4.1: *Principle of fluorescence confocal microscopy: an excitation laser (shaded gray) is reflected off a dichroic mirror and produces fluorescence at the focal spot of an objective lens. Focal-spot fluorescence (dark blue) is collected by the same lens, transmitted through the dichroic mirror and imaged through a pinhole onto a detector. Light originating from the focal plane but out of focus (yellow) and light from outside the focal plane (light blue) are prevented by the pinhole from reaching the detector. Thus a single focal position is imaged with high signal compared to background.*

lateral resolution r_{lat} given as

$$r_{lat} = \frac{1}{\sqrt{2}} \cdot 0.61 \cdot \frac{\lambda_0}{\mathrm{NA}}, \tag{4.1}$$

where λ_0 is the vacuum wavelength and NA is the numerical aperture of the microscope objective. The Airy disk diameter is then $2 \cdot M \cdot r_{lat}$, with M being the magnification of the objective lens [25].

For system parameters close to the experimental conditions, namely $\lambda_0 = 650$ nm, an NA of 0.7 and a magnification of 100, r_{lat} becomes 0.4 μm with an Airy disk diameter of 80 μm. As signal collection was more important than resolution in the experiment, we opted for an increased pinhole size. The pinhole was set up in the form of a further focusing lens coupling into a multimode fibre with 8.2 μm core diameter.

An overview of the used confocal and widefield microscope setups is given in figure 4.2a. Both were used at RT and LT settings of the sample. For the confocal microscope setup, a homebuilt green laser of 520 nm was passed through a fibre onto a dichroic mirror (Thorlabs DMLP650) to be sent in a collimated fashion to a microscope objective. Two types were used: a Mitutoyo 100x PlanAPO 0.7 NA with a long 6 mm working distance at LT and an Olympus UPLFLN 60x 0.9 NA with short working distance for RT operation with open cryostat chamber. At LT the beam was passed through a thin 0.5 mm cryostat window onto the sample. Fluorescence was collected through the same objective: it was split off the (green) excitation beam path at a dichroic mirror, filtered for green
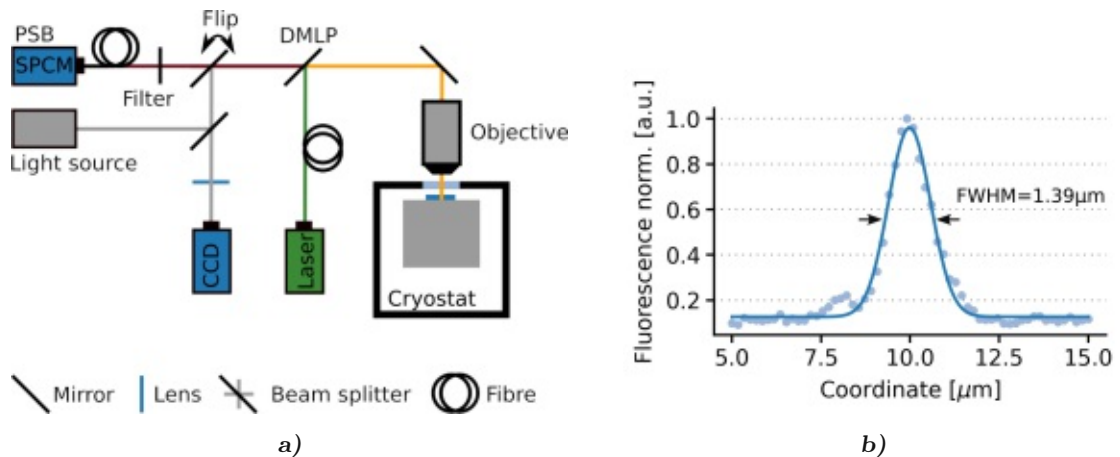
Figure 4.2: a) *Confocal and widefield microscopes and imaging setup.* **b)** *Cross-section from lateral point spread function (PSF) of the confocal microscope. Fit is a Gaussian function.*

light (Thorlabs NF533), traversed the pinhole multi-mode fibre (Thorlabs SMF28e), as described above, and was finally detected by a single-photon counting module (SPCM) (Excelitas SPCM-AQRH-FC).

The widefield imaging setup, consisting of a white light source and a CCD-camera, was available by flipping a mirror into the path, providing a surface view of the sample used for navigation.

In order to characterize the lateral resolution of the confocal microscope we measured the lateral PSF (figure 4.2b), which defines the intensity distribution of a point source image, here the NV centre. The resolution in this case is expressed as the full width at half maximum (FWHM) of the PSF [25].

Aside from the use of a pinhole, another discerning feature for confocal microscopes is the operation in a scanning mode, as the pinhole restricts the detection volume to the vicinity of the focal spot. The beam was scanned in discrete steps over the diamond sample volume, while collecting fluorescence from every such pixel. Small region scanning of about $20\,\mu m$ times $20\,\mu m$ with 100 pixels per direction was enough to locate single NV centres. Instead of moving the beam itself, the beam scanning operation was performed by mounting the microscope objective on a three-axis piezoelectric-translation stage (Thorlabs MAX311D/M). With a dwell time of $50\,ms$ per pixel a scan would take about 10 minutes.
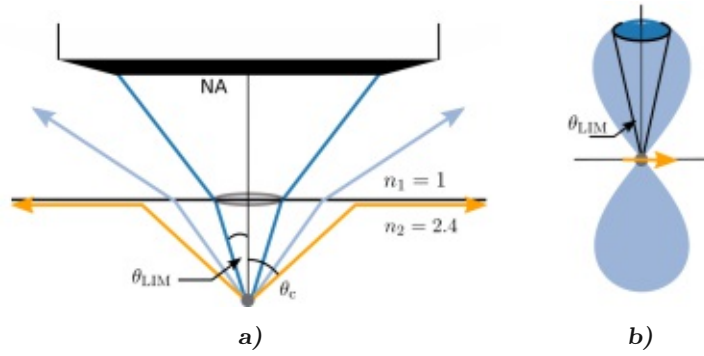
Figure 4.3: *a) Fluorescence collection efficiency: total internal reflection in the diamond material is already present at small angles. Refraction hampers collection by the objective. b) Dipole emission pattern of point emitter with dipole (orange arrow) oriented parallel to the diamond surface and indication of the cut-off angle θ_{LIM} due to refraction and the NA of the objective.*

4.1.3 Fluorescence collection improvements

An optically cycled single NV centre at saturation emits on the order of 10^6 photons per second [27]. Unfortunately, due to the high refractive index of the material, of those only some tens of kilo counts per second are usually collected from bulk diamond.

Fresnel reflection on normal incidence, given as

$$R = \left| \frac{n_1 - n_2}{n_1 + n_2} \right|^2 = \left| \frac{2.4 - 1}{2.4 + 1} \right|^2, \tag{4.2}$$

in dependence of the refractive indices in a diamond (n_1) to vacuum (n_2) interface (as typically found in a cryostat) accounts for $17\,\%$ alone.

Furthermore, total internal reflection severely limits transmission of higher angle portions from the dipole emission pattern (fig. 4.3a), with the cut-off angle θ_{c} in this case being as low as

$$\theta_{\mathrm{c}} = \arcsin\left(n_2/n_1\right) \approx 24.6°. \tag{4.3}$$

Including the NA of 0.7 from the objective through use of Snell's law, the angle decreases to θ_{LIM} by

$$\mathrm{NA} = \sin\left(\theta_{\mathrm{LIM}}\right) n_1 = \sin\left(\theta_2\right) n_2,$$
$$\theta_{\mathrm{LIM}} = \arcsin\left(\frac{NA}{n_1}\right), \tag{4.4}$$

with a value of $16.9°$.

a)   **b)**   **c)**
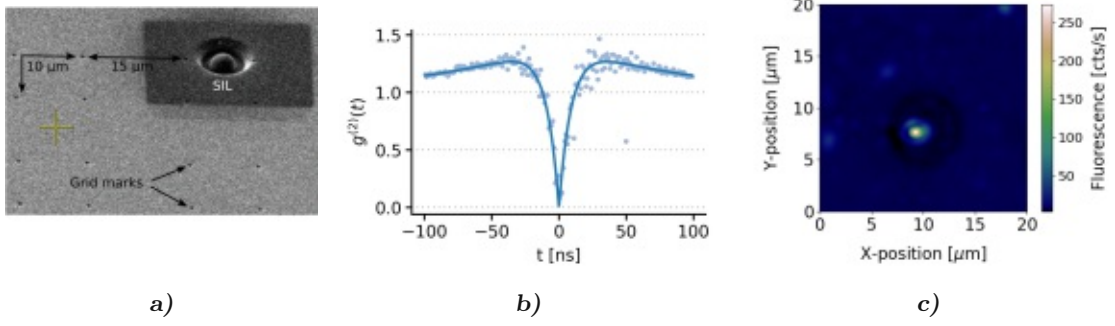
Figure 4.4: a) *Electron microscope image of grid coordinate system, harbouring a solid immersion lens (SIL) with* 1.9 μm *radius.* **b)** *Fluorescence autocorrelation measurement to determine single emitter behaviour. Fit function taken form Kurtsiefer et al. [56].* **c)** *Lateral confocal microscope scan at the depth of the NV centre beneath the SIL from figure a). SIL outline is visible as dark spherical shape in the background. NV centre is slightly off-centre.*

A rough quantification of the collection efficiency is achieved by integration over the dipole emission pattern (fig.4.3b) up to the cut-off angle with the normalized emission power [44]

$$dP_n = \frac{3}{8\pi} \cos(\theta)^2 d\Omega, \tag{4.5}$$

and the angle measured from the surface normal (fig. 4.3b). Integration yields a collection efficiency η of

$$
\begin{aligned}
\eta &= \int_0^{\theta_{\text{LIM}}} \frac{3}{8\pi} \cos(\theta)^2 d\Omega = \\
&= \frac{3}{8\pi} \int_0^{2\pi} \int_0^{\theta_{\text{LIM}}} \cos(\theta)^2 \sin(\theta) d\theta d\varphi \\
&= \frac{1}{4} \left(1 - \cos\left(\theta_{LIM}\right)^3 \right),
\end{aligned} \tag{4.6}
$$

which results in 3.1 % of total emission.

The problem of total internal reflection can be avoided entirely by shaping the surface of the diamond around the centre into a hemispherical solid immersion lens (SIL), providing uniform normal ray incidence [118]. Fabrication of these SILs was done via focused ion beam milling. In a first step, a reference grid coordinate system was milled into the diamond sample surface (fig. 4.4a), followed by allocation of suitable NV centres within this grid. Suitable centres would be shallow (up to some μm deep) and were checked for principal axis orientation and single centre characteristics.

In order to determine the symmetry axis orientation, the green excitation laser polarization was rotated and at the same time fluorescence counts were monitored. A uniform

count rate throughout the procedure indicated the desired [111]-axis orientation [2].

Fluorescence autocorrelation was measured in a Hanbury-Brown-Twiss arrangement, to confirm single centre properties, which was the case when anti-bunching of light was observed with the dip in the autocorrelation curve lower than 0.5 (fig. 4.4b) [51, 56].

After fabrication of SILs, with typically $2\,\mu$m to $10\,\mu$m in diameter, their performance was investigated through measurement of the saturation behaviour of the emitter beneath. Best performing lenses improved collection efficiency by a factor of 10, from $33(1)\,\mathrm{kcts\,s}^{-1}$ to $357(3)\,\mathrm{kcts\,s}^{-1}$.

Finally, to diminish reflection of excitation light into the detection path and fluorescence at the diamond surface, the sample was coated with a silicon dioxide $\frac{\lambda}{4}$-anti-reflection layer with a design thickness of

$$\frac{\lambda}{4 \cdot n_{SiO2}} = 110\,\mathrm{nm}. \tag{4.7}$$

A confocal microscope scan around the region of the SIL used in this work after surface coating is shown in figure 4.4c.

4.1.4 Cryogenic environment

The entangling protocol relied on addressability of a single optical transition of the centre, which required narrow line widths to remove overlap and to increase the absorption cross section. The sample was therefore put into a cryogenic environment, such that most coupling phonons were frozen out of the crystal lattice [31].

A closed-cycle cryostat (Montana Cryostation C2) kept the sample at about 4 K. Optical access was granted by a thin sapphire window of 0.5 mm thickness. Nevertheless, the window still led to a reduction of collection efficiency to $50\,\%$, supposedly due to wavefront aberrations. The diamond was mounted onto a cold finger as close as possible to the window to be within the long working distance range of the microscope objective, positioned outside the cryostat.

4.2 Instrumentation and data acquisition

Contemporary complex quantum experiments wouldn't function without efficient and, wherever feasible, automated hard- and software control. In the course of this thesis, such control was implemented from basic building blocks and ideally worked as invisibly and

autonomously as possible. A lot of hardware had to operate concurrently while elaborate experimental sequences were performed. Especially important for us was high-resolution timing of instructions and play control of sequences, which led to designing, programming and implementing a homebuilt open-source field-programmable gate array (FPGA) based pulser as described in the first part of the section. Thereafter, the developed hard- and software environment is presented and lastly, the time-resolved photon counting technique used throughout this work is introduced.

4.2.1   Controlling quantum emitters

In the course of planning the experiment, the question of how to control a quantum emitter hardware-wise efficiently needed to be addressed. The control of a single NV centre, like other quantum emitters, needs an elaborate set of precisely synchronized hardware to be manipulated in a controlled fashion: laser sources, electro-optic modulators, acousto-optic modulators, microwave sources, microwave switches, waveform generators and other device trigger signals. In a separate project, all the requirements were established and a FPGA based solution was designed and implemented as described in the following. The project named "Lith" (logical input-triggered high-resolution) pulser resulted in a separate publication.

Requirement analysis

The first part of the project consisted in the establishment of the exact requirements for the device:

Timescale of operation: The most interesting timescales for controlling an NV centre are the involved states coherence times, lifetimes and durations to manipulate states, for example through a microwave pulse. These timescales are commonly in the range of some tens to hundreds of nanoseconds. When performing manipulation operations, the available time increment has to be precise enough to not produce systematic errors in the resulting state fidelity. The bandwidth needed to be high, so that even short gates would be produced with correct timing. A short but realistic gate with 10 ns duration called for a minimum bandwidth of 100 MHz.

46

Hardware channels: It was foreseen that the experiment would involve various devices, as described above. All of these had to be synchronized, which necessitated that each device had a channel to the control system. Commercial solution often offered two, four, sometimes eight channels but we expected to require more than ten.

Sequence commands: Sequences are considered a list of timed instructions to the channels. A gate within a sequence consists of at least two commands for producing a rising and a falling edge in the signal. For our sequence implementation we anticipated to require many commands per sequence and channel.

Multiple sequences and real-time conditional logic: Due to a single-shot state readout mechanism available for the NV centre [71], we opted to implement conditional logic gates into our control device directly, to avoid post-selection processes entirely. We would run necessary initialization sequences until the desired state was successfully established (trial until success), detected by a real-time conditional logic interface, before proceeding to the actual experimental sequence (see fig. 4.5a). In contrast to post-selecting experimental sequences for those performed in a tuned state, trial until success increases the frequency of runs of the experimental sequence in a tuned state drastically (fig. 4.5b), especially with the number of conditions imposed, as shown in a simulation in figure 4.5c. Combined with a time out mechanism, the state of the system can periodically be rechecked later on. Unfortunately in the course of the work on this thesis project, it turned out that a single-shot readout mechanism was not available to us. The mentioned features were nevertheless implemented into the control device.

Commercial solutions were compared with our requirements and included arbitrary waveform, function and pulse generators, the Jaeger Messtechnik Adwin system and National Instruments CompactRIO platform. All of these systems would have fulfilled the timing, channels and commands requirements. The conditional logic requirement could have been implemented in the Adwin and CompactRIO systems, but with lower performance. All envisioned control systems would have cost >15k Euro, which is often beyond the budget limit of small research labs. We therefore published our solution as open source software under GNU GPLv3.0 licence[1]. The device is not exclusively suited for the control of NV centres but can be useful in controlling a broad range of quantum emitters as well as quantum optics and other precisely timed complex experiments.

---

[1] https://github.com/im-pro-at/lithpulser
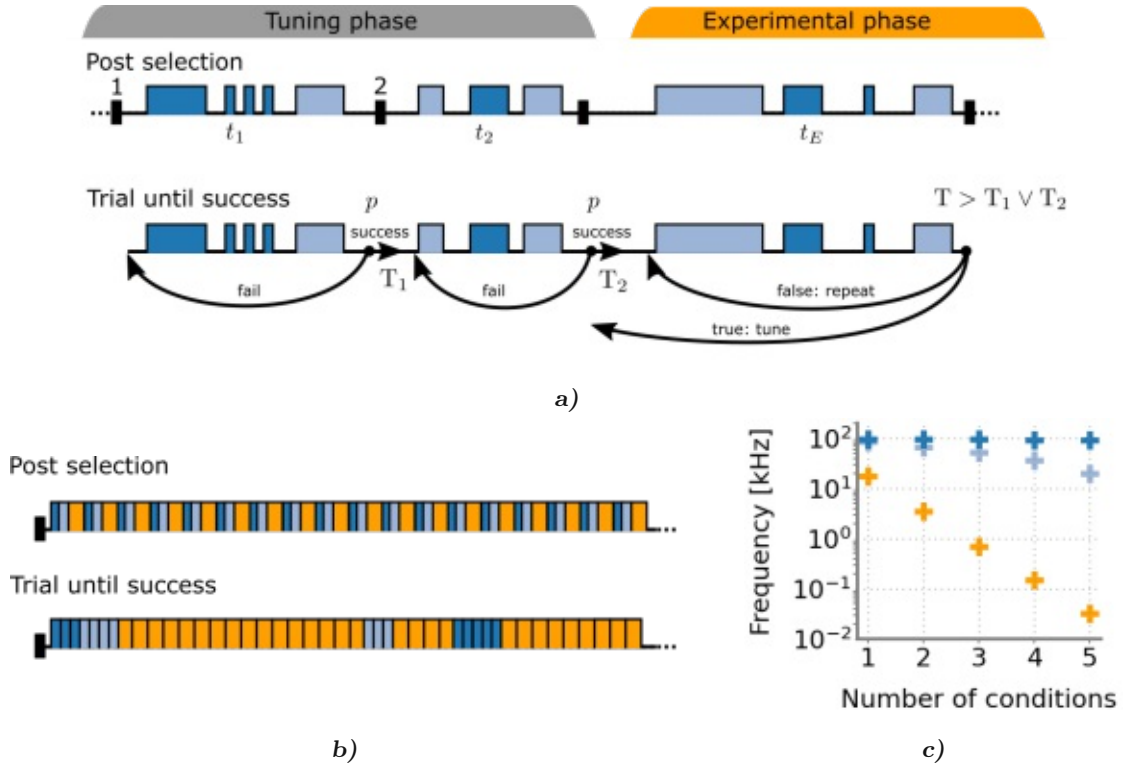
Figure 4.5: *Trial until success vs. post-selection:* **a)** *assumption of two routines (with duration t_1 and t_2) for tuning the system with success probability p (assumed to be equal for both) and experiment done thereafter (duration t_E). Post-selection case - the three sequences are repeated one after the other, regardless of successful tuning. Trial until success - with a single-shot readout mechanism present a condition heralding success has to be passed after each tuning attempt. Given a success, the next sequence is entered and a time out value (T_1, T_2) is set. If it fails, the tuning step is repeated. Once the tuning phase is left, experimental sequences are repeated as long as no time out expires, otherwise the respective tuning step is repeated until it succeeds.* **b)** *Visualization of the active sequences; blue boxes relate to the tuning phase, yellow are experimental runs.* **c)** *Simulation of frequency of tuned repetition of the experimental sequence in post-selection (yellow scatter) and trial until success (blue scatter) cases depending on the number of tuning steps to absolve. Parameters used: tuning sequence duration of $4\,\mu s$, experimental sequence duration of $10\,\mu s$, success probability of a tuning sequence trial of 0.25; blue scatter relates to two different time out values - dark blue has $1000\,\mu s$ time out, light blue $100\,\mu s$.*
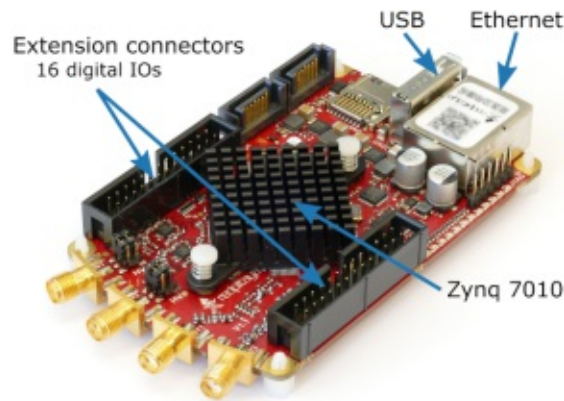
Figure 4.6: *The Redpitaya STEMLab board [33].*

Control system specifications

The control system was hardware based onto the Redpitaya STEMLab board (fig. 4.6) with integrated Xilinx Zynq 7010 system on a chip design[2]. This chip layout has a dual-core ARM Cortex-A9 processor hosting a Linux environment connected to a FPGA and numerous in- and output connectors. The processors and the FPGA work independently and asynchronously from each other, but may communicate over predefined registers. The board can be connected via USB or Ethernet.

The FPGA based pulse generator features a timing resolution of 1 ns, on 14 digital output and 2 digital input channels, connected to the Redpitaya STEMLab board extension connectors. There are at least 128 commands per sequence possible[3], each producing a new edge on the signal output of the relevant channel. 16 different sequences may be preloaded onto the device. Sequence repetition options are available in three different modes: the sequence may be specified to be played only once, to be repeated indefinitely or to be repeated only after a time out has expired. Sequences may have a maximal duration of 4.2 seconds and the number of repetitions is tracked in a readable register. For periods when sequence execution is deactivated and for the switching time between sequences, a default output pattern for the channels can be programmed.

Quantum emitters may require to be tuned into the right state which can be done by performing conditional gates within sequences. States may decohere due to environmental influences so regular automatic checks on the state fidelity are necessary. This is

---

[2]`redpitaya.com`
[3]A minimum of 128 commands can be guaranteed, more are possible - see appendix B.

done through the software by two mechanisms that achieve real-time play control of up to 16 sequences:

The first mechanism, which assigns a priority to a sequence, is always present. On reaching the end of a sequence, the next sequence that is chosen to be played will be the one that has highest priority and is currently timed out.

The second mechanism allows to send digital signals (e.g. from a photon counter) to two digital input channels of the board. These inputs are counted and compared with user-set threshold values. When within a specified range, a conditional gate is passed and repetition of the current sequence ceases (the time out is reset). The digital inputs are counted only in up to two specified time windows within the sequence and the condition may be chosen from: the first count value is within limits, the second count value is within limits, both are within limits and either is within limits.

The two mechanisms work simultaneously and independently from each other. After each sequence execution, a constant delay time of 48 ns is present followed by either the same sequence being executed thereafter or a sequence change as regulated by the two mechanisms introduced above.

Details on the system layout and sequence play control can be found in appendix B.

4.2.2 Hard- and software structure

The control structure for hardware constituted of a main control PC for 'slow' (computer speed) operations and the Lith pulser providing a precise timescale. A time-tagging module (TTM8000 Roithner LaserTechnik) for photon counting presented a third central piece of hardware as shown in figure 4.7a. The loop highlighted in the figure operated as follows: a measurement setting was sent from the main PC to the pulse generator and other hardware, the pulser then started operating and simultaneously produced a synchronization signal, that was handed to the time-tagging module and appeared as 'flags' in the time-trace of tags. The tags from the time-tagging module were channelled to the main PC for storage and evaluation. Through the synchronization flags the relative arrival times of photons could be reconstructed within the pulse sequences.

The TTM8000 supports measurement of rising and/or falling digital edges on up to eight channels with a time resolution of 82.3 ps. The device monitors inputs for voltage transitions and upon detection of such an event it records the channel, the type of edge (rising or falling) and the value of a high resolution clock as a 'time tag' into an event
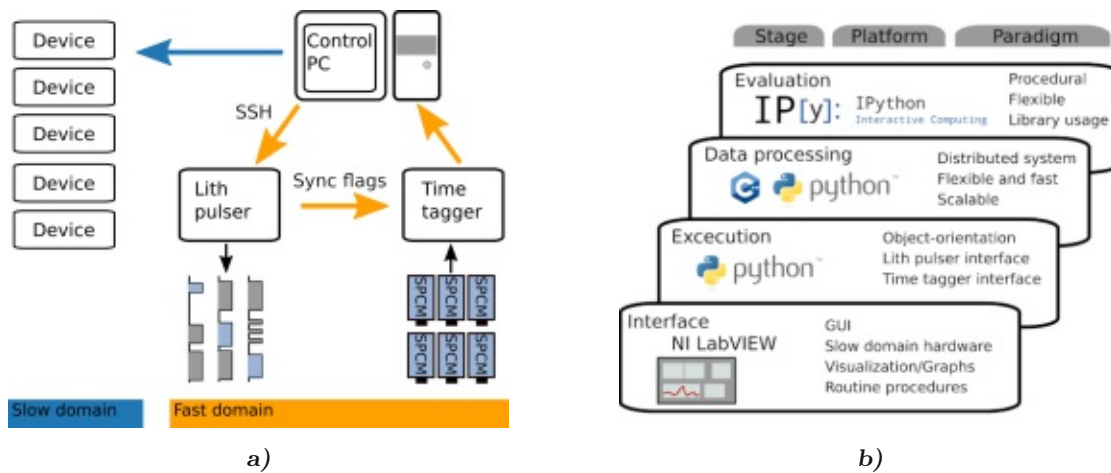
Figure 4.7: *Hard- and software concepts.*

table.

Figure 4.7b[4] offers a graphical representation of the homebuilt software system. National Instruments LabVIEW was employed as an event-driven user interface, providing easy access to a GUI, event capture and inherent multi threading. It is programmed through a visual programming language and offers straightforward hardware integration and data acquisition as well as visualization utilities. For the logic and data handling structure of the software, working as a back end, Python scripting language was chosen to capitalize on its versatility by using an object-oriented programming approach. Wherever fast processing of data was necessary, C++ based compiled tools were integrated into the Python ecosystem. Details on data processing are discussed in chapter 6 and appendices E, F. Finally, data evaluation was done mostly via procedural routines in IPython Jupyter notebooks relying on the Python data handling modules NumPy, SciPy and Pandas.

4.2.3 Time-resolved photon counting

Almost every method presented in following chapters relies on analyzing arrivals of photons in a time-resolved manner, usually in the form of a time-trace histogram. These histograms were built up as shown schematically in figure 4.8, using flag time tags to mark sequence starts. Different flag input channels on the time-tagging module symbol

---

[4]IPython image under Creative Commons Attribution-Share Alike 3.0 Unported license, authors: Python Developers.
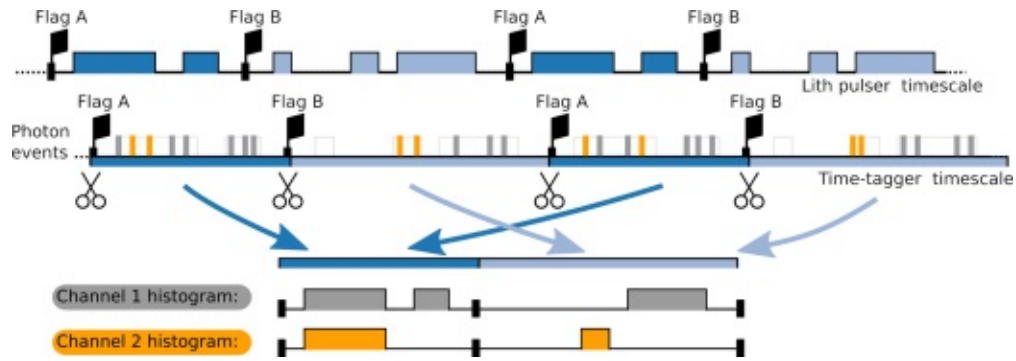
Figure 4.8: *Time-resolved photon counting data processing procedure: Lith pulser playing two sequences A and B in alternating fashion with a flag impulse sent to the time-tagging module at each sequence start. Flags synchronize the time-tagging module timescale. Time tags in between flag events recorded are sorted into histograms according to the channel on which the event was received, offering a time-resolved trace of photon events.*

a change of sequence (A and B in the figure). The time tag trace is cut at flag positions and equal sequence pieces of time tag traces are sorted into histograms, one for each input channel, translating to one histogram per SPCM port. Histograms were produced in almost real-time from extensive time-tags tables, received on the fly during the measurement procedure. Time tag tables could be contained in files with sizes up to some GB, so that care had to be taken when loading them into memory. Loading and tag processing was therefore done in chunks with 41 kB size. To achieve fast processing the task was delegated to a throughput-optimized command line C + + tool, that was able to process 1 GB of time tag data per minute.

This concludes the instrumentation and data acquisition section but further details on hard- and software are given in the relevant chapters.

4.3 Spin-qubit manipulation and coherence

The spin qubit part of the entangled state in the entangling experiment resides in two ground state electron spin levels of the NV centre, chosen from $M_S = 0$ and either of $M_S = \pm 1$. Electron paramagnetic resonances in the microwave spectrum connect these states.

The section opens with a detailed description of the microwave infrastructure set up during the installation of the experiment for high fidelity state manipulation, followed by a discussion of its first application for measuring NV ground state spectra by optically
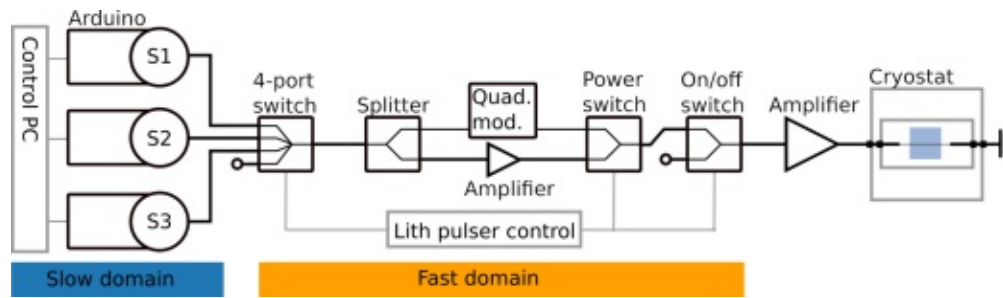
Figure 4.9: *Microwave hardware chain.*

detected magnetic resonance (ODMR). The last part is concerned with ground state spin manipulation theory and routines, investigation of coherence and purity of states.

4.3.1 The microwave hardware chain

The microwave hardware, shown in figure 4.9, was split into a slow computer controlled domain and a domain controlled by the Lith pulser for in-sequence microwave manipulation. The hardware chain featured three independent microwave sources S1-S3, each offering access within the experimental cycle to a different user set frequency via multiplexing. Sources consisted of an Analog Devices ADF4351 wideband synthesizer board (5 dBm max. power) connected to an Arduino Due micro controller for communication. Setting a frequency involved transfer of the parameters from the PC to the Arduino, which ran a communication program to translate to the ADF4351 source. A source was set active through selection of the input channel on a 4-port switch (pSemi EK42442-01) by a binary output pattern from two channels of the Lith pulser. The chain further consisted of a 50/50 power splitter to produce a high-power and a low-power branch. High power was used for fast but imprecise state manipulation, while low power was used for slow but state selective operations and ODMR measurements (see the following sections). Attenuation of power was achieved via a voltage controlled broadband quadrature modulator (Analog Devices ADL5375) in the low power path, and a pre-amplifier (TI TRF37B73, +11 dB) was used in the high power one - to push up the power to the maximum allowed input value for the following main amplifier. Power selection was done with a Mini-Circuits ZASWA-2-50-DR two-port switch commanded by the pulser. The line was sent to another switch for amplitude modulation with rise times of typically 5 ns. The signal was amplified by approximately 45 dB with a Mini-Circuits ZHL-16W-43+
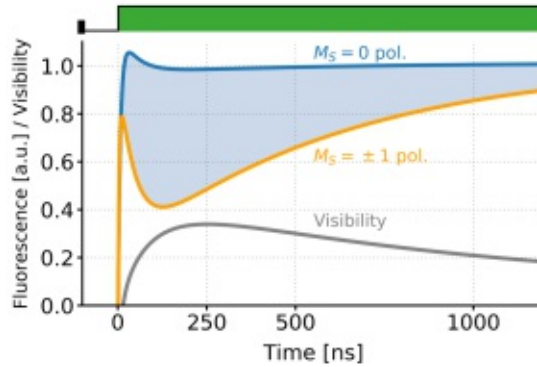
Figure 4.10: *Simulation of fluorescence behaviour for two spin polarizations (blue / orange curves): $M_S = 0$ pol. refers to 80% population in $M_S = 0$, $M_S = \pm 1$ pol. to 80% $M_S = \pm 1$ population. Five levels were included (two ground state levels, two excited state levels and a metastable one) with typical transition rates (see ch. 3.2.7). At 0 ns a CW green laser pulse begins. The $M_S = \pm 1$ polarized case exhibits reduced fluorescence, due to strong shelving of the population in the metastable state. Visibility, derived from both polarization cases with temporal integration of the fluorescence traces up to the time on the x-axis, is given by the gray curve.*

high power amplifier[5] before reaching the cryostat feed-through port.

Inside the cryostat the coaxial line was connected to a PCB extension board featuring a coplanar waveguide surrounding the diamond sample. From this board, two $25\,\mu m$ diameter wires were spanned across the diamond sample next to the SIL ($15\,\mu m$ distance). Finally, the line was grounded on the output port of the cryostat.

4.3.2 Optically detected magnetic ground state resonance

ODMR routines [27] were employed in determining spectra of the ground state spin resonances, detected by state-dependent fluorescence intensity.

State-dependent fluorescence

The $M_S = 0$ and $M_S = \pm 1$ ground states show different fluorescence intensities under off-resonant (e.g. green) excitation, due to different inter-system crossing rates in their respective excited states [26, 38]. In more detail, when the centre is prepared in the $M_S = 0$ state, high fluorescence will be observed, since the state has a low crossing rate to the singlet level $^1A_1$ (see ch. 3.2.7, fig. 3.10), whereas after preparation in the $M_S = \pm 1$ levels there is a significant chance of crossing. The fluorescence reduction

---

[5]The high gain was necessary due to the summation of losses at each element in the microwave chain.
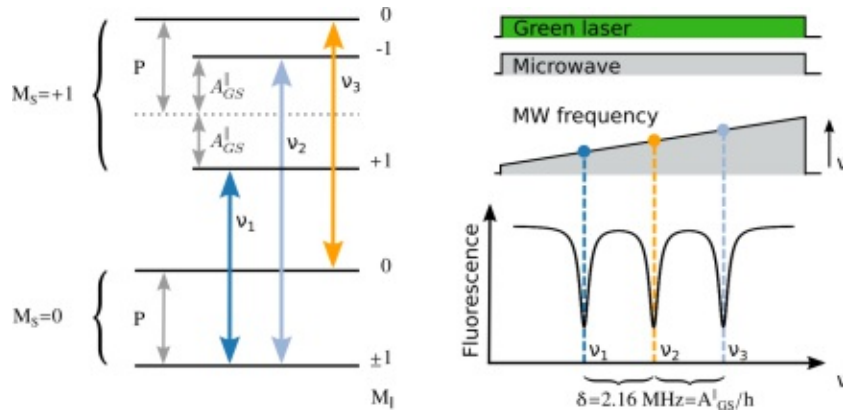
Figure 4.11: *Optically detected magnetic resonance principle: microwave driven resonances linking the $M_S = 0$ and $M_S = 1$ electron spin levels (coloured arrows on left side) in a ^{14}N nuclear spin-1 NV centre. Low power green laser produces fluorescence from the centre while low power CW microwave frequency is swept (right side). On resonances $M_S = 0$ population will transfer to the $M_S = 1$ state, which has lower fluorescence yield, producing a triplet of dips in the optical spectrum, separated by the hyperfine coupling constant in frequency units.*

results from a 'shelving' period by the ^1E singlet level's lifetime of about 300 ns to 400 ns at low temperature. The effect is present at both room and low temperature conditions.

Figure 4.10 illustrates state-dependent fluorescence in the form of time traces of different initial spin polarizations, which make obvious two concurring mechanisms: state-dependent fluorescence dominates in the short term, while optically induced spin polarization erases the fluorescence difference in the long term, reaching a steady-state spin population distribution. The procedure enables optical readout of the spin state with a typical visibility of 20 % to 40 %, on comparing the integral fluorescence of a short time period with a calibration reference. Typically, we chose a duration of 300 ns, a good compromise between high visibility and low error, due to the increased photon count.

Optically detected magnetic resonance spectrum

Off-resonant CW excitation of the centre with green laser light polarizes the electron spin into the $M_S = 0$ state, yielding a steady-state fluorescence intensity. When additionally a CW microwave field is present and its frequency is swept over a resonance with the $M_S = 1$ or $M_S = -1$ state, the field will repopulate them, forcing a drop in the observed fluorescence intensity, by virtue of their lower fluorescence yield, shown by example in figure 4.11 for the three $M_S = 0$ to $M_S = 1$ hyperfine resonances (see ch. 3.2.3). Without a magnetic bias field, the resonances are located at about 2.88 GHz at low temperature.

55
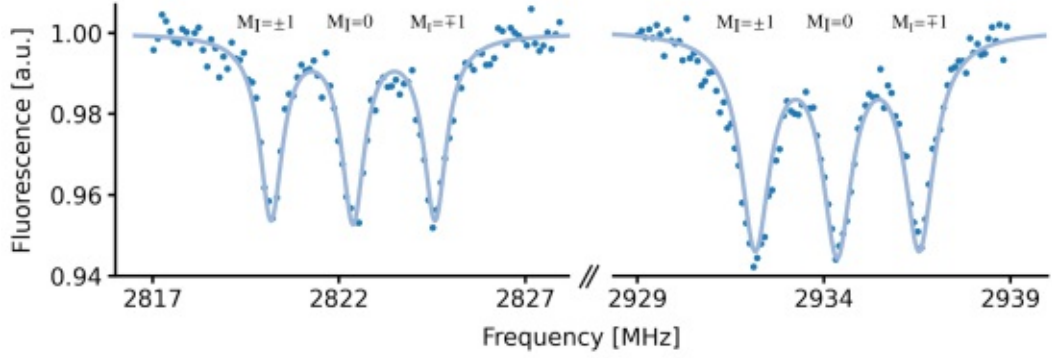
Figure 4.12: *ODMR spectrum: measurements of PSB fluorescence intensity in dependence of the microwave frequency were repeated for about 200 times. Used fit function is from equation 4.10. The two sets of triple resonances are split by application of a static magnetic field in the direction of the NV centre axis with unknown orientation, so that the involved nuclear spin states can be discerned in character but not definitively. The small difference of triplets in contrast is due to fluctuations in microwave power.*

The ODMR intensity profile I for a single hyperfine resonance in dependence of the microwave frequency v can be described by a Lorentzian function [27]

$$I(v, v_0) = R \left[1 - C \frac{1}{\pi} \frac{\Delta}{(v - v_0)^2 + \Delta^2} \right], \tag{4.8}$$

where R is the rate of detected photons, C is the contrast of the measurement, v_0 is the resonance frequency and Δ is the half width at half maximum (HWHM). The contrast is defined as

$$C = \frac{R_0 - R_{v_0}}{R_0}, \tag{4.9}$$

with R_0, (R_{v_0}) the photoluminescence rate without microwave field (with resonant microwave field), respectively. The three hyperfine resonances belonging to the same fine structure transition are separated by $2.16\,\mathrm{MHz}$ (see fig. 4.11, 4.12, with reference to the splitting constants introduced in chapter 3.2.3) for the common $^{14}\mathrm{N}$ nuclear spin-1. Assuming equal nuclear spin populations, the full triplet consists of the sum of three Lorentzian functions

$$I(v, v_I) = R \left[1 - C \frac{1}{\pi} \sum_{I=1}^{3} \frac{\Delta}{(v - v_I)^2 + \Delta^2} \right], \tag{4.10}$$

with v_I the resonance frequencies. ODMR spectra are useful to determine resonance frequencies, but furthermore offer information about nuclear spin populations and couplings to adjacent nuclei and their respective strength.

4.3.3 Coherent spin manipulation and spin coherence time

With transition frequencies determined by ODMR, the option of targeted ground state manipulation through precise resonant microwave pulses becomes available. Here, the underlying theory is developed, the manipulation scheme is discussed and environmental influences are considered.

Two-level system interacting with a classical field

The question raised, concern the evolution of the NV centre ground state under microwave irradiation and how this mechanism can be capitalized on for state manipulation. The discussion, inspired by reference [65], departs from the approximation of a two-level system (ground state $|0\rangle$, excited state $|1\rangle$), with energies 0, $\hbar\omega_0$, respectively, in a resonant field of frequency ω_0.

Owing to correspondence of SU(2) and O(3), the state described by a density matrix $\hat{\rho}$ can be expressed as a vector, called Bloch vector $\mathbf{r}$, in three-dimensional space, through the relations

$$\hat{\rho} = \frac{1}{2}\sum_{\alpha=0}^{3} r_\alpha \hat{\sigma}_\alpha, \tag{4.11}$$

$$r_\alpha = \mathrm{Tr}\left(\hat{\sigma}_\alpha \hat{\rho}\right). \tag{4.12}$$

Here $\hat{\sigma}_\alpha$ are the standard Pauli operators with $\alpha \in \{x, y, z\}$. The components of the pure state unit length Bloch vector are

$$\begin{aligned}
r_1 &= 2\,\mathrm{Re}\{\rho_{12}\}, \\
r_2 &= 2\,\mathrm{Im}\{\rho_{12}\}, \\
r_3 &= \rho_{22} - \rho_{11}, \\
r_0 &= \rho_{22} + \rho_{11} = 1,
\end{aligned} \tag{4.13}$$

(with ρ_{ab} the elements of $\hat{\rho}$), pointing to the surface of a unit-radius sphere, where the ground (excited) state relates to the spheres north (south) pole respectively. By equation 4.12, the components of the Bloch vector are the expectation values of spin operators

$$r_\alpha = Tr\left(\hat{\rho}\hat{\sigma}_\alpha\right) = \langle\hat{\sigma}_\alpha\rangle. \tag{4.14}$$

These equations imply a known evolution of $\mathbf{r}$ on the sphere, when the temporal evolution of the density is derived. The von Neumann equation

$$\frac{\partial}{\partial t}\hat{\rho} = \frac{1}{i\hbar}[\mathrm{H}, \hat{\rho}] \tag{4.15}$$

57

expresses time evolution of the density, under the Hamiltonian H, consisting of an unperturbed diagonal part H_0 and a part interacting with the field H_1,

$$H_0 = \begin{bmatrix} 0 & 0 \\ 0 & \hbar\omega_0 \end{bmatrix}, \quad H_1 = -\boldsymbol{\mu}\mathbf{B}(t), \tag{4.16}$$

with ω_0 the resonance frequency, $\boldsymbol{\mu}$ the magnetic dipole moment and $\mathbf{B}(t)$ the magnetic field. Analysis of the matrix elements of the interacting part yields contributions only from off-diagonal elements due to parity. With the derivative of $\hat{\rho}$ established, the evolution of the Bloch vector components under the action of the field is accessible through equations 4.13 as

$$
\begin{aligned}
\dot{r}_1 &= \frac{2}{\hbar}\,\mathrm{Im}\{M_1\}r_3 - \omega_0 r_2, \\
\dot{r}_2 &= -\frac{2}{h}\,\mathrm{Re}\{M_1\}r_3 + \omega_0 r_1, \\
\dot{r}_3 &= \frac{2}{\hbar}\left[\mathrm{Re}\{M_1\}r_2 - \mathrm{Im}\{M_1\}r_1\right],
\end{aligned}
\tag{4.17}
$$

with $M_1 = \langle 0|H_1|1\rangle$. One notices that the third component is solely dependent on the presence of the field. The length of the Bloch vector remains constant under evolution, only the direction of the vector is changed. Another aspect, making the discussion geometrically more intuitive, is the possibility to express the above equations as a vector product between the Bloch vector and a further vector, which we call $\mathbf{Q}$,

$$\frac{d\mathbf{r}}{dt} = \mathbf{Q} \times \mathbf{r}. \tag{4.18}$$

In this picture, $\mathbf{r}$ precesses around the axis defined by the equatorial vector $\mathbf{Q}$ at a rate that is proportional to $|\mathbf{Q}|$, given by the strength of the interaction. To see the relevant time evolution more clearly, rapidly oscillating terms from the solution are usually removed through description of the states in a rotating frame, under a linearly polarized field. Another mitigation of complexity is the introduction of the Rabi frequency parameter Ω, as

$$\Omega = \left|\frac{\mu_{01} \cdot B}{\hbar}\right|, \tag{4.19}$$

which includes the matrix element of the dipole interaction μ_{01} and the field B.

Driving the transition with a detuned field of frequency ω_1 and again expressing the evolution of the components of $\mathbf{r}$ in the rotating frame by a vector product leads to a

precession axis of

$$\mathbf{Q}' = \begin{pmatrix} -\Omega \cos \varphi \\ \Omega \sin \varphi \\ \Delta \end{pmatrix}, \tag{4.20}$$

with $\Delta = \omega_0 - \omega_1$ being the detuning from resonance and φ the phase of the field. The rate of precession around this axis is determined by

$$|\mathbf{Q}'| = \sqrt{\Omega^2 \cos^2 \varphi + \Omega^2 \sin^2 \varphi + \Delta^2} = \sqrt{\Omega^2 + \Delta^2}, \tag{4.21}$$

dependent on the power of driving and the detuning from resonance.

A solution for a sinusoidal field with constant phase for the rotating frame z-component of the Bloch vector, proportional to the projection of the spin component along the z-axis of the Bloch sphere, is derived as

$$r_3'(t) = \frac{\Delta^2}{\Omega^2 + \Delta^2} - \frac{\Omega^2}{\Omega^2 + \Delta^2} \cos\left(\sqrt{\Omega^2 + \Delta^2}t\right), \tag{4.22}$$

which captures an oscillatory behaviour, known as the Rabi oscillation, around the value set by the first term, with a frequency of $\sqrt{\Omega^2 + \Delta^2}$ and an amplitude of $\Omega^2/(\Omega^2 + \Delta^2)$.

The effect of strong detuning from resonance manifests in two ways: the rotation of the axis of precession away from the Bloch sphere equator and a decrease in the achievable amplitude of driving the state along the z-axis. This means that a full rotation of the state from $M_S = 0$ to $M_S = 1$ may become unfeasible. An illustration of these effects is shown in figure 4.13. The amount of state rotation by a finite time-dependent microwave pulse is derived from the area of the pulse,

$$\theta = \int \Omega(t)dt = \left| \frac{\mu_{01}}{\hbar} \int_0^t B(t')dt' \right|. \tag{4.23}$$

A rotation of $\theta = \pi$, that flips the spin, is called a π-pulse for abbreviation.

Coherently driven electron spin

We now focus on the experimental exploitation of the theory, to coherently drive the ground state electron spin. The reason for establishing the exact resonance frequencies by ODMR has now been more strongly motivated, considering we can resort to the case where little or no detuning is present in the system. Then the evolution of the z-component of the spin state (eq. 4.22) depends on the Rabi frequency parameter Ω, which is tunable via the intensity I of the microwave field (eq. 4.19), seeing that $\Omega \propto \sqrt{I}$. We
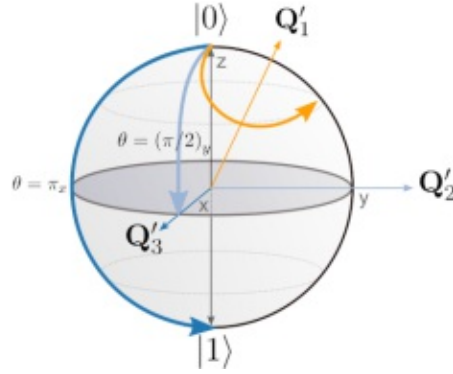
Figure 4.13: *Bloch vector rotation due to an external field in the rotating wave approximation picture: detuning pushes the rotation axis $\mathbf{Q}'_1$ away from the equatorial plane, with $|\mathbf{Q}'_1| = \sqrt{\Omega^2 + \Delta^2}$. $\mathbf{Q}'_2$ and $\mathbf{Q}'_3$ define the detuning free rotation axes, illustrated with a $\pi/2$-pulse around the y-axis and a π-pulse around the x-axis respectively.*

aimed to achieve a high Rabi frequency by putting the microwave wires, spanned across the sample, as close as possible to the NV centre and by using a powerful microwave amplifier. High Ω relates to short spin-flip times, which reduces sequence duration and thereby decoherence effects. Furthermore, with high Ω all hyperfine states of an electron spin level are driven at once, by maximizing the amplitude factor in equation 4.22

$$\frac{\Omega^2}{\Omega^2 + \Delta^2},\tag{4.24}$$

where the detuning Δ within the three hyperfine states is symmetrically $2\pi \cdot 2.16\,\mathrm{MHz}$ each from the central line.

Rabi nutation measurements were conducted to determine the exact value of the spin flip times for the $\mathrm{M_S} = 0$ to $\mathrm{M_S} = \pm 1$ transitions, at a given microwave power. Measurements were done in two different modes: with off-resonant and with resonant laser readout. The difference was a higher achievable nutation visibility in the resonant case, as a result of the resonant laser addressing only the $\mathrm{M_S} = 0$ ground to excited state transition (see section 4.4.2 below). However, this mode necessitates a low-temperature environment. Although off-resonant readout shows lower oscillation visibility, it is still beneficial for room-temperature calibration measurements.

The measurement sequences used are visualized in the inset of figure 4.14, for both the off-resonant and resonant readout cases. Sequences started with a green initialization pulse to spin-polarize the centre in the $\mathrm{M_S} = 0$ state, followed by a variable length microwave pulse. In the off-resonant case, the state was read out via a green laser
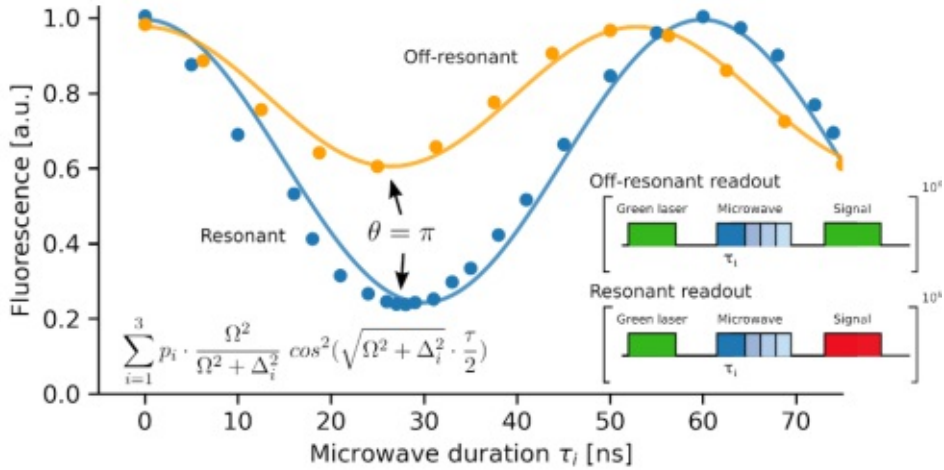
Figure 4.14: *Rabi oscillation measurements with off-resonant (RT) and resonant readout (LT). Both curves were fit with the indicated sum of three cosine functions ($p_i = 1/3$, $\Delta \in \{-2.16, 0, 2.16\}$ MHz) for the hyperfine states, with additional inclusion of background. The background in the off-resonant case mostly originates from the low readout contrast, while in the resonant case the limiting factor was the incomplete spin state initialization. The inset depicts the respective experimental sequences, repeated for improved photon statistics for about 10^6 times.*

pulse (which can be the same as the initialization pulse as the sequence is repeated), in the resonant case with a resonant red pulse (details of the state readout are discussed in chapter 5.1). On plotting the signal as a function of microwave pulse duration the typical Rabi nutations, a cosine-dependence due to initialization in the bright state, become visible (fig. 4.14[6]). The time period to the first minimum, corresponding to a spin flip, yields the duration of the π-pulse. The achieved spin-flip times, for the work presented in this thesis, were in the range of 20 ns to 70 ns, which translate to a high transfer fidelity (including the two detuned hyperfine states) of 94.3 % to 99.5 %.

Magnetic field alignment

Environmental magnetic fields from earth and stray fields were oriented in an unknown way and most likely contained components transversal to the NV centre axis. As discussed in chapter 3.2.3, transversal B-fields mix the ground state levels, which led to a visible reduction of the amplitude of the Rabi nutations. The problem was removed by placing strong magnets next to the cryostat housing, aligned to produce an axial mag-

---

[6]The deviation of the signal from the fit function at short microwave pulse durations is suspected to originate from distorted pulses for such short durations.

netic field at the NV centre location of about $20\,\mathrm{G}$, manifesting in a Zeeman splitting of the ODMR spectral lines for $\mathrm{M_S} = -1$ and $\mathrm{M_S} = 1$ of approximately $100\,\mathrm{MHz}$ (see fig. 4.12).

Spin coherence time

Spin relaxation times determine a temporal window within which high-fidelity operations on a quantum state are possible. There are two major timescales, the longitudinal relaxation time T_1 and the transverse relaxation time T_2^*, which capture the timescale for population decay and inhomogeneous dephasing, respectively [94]. While the T_1 time of $\mathrm{M_S} = \pm 1$ states is suitably long [4], the shorter T_2^* time of the state usually presents a bottleneck [27]. Additionally to environmental influences like phonons and paramagnetic impurities [8], there is also a dephasing contribution from the different oscillation frequencies of the hyperfine states. To determine the T_2^*-time, a Ramsey experiment was carried out as displayed in figure 4.15a, with the microwave tuned to the central hyperfine state.

   A $\frac{\pi}{2}$-microwave pulse brought the $\mathrm{M_S} = 0$ ground states into a superposition state and the corresponding Bloch vector to the equator of the Bloch sphere (or close to it in the case of the slightly detuned hyperfine states). After a variable wait period τ a second $\frac{\pi}{2}$-pulse was applied, which transformed the accumulated phase differences from the equator region to a readable population difference. The oscillation was fitted with the function

$$S_{Ramsey} = \frac{A}{2}\left[1 - cos(\delta\tau)e^{-\left(\frac{\tau}{T_2^*}\right)^2}\right] + B, \tag{4.25}$$

with the oscillation amplitude A, the detuning of states δ and a background B [96]. A T_2^*-time of $1.9\,\mathrm{\mu s}$ was retrieved (fig. 4.15b), sufficient for the entangling sequence gate operations.

4.4   Coherent optical interface

The photonic qubit generation scheme demanded an optical interface for coherent excitation on an NV centre optical transition. Furthermore, fluorescence detection was alleviated by scattered light suppression mechanisms. This section begins with the obligatory hardware for those tasks. Afterwards, light is shed on the identification of spectral
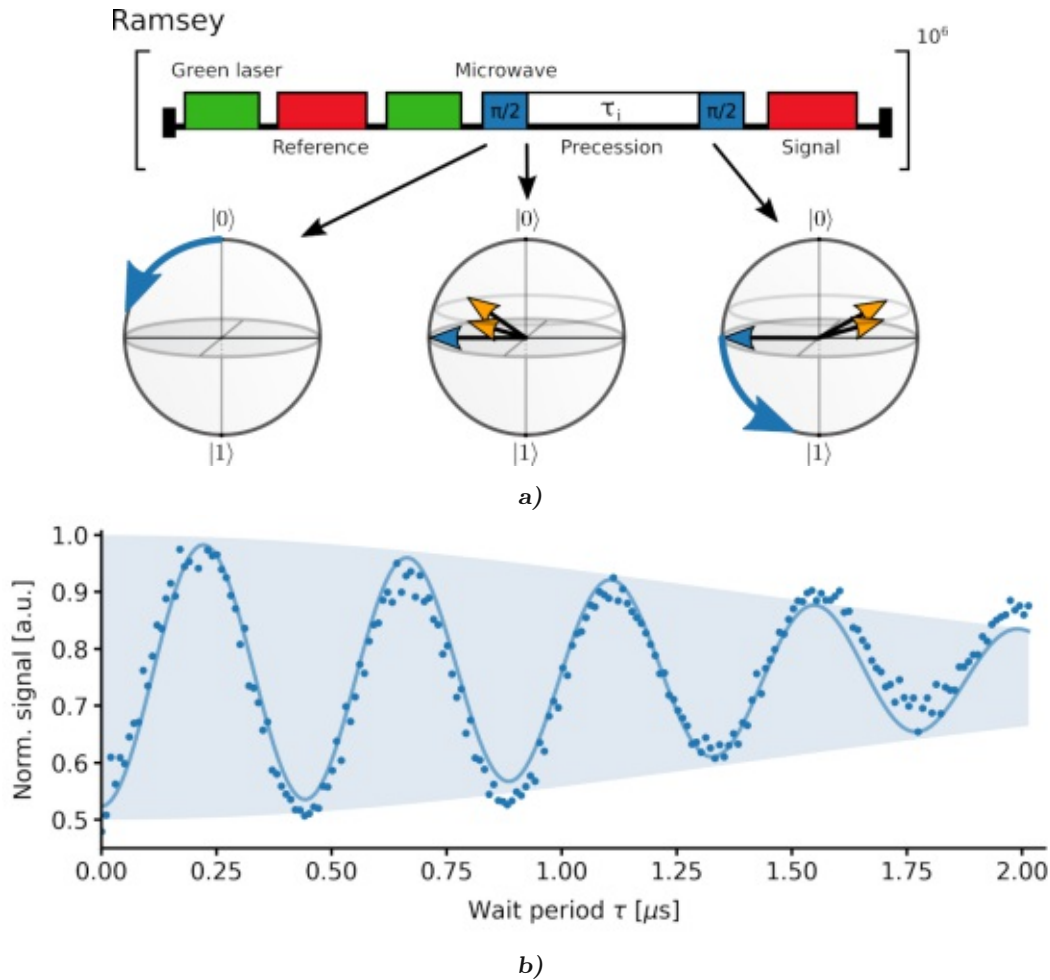
Figure 4.15: *Ramsey measurement:* **a)** *illustration of the experimental sequence with resonant state readout. Green laser spin-polarizes the centre, a reference readout was taken followed by re-initialization with a second green pulse. The Ramsey experiment started with a $\frac{\pi}{2}$-microwave pulse to establish a superposition state of $\mathrm{M_S} = 0$ and $\mathrm{M_S} = 1$, as indicated in the left Bloch sphere picture below. In the precession period with duration τ the three hyperfine states evolved freely, close to the equator of the Bloch sphere. The sequence concluded with a second $\frac{\pi}{2}$-pulse and state readout.* **b)** *Ramsey oscillation pattern with frequency of the hyperfine state detuning, showing a stretched exponential-decay envelope due to the T_2^*-time of 1.9 µs.*

63
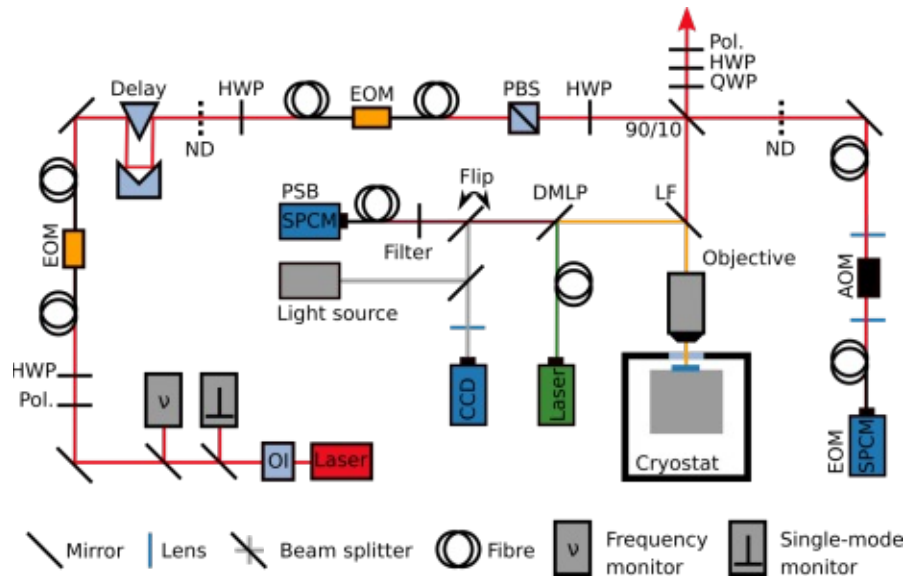
Figure 4.16: *Confocal microscope setup including resonant optical pathways. Acronyms: optical isolator (OI), accousto-optic modulator (AOM), electro-optic modulator (EOM), polarizer (Pol.), half-wave plate (HWP), quarter-wave plate (QWP), polarizing beam splitter (PBS), neutral density filter (ND), single-photon counting module (SPCM). The resonant paths and the previously introduced off-resonant confocal microscope setup (fig. 4.2a) were connected by a narrow laser line filter (LF, Semrock FF01-637/7), that would only transmit resonant excitation/fluorescence light. The left arm depicts the red laser excitation light path as described in the text. The monitoring of electro-optical modulator (EOM) operation was achieved in the vertical path on the right. A neutral density filter was present for transmission power adjustment and an acousto-optic modulator (AOM) for on/off switching. (The final and full optical setup for the experiment is shown in fig. 6.3)*

optical transitions and the determination of the NV dipole orientation in relation to the excitation light. The mechanism and process of producing optical excitation pulses is examined and the chapter concludes with the optimization of excitation and detection light parameters.

4.4.1 The resonant optical path

The resonant optical path and its parts are illustrated in figure 4.16. Working resonantly with NV centres requires a narrowband tunable laser at 637 nm, in our case a Toptica diode laser DLC DL pro HP637 with integrated optical isolator. Additionally, a second isolator (Thorlabs IO-3-633-LP) was placed right at its output, for improved laser coherence via reduction of backscattered light. Beam samplers picked up some light sent to a Fabry-Perot cavity for single mode operation monitoring and a wavelength meter.

Two EOMs from Jenoptik (AM635) provided fast (<1 ns) amplitude switching with high suppression in the off-state of 27 dB each. EOMs are very sensitive to light polarization, therefore they were each nested in optics for polarization adjustment, such as a polarizer and half-wave plates (HWP). For temporal fine tuning a retro-reflecting delay line was present (details further down in this section) and the power was adjusted with a variable neutral density filter. The beam was cleaned in polarization with a PBS and sent onto a 90/10 beam splitter with $10\,\%$ of the excitation light sent to the sample and $90\,\%$ transmitted into a path for monitoring the operation of the EOMs. This beam splitter setting simultaneously maximizes ZPL fluorescence in direction of the detection port (red arrow in the figure), with $90\,\%$ fluorescence transmission into this ZPL detection path.

4.4.2 Excited state spectrum and dipole orientation by photoluminescence excitation

In order to address a single optical transition the spectrum had to be determined first. The photoluminescence excitation (PLE) method was well suited for the task, as it works by sweeping the excitation light frequency over a range of interest while monitoring luminescence. Meanwhile, a continuous low power microwave driving, resonant to the $M_S = 0$ to $M_S = \pm 1$ states, was applied. This repopulation of $M_S = \pm 1$ spin states gave access to all possible transitions. Figure 4.17a shows fluorescence traces of individual scans of the excitation laser frequency over a range of 5 GHz. Considering a two-photon absorption may de-ionize the centre (lines going dark in the figure) [84], a green laser pulse was inserted at the sequence end repumped to the negative charge state. The traces gave insight into the spectral stability of the resonances over time. In long-term measurements over hours we found only slow drifting, which we could track in real time during measurements by slowly scanning the laser frequency and readjusting the frequency to maximize the luminescence. The upper figure in 4.17b shows the mean of the traces in the measurement shown in figure a) (blue dots) and a fit with six Lorentzian functions. The involved spin character is indicated above the peaks and was determined by the vanishing of $M_S = \pm 1$ related transitions when switching the microwave off. $M_S = \pm 1$ transitions do not optically cycle well due to likely shelving in the long lived singlet state and optical spin polarization into $M_S = 0$. The three spin non-conserving transitions show only small peaks, where the rightmost one is marked with a black arrow in the figure.
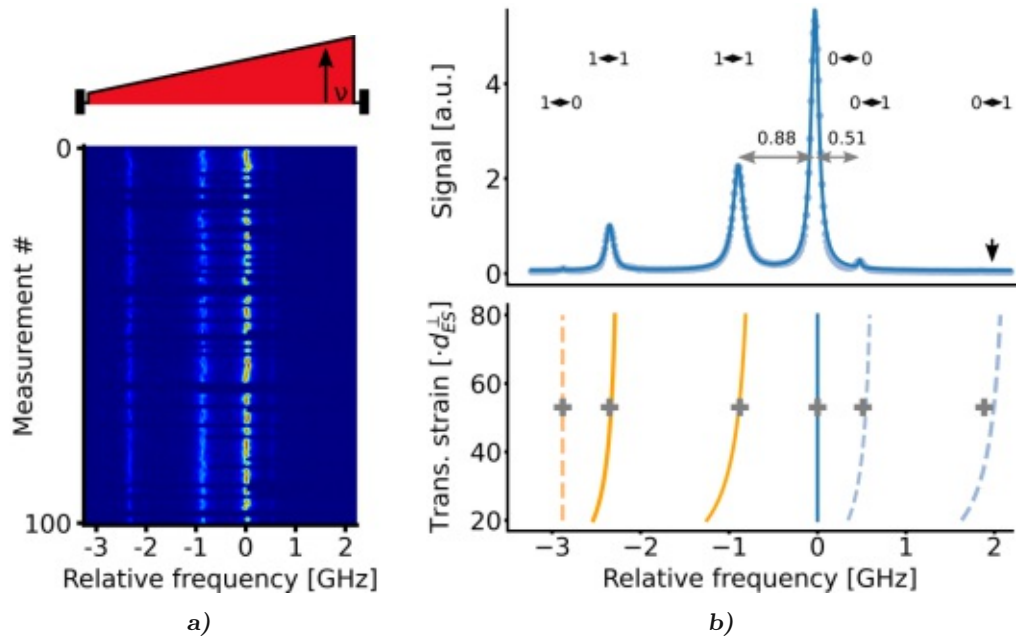
65

Figure 4.17: *Photoluminescence excitation measurement:* **a)** *resonant laser (some μW of power) was swept in frequency while monitoring fluorescence. Measurement traces of individual runs exhibit bright fluorescence regions on resonance. Colour scale in arbitrary units. CW microwave signal resonant with one ground state transition gave access to all possible lines. A green laser pulse at the sequence end (not shown) repumped the negative charge state. The frequency scale was established by fit in figure b.* **b)** *Upper graph light blue dots represent the average signal of all traces from the measurement in figure a). The involved spin characters are indicated above the peaks, with the left value denoting the ground state and the right the excited state; 1 refers to both ±1. The signal was fit with six Lorentzian spectral line shape functions to obtain exact peak positions. In the lower part those positions were associated with transversal crystal strain in the sample and could be identified with the lower branch of the excited state manifold. The best fit was obtained for about equal amounts of x- and y-oriented crystal strain of $53 \cdot d_{ES}^{\perp}$ each.*

In the bottom graph, a simulation of transition frequencies of the lower excited state branch versus transversal crystal strain shows excellent overlap with peak positions (gray plus signs) and indicates the high strain regime the centre was found to be in. The color coding is identical to the one in chapter 3.2.5, figure 3.8b, indicating the involved ground state electron spin character (blue for $M_S = 0$, orange for $M_S = \pm1$) and wheather the spin is conserved (solid lines). The amount of strain suggests the upper branch being located about 150 GHz higher in frequency but could never be found experimentally.

The linewidth of the averaged $M_S = 0$ ground state to $M_S = 0$ excited state transition was 100 MHz FWHM. It was detuned from the lower-frequency spin-allowed transition
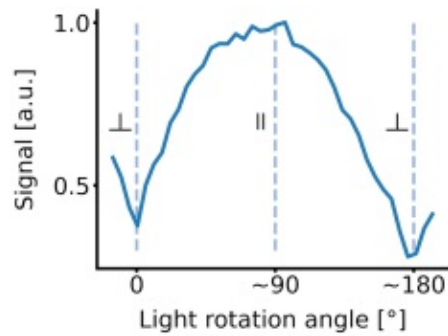
Figure 4.18: *Dipole measurement: excitation light polarization was rotated while on resonance with $M_S = 0$ ground to excited state transition. Signal is the collected PSB fluorescence. Extrema and corresponding alignment of polarization relative to the dipole are marked (dashed lines). Rotation angles are accurate up to some degrees due to experimental hardware.*

by 0.88 GHz and to the higher-frequency forbidden one by 0.51 GHz. The spectrum implied that the centre offered only one strong spin-conserving transition to work with. Similar spectra were observed for other centres on the same sample.

Dipole orientation. The observation of only one branch was supported by measurements of the involved NV dipole. On rotating the excitation light polarization with the HWP in front of the 90/10 beam splitter, while on resonance and performing PLE, a periodic pattern became visible, promoting high fluorescence when the excitation light polarization is aligned with the dipole of the excited state branch and minima when perpendicular [31]. Our measurements resulted in a close to 180°-periodic pattern of only one addressable dipole, shown in figure 4.18. Rotation of polarization over the dipole gave access to tuning the projected power onto the NV.

4.4.3 Resonant excitation laser amplitude modulation

The PLE experiments above were conducted with resonant CW excitation. We now devote our attention to the issue of producing amplitude modulated light for three purposes: coherent excitation within a short time period, spin state initialization and resonant state readout. For the first kind a high power light pulse with pulse area of π and FWHM on the order of 1 ns was required, as a result of only temporal discrimination being an option to discern the same frequency excitation and ZPL fluorescence light. For the initialization and state readout, a low power step-shape pulse with duration in the range of microseconds was employed.

67
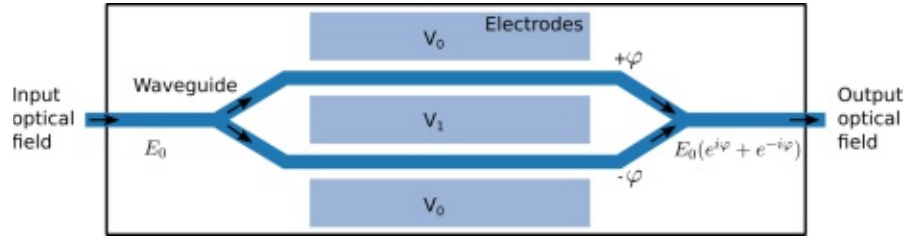
Figure 4.19: *Working principle of a Mach-Zehnder modulator: the input field, inserted into a waveguide crafted into the LiNb0$_3$-substrate, is split equally. Both arms traverse longitudinal electrodes with opposite electric fields, that imprint opposing phase differences onto the light fields. Upon recombination of waveguides, the interference term $e^{i\varphi} + e^{-i\varphi} \propto cos(\varphi)$ gives access to amplitude modulation via the phase [46].*

Producing an off-state

Before actually producing pulses, an off-state had to be established, which meant a power suppression from $30\,\text{mW}$ of the laser beam to at maximum $0.3\,\mu\text{W}$ before the 90/10 beam splitter ($0.03\,\mu\text{W}$ at the objective), the power at which fluorescence just became visible in PLE measurements. This implied a suppression of at least $10 \cdot \log \frac{0.3}{30000} = -50\,\text{dB}$. Two EOMs used in series were chosen for the task at hand, yielding a suppression of $2 \cdot 27\,\text{dB} = 54\,\text{dB}$ from specification [47]. Jenoptik amplitude EOMs are integrated optics devices featuring a Mach-Zehnder interferometer arrangement of waveguides (fig. 4.19). Via the electro-optical Pockels effect, a modulation voltage present in the arms of the interferometer affects the refractive index of the LiNb0$_3$ material, offering a controllable phase shift, that is translated into amplitude modulation by the interferometer layout.

Electro-optic retardation

To understand the operation of the device better the electro-optic Pockels effect is discussed shortly in appendix C.

The non-transmitting state (dark state) is achieved by inducing a phase shift of π between the interferometer axes by retardation. The required change in refractive index over a length L is derived from

$$\begin{aligned}\varphi_1 = a = 2\pi\frac{Ln_1}{\lambda}, \\ \varphi_2 = a + \pi = 2\pi\frac{Ln_2}{\lambda},\end{aligned} \tag{4.26}$$

$$2\pi\frac{L}{\lambda}\left(n_2 - n_1\right) = \Delta\phi. \tag{4.27}$$
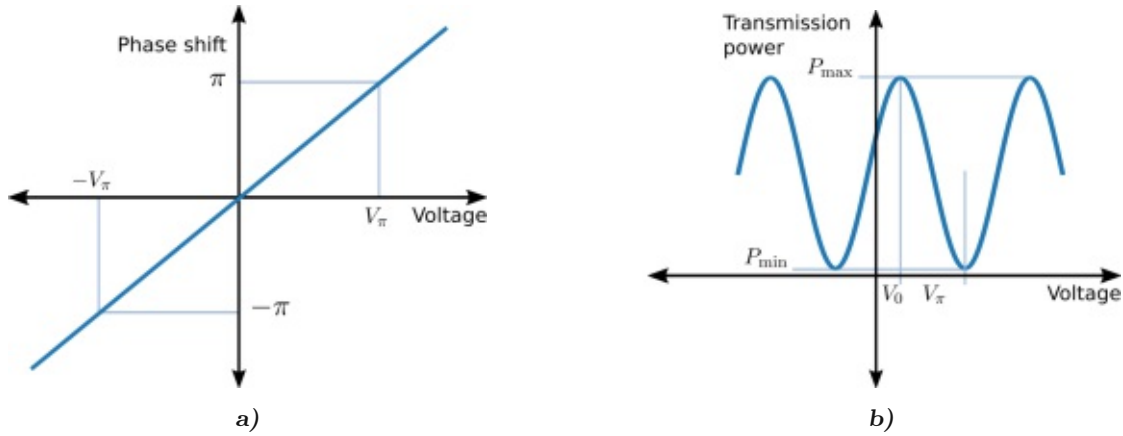
Figure 4.20: a) *The retardation has a linear dependence on the electrode voltage and therefore electric field.* **b)** *Amplitude-modulator transmission in dependence of applied voltage according to equation 4.30.*

Combining with equation C.11 yields the retardation going linearly (fig. 4.20a) with the electric field (voltage) as

$$\Delta\varphi = -\frac{\pi L}{\lambda} n_z^3 r_{zz} \frac{V}{d}\Gamma,$$
(4.28)

where Γ is the overlap between the optical and electric field (in our case about 0.65 [47]). The voltage for going from a maximum to a minimum in transmission is called the half-voltage V_π and is given by setting the above equation equal to a phase shift of π,

$$V_\pi = -\frac{\lambda d}{L n_z^3 r_{zz}\Gamma}.$$
(4.29)

V_π is device specific, typically on the order of 1.5 V, and doesn't change during operation.

The periodic transmission power P of the interferometer in dependence of the applied voltage is illustrated in figure 4.20b and described by

$$P = P_{\min} + (P_{\max} - P_{\min})\left(\frac{1}{2}\cos\left(\frac{\pi(V-V_0)}{V_\pi}\right) + \frac{1}{2}\right).$$
(4.30)

Picking a voltage corresponding to a minimum in the transmission curve leads to the desired off-state. An auxiliary feature of the transmission curve is the low sensitivity to voltage errors due to the flat cosine behaviour at extrema. Unfortunately though, the offset voltage from zero V_0 (fig. 4.20b) is subject to a strong but slow drifting behaviour, called DC drift, dependent mainly on changes in the modulation voltage and input power, thereby shifting the whole transmission curve left or right. This is due to a slow electric field compensating process through charge transports within the crystal and typically

69

reduces the applied voltage to about 75 % of the initial one at saturation (after several hours) [47]. Since every change of parameters would have led to an hour long wait period for stable conditions it was decided to develop and install an active feedback stabilization.

Feedback stabilization

Jenoptik provided documentation for a bias voltage circuitry for the modulators [47]. The bias electronics was homebuilt and remotely controlled, but the additional electronics increased the half-voltage V_π to V_π^* of about 3 V. A feedback signal was extracted from the optical path on the right side in figure 4.16 where 90 % of the excitation light was sent to, yielding high sensitivity. An AOM in the path offered the possibility to deflect the beam from the path on light pulses from pulsed EOM operation, so that the feedback would always stem from the background only. The feedback signal was sent to the main computer, where a constantly running homebuilt tracking software adjusted the bias voltage in small increments on the EOMs, to track one of the transmission minima. The dark state voltage optimization was conducted in alternation on the devices (every few seconds) and didn't influence measurements done simultaneously.

Pulsing through electro-optical modulation

The two desired pulse types for resonant operations were achieved by modulation of the EOM voltage in two ways: for the low power readout pulses the voltage was slightly detuned from the dark state voltage for the duration of the pulse. For the coherent excitation pulses, called 'needle' pulses from here on, the voltage was switched to a neighbouring minimum in the transmission curve within some nanoseconds, producing a sharp 1 ns to 2 ns light pulse. The process is depicted in figure 4.21a. Figure 4.21b offers insight into the available fluorescence in dependence of the pulse duration.

The chosen control hardware for the two modes of operation was a dual channel arbitrary waveform generator (AWG), of type Agilent 33622A, with synchronized output of 1 GSa per second at high voltage levels (since $2V_\pi^*$ are about 6 V) for the needle pulse generation and the options of triggered arbitrary waveform play and remote access. The software control included a homebuilt python module for setting parameters and translating the sequence pulse pattern into the AWG waveform space. Execution of the pattern was triggered from the Lith pulser module. Seeing that the two EOMs, connected to one AWG output each, were physically separated by about 3.2 m in free space and
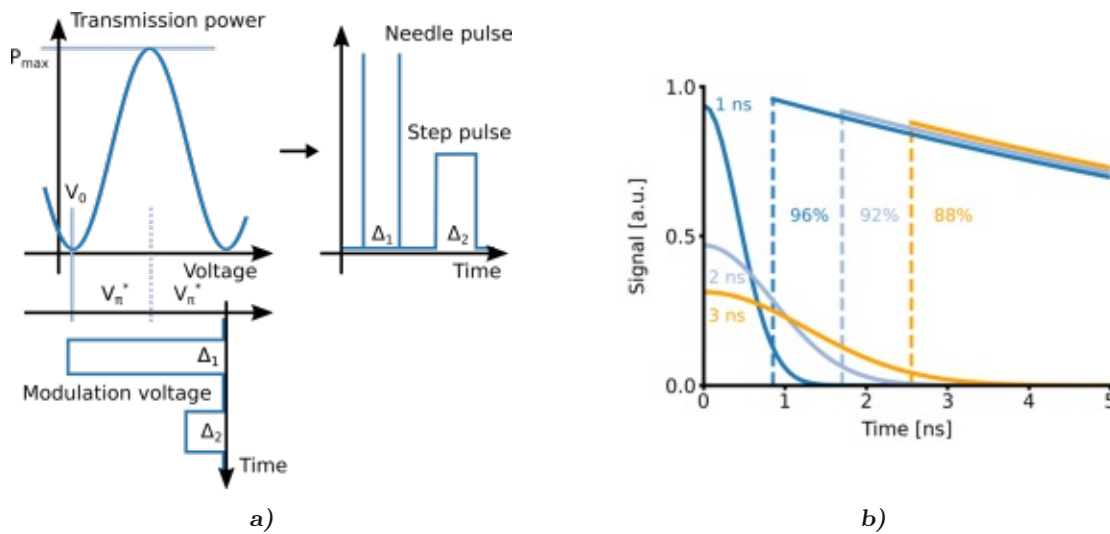
Figure 4.21: **a)** *EOM transmission power amplitude modulation: feeding the modulator with a voltage profile as shown in the lower part of the figure translates into the pulse pattern on the right side, due to the sinusoidal transmission curve. The modulation voltage is assumed to be biased at a transmission dark state. Needle pulses are produced by fast switching of the modulation voltage by $2V_\pi^*$ to a neighbouring dark state.* **b)** *Fluorescence detection simulation for excitation pulses with 1,2 and 3 ns FWHM. Assumptions: single exponential fluorescence decay trace with decay time of 13 ns starts when 75 % of pulse (Gaussian shape) is done, detection starts when only 2.5 % of excitation light from the pulse remains (dashed lines). Captured percentage is shown in the figure.*

fibre, the waveform patterns were additionally time-shifted by a 14 ns time delay in the python module before being written to the AWG, to allow a temporally matched passage of the light pulse.

In the following the optimization of the needle pulses is discussed, while the readout pulses are examined in chapter 5.

Excitation pulse optimization

Two figures of merit existed for the temporal pulse shape optimization process: a narrow pulse width and a clean detection window right after the pulse.

The FWHM of the needle pulses was primarily determined by the duration of the voltage switching process due to the AWG (specified nominally as 3.5 ns) and the temporal overlap of the light passage windows in the EOMs. For fine-tuning the temporal overlap in the EOMs with sub-nanosecond accuracy, a 30 cm manually adjustable optical delay rail was installed in between the modulators (fig. 4.16). The typical pulse width

71
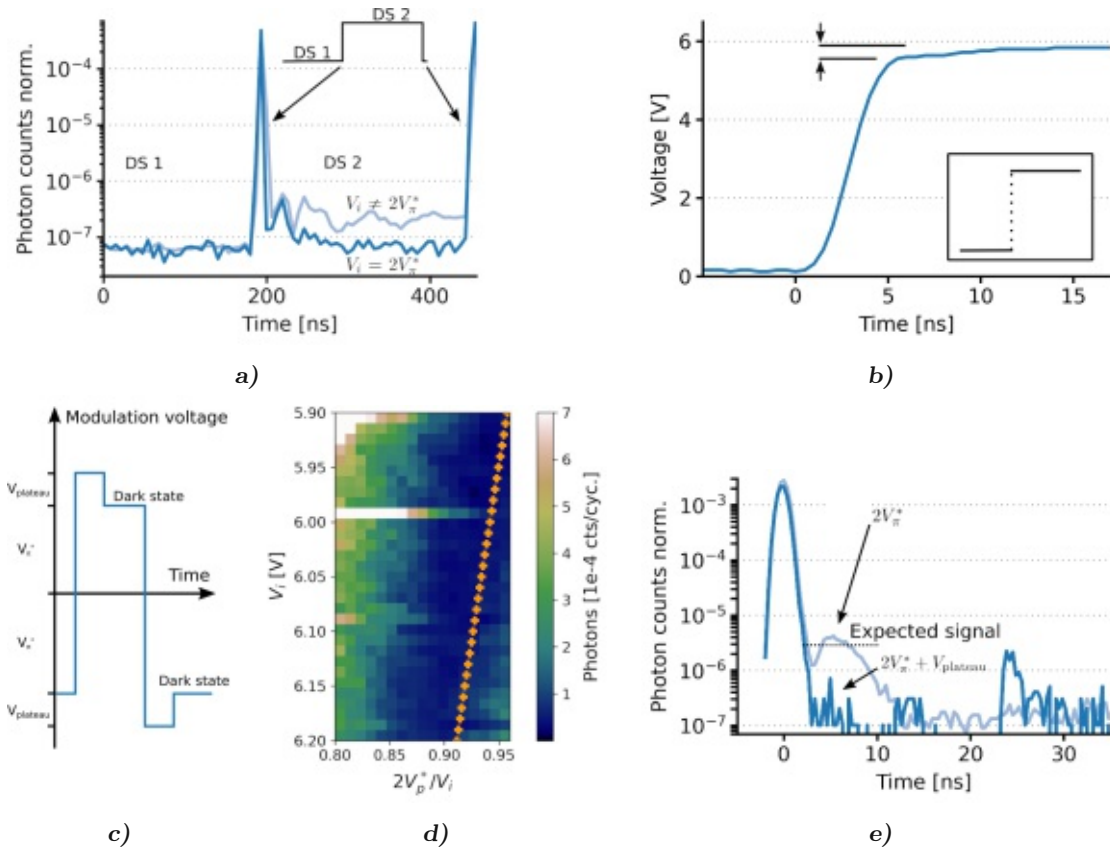
Figure 4.22: a) V_π^*-measurement: a step function voltage profile was set at the AWG (inset), generating two needle pulses. The amplitude of the step pulse V_i was scanned to find the voltage at which the photon transmission in the interval between the needles (DS 2) reached the level of the off-state before the first needle (DS 1), so that $V_i = 2V_\pi^*$ was determined (dark blue line). When V_i was slightly off the region between pulses shows elevated photon detection, as the second dark state was not reached (light blue). **b)** Set (inset) versus measured edge of step pulse. After a steep rise within 5 ns the target voltage is fully reached only after 15 ns. **c)** Schematic illustration of the two accessible modulation voltage parameters V_π^* and V_{plateau} for pulse optimization, implemented for both pulse edge directions. **d)** Scattered light per cycle in a 20 ns detection window after the pulse for different pulse edge amplitudes V_i. The relation $V_i = 2V_\pi^* + V_{\text{plateau}}$ (yellow line) indicates the voltage ratio at which the second off-state is reached. **e)** Pulse shape optimization with V_{plateau} parameter: $V_{\text{plateau}} = 0$ (light blue line) and $V_{\text{plateau}} = V_i - 2V_\pi^*$ (dark blue line). Reduces scattered photons (per excitation cycle) in the detection window by over an order of magnitude in the first 15 ns (the expected fluorescence signal level is indicated and becomes observable). The feature at 25 ns is attributed to afterpulsing of the detector.

was in the range of 1.4 ns to 1.6 ns FWHM.

The parameter accessible for improving the detection window was the voltage profile sent to the AWG. Firstly, the voltage difference of two neighbouring dark states, $2V_\pi^*$, had to be established from measurement for each EOM individually. A step profile was set on the AWG with variable amplitude V_i from a baseline sitting in a known dark state, which would produce a two needle pulse output (fig. 4.22a). When $V_i = 2V_\pi^*$, the two step pulse voltage levels would both be in a dark state and therefore the detection baseline between the pulses would have the dark state value everywhere. Otherwise the baseline in between the pulses was elevated.

However, setting the step pulse amplitude for both EOMs to their respective $2V_\pi^*$-value (5.65 and 5.77 volts) yielded polluted detection windows, observed in the scattered light leaking into the ZPL fluorescence path (light blue line in fig. 4.22e). To investigate the issue, the voltage edge produced by the AWG was recorded (fig. 4.22b), showing a fast rise with a final slow asymptote to the target voltage, which fit the observed pulsing behaviour.

As a countermeasure, a new parameter was introduced into the step voltage profile of one EOM. Instead of sending a plain step pulse with amplitude $2V_\pi^*$, the shape function then supported another adjustment V_{plateau}, shown in fig. 4.22c. For a period of 15 ns after the edge, the voltage was overshot, before settling at the neighbouring dark state level. The additional parameter was implemented for both pulsing directions - from low to high and high to low voltage. To determine V_{plateau}, two aspects were considered: minimal light in the detection window and staying in an off-state in between pulses. Theoretically, the off-state condition was fulfilled when $V_i = 2V_\pi^* + V_{\text{plateau}}$. A parameter scan of the edge voltage V_i and V_{plateau}, expressed as voltage ratio, is shown in figure 4.22d. The chosen values of $V_i = 5.94$ V and $2V_\pi^*/V_i = 0.94$ were those with good match for both imposed conditions and provided the improved pulse shape shown in figure 4.22e.

In the next section the optimization of the pulses is discussed further in the context of excitation power.

4.4.4 Optical Rabi oscillations for π-pulses

The equation for the pulse area, introduced in section 4.3.3

$$\theta = \left| \frac{\mu_{01}}{\hbar} \int_0^t B(t')dt' \right|, \tag{4.31}$$
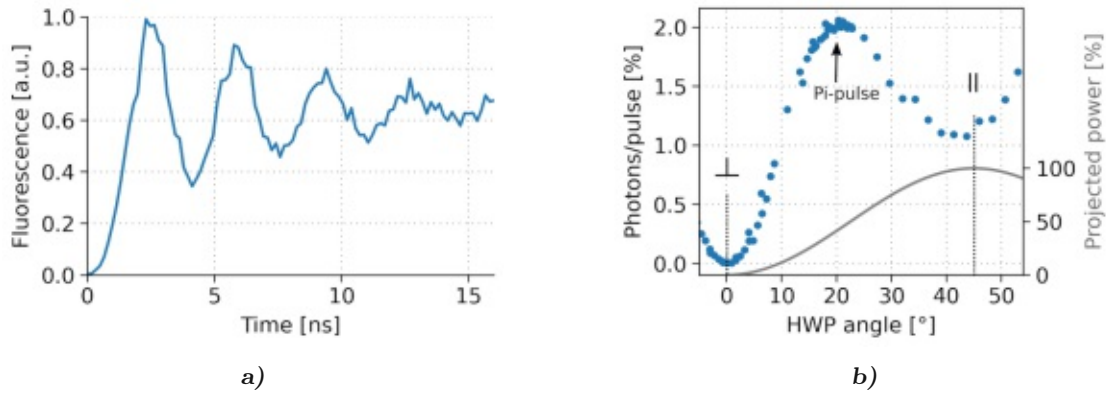
73

a)   b)

Figure 4.23: *Optical π-pulse:* **a)** *Approximation of required optical power in the excitation beam by applying a step profile pulse with high power. Strongly damped optical Rabi oscillations are visible in the collected PSB fluorescence profile. The period depends on the optical power, so that the measurement can be used to coarsely estimate the necessary power for the needle pulses.* **b)** *Optical power scan in needle pulses by rotating the light polarization. Starting at polarization being normal to the NV centre dipole (0°), the half-wave plate (HWP) angle was rotated so that projected power on the dipole (grey line) increased. Maximum fluorescence heralds the position of the desired π-pulse in this Rabi oscillation measurement. Further power increase brings population back to the ground state and would at some point (not shown) lead to a rotation of 2π. Maximal projected power was reached at 45°.*

practically offers two tunable parameters to achieve a π-pulse for coherent excitation, the pulse duration and the field strength. The strong constraints on the temporal shape of the pulse have been discussed, leaving the field strength as the only tunable quantity. This option was explored in optical Rabi nutation experiments.

An approximate search for the required optical power was done using a step pulse with maximum amplitude $(2V_\pi^*)$ switching voltage. The fluorescence signal showed damped Rabi nutations, as shown in figure 4.23a, with the oscillation period reducing with higher optical power. The strong damping was expected from the short lifetime of the excited state of $\tau = 11$ ns and from dephasing.

The fine-tuning of the field was done in a measurement series using needle pulses. The optical power in the pulses was changed by rotating the light polarization with respect to the NV centre dipole. Figure 4.23b shows the integrated PSB fluorescence after excitation with a needle pulse versus light polarization angle. The x-axis corresponds to the alignment of the polarization vector of the excitation light and the dipole axis. The projected power along this axis is indicated. Fluorescence maxima of the Rabi oscillation relate to odd multiples of π-rotations of the state, while minima would be
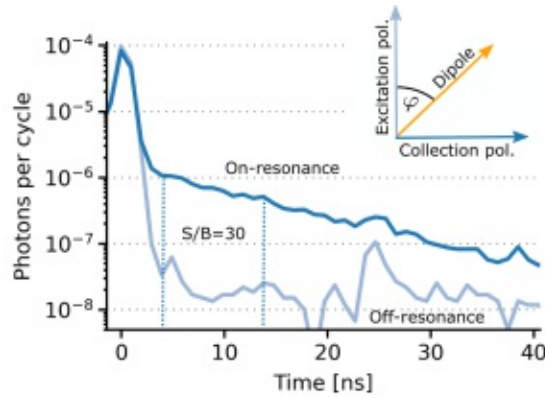
Figure 4.24: *Signal to background in ZPL fluorescence under scattered light rejection: The plot shows the fluorescence decay after a π-pulse at t=0 (dark blue) and a reference with the laser detuned from resonance (light blue). In a 10 ns window (indicated), a signal to background of 30 is observed. The inset illustrates the scatter rejection mechanism by having excitation and collection polarization on orthogonal axes.*

even ones. The desired π-pulse was achieved at the power and angle setting of the first maximum, projecting about $1.5\,\mu$W of optical power along the dipole axis.

4.4.5 Scattered light rejection

Scattered excitation light, caused by reflections from the diamond surface and transmitted into the ZPL path, was diminished in two ways: on the one hand, the above discussed temporal windows for excitation and collection, on the other hand, light polarization axes aligned as described in Bernien et al. [12] - the idea being orthogonal excitation and collection polarization axes. The axis of collection was set by polarization rotation using a HWP in the ZPL path. Additionally, a QWP was put in front of the HWP to guarantee linear light polarization. The dipole and excitation axes were oriented at an angle φ (of about 45°), which fixed the position of the HWP in the excitation path. The tuning of power in the beam was therefore achieved using a neutral density filter wheel, installed in between the EOMs into the red laser path, to still achieve optical π-pulses as discussed above. The projected excitation power then was proportional to $cos(\varphi)^2$.

The scheme, shown in the inset of figure 4.24, led to a factor $1 - sin(\varphi)^2$ loss of ZPL fluorescence, but achieved a far greater scatter suppression, due to the excitation and fluorescence collection axes being normal to each other. This setting granted a signal to background ratio of 30, as shown in figure 4.24.

<div align="right">

CHAPTER 5

</div>

Single Optical Transition Control of a High Crystal Strain Centre

In contrast to many state of the art experiments operating NV centres in the low crystal strain regime [101, 12, 37], we followed a different route by developing control mechanisms for highly strained centres. These included a mechanism for initialization of the electron and nuclear spin states, qubit manipulation techniques through well-defined microwave gates, and state tomography.

From spin coherence experiments (chapter 4.3.3) it was determined that spin dephasing was a major source of decoherence in the system. State fidelity in the entanglement experiment would suffer, which motivated the search for a pathway to initialize the nuclear spin state of the centre, additionally to the obligatory initialization of the electron spin. State initialization routines were developed using optical pumping and microwave manipulations to perform deterministic population trapping. These are very robust to many kinds of experimental imperfections and have low hardware requirements.

Three types of qubit gates provided the state control necessary for electron and nuclear spin state initialization - an optical gate for state depletion and readout, and two microwave gates for nuclear spin non-selective and selective electron spin transfer, in the form of a NOT gate (population inversion) and CNOT gate (population inversion conditioned on the nuclear spin), respectively. In the next section, the microwave gates are discussed in detail and state tomography is introduced (5.1), followed by the electron and nuclear spin initialization routines in section 5.2. In the course of refining the initializa-
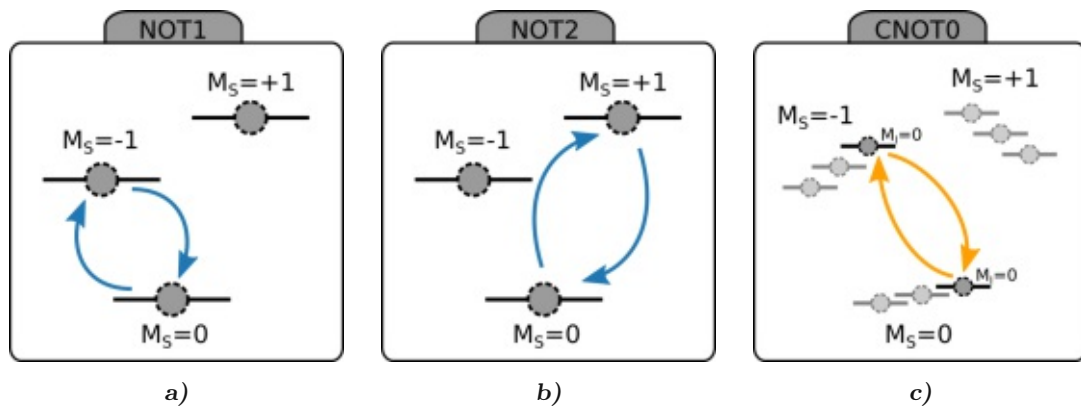
Figure 5.1: *Two NOT gates and a CNOT gate were calibrated. The gates produce a population inversion on the involved states.*

tion routines, important parameters and population transfer rates were established and an effective rates model for optically induced population dynamics in the ground state was shaped, as discussed in section 5.3. The model relies on only three independent effective rates, determined from measurements, and was used to predict populations for optimization of the initialization routines.

For the remainder of the thesis, we are going to define the lower frequency electron spin state in the ODMR measurements from chapter 4.3.2 (and fig. 4.12) as $M_S = -1$ state, and the higher frequency one as $M_S = 1$, since the exact orientation of the magnetic field along the NV centre axis was never established and does not influence any procedures or results presented herein.

5.1 Qubit gates and state tomography

5.1.1 Microwave qubit gates

Deterministic population transfers in the ground states are enabled by precisely timed microwave operations, as introduced in section 4.3.3. Application of a resonant microwave pulse with duration of the spin-flip time constitutes an electron spin specific population inversion or NOT operation, if conditional on a certain nuclear spin state, a CNOT operation (see fig. 5.1).

Two NOT gates were calibrated, one acting on the $M_S = -1$ and $M_S = 0$ states (NOT1) and the other on $M_S = 1$ and $M_S = 0$ (NOT2). As mentioned before, the
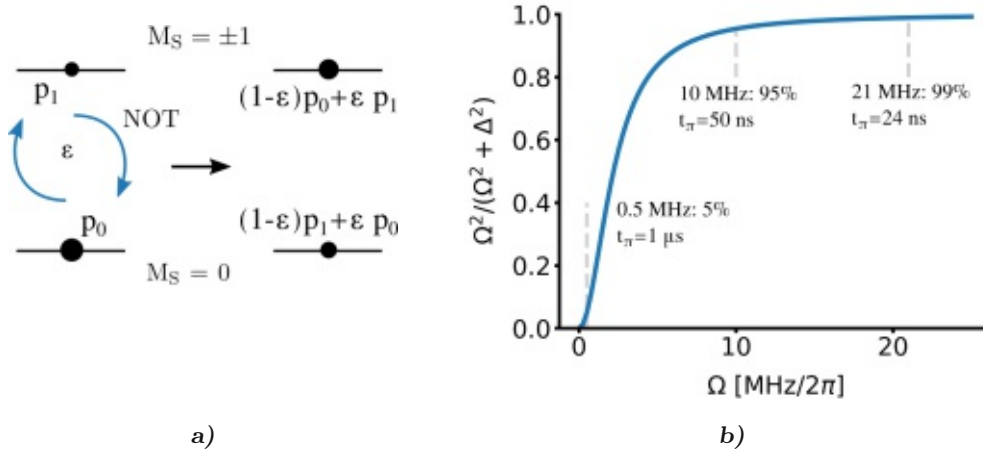
Figure 5.2: *a) Resulting population of states in a statistical mixture, with initial populations p_0 and p_1, through a NOT gate with error ϵ. b) Transfer amplitude (see eq. 4.22) depending on Rabi frequency $\frac{\Omega}{2\pi}$ with hyperfine state detuning $\frac{\Delta}{2\pi} = 2.16$ MHz. Three positions of Rabi frequencies are indicated, with their respective maximum transfer amplitude and corresponding pulse duration.*

spin-flip time was on the order of 20 ns to 70 ns, with high transfer fidelities of 94.3 % to 99.5 %, enabled by the high-power microwave channel.

We considered a realistic NOT gate with some microwave transfer error ϵ to gain insight into the transfer uncertainty. The evolution of the population of states under the operation is is illustrated in figure 5.2a. In matrix notation, the two imperfect NOT gates in the basis (-1,0,+1) acting on the populations may be written as

$$\text{NOT1} = \begin{bmatrix} \epsilon_1 & 1-\epsilon_1 & 0 \\ 1-\epsilon_1 & \epsilon_1 & 0 \\ 0 & 0 & 1 \end{bmatrix}, \quad \text{NOT2} = \begin{bmatrix} 1 & 0 & 0 \\ 0 & \epsilon_2 & 1-\epsilon_2 \\ 0 & 1-\epsilon_2 & \epsilon_2 \end{bmatrix}, \tag{5.1}$$

with their respective errors ϵ_1 and ϵ_2.

The CNOT gate, contrarily, transfers the electron-spin population conditional on the nuclear spin state. Nuclear spin state-dependant transitions become available if slow, low-power driving addresses each hyperfine state differently. However, trying to avoid driving the detuned levels is not feasible, since the Rabi frequency would have to be so low that gate operations would take a long period of time. Picking a limit of 1 % for the transfer amplitude of the undesired states implies an upper bound on the Rabi frequency of 0.22 MHz, which translates into a 4.5 µs spin-flip pulse (fig. 5.2b) - longer than the coherence time of the system.

79
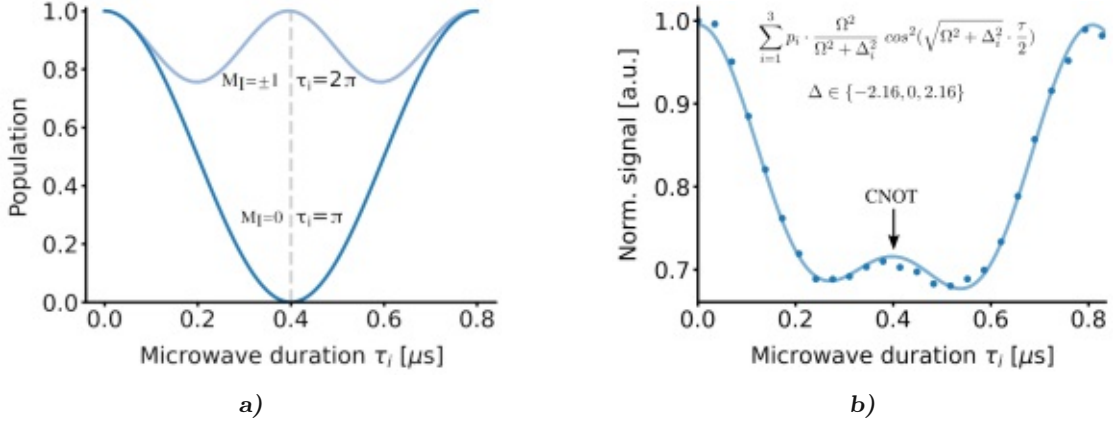
Figure 5.3: *a) Simulation of Rabi oscillations under the calculated condition for a CNOT gate with $\Omega = \frac{1}{\sqrt{3}} \cdot 2.16$ MHz. Evolution of $M_I = 0$ state (dark blue) undergoes a π-flip at 0.4 µs, while $M_I = \pm 1$ (light blue) are rotated through 2π at this microwave pulse duration. b) CNOT gate calibration: Rabi oscillation measurements with variable power were fitted to retrieve Ω, here 1.23 MHz, by the indicated fit function, with p_i the hyperfine state populations (here assumed equal).*

Instead of opting for no transfer, the approach taken was to transfer the off-resonant states through a 2π-rotation angle, while the resonant $M_I = 0$ state underwent a π-rotation, to produce the desired spin flip [29]. Investigating the process with equation 4.22, derived in chapter 4.3.3, for the detuned and the tuned resonance with the two conditions for the rotation angles at a time τ yields, for the arguments of the cosine,

$$\sqrt{\Omega^2 + \Delta^2} \cdot \frac{\tau}{2} = 2\pi, \tag{5.2}$$

$$\Omega \cdot \frac{\tau}{2} = \pi. \tag{5.3}$$

Solving for Ω results in the condition

$$\Omega = \frac{1}{\sqrt{3}}\Delta, \tag{5.4}$$

fixing $\Omega/2\pi$ at 1.25 MHz (see fig. 5.3a). In the gate calibration, the microwave power in the low power channel was adjusted by incrementing the control voltage on the quadrature modulator and Rabi nutation measurements were conducted. The curve fit (figure 5.3b) informed us about the current Rabi frequency, to set it as closely as possible to $2\pi*1.25$ MHz. The gate lasted for 400 ns.

Two types of CNOT gates were implemented acting in the $M_S = -1$ and $M_S = 0$ manifolds: CNOT0 consisted of $M_I = 0$ transfer, CNOT1 was built from a CNOT0 followed by a NOT operation so that $M_I = \pm 1$ states were transferred.

The matrix of the CNOT0 operation conditional on the $M_I = 0$ state in the population basis $\{(M_S, M_I)\} = \{(-1,0), (-1, \pm 1), (0,0), (0, \pm 1)\}$ is

$$
\text{CNOT0} = \begin{bmatrix} \epsilon_3 & 0 & 1 - \epsilon_3 & 0 \\ 0 & 1 - \epsilon_4 & 0 & \epsilon_4 \\ 1 - \epsilon_3 & 0 & \epsilon_3 & 0 \\ 0 & \epsilon_4 & 0 & 1 - \epsilon_4 \end{bmatrix},
\tag{5.5}
$$

with the transfer errors ϵ_3 (ϵ_4) for the $M_I = 0$ ($M_I = \pm 1$) states respectively.

5.1.2 State tomography

The option to measure state populations accurately presents an important quantification tool in all kinds of measurement routines. The developed scheme for readout of populations in electron and nuclear spin sublevels of the ground state are discussed.

Readout pulse calibration

Population of the $M_S = 0$ state can be retrieved from the fluorescence under resonant optical excitation. The routine was optimized for a high contrast, good statistics and a short procedure. The optical power in step-shape readout pulses had to be traded off between a high value that would improve photon statistics and avoiding power induced crosstalk, that diminished contrast. Crosstalk to other optical transitions than the desired one increased with power due to the centre's optical spectrum.

A population difference for measuring the contrast was established by taking advantage of the non-spin conserving behaviour on illumination, due to the spin-mixed excited state. Applying a long resonant pulse (10 μs to 30 μs) effectively emptied the $M_S = 0$ state when crosstalk was low. This state 'depletion' was used to initialize the electron spin state to $M_S = 1$ (details further down in next section). The $M_S = 0$ state was then read out for the remaining population with a step pulse that had an optical power defined by a power factor f_p. The power factor relates to the amplitude of the voltage sent to EOMs, and therefore, optical power in the pulse is proportional to $cos^2(f_p \cdot \pi + \pi/2)$ (see fig. 5.4a upper left). Population from $M_S = 1$ was swapped to the readout $M_S = 0$ level with a NOT gate (π-pulse), followed by another reading pulse (fig. 5.4a lower left). Exemplary fluorescence traces of the pulse calibration are shown in figure 5.4a on the right, for different values of f_p and both readout instances. Low power produced few photons,
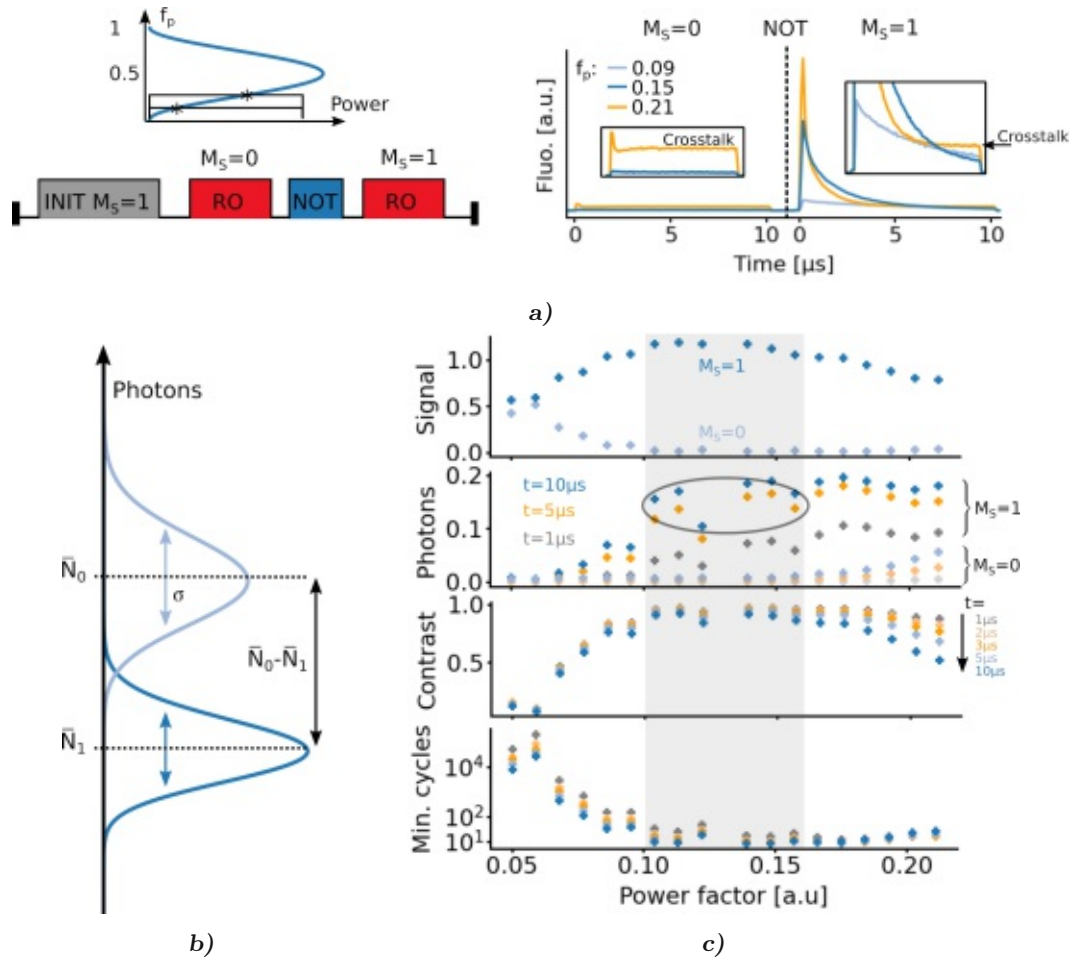
Figure 5.4: a) *Readout pulse calibration measurement: left side shows the experimental
sequence and the non-linear relation of f_p with power of the readout pulses. Right: three
exemplary fluorescence traces of a scan of f_p from 0.05 to 0.22 for both readouts. Insets are
enlarged lower regions of the graphs. Low power yields few fluorescence photons (light blue)
while high power causes crosstalk (orange).* **b)** *Contrast: photon yield of state readout follows a
Poissonian distribution with standard deviation $\sigma = \sqrt{N}$. The contrast includes the difference
of means. Moreover, states may become indiscernible when the difference is on the order of
the sum of standard deviations.* **c)** *Step pulse calibration results: power and duration of step
pulses were swept to investigate photon yield, readout contrast and the minimum number of
experimental cycles to discern the states. Different readout durations were investigated (from
$1\,\mu s$ to $10\,\mu s$). The displayed signal is the number of readout photons of states normalized to the
reference population on spin polarization with green light (photons in first $0.2\,\mu s$ of the pulse were
counted). Power factors in the shaded region achieved the best state initialization and signal.
The photons graph shows the photon yield per cycle for both the $M_S = 0$ and $M_S = 1$ readouts
and different pulse length integrations. Photon yield increases with power, but remains at a low
level of 0.1 to 0.2 per cycle in the shaded region (circled), hindering single-shot state readout.
Contrast is maximal in the shaded area, while the necessary minimum of cycles to discern the
states is small therein. For better visibility of the graphs, only the mean values are given.*

while for high power the crosstalk became dominant. The strong exponential decay is indicative of a high spin-flip rate.

The readout contrast in a single shot is defined as

$$C_{RO} = \frac{R_0 - R_{\pm 1}}{R_0 + R_{\pm 1}}, \tag{5.6}$$

where R_0 $(R_{\pm 1})$ is the signal gained from reading the $M_S = 0$ $(M_S = 1$ or $M_S = -1)$ population respectively. The contrast distribution depends on the difference between the mean values of the photon counts of the states and their variance, shown in figure 5.4b. To optimally discern the signals with mean photon counts $\bar{N}_i$, the quantity

$$\left(\bar{N}_0 \pm \sqrt{\bar{N}_0} \right) - \left(\bar{N}_1 \pm \sqrt{\bar{N}_1} \right) \tag{5.7}$$

needs to be maximized. Assuming higher photon counts from $M_S = 0$, to distinguish the states, the condition

$$\left(\bar{N}_0 - \sqrt{\bar{N}_0} \right) - \left(\bar{N}_1 + \sqrt{\bar{N}_1} \right) > 0, \tag{5.8}$$

has to be fulfilled, with a similar condition for the case that $M_S = 1$ (or $M_S = -1$) has higher counts. The question asked was: how many measurements needed to be performed for a certain excitation power to distinct between the states? The standard error of the mean relates to the number of measurements n as $\frac{1}{\sqrt{n}}\sigma_N$, where σ_N is the sample standard deviation. Inserting into 5.8 yields the condition

$$\left(\bar{N}_0 - \frac{\sqrt{\bar{N}_0}}{\sqrt{n}} \right) - \left(\bar{N}_1 + \frac{\sqrt{\bar{N}_1}}{\sqrt{n}} \right) > 0, \tag{5.9}$$

or

$$n > \left(\frac{\sqrt{\bar{N}_0} + \sqrt{\bar{N}_1}}{\bar{N}_0 - \bar{N}_1} \right)^2, \tag{5.10}$$

which is valid for any population ratio.

Pulse calibration yielded good results for f_p in the range of 0.1 to 0.16, shown in figure 5.4c. At the higher end, this reflected a power of $0.35\,\mu\text{W}$ at the microscope objective. A duration of $3\,\mu\text{s}$ to $5\,\mu\text{s}$ was chosen for good photon yield, while keeping cycle length at a reasonable overall duration. The probability for a photon per readout pulse for an initialized $M_S = 0$ state was then 0.167 ± 0.001 from the $M_S = 0$ state and 0.00442 ± 0.00015 from $M_S = \pm 1$, resulting in a high readout contrast of 0.948 ± 0.000172, which compares well with state-of-the-art systems (see e.g. Robledo et al. [84]). However, the low overall photon yield per readout pulse rendered single-shot readout of the spin state impossible.

83
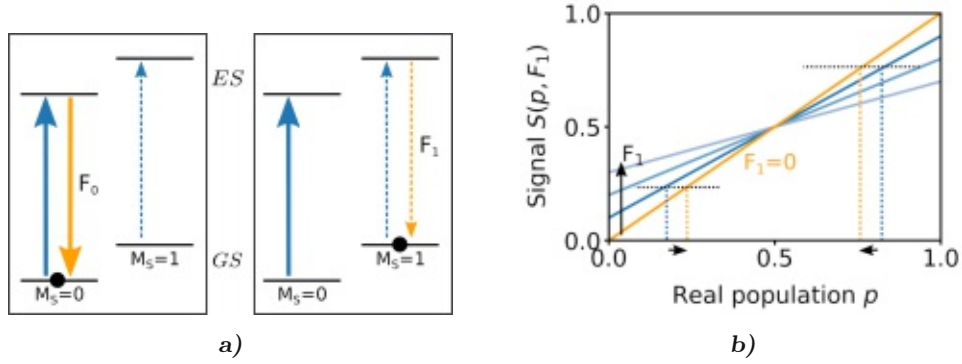
Figure 5.5: a) *Fluorescence F_0 and F_1 definitions: crosstalk fluorescence F_1 only occurs if crosstalk is present (dotted lines) and $M_S = 1$ is populated.* **b)** *Deduction of real population from a signal: without crosstalk ($F_1 = 0$) the population is exactly reflected in the signal (orange line). Crosstalk (blue lines) leads to an overestimation (underestimation) of population for a certain signal if the population is < 0.5 (> 0.5) - (arrows on x-axis).*

Error on the population measurement

There are two major sources for errors in the readout procedure: optical crosstalk and inaccurate microwave transfer in the NOT gate.

The effect of crosstalk is discussed in a two-level system with a readout state $M_S = 0$ and a somewhat detuned transition of $M_S = 1$. The fluorescence from a fully populated state $M_S = 0$ will be F_0 on average (fig. 5.5a left) and the crosstalk fluorescence of a fully populated state $M_S = 1$ F_1 (fig. 5.5a right). How does F_1 influence the signal and therefore the deduced population p of a state? A readout of an unknown population distribution achieves

$$F_0 \cdot p + F_1 \cdot (1 - p) + B \tag{5.11}$$

fluorescence photons, with B the background. The background was established with a detuned laser to be very low (about 10^{-3} photons per readout) and is neglected. The normalized signal S (will be referred to as signal from here onwards) reads

$$S(p, F_1) = \frac{F_0 - F_1}{F_0 + F_1} \cdot p + \frac{F_1}{F_0 + F_1}, \tag{5.12}$$

a linear function in p plotted for increasing F_1 in figure 5.5b. If no crosstalk is present, $S(p, F_1 = 0) = p$. Otherwise, F_1 limits the the maximally and minimally observable signal by the intercept with the y-axis at $\frac{F_1}{F_0 + F_1}$. Initialisation into $M_S = 1$ led to $S(p \approx 0, F_1) \leq 0.01$, which means

$$\frac{F_1}{F_0 + F_1} \leq 0.01, \tag{5.13}$$

84
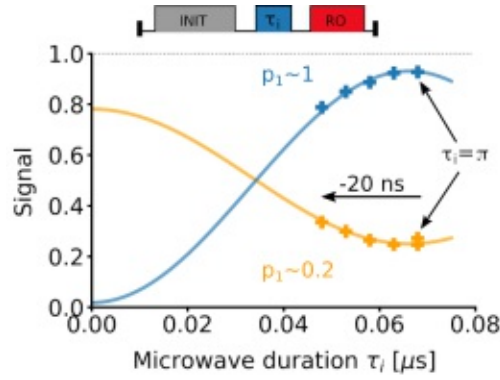
Figure 5.6: *Microwave induced error on population readout: top shows sequence used with two different types of initialization procedures to produce varying population in $M_S = 1$. Microwave gate (blue) transferred population to the readout level $M_S = 0$ in dependence of pulse duration and Ω. Here, the lowest power microwave case with $\tau_\pi = 68$ ns is shown, producing maximal deviation of signal to population. Pulse duration was then detuned up to 20 ns. Nuclear spin populations were completely mixed. Fit with eq. 5.18 to retrieve the population values, which was close to one when $M_S = 0$ was initialized to be empty (blue line) and 0.2 when a green laser pulse was used for initialization (orange line).*

setting an upper bound on $F_1 \approx 1\%$ of F_0, so that we assume $S(p, F_1) \approx p$ from here on.

The state readout procedure for $M_S = \pm 1$ involved a microwave operation that entails a certain error on population transfer. The same question as above is raised - what is the real population of the $M_S = 1$ or $M_S = -1$ state before the microwave operation was performed when a certain signal is observed? In the most general perspective the NOT microwave operation with error ϵ acting on states $\psi_0 = \alpha \ket{0}$ and $\psi_1 = \beta \ket{1}$ leaves a probability amplitude of $\alpha\sqrt{\epsilon} + \beta\sqrt{1-\epsilon}$ on the ψ_0 state. A measurement of ψ_0 produces a signal

$$S = \left| \alpha\sqrt{\epsilon} + \beta\sqrt{1-\epsilon} \right|^2 = |\alpha|^2 \epsilon + |\beta|^2 (1-\epsilon) + \left(\alpha^* \beta \sqrt{\epsilon}\sqrt{1-\epsilon} + \quad \text{c.c.} \quad \right). \tag{5.14}$$

The interference term is not present (or very small) in the state readout procedure, since the microwave pulse doesn't act on a coherent state but a statistical mixture. Therefore,

$$S \approx |\beta|^2 + \epsilon \left(|\alpha|^2 - |\beta|^2 \right), \tag{5.15}$$

with a linear deviation that depends on the microwave error and the initial population difference. In a two-level system, with p_1 the population of the state (to be transferred to the readout $M_S = 0$ level) before the microwave operation, the expression becomes

$$S = (1 - 2\epsilon)p_1 + \epsilon, \tag{5.16}$$

85

a linear function acting on the signal in a similar fashion to optical crosstalk. The larger
ϵ, the smaller the readout contrast and error is maximal at the population extrema.

The error ϵ arises from two different origins, the detuning of hyperfine states and
possible pulse duration errors. The later was investigated in a Rabi oscillation type
measurement for two initial population values p_1 in the state-to-read-out (fig. 5.6). The
π-pulse region (where the NOT gate operates) viewed in a Rabi nutaion context is almost
flat, so that small errors from inaccurate timing are expected.

Both error types are captured through a treatment of the microwave operation as
pictured in chapter 4.3.3, with ϵ equal to $1 - T_a$, where T_a is the total transfer amplitude
of population,

$$T_a(\Omega, \Delta, \tau) = \sum_{i=1}^{3} p_i^N \cdot \frac{\Omega^2}{\Omega^2 + \Delta_i^2} \, cos^2(\sqrt{\Omega^2 + \Delta_i^2} \cdot \frac{\tau}{2} + \frac{\pi}{2}), \; \Delta \in \{-2.16, 0, 2.16\}, \quad (5.17)$$

summed over the nuclear spin states with population p_i^N, and Δ in MHz. Insertion yields

$$S(p_1, T_a) = (2T_a - 1)p_1 - T_a + 1, \quad (5.18)$$

which was used to fit the data in figure 5.6. Inversion gives the population of interest
before the microwave operation, p_1, in dependence of the signal S, as

$$p_1(S) = \frac{S + T_a - 1}{2T_a - 1}, \quad (5.19)$$

with $T_a = T_a(\tau = \pi)$ for readout procedures. For microwave fields with high Ω, $p_1(S) \approx S$.

Population normalization and ionization

In order to derive an accurate signal, the populations of all electron spin levels could be
read out in three consecutive measurements. This was done within the same measurement
sequence, to avoid systematic errors and to normalize population correctly, as indicated
in figure 5.7a top.

A similar protocol was used to attain nuclear spin level populations for $M_I = 0$ and
for $M_I = \pm 1$ (fig. 5.7a bottom). CNOT gates were used to transfer population to the
readout state $M_S = 0$. As two CNOT gates were established, the difference in population
of $M_I = 0$ and the total of $M_I = \pm 1$ was retrieved.

To investigate if such a population normalization procedure is valid, since it builds
on the assumption of spin population conservation, possible losses of populations during
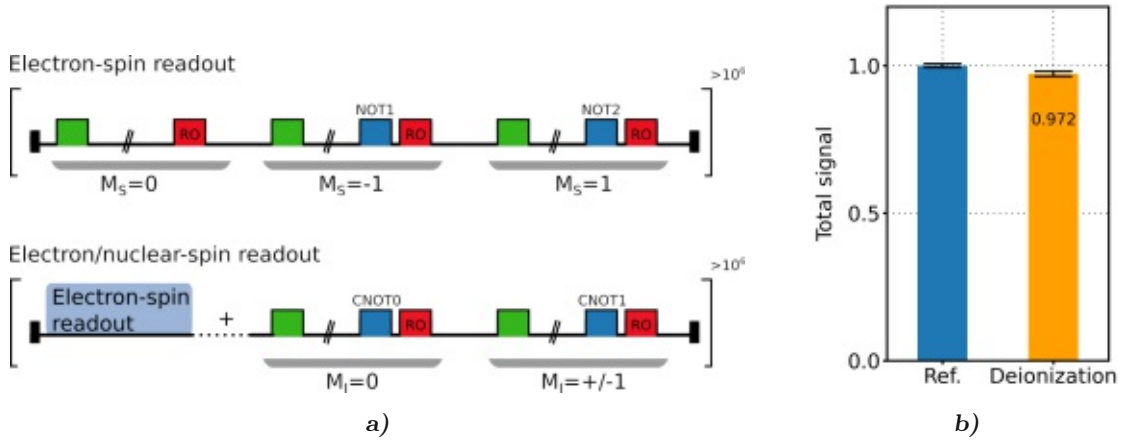
Figure 5.7: a) *Population normalization procedure: top shows the establishment of electron spin populations, bottom includes the nuclear spins. Both processes were done in a single sequence to minimize error.* **b)** *Deionization measurement results: the reference consists of the sum of all readouts from* $M_S = 0$, $M_S = 1$ *and* $M_S = -1$, *after the same initialization procedure. The ionization value represents the same readout but with a sequence of 32 times* [NOT1][D][NOT2][D] *in between. Only a small decrease in signal and therefore population was determined. Indicated errors are* $\pm 1\sigma$.

sequences needed to be checked. Under resonant optical excitation the NV centre may deionize to the uncharged state NV^0, which is a pathway for population loss reported in literature [84]. A measurement was designed to monitor the influence of deionization on population retrieval results. The sequence used consisted of an initialization part, a reference population readout of all states and reinitialization followed by a gate sequence of

$$[[\text{NOT1}][\text{D}][\text{NOT2}][\text{D}]]^{32}, \tag{5.20}$$

with [D] depletion (readout) gates, shuffling population between the levels to garant many optical excitation cycles. Finally, states were read and compared to the reference reading, yielding a drop in overall population of only 2.8% (fig. 5.7b), so that it was a fair assumption that the population was conserved even over lengthy sequences with many gate operations.

This concludes the discussion of state readout procedures, which were put to use in the topics of the next sections.

87

5.2 Spin initialization by population shelving through optical pumping

Polarizing the nuclear spin, ideally resource efficiently, while not harming its state by operations on the electron spin was not only important in our experiment but is of prime importance in many quantum information protocols using the NV centre [96, 75].

However, the low electron-nuclear spin coupling, while being an advantage for a quantum memory, impedes initialization and manipulation effectively. Furthermore, many schemes reported so far have strict requirements on the centre used. Common is a tremendous increase of hardware overhead for engineering the coupling rate between electron and nuclear spin [48].

High fidelity nuclear spin initialization has been shown through (recursive) population transfer with microwave and radio frequency pulses [74, 19]. Furthermore, single-shot readout techniques combined with trial until success or post selection have been demonstrated for selecting nuclear spin states [71, 85]. Well established methods, requiring high magnetic fields, use level anti-crossings in the ground and excited state of the centre to induce spin flip-flops between the electron and nuclear spins. Under optical pumping these lead to nuclear spin polarization [45]. Coherent population trapping, via the ground states as well as optically via the excited state have been used for this purpose as well [100, 20, 37]. Other methods employ coherent Larmor precession of nuclear spins or operate in a high microwave power Hartmann-Hahn regime [28, 62].

Our iterative initialization methods for electron and nuclear spin polarization by population shelving through resonant optical pumping in arbitrary magnetic fields are robust and with low hardware demand. We only require selective microwave transfer and random spin-flips induced by the resonant optical pumping process on a single optical transition, yielding a nuclear spin polarization of 88 %. Our method is resilient to experimental imperfections and doesn't require radio frequency fields, single-shot readout, initial electron spin polarization or tuning of fields, energy levels or frequencies.

5.2.1 Initialization routines

The developed routines rely on alteration of state targeted microwave transfer gates with population distributing depletion pulses.
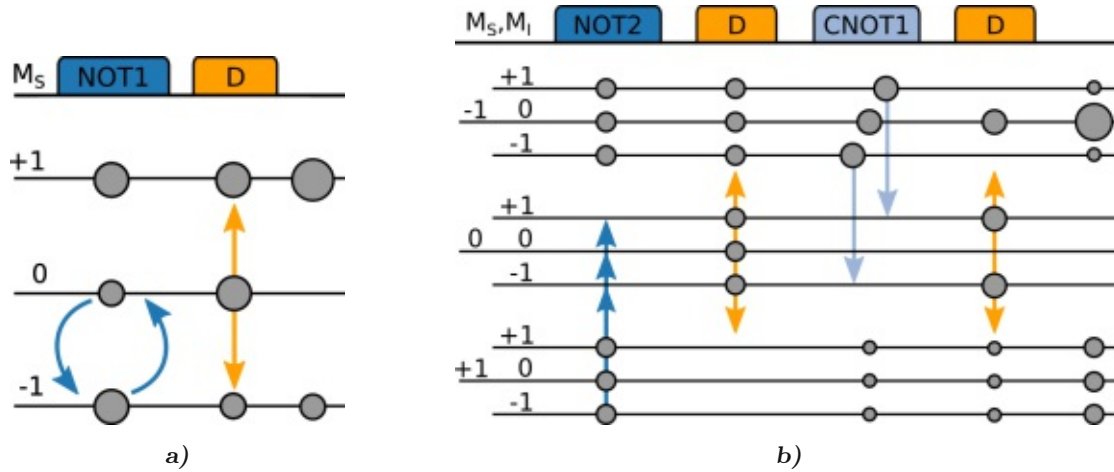
Figure 5.8: *a) Electron spin initialization iteration: a NOT gate (here NOT1) repopulates the $M_S = 0$ state for the next round of depletion. Depletion pulse (D) transfers population out of $M_S = 0$ and equally distributes to $M_S = 1$ and $M_S = -1$. Population in the example accumulates in $M_S = 1$. b) Combined electron and nuclear spin initialization iteration: target state $M_S = -1$, $M_I = 0$ is the only state not touched by microwave gate operations so that population becomes trapped.*

Electron spin initialization. Depletion pulses empty the $M_S = 0$ state and distribute the population evenly in $M_S = 1$ and $M_S = -1$. Microwave NOT operations on one of those states followed by a depletion gate will, upon repetition, trap more and more population in the state untouched by the NOT gate (fig. 5.8a). The sequence protocol in gates is

$$[G]\,(\,[NOT][D]\,)^N\,[Tomo],\tag{5.21}$$

with [G] being a 1 µs and 380 µW green laser pulse. The pulse sets the charge state of the centre. The NOT gate and the 5 µs depletion pulse [D] are repeated N times to accumulate population asymptotically, taking 5.05 µs per run. Tomography [Tomo] after $N = 8$ iterations resulted in an initialization fidelity of the electron spin qubit of $F_e = 95.3 \pm 0.5\%$ in the $M_S = 0$ and ($M_S = -1$ or $M_S = 1$) qubit space.[1] Inference with a numerical model (see next section) matched and predicted an asymptotic limit of $F_e = 96.1\%$. The deviation from unit fidelity is due to optical cross-transfer, which slightly depopulates the target state.

---

[1] With target state $M_S = -1$ the population distribution $(M_S = 0, M_S = -1, M_S = 1) = (4.6, 92.5, 2.8) \pm 0.5\%$ was achieved.

89
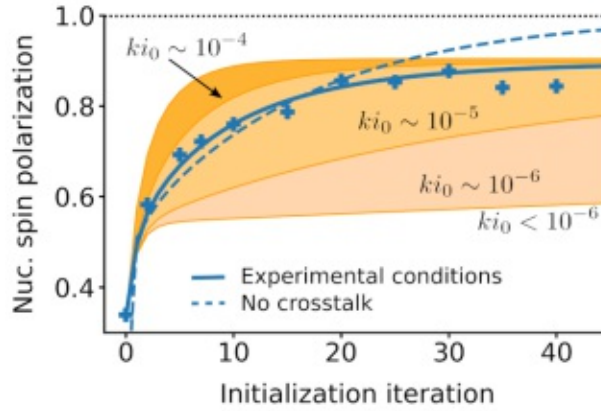
Figure 5.9: *Iterative nuclear spin polarization by population trapping: blue scatter is the extracted nuclear spin polarization after 0, 2, 5, 7 (and so forth) iterations of the initialization routine. Data has $\pm 2\%$ standard error. The solid blue line fit was done with a numeric model (see next section) to extract the involved nuclear spin flip rate ki_0 (per nanosecond), where shaded domains indicate the order of magnitude. If no crosstalk was present, the polarization curve would follow the dashed line, ultimately reaching unity.*

Combined electron and nuclear spin initialization. Expanding the above routine by another population recollection step with a CNOT1 operation on the target electron spin state leaves only the (electron spin target state, $M_I = 0$) level untouched by microwave gate operations to iteratively trap population (fig. 5.8b). The gate sequence becomes:

$$[\mathrm{G}]\,(\ [\mathrm{NOT2}][\mathrm{D}][\mathrm{CNOT1}][\mathrm{D}]\ )^{\mathrm{N}}\ [\mathrm{Tomo}], \tag{5.22}$$

with one iteration of the central block taking $13\,\mathrm{\mu s}$ (using $5\,\mathrm{\mu s}$ depletion pulses and some safety wait periods). For $N = 40$ iterations, the fidelity[2] for nuclear spin initialization amounted to $F_n = (88 \pm 2)\%$, which is close to the asymptotic limit (fig.5.9).

The blue scatter in figure 5.9 was the measured nuclear spin polarization after a certain amount of protocol iterations. The fit was simulated with a model developed in the next section. Varying the transition rate for nuclear spin flips produced the coloured domains in the plot, visualizing the impact on the convergence to the asymptotic limit, which was defined by the strength of optical cross-excitation processes that slightly deplete the target state.

In general the algorithm is very robust to different kinds of experimental imperfections like microwave gate duration errors, variations in the depletion pulse duration and power

---

[2]The nuclear spin initialization fidelity was defined as the fraction of $M_I = 0$ population within the $M_S = -1$ manifold, i.e. $F_n = \mathrm{p}(M_I = 0, M_S = -1)/\mathrm{p}(M_S = -1)$, where p is the population.
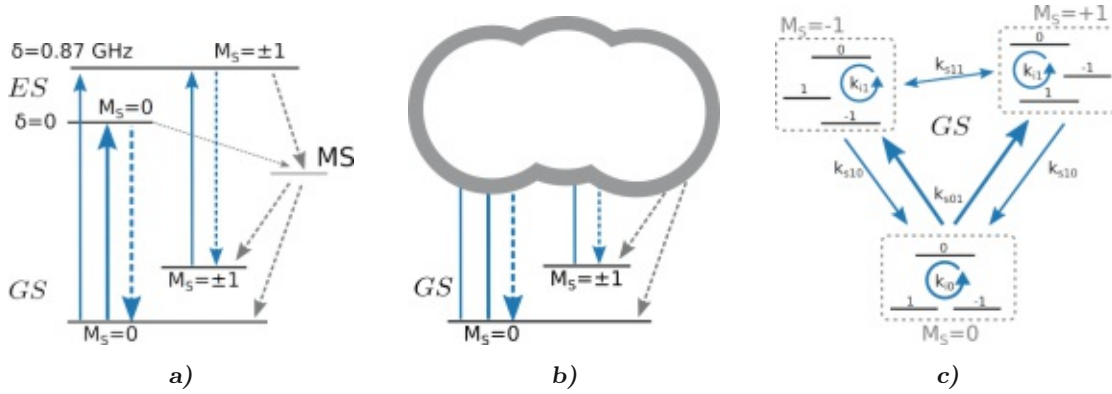
Figure 5.10: *a) Full description of NV centre optical dynamics involves up to nine ground state levels (GS), 18 excited state levels (ES), metastable (MS) levels and knowledge of relevant transition rates. b) Reduction of complexity: model treats excited state as black box and only considers effective transition rates between the nine ground state levels. Timescales for optical operations are assumed to be on the order of microseconds or longer. c) Effective rates used in the ground state model (see text).*

and may be used in a wide range of magnetic fields.

5.3 A simple optical spin dynamics model

5.3.1 Introduction to the model

A model was developed to describe the behaviour of spin populations upon resonant excitation on the working transition. Modelling the full dynamics of the electron and nuclear spin has been done, with elaborate many-level rate equation simulations, of up to nine ground states, 18 excited states and intermediate levels, that require accurate transfer rates as an input [37, 76] (fig. 5.10a).

As a result of using a single optical transition, many of these states were not relevant for the dynamics in our case, so that a reduced and effective rate model could be proposed (fig. 5.10a to 5.10c). The model departs from a master equation approach. The time evolution of state populations in the population vector $\mathbf{P}$ is then given as

$$\frac{\mathrm{d}\mathbf{P}}{\mathrm{d}t} = \hat{M}\mathbf{P}, \tag{5.23}$$

with transfer matrix $\hat{M}$ (see appendix D) and the population vector encoded as $\{(M_S, M_I)\} = \{(-1, -1), (-1, 0), (-1, +1), (0, -1), (0, 0), (0, +1), (+1, -1), (+1, 0), (+1, +1)\}$. $\hat{M}$ was proposed to contain the five time independent effective rates:

91
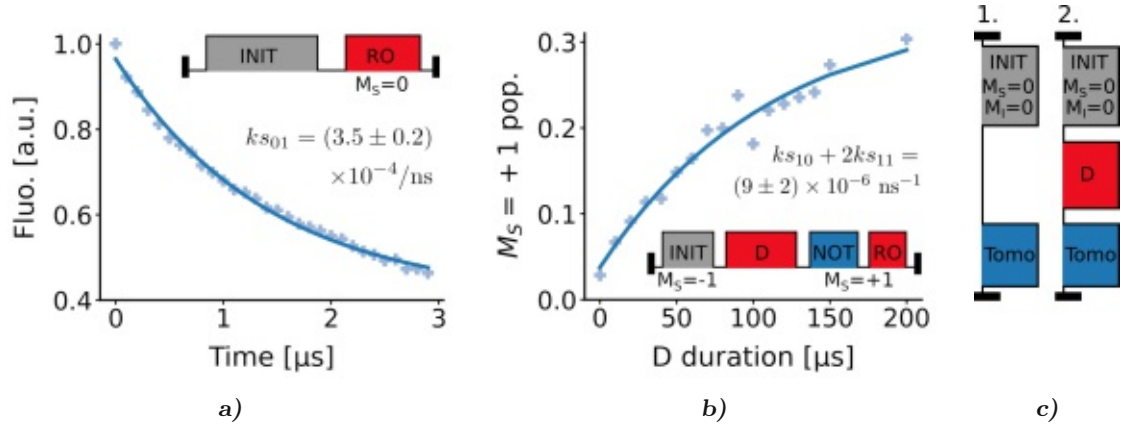
Figure 5.11: **a)** *Rate ks_{01}: fluorescence trace of a $3\,\mu s$ readout/depletion pulse (RO) with
single exponential fit.* **b)** *Coupled rates ks_{10} and ks_{11}: initialization into $M_S = -1$ followed by
long depletion pulses (D) to induce transfer through crosstalk. Finally $M_S = 1$ was read (NOT
and RO).* **c)** *Extraction of upper bound on the nuclear spin flip rates ki_0 and ki_1. Strongly
populated state $M_S = 0$, $M_I = 0$ was fully read out for a reference (left) or depleted and read
out (right).*

- ks_{01} - electron spin transfer rate from $M_S = 0$ to $M_S = \pm 1$,

- ks_{10} - electron spin transfer rate from $M_S = \pm 1$ to $M_S = 0$,

- ks_{11} - electron spin transfer rate from $M_S = -1$ to $M_S = 1$ and vice versa,

- ki_0 - nuclear spin transfer rate from $M_I = \pm 1$ to $M_I = 0$, when $M_S = 0$,

- ki_1 - nuclear spin transfer rate from $M_I = \pm 1$ to $M_I = 0$, when $M_S = \pm 1$,

illustrated and related to the physical processes on optical pumping in figure 5.10c.

5.3.2   Rate determination

State depletion.   Rate ks_{01}, the transfer from $M_S = 0$ to $M_S = \pm 1$, was extracted from
fast spin dynamics upon optical illumination (after off-resonant initialization), evident
in the decay of PSB fluorescence during application of a $3\,\mu s$ step pulse[3] (fig. 5.11a).

By fitting the observed decay with a single exponential function, only the ks_{01} domi-
nated aspect was captured and long-term effects such as optical crosstalk to other excited
state transitions were removed. The retrieved value was $ks_{01} = 3.5 \times 10^{-4}\ \text{ns}^{-1}$.

---

[3]The step pulse was carefully calibrated as introduced above

State cross transfer. The rates from the $M_S = \pm 1$ states to $M_S = 0$ (ks_{10}) and between the $M_S = 1$ and $M_S = -1$ state (ks_{11}), are present when off-resonant cross-excitation is possible. For high strain NV centres, like ours, this was the case due to a slight spectral overlap of lines and a strong spin mixing in the excited states.

To determine the effect of both rates within our model, the rate equations were integrated in search of an analytic solution. For a population distribution among the three electron spin levels $\mathbf{P}_S = [p_{-1}, p_0, p_{+1}]$, in basis $\{M_s\} = \{-1, 0, +1\}$, we determined the time evolution of the $M_S = 1$ population to be

$$P_{M_S=+1} \;=\; C_1 + C_2 \cdot \exp[(-2ks_{01} - ks_{10}) \cdot t] + C_3 \cdot \exp[(-ks_{10} - 2ks_{11}) \cdot t], \tag{5.24}$$

with

$$C_1 = \frac{ks_{01}(p_{-1} + p_0 + p_{+1})}{2ks_{01} + ks_{10}}, \quad C_2 = \frac{-p_0 ks_{01} + p_{-1} ks_{10}/2 + p_{+1} ks_{10}/2}{2ks_{01} + ks_{10}}, \quad C_3 = \frac{p_{+1} - p_{-1}}{2}. \tag{5.25}$$

With an initial state population vector $[p_{-1}, p_0, p_{+1}] = [92.5\%, 4.5\%, 3.0\%]$, and with setting $ks_{01} = 3.5 \times 10^{-4}$ ns^{-1}, we could extract numerically that the C_2 factor is much smaller than C_3, for the interval of reasonable ks_{10} values, with $C_2/C_3 \in [3.4\%, 5.0\%]$, thereby enabling a description where the evolution of $P_{M_S=+1}$ is approximated by a mono-exponential expression

$$P_{M_S=+1} = A \cdot \exp((-ks_{10} - 2ks_{11}) \cdot t) + B. \tag{5.26}$$

Experimental establishment of the rates was possible by first initializing the spin population in the $M_S = -1$ state, followed by depletion pulses resonant with the $M_S = 0$ transition of increasing duration (fig. 5.11b). Population of the $M_S = 1$ state was measured thereafter tomographically. A fit to the data yielded $\tilde{k} = ks_{10} + 2ks_{11} = (9 \pm 2) \times 10^{-6}$ ns^{-1}.

Nuclear spin transition rates. Nuclear spin flip rates ki_0 and ki_1 were determined through the nuclear spin polarization routine (fig. 5.9). As discussed, the routine consisted of discrete iteration steps. Tomography was performed after 2, 5, 7 to up to 40 iterations, yielding a population vector $\mathbf{P}$ and the corresponding nuclear spin polarization at each step. At this point, the only free parameters in the model for population evolution were the nuclear spin flip rates.

For the time being, rate ki_1 was neglected since it was expected to be much smaller than ki_0, due to the process relying on optical cross-excitation. The most likely value for ki_0 was extracted by minimizing the distance

$$d = \left| \mathbf{P^{fit}} - \mathbf{P} \right|, \tag{5.27}$$

with $\mathbf{P^{fit}}$ the fit-function for populations as given by the model with the derived rate ks_{01}, the combined rate for ks_{10} and ks_{11}, and the microwave qubit gates as given by their matrices (introduced in section 5.1). The expected population vector for the measurements was derived from the model by integration. The minimal distance was obtained at $ki_0 = 4.9 \times 10^{-5}\,\mathrm{ns}^{-1}$.

An upper bound on the nuclear spin flip rate, $ki_0^{(0)}$, was retrieved from two measurements done consecutively: the first was a reference, where the centre was initialized in the state $M_S = 0$, $M_I = 0$ and tomography was performed (figure 5.11c), yielding a population vector $\mathbf{P_1}$. In the second measurement a $10\,\mu\mathrm{s}$ depletion pulse was done in between, yielding the vector $\mathbf{P_2}$. The population evolution from $\mathbf{P_1}$ to $\mathbf{P_2}$ was simulated numerically by integration of the rate equation model to yield a theoretical $\mathbf{P_2^{th}}$. Distance minimization led to an optimal value $ki_0^{(0)} = 2.76 \times 10^{-4}\,\mathrm{ns}^{-1}$. This is interpreted as an upper bound on the flip rate since the system was prepared in one nuclear spin state, so that the highest observable flip rate was visible under optical illumination (more details further down in this section).

To ascertain the strength of ki_1 on the value for ki_0, ki_1 was swept within a range of $[0, 2\% \cdot ki_0^{(0)}]$ and for each iteration an optimal $ki_0^{(i)}$ was retrieved, resulting in a range: $ki_0^{(i)} \in [2.15, 2.76] \times 10^{-4}\mathrm{ns}^{-1}$. The two flip rates were found to be anti-correlated.

The extracted spin transition rates are summarized in table 5.1.

5.3.3   Spin flip mechanisms

We compared the experimental findings with a simulation of the excited state dynamics, to find out more about what causes the electron and nuclear spin flips and to what extent. The 18-level excited state was evolved by the Master equation

$$\frac{d\hat{\rho}}{dt} = -\frac{i}{\hbar}[\mathrm{H}, \hat{\rho}], \tag{5.28}$$

with H the excited state Hamiltonian, to go beyond a simple rate equation model. Spontaneous decay to the ground state was introduced as a stochastic process to the otherwise

Rate	Value	Error	Comment
ks_{01}	3.5×10^{-4} ns^{-1}	0.2×10^{-4} ns^{-1}	resonant excitation
ki_0	4.9×10^{-5} ns^{-1}	0.5×10^{-5} ns^{-1}	resonant excitation
$ks_{10} + 2ks_{11}$	9×10^{-6} ns^{-1}	2×10^{-6} ns^{-1}	cross-excitation
$ki_0^{(0)}$	$[2.15, 2.76] \times 10^{-4}$ns^{-1}	0.05×10^{-4} ns^{-1}	resonant excitation
ki_1	$[0, 2\% \cdot ki_0^{(0)}]$ ns^{-1}		cross-excitation

Table 5.1: *Extracted spin transition rates. Upper three values are found to model the depletion pulse operations, e.g. in the nuclear spin initialization routine. $ki_0^{(0)}$ was retrieved from depletion on a purified nuclear spin species and gives an upper bound on the nuclear spin flip rate. ki_1 was swept in the range $[0, 2\% \cdot ki_0^{(0)}]$ and found to be anti-correlated with $ki_0^{(0)}$.*

coherent model. The Hamiltonian included all terms discussed in chapter 3, starting with equation 3.17, and included strain of 53 times the transverse dipole moment, as determined from the best fit in the fluorescence spectrum (see section 4.4.2) as well as the laboratory magnetic field of 25 G.

The probability of finding the system in a certain state was integrated for up to 50 ns. The eigenstates and energies of the Hamiltonian are visualized in figure 5.12.

To relate the rates derived from measurements to the simulation model that returns probabilities for a spin flip per optical cycle, the optical cycling frequency had to be determined. Looking back at the readout pulse calibration measurement (fig. 5.4c), the collected photons per pulse approximately follow a saturation curve behaviour. In a two-level system, the fluorescence F saturates as

$$F = F_{\text{inf}} \cdot \frac{s}{s+1}, \tag{5.29}$$

where F_{inf} is the maximum fluorescence and s is the saturation factor, defined as the optical power over the optical power at saturation P/P_{sat} [27]. The calibrated pulses operated at about 2/3 of the saturation power. With a lifetime of 11 ns, as extracted by fitting the ZPL fluorescence decay in fig. 4.24 with an exponentially decaying function, the centre has a maximum fluorescence rate F_{inf} of 9.1×10^7 s^{-1} or 9.1×10^{-2} ns^{-1}, so that at two thirds of saturation, optical cycling has a frequency of 3×10^{-2} ns^{-1}, with a ± 1 standard deviation interval of $[2.4 \times 10^{-2}$ ns$^{-1}, 4.6 \times 10^{-2}$ ns$^{-1}]$.
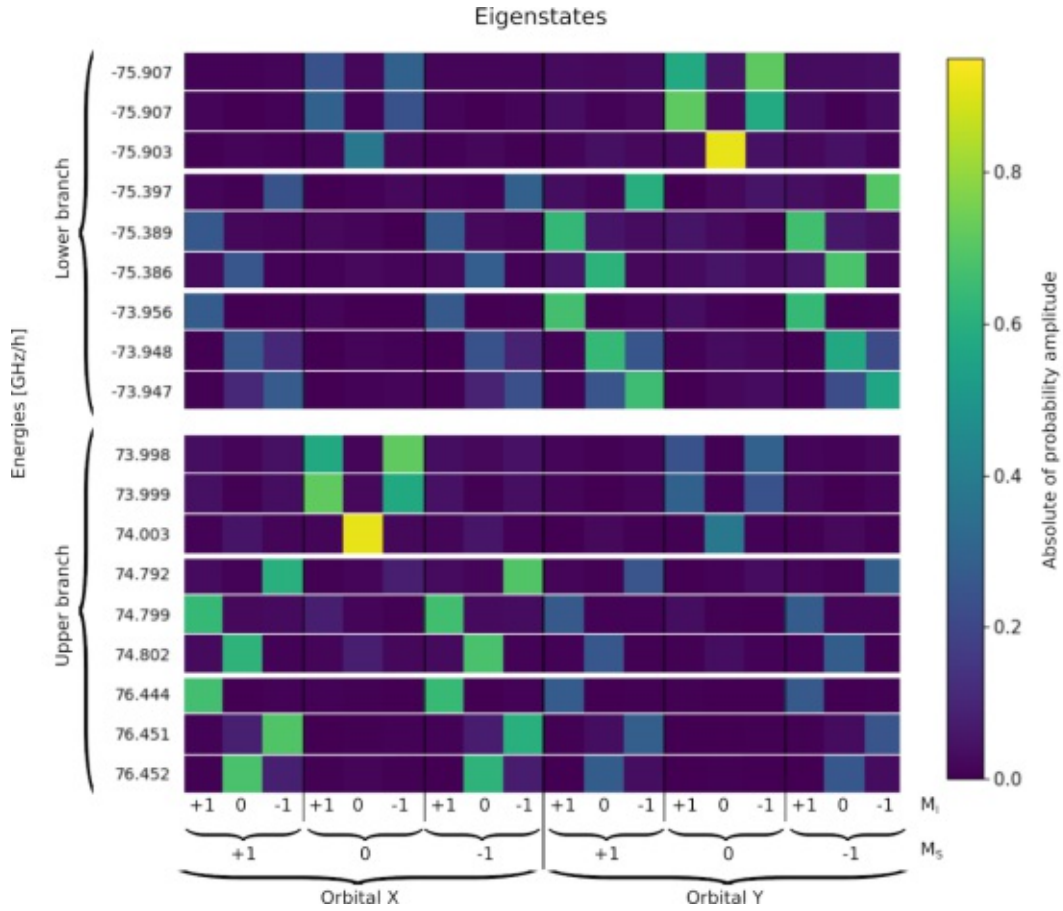
Figure 5.12: *Eigenstates (horizontal coloured lines) and energies of strained Hamiltonian used in simulation. Upper nine states are found in the lower branch of the excited state, while the lower part refers to the upper branch. Branches are separated by about* 150 MHz *and states are mixed by the crystal strain.*

Electron spin flip mechanism

We sought to investigate the origin of the electron spin flips, so far described by the flip rate ks_{01}. In three simulation rounds, density matrices with population in the initial states $M_S = 0$ and $M_I = -1$, $M_I = 0$, $M_I = +1$ were evolved and analyzed for electron spin flips in both orbital branches.

A visualization of the electron spin flip probability versus crystal strain is given in figure 5.13. All initial states had an electron spin flip probability in the range of 0.012 to 0.014 per optical pump cycle (compare inset of fig. 5.13). With the above extracted cycling rate this yields a ks_{01}^{th} of $3.6 \times 10^{-4}\,\mathrm{ns}^{-1}$ to $4.2 \times 10^{-4}\,\mathrm{ns}^{-1}$, where we measured
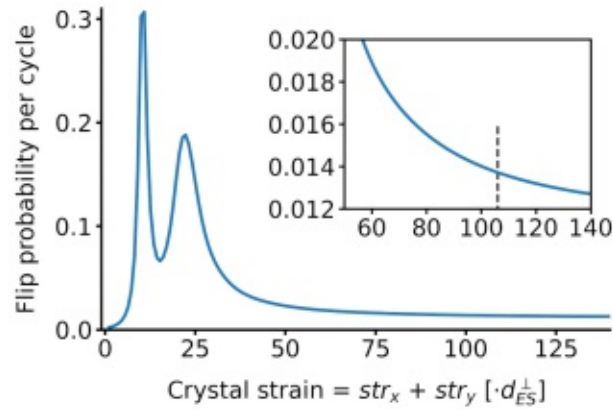
Figure 5.13: *Electron spin flip probability versus transversal crystal strain: the curve shows the electron spin flips out of the $M_S = 0$, $M_I = 0$ state. Peaks relate to positions of level anti-crossings (see fig. 3.8a). Inset for high strain region with marked positions at best fit for our NV centre.*

a $ks_{01} = 3.5 \times 10^{-4}$ ns^{-1}.

Looking at the terms in the Hamiltonian more closely, we found by sequential removal of interactions that:

- Switching off the hyperfine interaction only led to a small decrease of the electron spin flip probability per cycle so that a probability of 0.01 remained.

- Removing the hyperfine interaction and strain caused a large reduction in the flip probability, with only 10 % of the initial probability remaining.

- The small axial magnetic field only had marginal influence.

From these results it can be concluded that the state mixing caused by the high crystal strain is the leading cause of the high electron spin flip rate.

Nuclear spin flip mechanism

The nuclear spin flip rate may depend on various parameters. For our centre we could rule out some of the referenced mechanisms in literature:

- (De)ionization: for our centre it was shown above that the deionization rate of NV$^-$ was small and even if it should occur, the NV^0 population would not affect the measurement, as there was no charge state repump mechanism within our

97

sequences. Furthermore, it has been shown by Dhomkar et al. [23] that a nuclear
spin-polarized state is not harmed by completing a full deionization and repump
cycle.

- Nuclear spin transitions may be induced by acoustic phenomena, as discussed by
  Bolef [14]. However, it can be argued that in our observations the nuclear state only
  changes under optical excitation and remains constant otherwise. By argument this
  doesn't hint at a phonon-induced process present in the ground state.

- Spin-flips in the ground state were ruled out due to the axial magnetic field orien-
  tation preventing states from mixing by splitting them up energetically.

- Coupling to a nuclear spin bath [110] can also be a cause for flips, but such a
  coupling was never observed for our centre.

We were left with the evolution of the nuclear spin in the strained excited state, which
could be modelled with equation 5.28. In three simulation rounds density matrices with
population in the initial states $M_S = 0$ and $M_I = -1$, $M_I = 0$, $M_I = +1$ were evolved
and analyzed for nuclear spin flips.

Flip processes were grouped into categories by the type of transitions that occurred
and their respective strength:

- Pure M_S: category for processes where only the electron spin changed, the nuclear
  spin remained

- Pure M_I: only the nuclear spin would flip, the electron spin didn't change. This
  was sub-categorized into $\Delta M_I = \pm 1$ and $\Delta M_I = \pm 2$ (possible only for initial
  $M_I = \pm 1$).

- Conserved: here the total spin was conserved, as typically seen in hyperfine coupling
  processes, and included:

  - $M_S = 0$, $M_I = +1$ to $M_S = 1$, $M_I = 0$
  - $M_S = 0$, $M_I = -1$ to $M_S = -1$, $M_I = 0$
  - $M_S = 0$, $M_I = 0$ to $M_S = 1$, $M_I = -1$ and $M_S = -1$, $M_I = +1$

- Dual: both electron and nuclear spin increase or decrease by one: $\Delta M_S, M_I = \pm 1$
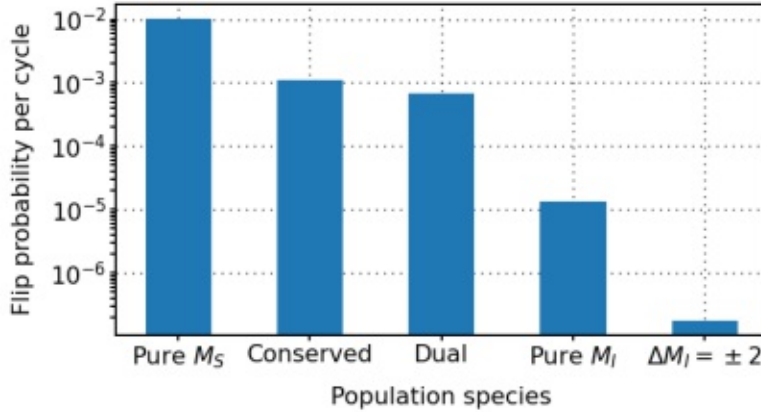
Figure 5.14: *Spin flip probabilities per optical cycle ordered by process categories.*

- $\Delta M_I = \pm 2$: the nuclear spin flips by two, the electron spin by one.

The resulting flip probabilities per optical cycle and category are shown in figure 5.14. In the simulation it becomes evident that only about $11\,\%$ of electron spin flips are accompanied by a nuclear flip.

With the process categorization, we can now revisit why the second measurement for extracting the nuclear spin flip rate $ki_0^{(0)}$ was assumed to yield an upper bound on the rate. Due to the preparation of the nuclear spin state in $M_I = 0$, four processes dominate the nuclear behaviour - the ones in category 'conserved' and 'dual' with a total rate of $1.1 \times 10^{-4}\,\mathrm{ns}^{-1}$ from simulation. In the nuclear spin initialization routine on the other hand, the net nuclear flip rate into $M_I = 0$ depends on the ratio of $M_I = 0$ and $M_I = \pm 1$ populations.

5.3.4 Initialization routine optimization

As an application of our effective rates model, the nuclear spin initialization routine was optimized by simulation. The optimization parameters were the depletion pulse duration and the gate sequence. A recursive decision tree algorithm was employed in combination with the effective rates model. At each step in the simulation a decision tree was spanned (fig. 5.15a). At each tree node, branches for gates chosen from [NOT2, CNOT1, D(t)] were created. The depletion pulse was set to be $0.5\,\mu s$ long, but the optimization process can produce longer depletion instances by putting two or more gates after another. A pruning technique was applied to cut down unnecessary branches, e.g. two consecutive

99

Figure 5.15: *Optimization with tree algorithm:* **a)** *schematic of algorithm, where at the current step a tree with a certain depth (here 10, with three layers shown) was spanned recursively. At each tree node a single gate was chosen from [NOT2, CNOT1, D(t)] to form a new branch (blue and black dotted lines). The highest population in the target state led to the choice of branch (orange). The first gate in the optimal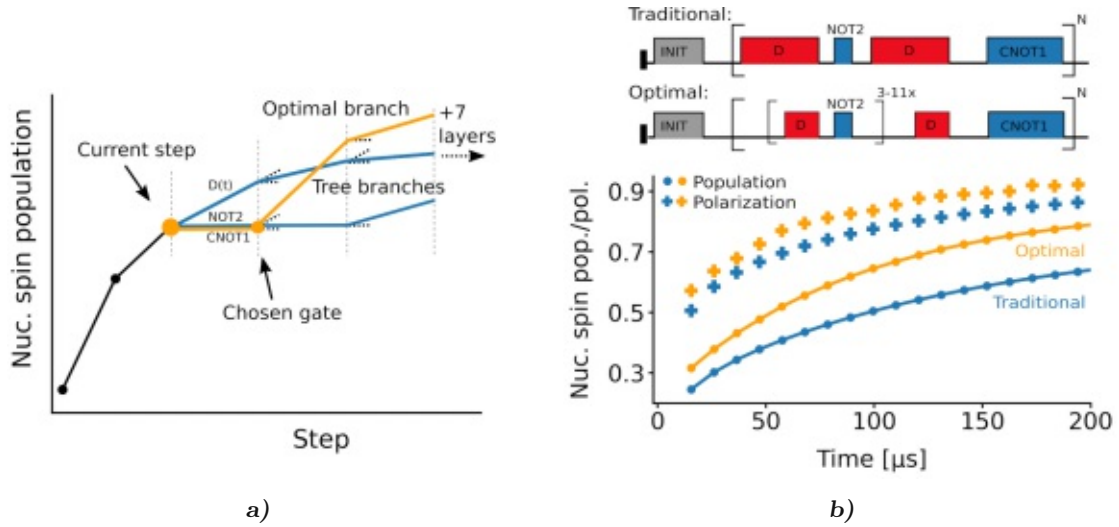 branch was chosen as next gate, all the rest of the tree was discarded. After progression with the single gate to the next step a full new tree was spanned and evaluated for retrieval of the next single gate. In the figure, gates are drawn without time dependence. Inclusion of gate duration stretches or compresses the branches strongly.* **b)** *Nuclear spin population (lines) and polarization (scatter) of the target state for traditional approach (blue) introduced in section 5.2 and for optimized version (orange). Here a time scale is used, but dots and scatter marks refer to integer iterations of the traditional approach. Since the optimal gate sequence was not periodic the polarization was averaged over ten gates in the temporal vicinity of the scatter mark. Above the respective sequences are indicated, with a depletion pulse duration in the traditional (optimal) case of 5 μs (mostly 0.5 μs) respectively.*

microwave gates. The number of nodes in the tree was set to deliver stable results, usually at least 10 layers were created. Optimization target was the population trapped in state $M_S = -1$, $M_I = 0$. At the current step in the simulation, the branch with the highest population increase per time in the trap state defined the single next chosen gate, through its first node. After state evolution through this gate, in the next step a new tree was spanned for finding the following optimal gate.

The simulation favoured depletion and NOT2 operations strongly over CNOT1 gates (fig. 5.15b), which was caused by the CNOT1 gate in reality taking 450 ns[4], while a NOT2 operation took only 50 ns. Early on in the optimized sequence, the [D,NOT2] block would be repeated about 11 times, later on gradually decreasing to about three

---

[4]This consisted of a CNOT0 operation of 400 ns and a NOT1 operation of 50 ns.

repetitions, before a CNOT1 occurred.

Potentially, the time spent on initialization could be halved on average, while the resulting complex gate sequences could be well handled by our Lith pulser pulse generator. Microwave pulse imperfections and optional wait periods between gates were not considered in the optimization but may be included. Similarly, the electron spin initialization routine can be optimized for the depletion pulse duration.

CHAPTER 6

Generating and Observing Spin-Photon Entanglement

6.1 Approaching the challenge

In this chapter we return to the main topic of the thesis of generating spin-photon entanglement with an imperfect emitter in the form of a nitrogen vacancy centre. In section 2.2, the concept of working with a single strong optical transition in combination with a TPC tool was introduced. It provides some advantages over the dual-resonance approach: excited state levels don't need to be tuned into resonance by application of an electric field, which would cause spin state mixing in low strain centres. Using only a single spin-faithful $M_S = 0$ line almost eliminates detrimental cross decay into the metastable state.

To recap, the generation of spin-photon entanglement by pumping a superposition ground state on two simultaneously resonant transitions from the original proposal [61] was modified to two temporally separated rounds of optical pumping on a single transition, combined with the temporal overlap of the two resulting partial wave packets. This time information erasure tool comes in the form of a heavily unbalanced interferometer, since the longer arm needed to store part of a wave packet for the duration of at least a spin-flipping microwave operation.

A double-pass constellation, where excitation and fluorescence light each once transit the interferometer, would convert the phase of the state to a global one and was therefore

103
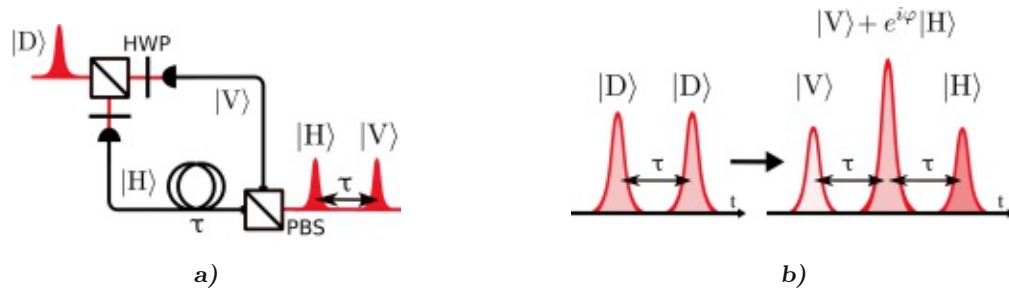
Figure 6.1: *Time-to-polarization conversion:* **a)** *Unbalanced fibre-based interferometer (short arm 2 m, long arm 55 m) acting on input in D-polarization. The HWP maps the PBS transmission from H- to V-polarization and reflection from V- to H-polarization, to ensure that each arm once experiences reflection and transmission on the two PBSs involved. The output is found in two time-bins, separated by the time delay τ.* **b)** *Interferometer action on two D-polarized input pulses with temporal spacing of τ. The output is mapped into three time-bins, according to the interferometer arms passed: short/short, short/long or long/short, and long/long. The first time-bin has V-polarization, the second contains the photonic qubit part including the interferometer phase accumulated between excitation rounds and third has H-polarized light.*

investigated primarily. Unfortunately, our approaches were unfruitful due to different reasons, which are nevertheless mentioned to breach negative publication bias. The chapter then continues with the successfully implemented configuration of a single-pass arrangement of the interferometer on the fluorescence path, combined with tracking of the phase.

Time-to-polarization conversion

With our NV emitter we aimed at producing an entangled state in the time domain. Such a state is well suited for long distance communication but is of little use in computational settings or for state tomography. An interferometer was employed, as a converter from the time to the polarization domain, by erasure of time information of early or late photon emission. The principle of the TPC is discussed with the interferometer version that was used in the successful experimental implementation.

The arms of the interferometer were strongly unbalanced to account for the later emission time of the second photon part (see fig. 6.1a). It consisted of a free space PBS combined with retarders at the injection (upper left in the figure), fibre-based arms (2 m, 55 m, Nufern PM630HP) and an integrated PBS (OZ Optics) at the output port. The 53 m arm length difference left a temporal window of 262 ns between excitation rounds, for photon emission and a spin-flip operation. The interferometer arms were coupled

with orthogonally polarized light, where the short arm was chosen to be V-polarized, while the long arm was H-polarized, so that each part of the light would receive one transmission and one reflection at the two PBSs. On sending D-polarized light to the input, one receives two signal time-bins at the output with orthogonal light polarization, as illustrated in figure 6.1a.

Two D-polarized input pulses, timed with a time delay of τ, exit in three time-bins, the first being V-polarized, the second has both polarization components, and the third is H-polarized, as shown in figure 6.1b. For the second bin, time information has been erased but the interferometer phase φ was imprinted on the state. This second bin contained the photonic part of the entangled qubits in the experiment. The first and third side-lobe are nevertheless useful, as they present measurements of the photons in the H/V-basis, which aided in state tomography (see section 6.4).

6.2 Double-pass configuration attempts

It was mentioned above that a double-pass configuration would be advantageous, in that it makes the imprinted phase on the central time-bin global, as long as phase drifts are slow compared to the interferometer delay time. Another advantage is that the relative timing of excitation pulses doesn't have to be considered, since one excitation pulse is sufficient. A single excitation pulse is split in the interferometer arms and the pulses arrive at the NV centre with the desired time separation for the two excitation rounds. Such an approach was investigated by testing three double-pass configuration setups.

Fibre-based Mach-Zehnder in double-pass configuration

The setup, shown in figure 6.2a, had the unbalanced fibre-based interferometer placed to be traversed by excitation and fluorescence light. A single input light pulse was cleaned in polarization (PBS) and set with a HWP to be injected equally into the long and the short arm of the interferometer. The two split pulses were calibrated to each achieve an optical π-pulse. Fluorescence also takes both paths, so that three time bins were observed in tomography. Looking only at the central time-bin, the two contributions to fluorescence originate from: excitation through the short arm / fluorescence taking the long arm and vice versa. Assuming that phase changes occur slowly compared to the protocol timescale, this leads to a global phase as each traversing part (excitation and
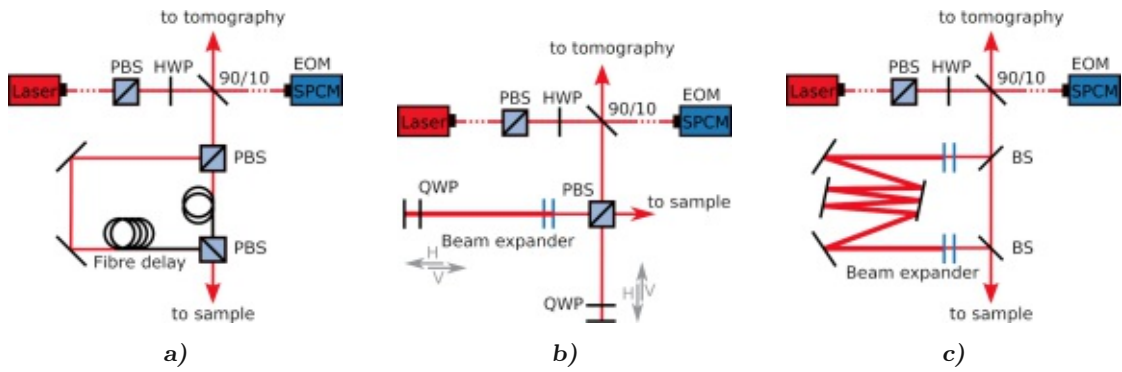
Figure 6.2: *Investigated interferometer options in double-pass configuration for excitation and fluorescence light. Laser and EOM path are included to allow easier comparison with fig. 4.16.* **a)** *Fibre-based unbalanced Mach-Zehnder.* **b)** *Free-space unbalanced Michelson interferometer.* **c)** *Free-space unbalanced non-polarizing Mach-Zehnder interferometer.*

fluorescence) has the same imprint of the interferometer phase between short and long arm.

However, due to the high power excitation pulse travelling through the 55 m long fibre, a significant amount of backscattered light was observed in the detection window, amounting to about 10^{-3} photons per ns (about 10^{-5} to 10^{-6} fluorescence photons per ns were expected). This results in 100-1000 scattered photons per detected fluorescence photon, making the approach infeasible. The optical return loss (ORL) parameter of fibres quantifies the power reflected and scattered back to the source (P_r), given a defined input power P_i into the fibre as [58]

$$ORL = 10Log_{10}\frac{P_i}{P_r}.$$ (6.1)

A rough estimation of reflected and scattered photons is done for a typical ORL value of 60 dB: a 1 ns step pulse with a power of 2.5 μW produces a P_r of 2.5×10^{-12} W, leading to 2.5×10^{-21} J ns^{-1} or 0.008 photons travelling to the detector. Accounting for losses at the beam splitter, the fibre coupler, and in the detector, about $3.5 \cdot 10^{-3}$ photons per ns are detectable. Integration of the emitter into a resonator, enhancing the fluorescence output, could be envisaged in the future to surpass this problem (see outlook in chapter 7).

Free-space Michelson interferometer in double-pass configuration

In the second double-pass setup we aimed to avoid the backscatter problem by removing the fibres from the interferometer. A polarization free-space Michelson interferometer (fig. 6.2b) with imbalanced arms was set up. The excitation light was split at the PBS, so that equal parts with opposite polarization were found in the arms. The path difference was about 30 m, achieved by expanding the beam in the long arm to keep the divergence low. Quarter-wave plates were used to swap light polarization for correct routing at the PBS. Unfortunately, the imperfections of the PBS introduced unwanted reflections that led to many discrete but strong scattered light peaks in the tomography path, with the consequence that the SPCMs encountered dead time during the detection windows.

Free-space Mach-Zehnder in double-pass configuration

As a last try for achieving a double-pass configuration, the free-space Michelson interferometer was changed to a free-space non-polarizing Mach-Zehnder (fig. 6.2c). The long arm beam was again expanded and folded on large mirrors to maximize path difference. Clean detection windows were seen under excitation through both the short and the long arm. However, we encountered a lack of mechanical stability, which caused decoupling of the long arm over hours, found to be correlated with small RT fluctuations and mechanical vibrations. Stabilization efforts did not alleviate the problem.

6.3   Single-pass configuration approach

With the double-pass interferometer setups found to be unfeasible, due to high (fibre) backscatter and stability issues, another approach was taken. The interferometer was set into the fluorescence path in a single-pass configuration. This implied the necessity to keep track of or to stabilize the phase of the interferometer, since the phase is not global in this approach. A description of the setup is given, the constraints and requirements for phase readout are analyzed and the phase reconstruction method is discussed.

6.3.1   Single-pass interferometry setup

The double-pass setups had the interferometer on the combined excitation/fluorescence path. Here, the TPC interferometer was instead repositioned to the fluorescence arm only (fig. 6.3). A tomography stage was present after the interferometer, which was of
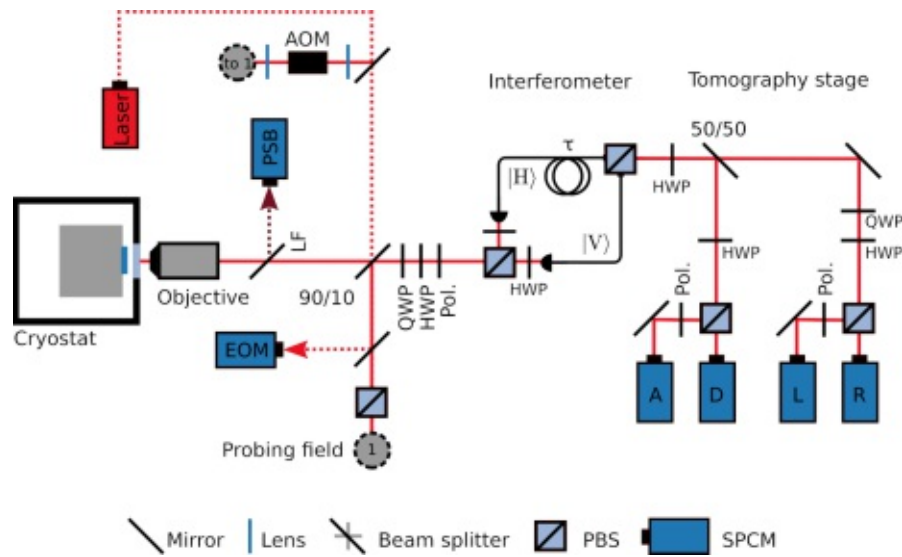
Figure 6.3: *Optical setup with interferometer and tomography stage. Dotted pathways have been introduced in section 4.4 and figure 4.16. Interferometer as discussed in fig. 6.1a. The tomography stage was set up to measure light polarization in the two orthogonal bases D/A and R/L. To monitor the phase of the interferometer by tomography, light, called the probing field, was injected into it, at the port marked with '1'. This port was fed by a split-off in the red laser path, including an AOM for amplitude modulation.*

dual purpose, the first being of course tomography of the state, but secondly, it allowed to access the interferometer phase.

Since the phase of the interferometer was prone to drifts through environmental influences, it either had to be stabilized to ensure equal phase for the entangled photons in the experiment or the phase had to be monitored, so that each fluorescence photon could be related to a certain interferometer phase. We opted for phase monitoring, where we used the random walk of the unstable interferometer phase in our tomography process. The downside was that accurate and fast phase readout became necessary and each photon event at a certain time had to be precisely relatable to a distinct phase.

The possibility of using the tomography setup, necessary to probe the photonic part of the produced entangled state, to monitor the interferometer phase as well was investigated early on. This implied using SPCMs for phase detection. SPCMs show error from shot noise and therefore require high count rates for accuracy. In the following the feasibility of SPCMs for phase readout and the impact on the error of the phase are discussed.
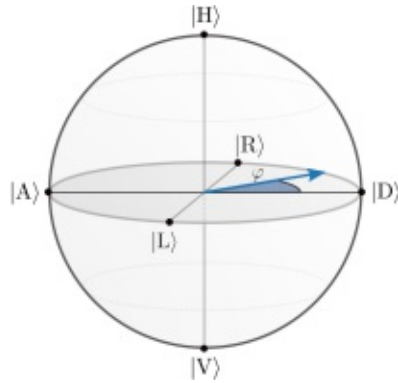
Figure 6.4: *Poincaré sphere representation of states: a state $|\psi_{in}\rangle = |\mathrm{D}\rangle$ exits the interferometer as equatorial state $|\psi_{out}\rangle$ (blue arrow) with phase φ imprinted.*

6.3.2 Interferometer phase readout and stability

Interferometer phase from photon tomography

Photons entering the interferometer in the state

$$|\psi_{in}\rangle = \frac{1}{\sqrt{2}} \left(|\mathrm{H}\rangle + |\mathrm{V}\rangle \right), \tag{6.2}$$

left it with a phase so that

$$|\psi_{out}\rangle = \frac{1}{\sqrt{2}} \left(|\mathrm{H}\rangle + e^{i\varphi} |\mathrm{V}\rangle \right). \tag{6.3}$$

The phase produced states on the equatorial plane of the photon analogue of the Bloch sphere, the Poincaré sphere (fig. 6.4), normal to the H/V-axis. The axial equatorial states are conventionally labelled as

$$
\begin{aligned}
|\mathrm{D}\rangle &= \frac{1}{\sqrt{2}} \left(|\mathrm{H}\rangle + |\mathrm{V}\rangle \right), \\
|\mathrm{A}\rangle &= \frac{1}{\sqrt{2}} \left(|\mathrm{H}\rangle - |\mathrm{V}\rangle \right), \\
|\mathrm{R}\rangle &= \frac{1}{\sqrt{2}} \left(|\mathrm{H}\rangle + i\,|\mathrm{V}\rangle \right), \\
|\mathrm{L}\rangle &= \frac{1}{\sqrt{2}} \left(|\mathrm{H}\rangle - i\,|\mathrm{V}\rangle \right).
\end{aligned}
\tag{6.4}
$$

For photon tomography, these equatorial states need to be discernible by projecting the state of the photon onto the D/A- and R/L-axes. From such a measurement it is generally possible to reconstruct the state using Stokes parameters S_α through [65]

$$\hat{\rho} = \frac{1}{2} \sum_{\alpha=0}^{3} S_\alpha \hat{\sigma}_\alpha, \tag{6.5}$$

109
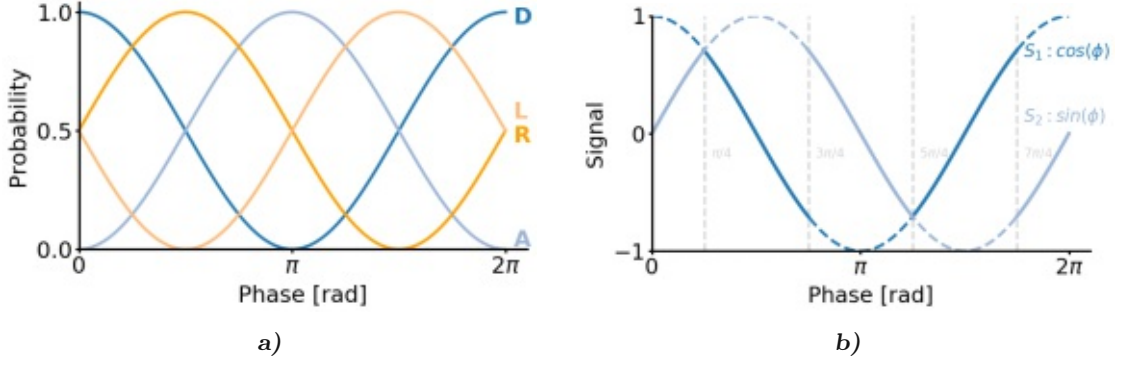
Figure 6.5: *Interferometer phase tomography:* **a)** *expected output port pattern for $|\mathrm{D}\rangle$ polarized input after the interferometer traversal with arbitrary phase imprinted on state.* **b)** *The two derived Stokes signals with truncation regions indicated (continuous lines). For phase reconstruction through the arcus function, the sign of the other signal was used to render the phase value unambiguous.*

with the S_α defined as

$$
\begin{aligned}
S_0 &= P_{|\mathrm{H}\rangle} + P_{|\mathrm{V}\rangle}, \\
S_1 &= P_{|\mathrm{D}\rangle} - P_{|\mathrm{A}\rangle}, \\
S_2 &= P_{|\mathrm{R}\rangle} - P_{|\mathrm{L}\rangle}, \\
S_3 &= P_{|\mathrm{H}\rangle} - P_{|\mathrm{V}\rangle},
\end{aligned}
\tag{6.6}
$$

where P is the probability of measuring the indicated state and S_3 is zero due to the balanced initial state. The probability for a measurement outcome for the observable M of the state ψ_{out} is

$$
P_{|\psi\rangle} = \langle\psi|M^\dagger M|\psi\rangle. \tag{6.7}
$$

Entering the equatorial axes to project onto yields phase dependences of the probabilities

$$
\begin{aligned}
P_{|\mathrm{D}\rangle} &= \langle\psi_{out}|\mathrm{D}\rangle\langle\mathrm{D}|\psi_{out}\rangle = \cos^2(\varphi/2), \\
P_{|\mathrm{A}\rangle} &= \sin^2(\varphi/2), \\
P_{|\mathrm{R}\rangle} &= \sin^2(\varphi/2 + \pi/4), \\
P_{|\mathrm{L}\rangle} &= \cos^2(\varphi/2 + \pi/4).
\end{aligned}
\tag{6.8}
$$

The resulting phase dependent pattern for detection of the output state on the four tomography ports is shown in figure 6.5a.

Insertion of the derived probabilities into S_1 yields

$$
S_1 = \cos^2(\varphi/2) - \sin^2(\varphi/2) = 2\cos^2(\varphi/2) - 1 = \cos(\varphi), \tag{6.9}
$$

a cosine behaviour on the phase evolution of the Stokes parameter signal, and likewise for S_2 a sinusoidal one. Dividing by S_0 gives two normalized signals shown in figure 6.5b. The phase was extracted by application of the corresponding inverse trigonometric function on the Stokes signals. Since both signals contained the full phase information, they were truncated into regions with high gradients to minimize the error on the phase value. The procedure cut the signals into intervals of length $\pi/2$. The arcus functions are defined on $-\pi/2$ to $\pi/2$ for the sine and 0 to π for the cosine. To achieve correct assignment of the phase on the whole interval $[0, 2\pi]$, the two possible phase results of the arcus function in the intervals was cross-referenced to the sign of the second signal function, rendering the phase unambiguous.

The elaborate process of extracting the phase through photon tomography is presented in full detail in appendix E, starting from the layout and functioning of the experimental tomography stage. The origin of the light used for probing the phase is discussed, together with an analysis of the error on the phase through two effects - time averaging in the measurement and Poissonian light statistics. To improve on the statistics, a high photon rate was used, which led to a data capture rate of 3 GB per minute and required a suitable data processing framework. The system design, according to the paradigm of real-time data analysis, is presented with its requirements and constraints from the experiment and a detailed description of the distributed software architecture is given. The appendix concludes with the practical aspects of deriving a phase signal from the recorded events, including the developed normalization process for the noisy signal.

6.4 Entangling spin and photon

At this point, all the ingredients to perform spin-photon entanglement have been introduced. In this section the entangling sequences are discussed, the results presented and the observed entanglement is quantified.

6.4.1 Unfolding the experimental sequence

The entangling sequences unfolded in three major building blocks - preparation of the system in the desired initial state, an entanglement generation attempt and finally partial tomography of the spin-photon state (fig. 6.6).

111
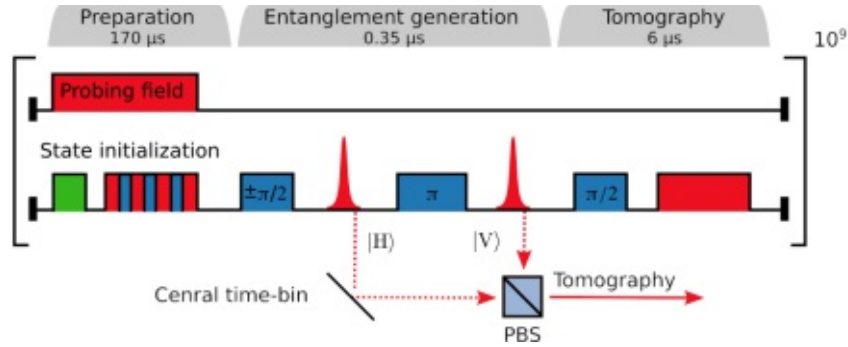
Figure 6.6: *The basic experimental sequences (detailed description in the text). Mind that the three blocks are not to scale. The two sequences, prepared in two different initial states through the first microwave operation, were repeated for about 10^9 times, taking about a week each.*

The preparation phase.   The sequence started with a short green laser pulse in order to maintain a negatively charged state in the NV centre. The second initialization routine concerned the electron and nuclear spin state. The spin initialization routine was conducted as discussed in the previous chapter, using the iterative approach of driving populations out of undesired states by inducing random spin flips (in the non-optimized version). We chose to prepare the spin in the $M_S = -1$, $M_I = 0$ state, and the electron spin subspace $M_S = 0$ and $M_S = -1$, defined as $\{|0\rangle, |1\rangle\}$, constituted a matter qubit for our protocol. The nuclear spin polarization, within the $M_S = -1$ manifold was $83.8 \pm 1.9\,\%$. In parallel to the spin initialization, the probing field laser pulses were sent through the interferometer, to ensure a high count rate on detectors, and thereby a high accuracy in the phase readout.

Altogether, the initialization step took about $170\,\mu s$, which was about $96\,\%$ of the total sequence duration.

Entanglement generation.   Two different sequences were executed for entanglement generation. With either an $R_y(\pi/2)$ or $R_y(-\pi/2)$-pulse, where R_y is a rotation around the y-axis, we transferred the electron spin into a superposition state, for the first case into

$$|\psi_0\rangle = \frac{1}{\sqrt{2}}\left(|1\rangle - |0\rangle\right), \tag{6.10}$$

with which the actual entangling protocol was performed. The procedure is discussed for this starting superposition, the other follows analogously.

112

A short, optically resonant pulse (see chapter 4.4.3), labelled a, excited population only from the $M_S = 0$ state, in the manner of an optical π-pulse. As a consequence, conditioned on the electron spin state, a subsequent photon was emitted ($|0\rangle$) or not ($|1\rangle$). In the emission case, the photon was routed probabilistically into the 262 ns TPC-interferometer delay line, comprising an H-polarized photon channel, resulting in the state

$$|\psi_a\rangle = \frac{1}{\sqrt{2}} \left(|1\rangle |0_a\rangle - |0\rangle |H_a\rangle \right), \tag{6.11}$$

where $|0_a\rangle$ denotes the absence of a photon and $|H_a\rangle$ the creation and routing of a H-polarized photon. Thereafter, the electron spin was flipped with a microwave π-pulse, yielding

$$|\psi_a\rangle = \frac{1}{\sqrt{2}} \left(|0\rangle |0_a\rangle + |1\rangle |H_a\rangle \right). \tag{6.12}$$

The second round of optical excitation, called b, took place exactly 262 ns after the first, in order to overlap the stored photon with the second photon on a PBS to achieve which-path information erasure. The conditionally created photon of the second round, routed into the V-channel of the interferometer $|V_b\rangle$, produced the desired polarization entangled state

$$|\psi_b\rangle = \frac{1}{\sqrt{2}} \left(e^{i\varphi} |0\rangle |V_b\rangle + |1\rangle |H_a\rangle \right), \tag{6.13}$$

with φ the interferometer phase, which was tracked as mentioned in the previous section. This operation concluded the entangling block of the sequence, and upon the described TPC process, the photon polarization was entangled with the electron spin of the NV centre in the state

$$|\psi\rangle = \frac{1}{\sqrt{2}} \left(e^{i\varphi} |0\rangle |V\rangle + |1\rangle |H\rangle \right). \tag{6.14}$$

Spin-photon tomography. A spin rotation by $R_y(\pi/2)$ put the state into the measurement basis in x-orientation as

$$|\psi_m\rangle = \frac{1}{2} \left(-|0\rangle \left(|H\rangle - e^{i\varphi} |V\rangle \right) + |1\rangle \left(|H\rangle + e^{i\varphi} |V\rangle \right) \right). \tag{6.15}$$

Events were evaluated and sorted by their phase values. Exemplarily, in the case $\varphi = 0$, the state would correspond to $\frac{1}{\sqrt{2}} \left(-|0\rangle |A\rangle + |1\rangle |D\rangle \right)$, with the expected port detections pattern shown in figure 6.5a at point $\varphi = 0$. After the $R_y(\pi/2)$ microwave operation, spin readout was performed with a 5 μs calibrated resonant readout pulse, conditional on the $|0\rangle$ state.
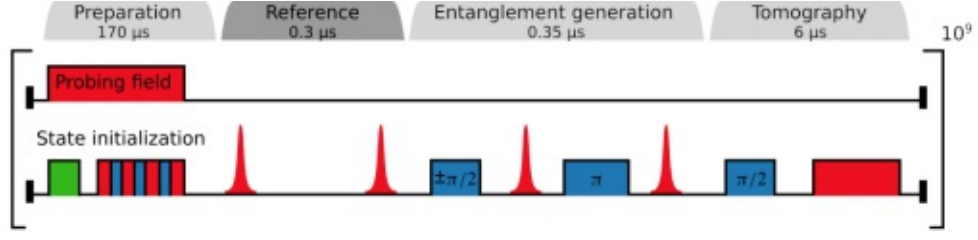
113

Figure 6.7: *Final experimental sequences including a reference section with two needle pulses equidistant to the entanglement generation section, producing three time-bins to extract a background signal.*

6.4.2 Background subtraction

We measured the probability $P(M_S = 0|photon)$ of the spin state being in $|0\rangle$ on the condition that a ZPL photon was detected on one of the four ports in the central time-bin detection window. In our measurement basis $|+\rangle$ and in dependence on the value of the interferometer phase,

$$P(+|E)(\varphi) = \frac{\mathrm{N}_{|+\rangle \wedge \mathrm{E}}(\varphi)}{\mathrm{N}_{\mathrm{E}}(\varphi)}, \tag{6.16}$$

where E is a photon event from an equatorial state, $\mathrm{N}_{|+\rangle \wedge \mathrm{E}}$ is the number of ZPL-photons with a projected spin-0 readout in coincidence and N_{E} is the total number of ZPL-photon events registered in the experiment for that interferometer phase. We estimated the conditional probability with and without a calibrated amount of background subtracted. In the case of background subtraction, the conditional probability is given by

$$P^B(+|E)(\varphi) = \frac{\mathrm{N}_{|+\rangle \wedge \mathrm{E}}(\varphi) - \mathrm{N}_{|+\rangle \wedge \mathrm{B}}(\varphi)}{\mathrm{N}_{\mathrm{E}}(\varphi) - \mathrm{N}_{\mathrm{B}}(\varphi)}, \tag{6.17}$$

where $\mathrm{N}_{|+\rangle \wedge \mathrm{B}}$ is the coincidences in the background and N_{B} are the background events in the ZPL detections. Background related values were extracted from a reference part inserted into the experimental sequence, where negligible fluorescence from the NV centre was present (fig. 6.7), due to the centre being in state $|1\rangle$. Background contributions were phase dependent since their main contribution originated from the probing field light (afterpulsing). Scattered light and dark counts only had a minor impact. The reference sequence contained a fingerprint of the background events in our experimental detection window (fig. 6.8).

6.4.3 Temporal optimization of the detection window

An accurate calibration for the temporal edges of the detection window in the fluorescence decay time trace was performed with the objective of improving the visibility of the correlation signal. The optimization was done on the central time bin of the three time bins in the experimental time trace. The optimized window was then used globally, for all time bins and ports.

The starting point was a time trace histogram from a part of the ZPL detection events. The optimization parameters were the temporal start and end points of the detection window. The expectation was that a long window would contribute to reduce the error on the signal, but that the uncertainty in emission time of the wave packet would wash out correlations for longer time scales. A window starting 2 ns after the scatter maximum and lasting for 5 ns proved most favourable (indicated in figure 6.8).

To improve statistics, the traces from the tomography ports were shifted to overlap. Figure 6.9 shows the resulting background free trace for each of the two initial states used, $|+\rangle$ and $|-\rangle$, in the form of the conditional probability $P^B(\pm|E)$, giving a measure of the spin in the projected $|+\rangle$ or $|-\rangle$-state, respectively, when a central time-bin photon had been detected in an equatorial state $|E\rangle$ before, showing a sinusoidal and anti-correlated behaviour in dependence of the phase. The mean value of the probability traces of about 0.1 agrees well with the expected spin readout probability for an equatorial state on the Bloch sphere.

6.4.4 Phase offset correction

The light used to read out the interferometer phase passed through an AOM, which was driven with a frequency of 350 MHz. This frequency was imprinted on the probing field light, therefore showing a phase offset when compared to light from scattered photons. Since it was a static offset, it was easily corrected for by shifting the phase for 1.16 rad, as shown in figure 6.10, and was already considered in the conditional probability traces in fig. 6.9.

6.4.5 Entanglement quantification

The aim of the experiment was to demonstrate successful entanglement generation with a TPC scheme. This required a means of verification. The figure of merit chosen was the
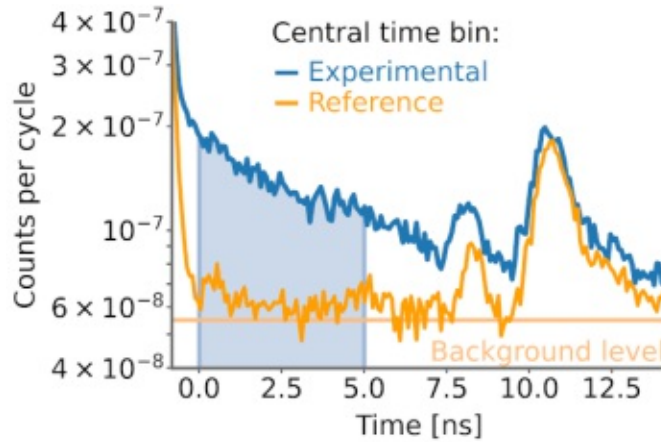
Figure 6.8: *Central time-bin detection window: the detection window was optimized with respect to maximum visibility in the conditional probability signal shown in figure 6.9. We optimized the window start and duration. The window start time was found to be optimal at 2 ns (0 on x-axis) after the excitation pulse maximum; the duration was set to 5 ns (shaded area). The reference trace, used for background subtraction, was taken from the reference section of the sequence and here shifted to overlap. Note that it almost reached the overall background level of the measurement. The peaks at later times were related to afterpulsing of detectors.*
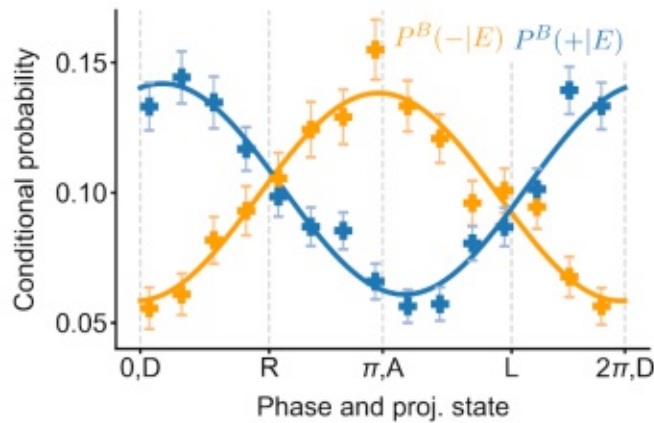
Figure 6.9: *Conditional probabilities $P^B(\pm|E)$ for the two input states oscillating in an anti-correlated fashion (thereby witnessing entanglement) over the interferometer phase angle, defining the projection state E for the photon. Basis states angle spacing was shifted by 0.1 rad to account for not fully orthogonal measurement bases (value found empirically). Measured data is shown with the standard error of the mean, and solid lines are sinusoidal fits. The phase uncertainty for each data point is ± 0.18 rad.*
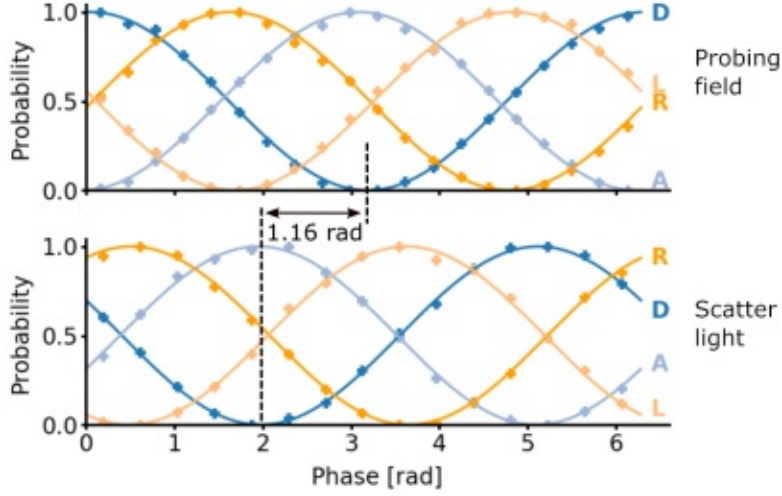
Figure 6.10: *Phase offset correction: measured phase shift on tomography ports for probing field and resonant scattered light, due to an AOM in the probing field path.*

entanglement fidelity, derived in the following according to references Blinov et al. [13] and Bernien et al. [12], which not only shows that entanglement is present but also allows to quantify it.

The final state in the central detection time bin from equation 6.14 is of the $|\psi^+\rangle$-Bell state type. Therefore, we chose to compare our resulting state to the $|\psi^+\rangle$-Bell target state $|\psi^+\rangle = \frac{1}{\sqrt{2}}(|01\rangle + |10\rangle)$.

In general, the fidelity of two density operators σ and ρ is defined as [73]

$$F(\sigma, \rho) = \left(\text{Tr} \sqrt{\sqrt{\sigma}\rho\sqrt{\sigma}} \right)^2. \tag{6.18}$$

After inserting the $|\psi^+\rangle$-state, this reduces to

$$F(\sigma_{\psi^+}, \rho) = \left(\text{Tr} \sqrt{|\psi^+\rangle \langle\psi^+| \rho |\psi^+\rangle \langle\psi^+|} \right)^2 = \langle\psi^+| \rho |\psi^+\rangle \left(\text{Tr} \sqrt{|\psi^+\rangle \langle\psi^+|} \right)^2 = \langle\psi^+| \rho |\psi^+\rangle. \tag{6.19}$$

Insertion yields

$$F(\sigma_{\psi^+}, \rho) = \frac{1}{2} \left(\rho_{22} + \rho_{33} + \text{Re}\{\rho_{23}\} + \text{Re}\{\rho_{32}\} \right) = \frac{1}{2} \left(\rho_{22} + \rho_{33} + 2\,\text{Re}\{\rho_{23}\} \right). \tag{6.20}$$

The diagonal element terms are derived from the correlated events in the basis $|X, X\rangle$ for the spin and photon states. To determine the off-diagonal elements, we rotated to the $|Z, Z\rangle$-basis by a $\pi/2$-rotation around the y-axis, yielding

$$\tilde{\rho} = (R_y(\pi/2) \otimes R_y(\pi/2))\, \rho\, (R_y^\dagger(\pi/2) \otimes R_y^\dagger(\pi/2)), \tag{6.21}$$

117

and compared the difference between correlations and anti-correlations in the new basis to the original density matrix. This yields an expression for the off-diagonal elements,

$$\tilde{\rho}_{11} + \tilde{\rho}_{44} - \tilde{\rho}_{22} - \tilde{\rho}_{33} = 2\,\mathrm{Re}\{\rho_{23}\} + 2\,\mathrm{Re}\{\rho_{14}\}. \tag{6.22}$$

From the properties of density matrices, a lower bound for $\mathrm{Re}\{\rho_{14}\}$ is

$$|\mathrm{Re}\{\rho_{14}\}| \leq \sqrt{\rho_{11}\rho_{44}}, \tag{6.23}$$

so that

$$2\,\mathrm{Re}\{\rho_{23}\} \geq \tilde{\rho}_{11} + \tilde{\rho}_{44} - \tilde{\rho}_{22} - \tilde{\rho}_{33} - 2\sqrt{\rho_{11}\rho_{44}}. \tag{6.24}$$

Inserting into 6.20 gives a lower bound for the fidelity:

$$F \geq \frac{1}{2}\left(\rho_{22} + \rho_{33} + \tilde{\rho}_{11} + \tilde{\rho}_{44} - \tilde{\rho}_{22} - \tilde{\rho}_{33} - 2\sqrt{\rho_{11}\rho_{44}}\right). \tag{6.25}$$

The diagonal entries of the density matrices in the expression above are accessed by measuring in two bases rotated by $\pi/2$-around the y-axis. In principle, the data was already contained within our measurement by the nature of our scheme. The path-revealing events in the first and third time bin can be associated with the $\tilde{\rho}$-values in the $|Z, Z\rangle$-basis, while the other values could be extracted from the path-erased data in the central time bin measured in the $|X, X\rangle$-basis. Nevertheless, the $|Z, Z\rangle$-basis measurement was additionally carried out separately, with the phase-probing field switched off to reduce the background.

The $|\psi^+\rangle$-state in $|Z, Z\rangle$ notation and in the $|X, X\rangle$ measurement bases was

$$\left|\psi^+\right\rangle = \frac{1}{\sqrt{2}}(|0, \mathrm{V}\rangle + |1, \mathrm{H}\rangle) = \frac{1}{\sqrt{2}}(|+, \mathrm{D}\rangle - |-, \mathrm{A}\rangle). \tag{6.26}$$

With phase dependence of the photon state

$$\left|\psi^+(\varphi)\right\rangle = \frac{1}{\sqrt{2}}(\left|+, E^+(\varphi)\right\rangle - \left|-, E^-(\varphi)\right\rangle), \tag{6.27}$$

where $E^\pm$ denote some equatorial basis state and the orthogonal state.

The density matrix diagonal entries for fidelity calculation were derived from the conditional events at phase positions 0 and π of figure 6.9, as summarized in figure 6.11a and 6.11c with background. The density matrix diagonal entries in the $|Z, Z\rangle$-basis were extracted from the mentioned calibration measurement with elements shown in figure 6.11b and in 6.11d, with and without background. With background subtraction the
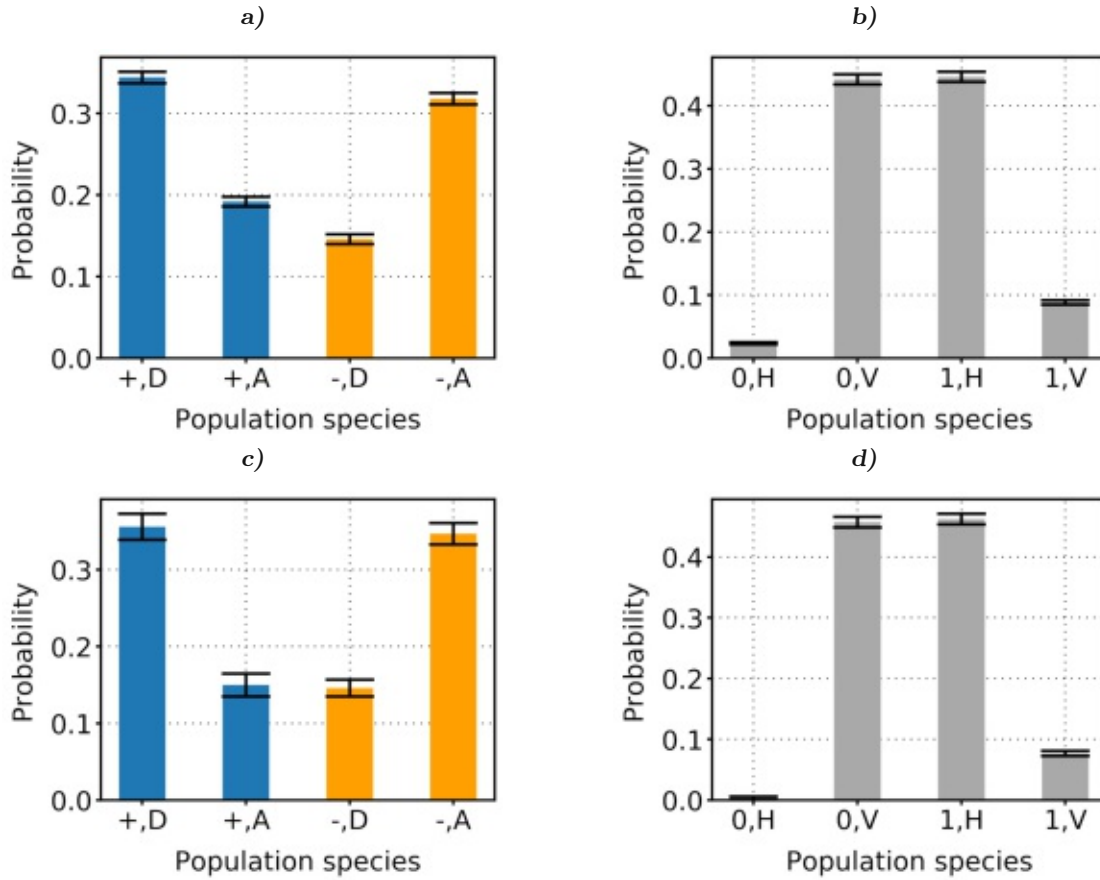
Figure 6.11: *Correlations of electron spin and photon state with desired states from equations 6.26 and 6.27. Upper (lower) row without (with) background subtraction. Error bars were derived from shot noise in the state readout.* **a), c)** *x-basis measurements results summarized, with a correlation of* $C_{xx} = 32.7 \pm 1.3\%$ *(a) and* $C_{xx}^B = 40.7 \pm 2.9\%$ *(c), when defining* $C = \tilde{\rho}_{11} + \tilde{\rho}_{44} - \tilde{\rho}_{22} - \tilde{\rho}_{33}$. **b), d)** *z-basis measurement results summarized.*

lower bound on the fidelity with respect to the $|\psi^+\rangle$-Bell state was $F \geq 64.7 \pm 1.3\%$, while including background, $F \geq 56.0 \pm 0.9\%$. Both values are significantly above the threshold of $F = 50\%$ for a classical state, thereby confirming entanglement in our spin-photon state, by over 11 standard deviations (over six without background subtraction). 25 spin-photon entangling events were captured per hour.

6.5 Discussion of the results

We successfully demonstrated the basic building block of our single-transition entanglement generation and TPC scheme by creating entanglement between the electron spin

Instance	Loss factor	Transmitted fraction ZPL	Transmitted fraction PSB
Sample surface, antireflection coating (PSB)	0.1		0.9
Sample surface, antireflection coating (ZPL)	0.05	0.95	
Cryostat window	0.57	0.41	0.39
Objective (NA and transmission)	0.87	0.053	0.05
Detector efficiency	0.35	0.034	0.032
Other optical PSB path elements	0.49		**0.017**
Fibre coupling to interferometer	0.5	0.017	
Interferometer TPC success rate	0.5	0.009	
Interferometer output PBS	0.26	0.006	
Other optical ZPL path elements	0.81	**0.0012**	

Table 6.1: *Optical transmission of the system: at every instance the fraction of lost photons is given as a loss factor and the transmitted fraction is indicated for both ZPL and PSB paths. The anti-reflection coating had wavelength specific losses. The compounded entries for 'other optical elements' contain optical components like mirrors, filters and beam splitters.*

of an NV centre and its own fluorescence photon. Unfortunately, our system possessed some severe limitations, making it impossible in practice to produce a further photon through iteration of the basic entangling block operations as described below. Some of these limitations are discussed in more detail.

Photon detection efficiency. The ability to collect photons efficiently is of course crucial for a photonic experiment. We estimated that the collection efficiency was on the order of 1 % for the PSB and 0.1 % on the ZPL, as summarized in table 6.1. The cryostat window caused wavefront aberrations and the TPC process was purely probabilistic. The interferometer PBS had losses specified by the manufacturer for the two used ports as $-1.1\,\mathrm{dB}$ and $-1.5\,\mathrm{dB}$ respectively, which were averaged. With only about 2 % of photons emitted into the ZPL path, the probability of detecting a photon becomes about 2×10^{-5}, or 0.5×10^{-5} per detection port. Possible improvements would include deterministic photon routing in the interferometer and better optics.

Spin mixing in the excited state. Spin mixing in the excited state, leading to spin flips during the experimental sequence, was empirically determined for needle excitation
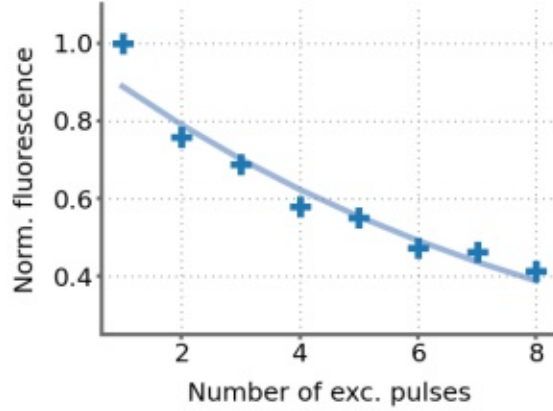
Figure 6.12: *Spin mixing in excited state: preparation of spin in state $M_S = 0$, then excitation with a train of needle pulses. The crosses are the normalized integrated fluorescence per pulse and the solid line is a fit with a single exponential decay to extract the spin-flip rate.*

pulses (fig. 6.12). The electron spin was prepared in the $M_S = 0$ ground state and a train of needle pulses separated by 4.5 excited state lifetimes was applied. The fluorescence, indicative of the remaining $M_S = 0$ population, is plotted. The exponential fit indicates a $13.5 \pm 1.5\%$ spin-flip probability per needle pulse. Ionisation could also explain the decay in the fluorescence curve, but at the excitation power used, it was not significant [84]. Spin-flips were therefore a major source of oscillation visibility reduction of the conditional probabilities in the entangling experiment (this is quantified further down). The error can be reduced by using a low crystal strain regime NV centre.

Optical cross talk. In section 5.1.2 optical cross-talk for low power excitation pulses was treated. We had to consider a similar effect in the experimental sequence by the needle excitation pulses. The temporally short pulses with 1.5 ns FWHM have a spectral width on the order of 100 MHz by their Fourier transform, increasing spectral overlap with off-resonant transitions. We quantified the expected cross talk in an empirical model, consisting of our $M_S = 0$ working transition and a 0.87 GHz detuned transition of $M_S = \pm 1$ character. The probability of detecting a photon in a calibration measurement CM after a needle pulse excitation (optical π-pulse) on the resonant state is

$$p_{CM}^{\gamma} = \eta \left(P_0 \; p_{EXC}^0 \; p_{RD}^0 + P_1 \; p_{EXC}^1 \; p_{RD}^1 \right) + p_B, \tag{6.28}$$

with η the detection efficiency, $P_{0/1}$ the state $M_S = 0$ ($M_S = \pm 1$) populations, $p_{EXC}^{0/1}$ the excitation probability for $M_S = 0$ ($M_S = \pm 1$) population, $p_{RD}^{0/1}$ the probability for

121

radiative decay after excitation from $M_S = 0$ ($M_S = \pm 1$) and the probability of detecting a background light photon, p_B. The investigated parameter describing the cross talk is p^1_{EXC}.

Two calibration measurements CM1 and CM2 were performed, both probing the photon yield after a single needle pulse on a well defined population distribution in the ground states. In CM1, the electron spin was polarized in the $M_S = -1$ state with population distribution $P_{-1} = 0.839$, $P_0 = 0.019$ and $P_1 = 0.142$, while the populations of $M_S = -1$ and $M_S = 0$ were flipped in CM2. p^0_{EXC} was assumed as one due to excitation with optical pulses and $p_B = 3.4 \times 10^{-5}$. Inserting these values for CM1 and CM2 in the above equation and solving gives a detection efficiency of 0.02, close to what is seen from our PSB measurements, and the product $p^1_{EXC} \, p^1_{RD} = 0.0124$. Goldman et al. [39] reported on lifetime and intersystem crossing rates that allow to calculate the probability for radiative decay of the $E_{1,2}$ excited states as 0.617. With that p^1_{EXC} would be estimated as 0.02 but the value could differ slightly since our NV centre had much higher crystal strain than in the Goldman reference.

Non-unity readout contrast. The spin readout contrast C_{RO} was 0.948 ± 0.000172 (see chapter 5.1.2). The non-unity value led to a decrease of about 5 % visibility in the oscillation of the conditional probabilities. Also, single-shot readout was not possible due to the low yield of readout photons per shot of 0.167 on average per attempt.

Tracking limitations of our current system. Decorrelating influences, like the ones discussed in the previous paragraphs, made our target state deviate from the desired ψ^+-Bell state. We analyzed their impact on our spin-photon system by modelling an overall density matrix

$$\rho_{event} = \alpha_{nv} \left(\alpha_{ent} \, \rho_{ent} + \alpha_{ninit} \, \rho_{ninit} + \alpha_{op} \, \rho_{mix} \right) + \alpha_{uc} \, \rho_{mix} + \alpha_{scat} \, \rho_{scat} + \alpha_{probe} \, \rho_{probe},$$
$$(6.29)$$

where the ρ_i relate to the density matrix of state i, and α_i are the probabilities that a spin-photon event was caused by a certain process. The parameters are discussed and summarized in table 6.2. α_{nv} marks the fraction of events stemming from the NV centre and is composed of three parts: the ideal entangled ψ^+-Bell state with density ρ_{ent} and factor α_{ent}, a density ρ_{ninit} for the cases when the NV is initialized in the wrong state (e.g. $M_S = 0$ instead of $M_S = -1$, which would produce the anti-correlated ψ^--Bell

α_{ent}	α_{ninit}	α_{op}	α_{nv}	α_{uc}	α_{scat}	α_{probe}	C_{RO}	p_{ld}
0.875	0.020	0.105	0.592	0.133	0.043	0.232	0.948	0.10
			0.601	0.130	0.042	0.227		

Table 6.2: *Parameters of the density model: when two values are given, the upper (lower) line corresponds to the $|+\rangle$ $(|-\rangle)$initialized case. α_{ent}, α_{ninit} and α_{op} were extracted from a decision tree model, which was based on the distribution of the electron spin population after NV centre initialization and the spin-flip probability per excitation pulse (13.5 %, but neglecting decay to the metastable state). Microwave pulse imperfections and optical cross talk were not considered due to their small influence. α_{nv}, α_{uc}, α_{scat} and α_{probe} were determined by calibration measurements and/or extracted from the entangling measurements. C_{RO} is the spin readout contrast and p_{ld} is the probability for a phase change through the laser.*

state and thereby reduce visibility) with corresponding fraction α_{ninit}, and a classically mixed density ρ_{mix} that is fed by various erroneous processes that may happen during the entangling routine with a fraction of α_{op}. These processes were traced with a decision tree model, which yielded the mixed character.

The events not related to the NV centre consisted of the uncorrelated background/dark counts described by α_{uc}, leaked scattered light from the resonant excitation α_{scat}, and α_{probe} takes into account the elevated background due to the operation of the probing field for interferometer phase readout.

Further, the finite coherence length of the laser and random changes thereof were included on the phase dependent parts of the density. Those consisted of the entangled state, the wrongly initialized part, the scattered light and the leaked light from the probing field (which was phase shifted by the AOM operation frequency of 350 MHz). If the laser phase changes between needle excitation pulses, this phase change is imprinted on the spin-photon state. Inclusion into the model leads to an update of all phase dependent processes by

$$\tilde{\rho}_{event}(\varphi) = (1 - p_{ld})\ \rho_{event}(\varphi) + p_{ld}\ \rho_{event}^{dephase} + \rho_{other}, \tag{6.30}$$

where the phase dependence was made explicit. p_{ld} is the probability for a laser phase change and was calculated from the interferometer visibility. $\rho_{event}^{dephase}$ was the fraction of dephased events, which was then averaged over all phases. ρ_{other} is the unaffected part.

With $\tilde{\rho}_{event}(\varphi)$, we investigated the visibility V of oscillations on the phase dependent

Setting	Visibility	Rel. increase in visibility	Parameter changed
Experimental conditions	0.489 (0.425)	-	-
No influence from probing field	0.581 (0.554)	0.188 (0.304)	$\alpha_{probe} = 0$
Perfect scattered light rejection	0.596 (0.600)	0.026 (0.083)	$\alpha_{scat} = 0$
Background fully removed	0.730	0.225 (0.217)	$\alpha_{uc} = 0$
Perfect state initialization	0.762	0.044	$\alpha_{ninit} = 0$
No spin mixing in ES	0.854	0.121	$\alpha_{op} = 0$
Perfect spin state readout	0.900	0.054	$C_{RO} = 1$
Infinite laser coherence	1.000	0.111	$p_{ld} = 0$

Table 6.3: *Visibility projection: experimental conditions yield theoretical visibility of the first entry for initialization into the $|+\rangle$ $(|-\rangle)$ state. In each following row, one parameter is changed to its desired value. The calculated density matrix was renormalized in every step.*

conditional probabilities.

$$V = \frac{P(\pm|E(\varphi))_{max} - P(\pm|E(\varphi))_{min}}{P(\pm|E(\varphi))_{max} + P(\pm|E(\varphi))_{min}}, \tag{6.31}$$

with

$$P(\pm|E(\varphi)) = \langle \pm, E(\varphi)|\tilde{\rho}_{event}(\varphi)|\pm, E(\varphi)\rangle \tag{6.32}$$

the probability of measuring a state $|+\rangle$ or $|-\rangle$ when a photon in an equatorial polarization state $E(\varphi)$ was detected. Ideally, for our target state $V = 1$, while for uncorrelated events, $V = 0$. The influence of the parameters listed in table 6.2 is presented in table 6.3, where parameters are switched to the desired value one after another and visibility is projected. In the experiment the observed visibility was 0.284 ± 0.014 (0.368 ± 0.014) for the $|+\rangle$ $(|-\rangle)$ start state respectively, which is smaller than the theoretical value in table 6.3, hinting at missing contributions in the model[1]. Strongest impact on visibility reduction stems from the probing field and uncorrelated light/counts. Removing all events that do not originate from the NV centre (probing field, background, dark counts and scatter) leads to $V = 0.73$. Experimental values with background subtraction gave visibilities of 0.474 ± 0.024 (0.620 ± 0.027). State initialization and readout have only minor contributions. Getting rid of spin mixing in the excited state improves V by 12 %.

---

[1]Some more contribution not included in the model could originate from the finite coherence time of the spin qubit or the imbalanced coupling ratio to the interferometer with value 0.92.

Although containing a lot of simplifications, the model makes clear how the spin-photon source can be improved most efficiently, as discussed in the following chapter.

CHAPTER 7

Outlook and Conclusion

Possible system upgrades

Some hardware upgrades could improve the situation drastically with respect to photon collection efficiency and visibility:

The polarization routing of the interferometer can be made deterministic with an optical switch. Optical elements can be upgraded and the NV centre could be placed in a cavity to improve on the fraction of emission in ZPL photons (see further down). The phase of the interferometer under active stabilization would render the probing field obsolete, which was a major source of visibility loss in the correlation signal and led to $2/3$ of data being thrown away. Spin mixing in the excited state, level cross talk and single-shot readout can be tackled by using a low crystal strain NV centre. Currently, 96% of the sequence are reserved for spin initialization. Shorter spin initialization methods are available with hardware upgrades (e.g. a second resonant laser module, for references see section 5.2).

To put it in a nutshell, we were limited to two-particle entanglement mostly by hardware. Resolving these issues, scalability of the scheme to multi-photon states can be achieved. The discussion follows in the next section.
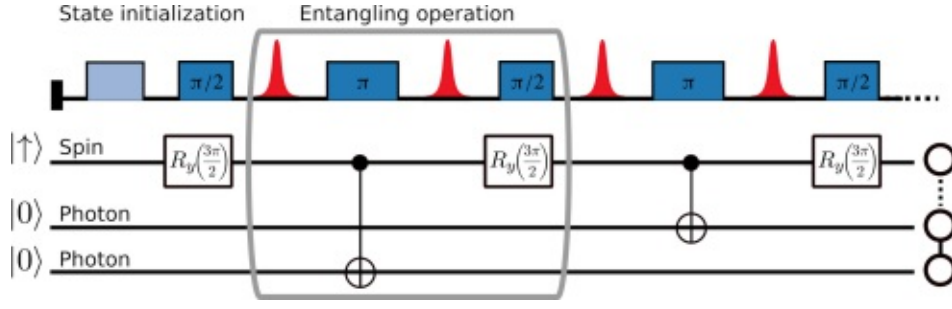
127

Figure 7.1: *Multi-photon cluster state protocol: iterating the entangling operations (grey rectangle) on an initialized spin state ($M_S = -1$) creates a new entangled photon each round. The experimental steps in the form of microwave and optical excitation pulses are illustrated in the upper part, below a circuit representation is indicated. A cluster state can be retrieved by local operations on the output qubits. The grey rectangle unit cell has been demonstrated experimentally in this work.*

Multi-photon state outlook

Iteration of the experimentally shown entangling operations generates a multi-photon linear cluster state. This couldn't be shown in the course of the work on this thesis due to the reasons discussed above. However, an outlook for the creation of such a state is given.

Experimentally, we demonstrated the creation of the spin-photon state

$$|\psi\rangle = \frac{1}{\sqrt{2}} \left(|0_S\rangle |1_P\rangle + e^{i\varphi} |1_S\rangle |0_P\rangle \right), \tag{7.1}$$

in the computational basis $|0_S\rangle = |M_S = 0\rangle$, $|1_S\rangle = |M_S = -1\rangle$, $|0_P\rangle = |H\rangle$, $|1_P\rangle = |V\rangle$. Assuming a constant phase of $\varphi = 0$, the state can be written as

$$|\psi\rangle = \left[\left(R_y\left(\frac{3\pi}{2}\right) \otimes \text{Id} \right) \text{ CNOT } \left(R_y\left(\frac{3\pi}{2}\right) \otimes \text{Id} \right) \right] |0_S\rangle |0_P\rangle, \tag{7.2}$$

with Id the identity operator. Figure 7.1 illustrates the entangling operations in the form of a circuit diagram. Repetition of the entangling block leads to the desired multi-photon cluster state, up to local rotations on the individual qubits.

We give an outlook for hardware upgrades that would mitigate the low photon detection efficiency and the weak decay into the ZPL.

A multi-photon cluster state containing N photons and with a system detection efficiency of η can be detected at a rate of (fig. 7.2a)

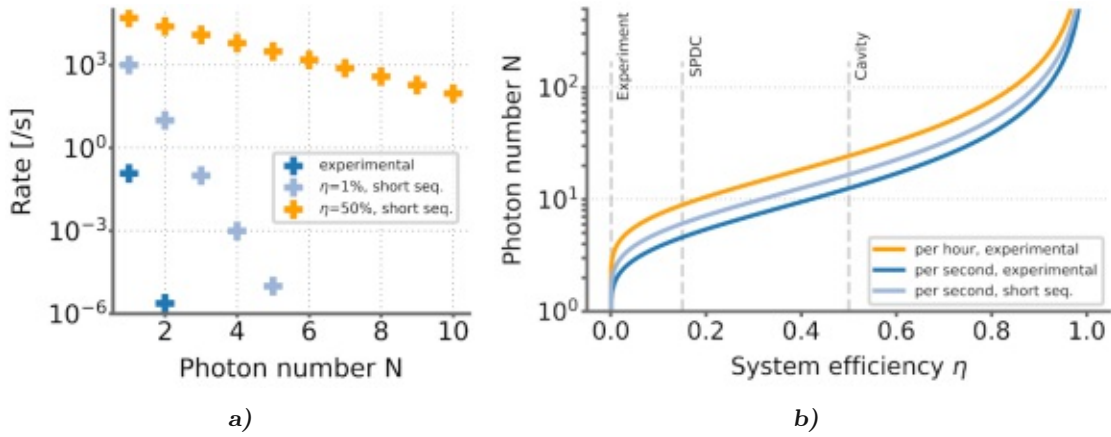$$R(N) = \frac{\eta^N}{\Delta t} = \frac{\eta^N}{t_{init} + N \cdot t_{ent}}, \tag{7.3}$$

128

Figure 7.2: *System efficiency η for multi-photon states:* **a)** *state detection rate for scenarios: experimental conditions with η of 2×10^{-5}, t_{init} of 170 µs, t_{ent} of 0.35 µs; shorted sequence with t_{init} of 10 µs, t_{ent} of 0.05 µs and two different system efficiencies.* **b)** *The photon number of the created and detected state per second (or hour) for experimental conditions and with shorted sequence. Indicated are system efficiencies of the experimental setup, of SPDC sources and an outlook for cavity integration (discussed in the text below).*

with Δt the timespan of a generation run, consisting of the time for state initialization t_{init} and the time for entanglement operations $N \cdot t_{ent}$. For a given rate R the number of photons is

$$N \approx \frac{log(R \cdot t_{init})}{log(\eta)}, \tag{7.4}$$

assuming that $t_{init} \gg N \cdot t_{ent}$. The system detection efficiency therefore strongly influences the maximum size of the detectable cluster state (see fig. 7.2b). This is currently limited by the ZPL emission of 2 % to 3 %. A cavity-based system may surpass this limitation by Purcell enhancement of emission into the ZPL and will beat state of the art SPDC sources [105] at a system efficiency of about 15 %.

An enhancement of the ZPL transition rate by a factor of 40 would lead to the cavity enhanced ZPL transition rate becoming comparable to the total free space decay rate. The ZPL linewidth would have doubled to a HWHM of 14 MHz, which still ensures detuning from the neighbouring resonance 870 MHz away (high crystal strain NV centre). One can go even further in a low crystal strain centre, where the splitting between transition frequencies exceeds 2 GHz, and application of a strong axial magnetic field (>3000 G) increases the splitting to almost 3 GHz (see fig. 7.3a, numerical values for calculation taken from Bassett et al. [10]).

In this case, a Purcell enhanced centre in a resonator with cavity efficiency of 90 %
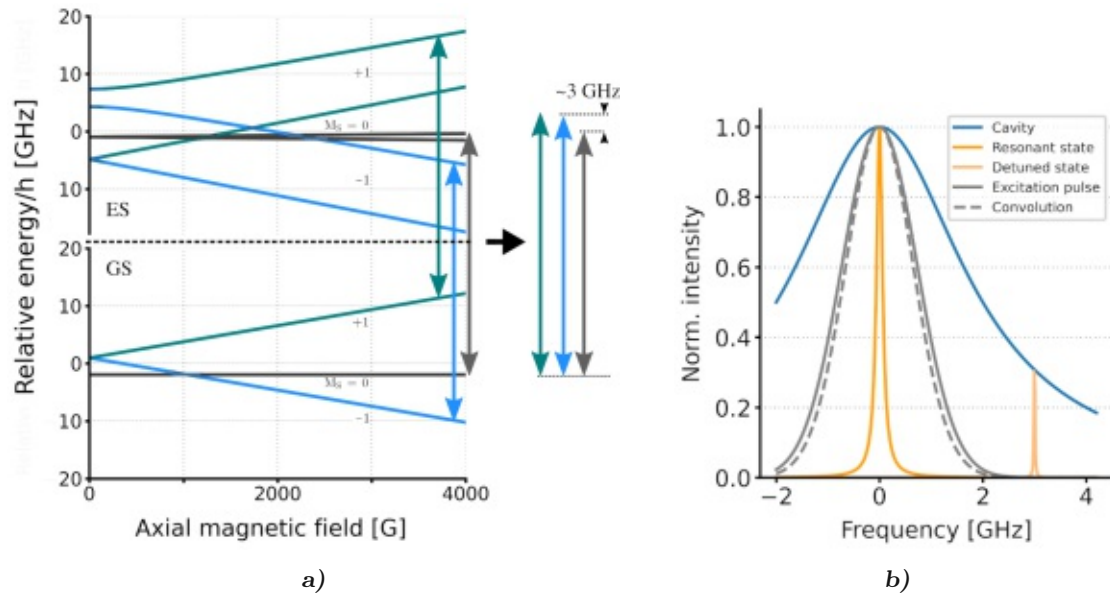
129

Figure 7.3: a) *Achievable frequency spacing of transitions by application of a strong axial magnetic field.* **b)** *Two transitions shown in a cavity setting, one resonant and strongly Purcell enhanced, the other detuned by* 3 GHz. *The shape of the Gaussian excitation pulse is altered only slightly (dashed line) by the Lorentzian cavity line shape.*

(emission rate into the cavity over total emission) has a HWHM of 70 MHz and a lifetime of 1.1 ns (see fig. 7.3b). With adaption to shorter duration optical excitation pulses, the fluorescence can still be extracted efficiently by temporal filtering of excitation and fluorescence light. A Gaussian pulse with a linewidth of 1.275 GHz allows to collect over 60 % of the enhanced fluorescence decay. An efficiency η larger than 50 % is therefore in reach once sufficiently good cavity systems become available[1]. The interferometer delay time may be shortened due to the faster fluorescence decay time. Assuming a reduced NV preparation time t_{init} of 10 µs and a reduced entanglement generation time t_{ent} of 50 ns, a five-photon state could be detected every 330 µs and a ten-photon state every 11 ms.

Conclusion

We have created and characterized a source for entangled spin-photon states as a building block for linear cluster state production, with an adapted version of to the proposal of

---

[1]Currently, state of the art systems have a ZPL enhancement of around 40, leading to a reduction in lifetime by a factor of 2 [83, 103].

Lindner and Rudolph [61], using an imperfect emitter - in the concrete form of an NV centre with high crystal strain. We compensated the imperfections with a time domain approach for state creation and using a TPC, transforming the state into the useful polarization basis. This method relaxed several constraints on the properties of the emitter. In principle the devised scheme is not emitter specific, so that other systems with strong single optical transitions may become useful sources for entangled states using the TPC protocol.

The basic entangling operation block for linear cluster state generation was demonstrated successfully, with the resulting two-particle entangled state having a fidelity which exceeded the classical bound of 0.5 by more than six standard deviations.

Furthermore, we analyzed and quantified system limitations, especially in view of scaling up the entangled state to a linear chain. These limitations were of a technical nature: a low photon collection efficiency, dominant decay into the PSB and lengthy spin initialization. These may be overcome in the near future - by integration of the centre into an optical resonator, the ZPL emission can be strongly enhanced. Likewise, there are known solutions for fast electron and nuclear spin state initialization if a single-shot readout mechanism is available [71, 85].

In the course of the project we developed a quantum toolbox for working with high strain NV centres, by using the high electron and nuclear spin flip rates to manipulate and initialize the centre. Another important component consisted in the design and creation of a high performance pulse generator based on FPGA technology, featuring conditional logic for sequence play control.

Concluding, our demonstration offers a new approach for linear cluster state creation. Going a step further and with some adaption, two dimensional graph states may be within reach by usage of the NV centre's nuclear spin, underlining the role of quantum emitters as interesting candidates for quantum information and communication technology [79, 87].

APPENDIX A

C_{3v} **Group Definition**

The appendix, relating to section 3.2.1, contains information on the general definition of a group, the C_{3v} group multiplication table and a derivation of suitable eigenfunctions for the C_{3v} group from single electron orbitals.

C_{3v} **group definition**

To confirm that the operations introduced in section 3.2.1 really constitute a group, these have to comply with the defining elements of a group [99]. A group is

1. a set of elements that according to the group multiplication law have products that are again elements of the group (it is closed under multiplication),

2. the elements are associative $A(BC) = (AB)C$,

3. there exists a unit element E so that $EA = A$,

4. there is an inverse element to each group member so that $AA^{-1} = E$.

Putting the above introduced operations into a table form, whereby the entries symbol the multiplication of the row value with the column value, one derives a multiplication table for the group. Since the entries are all elements of the group one immediately confirms that the set is closed under multiplication (table A.1).

The six group elements satisfy the remaining properties for groups as well.

133

C_{3v}	E	C_+	C_-	σ_1	σ_2	σ_3
E	E	C_+	C_-	σ_1	σ_2	σ_3
C_+	C_+	C_-	E	σ_3	σ_2	σ_1
C_-	C_-	E	C_+	σ_2	σ_3	σ_1
σ_1	σ_1	σ_2	σ_3	E	C_+	C_-
σ_2	σ_2	σ_3	σ_1	C_-	E	C_+
σ_3	σ_3	σ_1	σ_2	C_+	C_-	E

Table A.1: C_{3v} *group multiplication table.*

Group theory approach to system eigenfunctions

Two group elements are conjugate when they can be transformed into each other by similarity transformations

$$B = XAX^{-1}, \tag{A.1}$$

where B is conjugate to A by another group element X. Performing such transformations on all group elements leads to distinct classes of elements that can be transformed into each other via similarity transformations. These classes C have the feature that the trace is constant for all elements within, since it is invariant under such transformations. The trace over the j-th IR Γ of the class of the representation R

$$\text{Tr}\left\{\Gamma^{(j)}_{(C_R)}\right\} = \chi^{(j)}(C_{(R)}), \tag{A.2}$$

is called the character χ of the class. It is shown in Tinkham [99] that it is sufficient to know about χ of classes of a group to perform a projection with a projector corresponding to the j-th IR of type

$$P^{(j)} = \frac{l_j}{h} \sum_R \chi^{(j)*}_{(R)} P(R), \tag{A.3}$$

in order to retrieve suitable basis states from the dangling bond orbitals. Here, $P(R)$ is an operator for the representation R, the $\chi^{(j)}_{(R)}$ are characters corresponding to the j-th IR, h is the number of group elements and l_j the dimension of the representation. A table listing the characters of the representations for each class in the group can be composed by calculating the traces (table A.2).

C_{3v}	C_1	$2C_2$	$3C_3$
$\chi_{(A_1)}^{(1)}$	1	1	1
$\chi_{(A_2)}^{(2)}$	1	1	-1
$\chi_{(E)}^{(3)}$	2	-1	0

Table A.2: *Character table of the C_{3v} group: columns are the three classes of the group (number relates to group elements in the class), while rows indicate the belonging IR.*

By using $P^{(j)}$ on the dangling bond orbitals ρ_k, states $\psi_k^{(j)}$ can be derived

$$
\begin{aligned}
\psi_k^{(j)} = P^{(j)}\rho_k &= \frac{l_j}{h}\sum_R \chi_{(R)}^{(j)*}P_{(R)}\rho_k \\
&= \frac{l_j}{6}\left[\chi_{(E)}^{(j)}E + \chi_{(C+)}^{(j)}C_+ + \chi_{(C-)}^{(j)}C_- + \chi_{(\sigma_1)}^{(j)}\sigma_1 + \chi_{(\sigma_2)}^{(j)}\sigma_2 + \chi_{(\sigma_3)}^{(j)}\sigma_3\right]\rho_k,
\end{aligned}
\tag{A.4}
$$

which transform according to the C_{3v} group:

$$
\begin{aligned}
\psi_1^{(1)} = P^{(1)}\rho_1 &= \frac{1}{3}\left(\rho_1 + \rho_2 + \rho_3\right) \\
&= \psi_2^{(1)} = \psi_3^{(1)}, \\
\psi_N^{(1)} = P^{(1)}\rho_N &= \rho_N \sim \psi_N^{(3)}, \\
\psi_1^{(2)} = P^{(2)}\rho_1 &= 0 = \psi_2^{(2)} = \psi_3^{(2)} = \psi_N^{(2)}, \\
\psi_1^{(3)} = P^{(3)}\rho_1 &= \frac{1}{3}\left(2\rho_1 - \rho_2 - \rho_3\right), \\
\psi_2^{(3)} = P^{(3)}\rho_2 &= \frac{1}{3}\left(2\rho_2 - \rho_1 - \rho_3\right), \\
\psi_3^{(3)} = P^{(3)}\rho_3 &= \frac{1}{3}\left(2\rho_3 - \rho_1 - \rho_2\right),
\end{aligned}
\tag{A.5}
$$

assuming there is no overlap between orbitals to form these linear combinations. Clearly these states are not yet orthogonal, so that

$$
\int dx\,\psi_k^{(j)}\psi_l^{(i)} \neq 0.
\tag{A.6}
$$

To construct orthogonal states from the states resulting from the third IR we see that

$$
\psi_1^{(3)} = -\left(\psi_2^{(3)} + \psi_3^{(3)}\right).
\tag{A.7}
$$

Two states consisting of $a + b$ and $a - b$ will be orthogonal to each other, thus picking

$$\begin{aligned}
\psi_A &= -\left(\psi_2^{(3)} + \psi_3^{(3)}\right) = \psi_1^{(3)}, \\
\psi_B &= -\psi_2^{(3)} + \psi_3^{(3)} = \rho_3 - \rho_2,
\end{aligned} \tag{A.8}$$

fulfills the requirement. Normalizing the four derived states yields the basis

$$\begin{aligned}
a_C &= \frac{1}{\sqrt{3}}\left(\rho_1 + \rho_2 + \rho_3\right), \\
a_N &= \rho_N, \\
e_x &= \frac{1}{\sqrt{6}}\left(2\rho_1 - \rho_2 - \rho_3\right), \\
e_y &= \frac{1}{\sqrt{2}}\left(\rho_3 - \rho_2\right).
\end{aligned} \tag{A.9}$$

From group theoretical considerations it is known that the number of IRs is indicative of the number of distinct energy levels. This leads to three energy levels in the case of our IR with the four derived basis states at hand, but the ordering of states cannot be predicted using this approach [99].

After the appendix the main text continues with the ordering of the derived energy levels in section 3.2.2.

Lith Pulser System Details

This appendix delves into the inner workings of the FPGA based Lith pulser introduced in chapter 4.2.

System details

1 ns time resolution despite the FPGA's 125 MHz frequency domain: The FPGA clock fabric works at 125 MHz, which means a clock cycle takes 8 ns. To get to a time resolution of 1 ns, in one clock cycle, output for 8 ns has to be prepared in parallel. The digital channel output is generated by a dedicated serealizer per output channel, which operates at 500 MHz with the option of double data rate, whereby it achieves a signal output at 1 GHz. Both time domains were carefully synchronized.

The memory layout: Considering the above specified feature of full output channel pattern change at every ns instance, the system memory needs to be able to extract the necessary information on time. One memory access can be done per clock cycle, therefore memory was split into eight separate blocks that can all be accessed in parallel within a single eight ns FPGA cycle. Each memory block then relates to a single ns increment within the eight ns unit, visualized in figure B.1a. Timestamps corresponding to channel pattern changes may be stored in memory as <absolute time in sequence, channel pattern> entries. To be mapped to the desired ns time increment, the timestamps-channel entries are sorted into the right memory block by calculating the timestamp value modulo
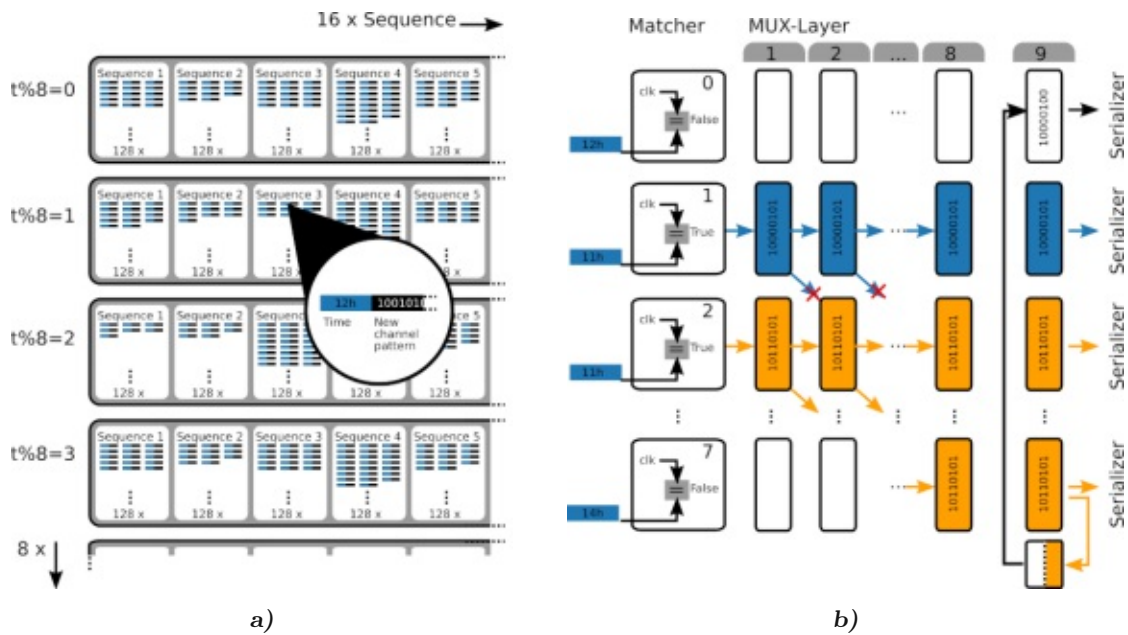
Figure B.1: **a)** *Memory layout: <absolute time in sequence, channel pattern> entries are stored by their three least significant bits (modulo eight operation) and by the sequence they belong to, to ensure memory access within a single clock cycle eight nanosecond period.* **b)** *Eight matcher modules, one per memory block, retrieve the next stored timestamp and compare it to the current clock cycle count in the 125 MHz domain. On a match (True) the respective channel pattern is propagated to the multiplexer unit (MUX). Each cell of the MUX transports matched events to the next layer and to the next layer cell corresponding to plus one ns (one down). When a cell obtains two matches as inputs, it accepts and further propagates the 'newer' match from the higher number matcher. At layer nine, empty cells are filled up with the the last ouput pattern from the previous clock cycle stored in a separate slot each round.*

eight. Each memory block has address ranges in registers for up to 16 sequences and per sequence there is space for 128 time-channel entries, which means that in principle more than the specified 128 commands per channel can be programmed per sequence (up to 8*128), as long as there is at maximum 128 entries per memory block.

Matcher operation and multiplexing of matches: A matcher module exists once per memory block (eight times in total) as shown in figure B.1b. The matcher compares the currently pointed at timestamp from memory with the current system time clock cycle. If it matches it reacts by handing the corresponding new channel pattern to the multiplexer. On such a match the register address is then increased to the next timestamp in the memory.

The matched channel patterns are sent to a multiplexing grid consisting of nine layers.
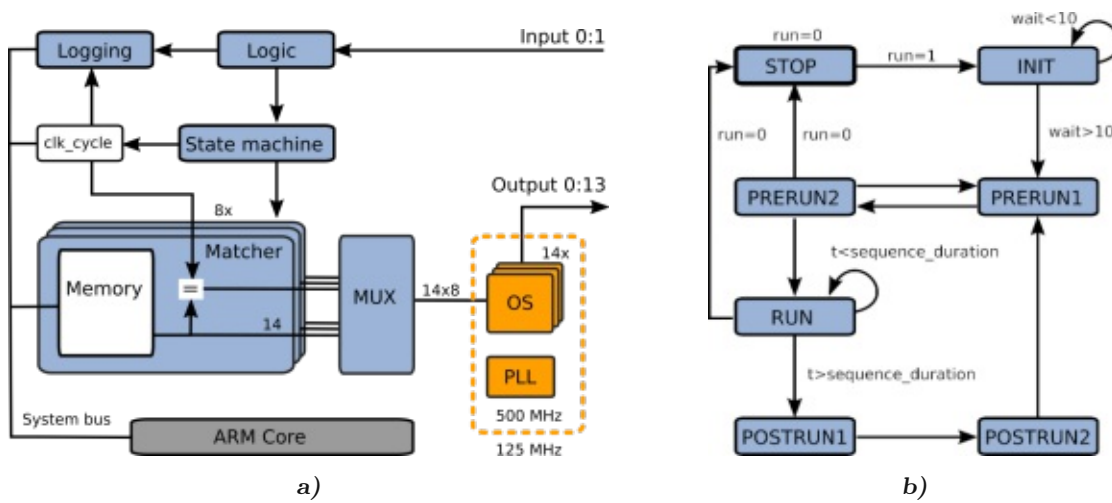
Figure B.2: *Lith pulser system overview and state machine.* **a)** *Two frequency domains are present in the system, one with 125 MHz (blue) and one with 500 MHz (orange), synchronized via a phase-locked loop (PLL). The input on two channels is taken by the logic module and processed to be logged and used by the state machine. The state machine keeps the variable clk_cycle up to date with the current system clock cycle count and controls the state the system is in (see fig. b). Output serializers (OS) write the prepared channel patterns from the MUX to the respective channels.* **b)** *Overview of the internal state machine: system is in STOP mode when the run variable is zero. Run = 1 switches into a INIT phase where counters and the logging buffer are reset (takes ten clock cycles). Thereafter, in the PRERUN1 state the next due sequence is determined. In state PRERUN2 the sequence is initialized. When in PRERUN2 no chosen sequence to run is present it will fall back to PRERUN1. RUN state is running the sequence, an optional logical decision is evaluated in the POSTRUN1 state and the sequence parameters are updated in POSTRUN2 state.*

In the multiplexer layers the output patterns changes are propagated to the serializers to produce a continuous output signal. The protocol is illustrated in figure B.1b. A grid with a depth of eight layers allows a matched channel pattern to be passed on to later time slots. Each cell in the grid checks if a new matched pattern from the layer before is present. In layer eight some slots might be filled with new matches while some may still be empty, happening when there was no pattern change within the eight ns period. The empty cells are filled in layer nine of the grid with the last output pattern from the cycle before, which was stored in a separate memory. As the multiplexer has nine layers, a global time delay form input to output on all channels of $9 \times 8\text{ns}$ is present. The exiting channel output patterns are then serialized to the output channels.

139

Logical decisions, logging and the state machine

The logic module performs the counting of input channel events for logical decisions. Logging of sequence parameters may be enabled, whereafter the logging module provides information on sequence start times and execution order as well as digital input channel counts. The system layout is shown in figure B.2a.

The state machine includes all the necessary control logic of the design. The structure and an overview is given in figure B.2b.

Pulser performance

Bandwidth: The bandwidth of the pulser was established with short gate signals being sent to trigger an AWG, Agilent 33622A, sensitive to a trigger signal level of $2\,\mathrm{V}$. From this, a lower bound on the output bandwidth of about $170\,\mathrm{MHz}$ was observed. A smaller trigger signal level of $1\,\mathrm{V}$ yielded $200\,\mathrm{MHz}$ bandwidth. In the measurement a homebuilt breakout board was connected to the the STEMLab board, therefore bandwidth is given as a lower bound.

Temporal jitter: The periodic temporal jitter $J_P = T_P(N) - T_0$, with $T_P(N)$ the time between rising and falling gate flanks of the N-th gate and T_0 the ideal gate duration, was measured sending the signal from an output channel set with a long sequence of regularly spaced identical gates to a time-tagging module (Roithner LaserTechnik TTM8000) with $82.3045\,\mathrm{ps}$ time resolution. The outcome is shown in figure B.3a. Accumulated jitter, causing a relative shift within a long sequence of gates in time, may be accounted for by sequence specification.

Conditional logic and play control

To understand the operation of the play control mechanisms introduced above better, these are illustrated by three examples:

Time out control - sequential play: Three sequences A, B and C, with durations t_A, t_B and t_C, are written to the pulser, intended to be played one after another (fig. B.3b 1). To accomplish this behaviour, it is sufficient to specify the time out values $T_{to}(N)$ of
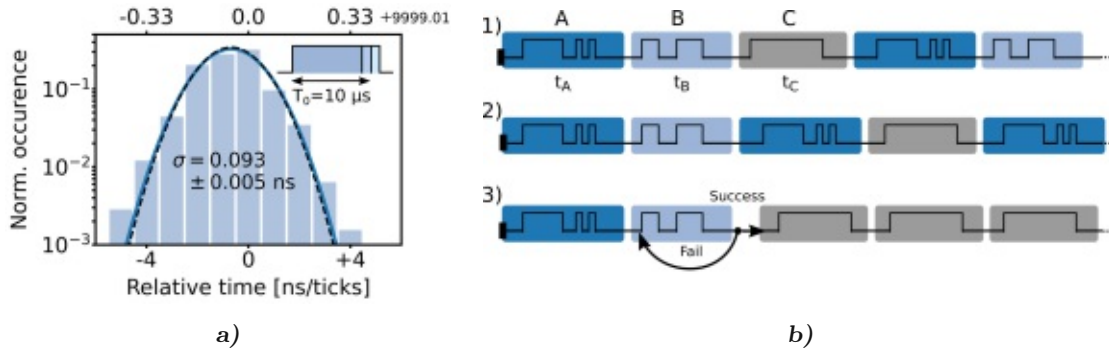
140

Figure B.3: a) *Periodic jitter: distribution of relative pulse durations for a nominal duration T_0 of gates of 10 µs. The normal distribution fit has a standard deviation of 0.093 ns. As a reference the clock signal of the time-tagging module was measured and fit (dashed black line). No relevant broadening of this curve was observed related to the pulser. The nanosecond offset of measured pulse duration versus the specified one is thought to be caused by the real shapes of rising and falling flanks.* **b)** *Sequence play control use cases (see text): 1) time out control with sequential play, 2) time out control with aperiodic play, 3) real-time conditional logic control of sequences.*

sequence N as:

$$T_{to}(A) \in [t_B + t_{switch} + 1clk, t_B + t_C + 2 \cdot t_{switch} + 1clk - 1], \tag{B.1}$$

$$T_{to}(B) \in [1clk, t_A + t_C + 2 \cdot t_{switch} + 1clk - 1], \tag{B.2}$$

$$T_{to}(C) = 0, \tag{B.3}$$

with sequence priorities $A > B > C$, t_N the duration of sequence N, t_{switch} the constant switch time in between sequences of 48 ns and $1clk$, a single 8 ns span of the clock cycle.

Time out control - aperiodic play: A play pattern of ABACAB... (see fig B.3b 2) is achieved by setting the time-outs to

$$T_{to}(A) \in [1clk, min(t_B, t_C) + t_{switch} + 1clk - 1], \tag{B.4}$$

$$T_{to}(B) \in [t_A + t_{switch} + 1clk, 2t_A + t_C + 3 \cdot t_{switch} + 1clk - 1], \tag{B.5}$$
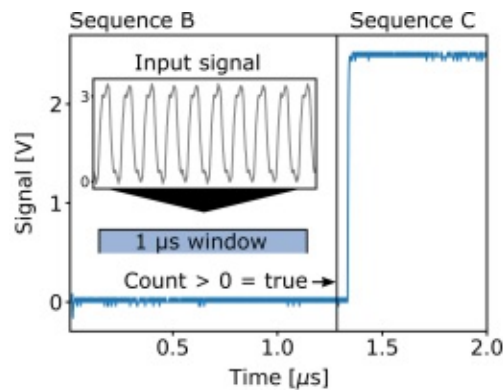
$$T_{to}(C) = 0. \tag{B.6}$$

141

Figure B.4: *Oscilloscope trace showing a conditional change of sequence: in a $1\,\mu s$ window within sequence B input is registered. In this case a condition was set that the registered events need to be larger than zero. The condition was met with the shown input signal, leading to the logical check at the sequence end to be passed to progress to sequence C. Sequence C was programmed to show a rising signal in the oscilloscope trace, thereby confirming the conditional sequence change.*

Real-time conditional logic control of sequences. In this example the action of time out control / sequence priorities combined with conditional logic is enlightened. Assume a case where the first sequence A is supposed to be played only once to initialize a state. Then a second sequence B needs to be played until a certain state is successfully confirmed, before proceeding to an experimental sequence C, which is then repeated as often as possible until it is necessary to recheck if the state achieved through sequence B is still present (see fig. B.3b number 3). Play control for sequence A is done by setting this sequence with highest priority and infinite time out. Second highest priority goes to sequence B, which is then executed right after sequence A was played once. Sequence B receives a conditional logic setting by specifying a time window within which a signal connected to a digital input will be monitored. Threshold settings are entered and a logical condition that needs to be met. The sequence is now being repeated as long as the logic gate is not fulfilled. Once fulfilled, the sequence repetition ceases and the time out counter for sequence B is refreshed, allowing the system to progress to sequence C. An oscilloscope trace of this example case is shown in figure B.4. Sequence C will receive a time out setting of 'always times out' and therefore is repeated as long as sequence B has not timed out again, by the power of sequence priorities. The time out of sequence B induces a rechecking of the state. After this appendix, the main text continues with a description of the hard- and software structure in section 4.2.2.

APPENDIX C

Electro-optic Retardation

The appendix treats concepts touched in section 4.4.3, concerning the origins of electro-optic retardation, in more detail.

Electro-optic retardation

To understand the operation of the EOM devices better, the electro-optic Pockels effect is discussed shortly. In the case of $LiNb0_3$, the change in refractive index due to the electric field is linear. The effect is only present in crystals that do not have inversion symmetry (like $LiNb0_3$), which can be argued by looking at symmetric crystals. Assuming a linear relation coefficient s between the refractive index nnd the electric field E,

$$\Delta n_1 = sE, \tag{C.1}$$

and for a reversed field

$$\Delta n_2 = s(-E). \tag{C.2}$$

But such a crystal must be physically equal in both orientations, so that

$$\Delta n_1 = \Delta n_2 \rightarrow s = 0. \tag{C.3}$$

The conclusion being that no linear electro-optic effect can be present [111, p. 327].

The electric field of light inside an anisotropic dielectric material has a polarization vector with components

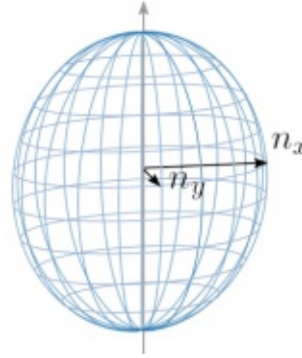$$P_i = \sum_{j=1}^{3} \varepsilon_0 \chi_{ij} E_j, \tag{C.4}$$

143

Figure C.1: *Ellipsoid spanned by refractive indices. Light propagating in vertical direction has the field vector in the xy-plane experiencing a refractive index in the range of n_x to n_y, when $n_x < n_y$.*

with ε_0 the vacuum permittivity and where the χ_{ij} are spanning the susceptibility tensor. Polarization is allowed to not be aligned with the field any more. The consequence being a changing electric permittivity with crystal direction, leading to anisotropic phase velocities v_{ph}, for a certain crystal direction given by

$$v_{\mathrm{ph}} = \frac{c}{n} = \frac{c}{\sqrt{\varepsilon_r}}, \tag{C.5}$$

with ε_r the relative permittivity. The overall relative permittivity is a 3 by 3 tensor, which can be diagonalized to reduce entries to three values, translating to three different refractive indices present. Geometrically, a 2D surface spanned by a body with three different orthogonal principal axes is an ellipsoid. Orienting the coordinate axes along the principals axes of the ellipsoid and scaling them with the respective refractive indices yields (fig. C.1)

$$\frac{x^2}{n_x^2} + \frac{y^2}{n_y^2} + \frac{z^2}{n_z^2} = 1. \tag{C.6}$$

An externally applied electric field along a certain principal axis will lead to a linear change of the refractive index by the electro-optic effect. A Taylor expansion of n to the linear term

$$\tilde{n} = n + \left.\frac{dn}{dE}\right|_{E=0} E, \tag{C.7}$$

relates to a linear change k_E in refractive index of

$$\Delta n = \tilde{n} - n = \left.\frac{dn}{dE}\right|_{E=0} E = k_E \cdot E. \tag{C.8}$$

144

The ellipsoid axes change as

$$\Delta\left(\frac{1}{n^2}\right) = -\frac{2}{n^3}\Delta n = -\frac{2}{n^3}k_E \cdot E = r \cdot E, \tag{C.9}$$

with r being the electro-optic parameter for the direction. More generally

$$\Delta\left(\frac{1}{n_i^2}\right) = \sum_{j=1}^{3} r_{ij}E_j, \tag{C.10}$$

with r_{ij} the electro-optic tensor [111, p. 326 ff.].

The strongest change in refractive index of LiNbO$_3$ occurs in the crystallographic z-direction [109], which has to be aligned with the input field polarization for proper operation, and amounts to

$$\begin{aligned}
r &= -\frac{2}{n^3}k_E, \\
k_E &= -\frac{n^3}{2}r, \\
\Delta n &= k_E \cdot E = -\frac{1}{2}n^3 r E, \\
\Delta n_z &= -\frac{1}{2}n_z^3 r_{zz}E_z = -\frac{1}{2}n_z^3 r_{zz}\frac{V_z}{d},
\end{aligned} \tag{C.11}$$

with V being the voltage, d the distance of the electrodes on the crystal and r_{zz} the electro-optic coefficient of $33\,\mathrm{pm\,V^{-1}}$ [47].

APPENDIX D

The Spin Model Matrix $\hat{M}$

The next page shows the transfer matrix introduced in chapter 5.3 for modelling dynamics of optical depletion gates in the basis:

$\{(M_S, M_I)\} =$

$(-1,-1), (-1,0), (-1,+1), (0,-1), (0,0), (0,+1), (+1,-1), (+1,0), (+1,+1).$

APPENDIX D. THE SPIN MODEL MATRIX $\hat{M}$

$$
\left[\begin{array}{ccc:ccc:ccc}
-k_{s10}-k_{s11}-2k_{\bar{1}1} & k_{\bar{1}1} & k_{\bar{1}1} & k_{s01} & 0 & 0 & k_{s11} & 0 & 0 \\
k_{\bar{1}1} & -k_{s10}-k_{s11}-2k_{\bar{1}1} & k_{\bar{1}1} & 0 & k_{s01} & 0 & 0 & k_{s11} & 0 \\
k_{\bar{1}1} & k_{\bar{1}1} & -k_{s10}-k_{s11}-2k_{\bar{1}1} & 0 & 0 & k_{s01} & 0 & 0 & k_{s11} \\
\hdashline
k_{s10} & 0 & 0 & -2k_{s01}-2k_{\bar{0}0} & k_{\bar{0}0} & k_{\bar{0}0} & k_{s10} & 0 & 0 \\
0 & k_{s10} & 0 & k_{\bar{0}0} & -2k_{s01}-2k_{\bar{0}0} & k_{\bar{0}0} & 0 & k_{s10} & 0 \\
0 & 0 & k_{s10} & k_{\bar{0}0} & k_{\bar{0}0} & -2k_{s01}-2k_{\bar{0}0} & 0 & 0 & k_{s10} \\
\hdashline
k_{s11} & 0 & 0 & k_{s01} & 0 & 0 & -k_{s10}-k_{s11}-2k_{\bar{1}1} & k_{\bar{1}1} & k_{\bar{1}1} \\
0 & k_{s11} & 0 & 0 & k_{s01} & 0 & k_{\bar{1}1} & -k_{s10}-k_{s11}-2k_{\bar{1}1} & k_{\bar{1}1} \\
0 & 0 & k_{s11} & 0 & 0 & k_{s01} & k_{\bar{1}1} & k_{\bar{1}1} & -k_{s10}-k_{s11}-2k_{\bar{1}1}
\end{array}\right]
$$

Figure D.1: *Transfer matrix.*

APPENDIX E

Interferometer phase tomography

The appendix details the principles and processes involved to extract the phase related to an entangling photon event through tomography of a light field probing the interferometer phase.

Principle of light polarization tomography through a probing field

Tomography setup. Setting up a four-port tomography stage for phase readout required two arms with two detectors each, one chosen to project onto D/A and one for R/L. In general an arm consisted of a quarter-wave plate, a half-wave plate, a PBS, as well as two SPCMs. The action of this setup is demonstrated using the Poincaré-sphere representation shown in figure E.1. The quarter-wave plate rotates the incoming photon into the plane of operation of the half-wave plate, to linear polarization states. The half-wave plate rotates the state into the measurement basis, where a PBS then separates the H and V parts. The horizontal part is transmitted while the vertical part is reflected into a detection port.

The layout of the two tomography arms in the setup is shown in figure 6.3. On exiting the interferometer, the photons were split by a 50:50 beam splitter. In both tomography arms, the beams that were reflected by a PBS, had another polarizing element installed afterwards to improve polarization, which degraded on reflection. To reduce coupling losses, light was coupled into multi-mode fibres (Thorlabs M42L02, $50\,\mu\mathrm{m}$ core)
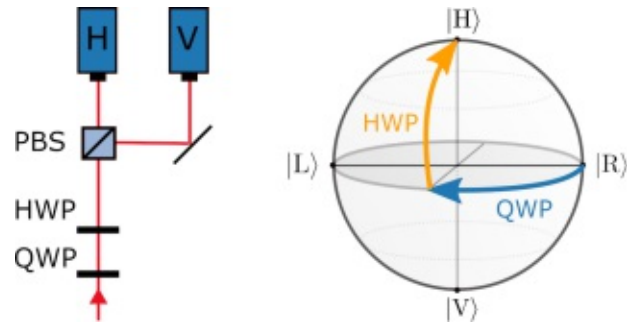
149

Figure E.1: *Photon polarization tomography stage: operation principle for measuring in R/L basis is shown on the Poincaré sphere. The $|R\rangle$-basis state, that the light was supposed to be projected onto, was transformed by the wave plate actions to $|H\rangle$. For the D/A basis the quarter-wave plate was omitted.*

wrapped in tinfoil for ambient scattered light suppression, before reaching the detectors. All elements of the tomography stage were put into a light shielding box, so that the background signal per SPCM was about 50 counts per second.

A probing field. Two questions had to be answered relating to probing the interferometer phase: what kind of light should be used to probe the phase, and is it feasible to use SPCMs as detectors?

In principle, scattered light could be used to perform the phase measurement, but since the aim in the experiment was to suppress it, it didn't suffice. A split-off path from the red excitation laser was coupled into the interferometer with a probing field (see figure 6.3), giving flexibility in the amount of power to send through and being of almost the same frequency as the experimental photons. A slight frequency difference was to be expected, as the probing field light passed an AOM for amplitude switching.

To determine whether SPCMs were suitable detectors, two constraints were examined: the count rate needed to reduce shot noise to an acceptable level while not introducing too many adverse effects (afterpulsing, etc.) and how short the temporal integration window had to be to track the phase accurately. Those issues were interwoven, shortening the integration window would lead to a more accurate phase readout but the number of photons decreases, leading to a higher phase error from shot noise. An optimum in this trade-off had to be found.

Measuring the probing field at one tomography port with a fast photo diode resulted in a time trace, consisting of slow oscillation with high frequency contributions on top,
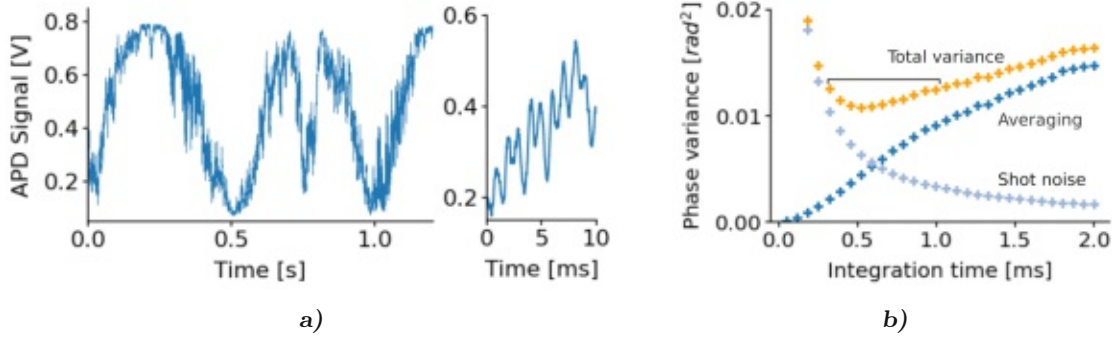
Figure E.2: *Interferometer phase oscillations and phase readout error:* **a)** *free running interferometer signal, measured with a fast avalanche photodiode (APD) at a single tomography port, where slow oscillations with high frequency oscillations on top became visible. On the right side the timescale of the fastest phase changes in the millisecond range is shown.* **b)** *The variance of the phase due to the APD signal integration time consists of contributions from shot noise and signal averaging, shown at a phase $\phi = \pi/2$ with the highest expected error. The signal was assumed with a maximum of $600\,\mathrm{kcts\,s^{-1}}$ for shot noise determination. The averaging error was extracted from the APD measurement in fig. a). Lowest phase error between $0.3\,\mathrm{ms}$ to $1\,\mathrm{ms}$ integration time.*

as shown in figure E.2a. A Fourier analysis of frequency contributions revealed high frequency phase noise that would be untraceable with a SPCM. Measures were taken to slow these oscillations down into an operable range, by boxing and insulating the interferometer.

To optimize the integration time, the photo diode trace was analyzed for the time-averaging error on the phase σ_{AVG} by chopping the signal into pieces using different integration times. The shot noise error σ_N, resulting from a given integration time and photon signal amplitude, was considered simultaneously. Then the total phase variance is

$$\sigma_\phi^2 = \sigma_N^2 + \sigma_{AVG}^2. \tag{E.1}$$

With the photon detection function

$$D(\phi) = N_0 \cdot \Delta t \cdot cos^2(\phi/2), \tag{E.2}$$

where N_0 is the maximum photo detection rate and Δt the integration time,

$$\sigma_\phi^2 = \left(\frac{\partial D}{\partial \phi}\right)^{-2} \cdot \Delta D^2 = \left(\frac{\partial D}{\partial \phi}\right)^{-2} \cdot (\sigma_N^{'2} + \sigma_{AVG}^{'2}). \tag{E.3}$$

The first term was evaluated analytically with

$$\sigma_N^{'} = \sqrt{D} = \sqrt{N_0 \cdot \Delta t} \cdot cos(\phi/2), \tag{E.4}$$
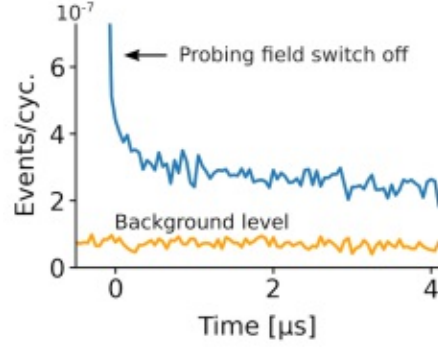
151

Figure E.3: *The background increase due to the probing field causes elevated SPCM after-pulsing.*

as

$$\left(\frac{\partial D}{\partial \phi}\right)^{-2} \cdot \sigma_N'^2 = \frac{1}{N_0 \cdot \Delta t \cdot sin^2(\phi/2)}, \tag{E.5}$$

while the second term was derived from measurement. Both were investigated for the position with the largest gradient in the photon detection rate,

$$\left|\frac{\partial D}{\partial \phi}\right| = N_0 \cdot \Delta t \cdot cos(\phi/2) \cdot sin(\phi/2), \tag{E.6}$$

at $\phi = \pi/2$. Figure E.2b shows the variance contributions versus integration time at that phase angle. The total error minimum represents the optimal parameter for the integration time, for a certain amplitude of probing field light.

Ideally, the phase monitoring was done with high count rate to reduce shot noise. This was constrained by the limitations of data acquisition rate and the SPCMs count rate, both at $10^3\,\mathrm{kcts\,s^{-1}}$. Working at a high rate, a strong increase (3.5 times) of the photon background on the SPCMs was encountered. This could have been attributed to either of two origins. Firstly, probing field light leaking through the AOM into the detection window, or secondly, afterpulsing from the SPCMs. Afterpulsing seemed more likely since the elevated background was higher right after switch-off of the probing field and had a slowly decaying behaviour as shown in figure E.3. To exclude light leakage, a second AOM was installed in series with the first one in the probing field optical path. However, no improvement was detected in the background of the time trace.

Considering all the above mentioned constraints, the maximum count rate on the APDs of the tomography stage upon constructive interference was set to about $600\,\mathrm{kcts\,s^{-1}}$ with an accompanying integration time for the phase readout of $1\,\mathrm{ms}$.

152

Visibility. An irregular envelope in the slowly varying photodiode signal on the to-mography ports was noticed over time periods on the order of 30 min. The visibility V, defined by the first order correlation function with the interferometer time delay of 262 ns [94],

$$V = \frac{I_{max} - I_{min}}{I_{max} + I_{min}} = \left| g^{(1)}(\tau = 262 ns) \right|, \tag{E.7}$$

and I the intensity, therefore showed spontaneous drops; from over 0.85 down to only 0.5. Laser light coherence was subsequently improved by placing an additional optical isolator in front of the red laser, to remove backscattered light. Furthermore, a safety measure was integrated into the data evaluation process to drop data if the visibility was below a set threshold.

Real-time phase tagging

Establishing the experimental parameters and the feasibility of a phase readout was only one side of the medal, the other being a computational system that is capable of handling the data load. A phase readout probing field amplitude of $600 \, \mathrm{kcts \, s^{-1}}$, additionally to the other experimental data, translated to a raw data rate of about 3 GB per minute that either had to be stored or handled. Another aspect to consider was the overall time the data analysis took. A crucial point being that processing the data as fast as possible would allow to adjust experimental parameters on the fly, avoiding the necessity of lengthy repetitions later on. Since complex operations needed to be performed on the data, until the entangling results could be extracted, these issues posed a challenge.

Requirement analysis and system constraints

The most important requirements and system constraints in terms of data processing are outlined in more detail:

1. **Data handling capacity.** The first and foremost aspect to consider was the data rate of about 3 GB per minute which, to put it into perspective, is about 10 % of the raw data rate of the CERN CMS experiment[1]. The 3 GB of raw data sum up to about 30 GB per minute of data handled in all the data processing steps, or 1.8 TB per hour. Assuming a measurement takes about 10 days, this adds up to a

---

[1]`https://home.cern/science/computing/processing-what-record`

total of about 430 TB. If we just considered storing the raw data for a while until processing, we needed to be aware that a space of 1 TB on the hard drive would be filled up within 5.6 hours of measurement.

2. **System components flexibility.** The system needed a certain degree of elasticity in the components and in the communication to ideally run with the already existing hardware in the laboratory environment. Moreover, given that measurement runs can take on the order of weeks, it may at some point become necessary to change components.

3. **Real-timeness.** Without developing a suitable data processing system, data evaluation could have taken up to weeks after a measurement run had finished. In case that something in the measurement had gone wrong, it would likely not have become visible until a substantial part of the data had been analyzed. In order to avoid such situations, our approach was guided by the paradigm of real-time data processing. This means that the whole data evaluation was designed in such a way, that a current entangling rate could be estimated at a current time in the measurement.

4. **Tolerance to faults.** Since not even PhD students can be in the laboratory all day long, a certain tolerance to faults in the data processing software was considered another requirement. Especially in the first steps of processing, where the relevant data was extracted from the raw data, a failure of the system would block data acquisition within some hours, by overloading the available hard drive space.

5. **Preservation of raw data for reanalysis.** In a well run experiment, it has to be possible, to do a reanalysis of the data if needed. For the reasons mentioned above, the raw data set could not be stored as a whole. We needed means to preserve the most relevant data to allow for such a reprocessing if necessary.

6. **Complex data analysis.** The data processing required that computational procedures mustn't stall or slow down the whole system.

The details of the developed software architecture and the hardware layout used can be found in appendix F. The system met all the above demands and produced MB-sized CSV-files containing the extracted event and phase data as the output.

Phase reconstruction

With the CSV-files containing the a of entangling events, we turn to the actual process of deriving the interferometer phase for an event from the four phase readout values of the tomography ports.

The acquired phase signal from each tomography port over time had a shape comprised of the interferometer's natural random phase walk and some detection background. Due to the random walk being confined to the equator of the Poincaré sphere, the signal was expected to have a sinusoidal shape in dependence of the phase, with noise from the Poissonian detection process.

Signal normalization

The starting point in the phase reconstruction was the derivation of normalized Stokes parameter signals $\hat{S}_1$ and $\hat{S}_2$ (see equation 6.9) as

$$\begin{aligned}
\hat{S}_1 &= \frac{\hat{P}_{|D\rangle} - \hat{P}_{|A\rangle}}{\hat{P}_{|D\rangle} + \hat{P}_{|A\rangle}}, \\
\hat{S}_2 &= \frac{\hat{P}_{|R\rangle} - \hat{P}_{|L\rangle}}{\hat{P}_{|R\rangle} + \hat{P}_{|L\rangle}},
\end{aligned} \tag{E.8}$$

with the four phase signals

$$\begin{aligned}
\hat{P}_{|D\rangle} &= A_D \cos^2(\varphi/2) + B_D, \\
\hat{P}_{|A\rangle} &= A_A \sin^2(\varphi/2) + B_A, \\
\hat{P}_{|R\rangle} &= A_R \sin^2(\varphi/2 + \pi/2) + B_R, \\
\hat{P}_{|L\rangle} &= A_L \cos^2(\varphi/2 + \pi/2) + B_L.
\end{aligned} \tag{E.9}$$

including the amplitude A and background B dependent on the tomography port. These amplitude and background values had to be extracted from the measured data, which was not a trivial process due to the noise. The process developed to derive A and B is discussed, departing from a pure sine-squared-function with an offset, as shown in the solid curve of figure E.4a. It is straightforward to normalize this signal with the minimum and maximum values on the y-scale, or alternatively, preparing the discussion for the real signal, a histogram of the phase signal counts versus angle may be used. The pivoted histogram is shown in figure E.4b, representing the frequency of count-values in the sine
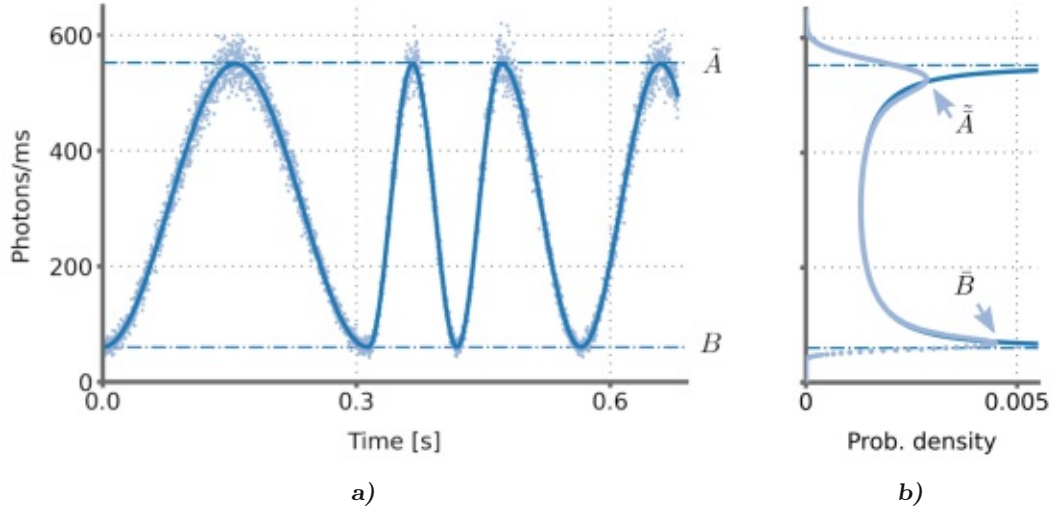
155

Figure E.4: *Phase signal normalization:* **a)** *The solid curve is a simulation of the phase signal in the form of a sine-squared function with offset and parameters similar to measurement conditions. The extrema for normalization are easily extracted as $\tilde{A}$, the amplitude plus background, and B, the background. The scatter simulates the phase signal from measurement including Poissonian noise.* **b)** *Probability density functions of the sine-squared function (dark blue) and the noisy phase signal (light blue). Probability maxima at $\bar{\tilde{A}}$ and $\bar{B}$ are shifted compared to pure sine-squared function extrema.*

curve or, in other words, the probability density function (PDF) of the sine-squared function [102]. The PDF of a function

$$y = (\tilde{A} - B)\sin^2(x) + B, \tag{E.10}$$

with $\tilde{A}$ the function's maximum of $A + B$, depending on the parameter y, is given by

$$p(y, \tilde{A}, B) = \frac{1}{2\pi(\tilde{A} - B)} \cdot \left(\sqrt{\frac{(\tilde{A} - y)(y - B)}{(\tilde{A} - B)^2}} \right)^{-1}, \tag{E.11}$$

shown in figure E.4b. The two sought extrema show up as the maxima of the function.

The situation changes if the signal exhibits noise from the detection process and the nature of the measured light. To model this situation, Poissonian noise is added to the sine-square function from above (fig. E.4a), through convolution with the PDF:

$$p_{noisy}(y) = \sum_{m=0}^{\infty} p(m, \tilde{A}, B) \cdot \frac{y^m}{m!} e^{-y}. \tag{E.12}$$

The noisy probability function's extrema, indicated in figure E.4b, are shifted in comparison to the noise-free function.

The shift was investigated to derive an analytic expression for calculating $\tilde{A}$ and B from the noisy PDF maxima $\bar{\tilde{A}}$ and $\bar{B}$ directly, since fitting each data set to the analytic expression would have taken too much time. We found a linear dependence between $\bar{\tilde{A}}, \bar{B}$ and $\tilde{A}, B$, which allowed to calculate them from the histogram maxima directly. The linear regression model consisted of the two equations

$$
\begin{aligned}
\tilde{A} &= 1.010 \cdot \bar{\tilde{A}} + 0.010 \cdot \bar{B} + 11.343, \\
B &= 0.006 \cdot \bar{\tilde{A}} + 0.941 \cdot \bar{B} - 1.483.
\end{aligned}
\tag{E.13}
$$

The error was on average negligible for the $\tilde{A}$ values and amounted to about a $0.7\,\%$ relative error for B. These expressions allowed to develop a fast normalization routine based on the two raw data maxima in the histogram of the tomography port phase signals taken from the events in the CSV-file.

So far, the discussion has assumed the entangled photon sitting in the equatorial plane of the Poincaré sphere. In reality, the wave plates of the tomography ports would have some deviation from their ideal setting. Two kinds of offsets are plausible: a shift out of the equatorial plane and a phase shift in the equatorial plane. The first leads to a compressed signal amplitude and is already corrected for by the signal normalization procedure. The second leads to the signals S_1 and S_2 (see equation 6.9) to be shifted by a fixed angle $\Delta\phi$. This small angle was extracted from a subset of the data to be used throughout the phase analysis. It was stable over measurement runs, so long as the experimental hardware was not touched.

Driven interferometer

$\tilde{A}$ and B did slowly change over time. The next step in developing a reliable normalization procedure was to optimize the measurement time for deriving one set of $\tilde{A}$ and B values.

As mentioned above, the measurement duration per data file was fixed at $30\,\mathrm{s}$ in order to limit the raw data files to a manageable size, so that after data processing, each result-CSV file contained data from these $30\,\mathrm{s}$ of measurement. The result files were bunched together in the normalization procedure to optimize for getting the most reliable $\tilde{A}$ and B values on average during the measurement. The figure of merit chosen in the optimization was a weighted squared sum of residuals in the form of

$$
R^2 = 1 - \frac{\sum_{i=1}^{n}(z_i - z_{fit})^2}{\sum_{i=1}^{n}(z_i - z_{mean})^2} \leq 1,
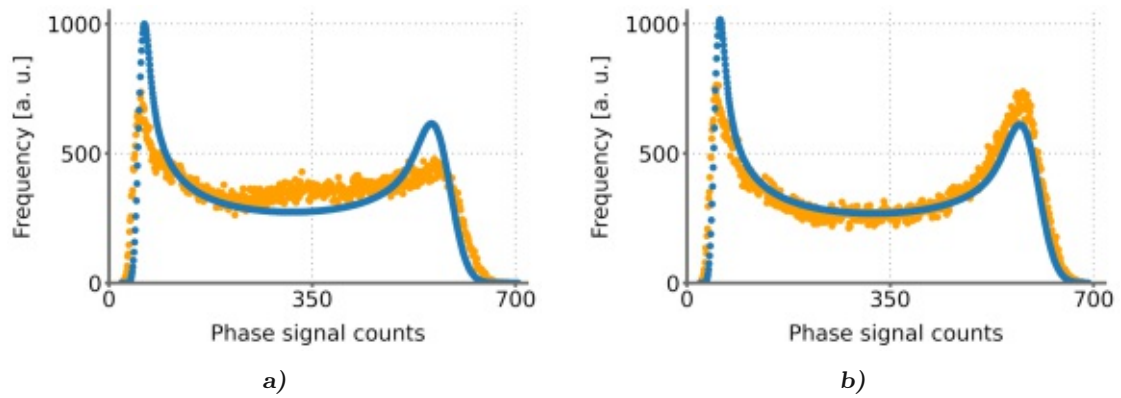\tag{E.14}
$$

157

Figure E.5: *Fits (blue) on phase data histograms (yellow): the data was taken from 180 s of measurement.* **a)** *a low R^2-score of 0.47, leading to increased error on the derived phase.* **b)** *a more accurate fit with R^2-score of 0.77.*

with n the number of observations, z_i the data points, z_{fit} the predicted value and z_{mean} the mean of the data [30]. Figures E.5a and E.5b contain phase signal data from measurements with different R^2-scores.

An often present feature was a bump in the centre of the histograms (fig. E.5a), which deviates from the fit function shape. In search for the origin, we found that the underlying events had a regular pattern in the time trace, which in turn could be related to a specific high-pitched noise of our cryostation. This noise changed the phase so quickly that the phase readout couln't follow and ports would appear uncorrelated, piling events at the mean counts value in the histogram centre. Those events were subsequently sorted out of the data.

For optimization, an integer amount of measurement data files was bunched together and the derived R^2-value was compared to an heuristically set threshold value of 0.6. If the threshold was met by each of the four phase signals, the data was accepted. The acceptance probability for the different bunched measurement durations is plotted in figure E.6, having a maximum at about 420 s being processed at once. This led us to investigate the interferometer phase drifting process more closely, in order to check if the phase space is fully explored by the random walk on short time scales. A piezoelectrically-acutated mirror was installed into one of the interferometer arms as a phase driver, imprinting a 1 Hz modulation onto the phase walk. The file bunching procedure was repeated, yielding the blue scatter in the figure, improving the acceptance probability by about 10 % to 15 %. Also, the maximum was shifted to smaller bunches - six measurement
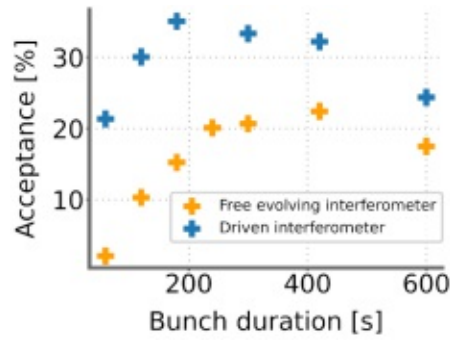
Figure E.6: *Acceptance rate versus measurement time in file bunches: an integer number of files, each relating to 30 s of measurement, was evaluated at once and accepted when the R^2-value of every port was above 0.6. The late maximum in the free interferometer phase evolution case (yellow curve) led to investigation for incomplete random phase walk and installation of a phase driving mirror (blue curve).*

files (180 s) gave maximum acceptance of 35 %, which nevertheless meant a rejection of 2/3 of the data in this step.

After this appendix, the main text continues with section 6.4.

APPENDIX F

Phase Tagging Software Architecture

Relating to appendix E, the design and architecture of the data processing system developed by the thesis author are discussed in more detail.

Distributed design and client-server architecture

For developing and running a flexible and architecturally elaborate data processing system, the versatile Python platform[1] was well suited. If fast processing of data was necessary, C++ based compiled tools were integrated.

In expectation of large amounts of data, the paradigm of a distributed system running on multiple computing units can harness the computational power of existing resources. A distributed system consists of many components being interfaced to each other and communicating via a network.

A decentralized algorithm was considered, which according to Tanenbaum [97] has the following characteristics:

1. No machine has complete information about the system.

2. Machines make decisions based only on local information.

---

[1]https://www.python.org

3. Failure of one machine does not ruin the algorithm.

4. There is no implicit assumption that a global clock exists.

All these characteristics do not contradict any of the data processing requirements mentioned in appendix E and point three already considers the required fault tolerance of the system. Point one requires the components of the system to be broken down into specialized pieces that together with point two can run independently on their local machine. Such a system can be designed in a way that components can easily be changed or components extended, even during system operation. Point four plays a role in inter-component communication. These four points were considered in every step of the design process.

The client-server model is a well known distributed architecture paradigm suited to many problems where communication and sharing of tasks in a network is needed. A server thereby is a process implementing a specific service, while a client represents a process that needs a service from a server by sending a request and waiting for the answer [97]. The server can be interpreted as an abstracted form of computational resources somewhere on the network and communication is based on a request-response principle - after the client issued a request, the server communicates a response. The client does not need to know how the server reaches a certain result, all that matters for the client is the servers response and it being in a format that can be interpreted by the client.

This architecture fitted our system requirements. The data handling capacity can be scaled to the requirement for real-time data analysis by running a number of servers in parallel. Servers could be started and stopped without endangering the functioning of the system as a whole. This implied that system updates on the server side software can be done at runtime. By that a close to real-time system is a realistic approach even without high end computer components or a cluster at hand. Through the architecture the system would be inherently tolerant to faults in the most data processing intense steps.

Flexible distributed processing framework

Here, the developed and implemented system architecture is illustrated, followed by a discussion of the corresponding data flow model.
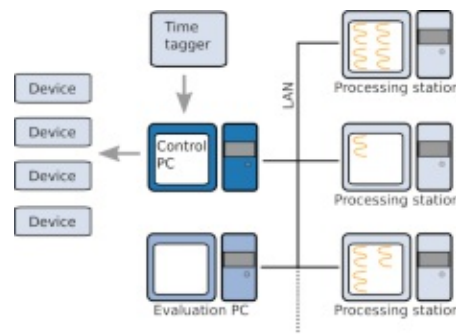
Figure F.1: *Distributed processing framework and device communication: distributed hardware infrastructure for data processing. Idle office computers were used as data processing stations and had a multi-threaded server program running in the background, with the number of active threads (orange) adapted to the PC's free resources. Stations could be added on demand.*

Hardware resources. The laboratory harboured a PC where the control and measurement software was situated, but whose resources were occupied with performing the measurement tasks. Besides that, a secondary PC was available being used for minor tasks only and offered two almost empty hard drive discs with 1 TB capacity each, providing good conditions for performing the data analysis after processing of the raw data. In the offices around the laboratory various standard workstation PCs were operated.

Office workstations are usually not fully busy in terms of computing capacity and network bandwidth, predisposing them as distributed processing stations for handling the raw data. Each such processing station had a multi-threaded server program running, working in the background, using some of the free computing resources (fig. F.1).

System design The processing servers on the workstations needed a client counterpart. This client was intended to provide the severs with requests in the form of data processing tasks and handling of the response. When the server had finished processing a chunk of raw data, it delivered a file output containing the processed data. Furthermore, the clients job was to look for new raw data from the measurement process. On finding a new file, it would look for a processing station with free capacity and send it there over the network (request), waiting for the response in form of the processed data and storing it concluded the clients actions.

For the wait period a non-blocking approach was chosen, the client would continue with other tasks and would check in regular intervals for finished jobs by the servers. Moreover, the client was allowed to spawn a certain number of threads in parallel for the

163

file transfers to the processing stations to avoiding build-up of raw data on the control PC. The chosen physical location to run the client was the control PC since it didn't need computational resources and an individual failure of the client while the measurement was running was avoided. The client was programmed to react flexible to processing servers going off-line or new servers appearing in the system.

The servers were designed following all the points in the characterisation of distributed systems introduced above. They would act only on local information available on the processing station. A file communication approach was chosen and fitted naturally to the task at hand. On start-up, the server would set a flag-file into the servers local directory on the workstation, indicating to the client that it was available. Once the client put a request in form of a raw data file in the servers directory, the server would start processing it, if it had free resources. This implements point two of the characteristics as to the server acting only on the local information by inspecting the files in the local directory.

The server was allowed to spawn a number of threads that would work in parallel on different request. When finishing the processing of a request, the server put the result into the working directory and threw away the raw data file, thereby compressing data volume to the minimum necessary. This implied that the server had means to perform detailed data analysis, which included a tool to preserve some of the raw data for a possible re-evaluation later on.

The whole orchestration of the data flow didn't rely on a global clock, but was asynchronous as stated by point four of the characteristics of decentralized systems. Point three is tackled by running servers in parallel on different workstations, but in addition to the redundant stations, a time redundancy was put on top. In case a station went off-line during processing of a file, the client would register that it didn't respond after a time out period and would send the file to a different processing server instead.

Fast data handling, by immediately sending it to parallel processing servers working multi-threaded, achieved to compress data very efficiently and offered close to real-time data analysis. The final data analysis software, working out the results from all the sever responses, was selected to run on the secondary laboratory computer, since it required a lot of computational resources and some disc storage. This analysis process was working as autonomously as possible. It regularly checked if there was new data, that had been processed by the servers, and included it into the evaluation (eager polling). Details of the data evaluation are treated further down.
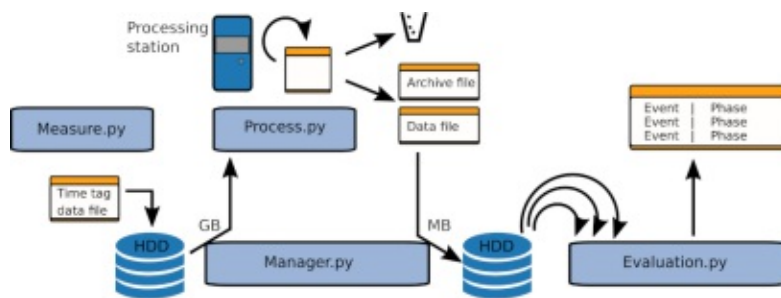
Figure F.2: *Data flow model: the python based measurement process captured photon events in the form of time tag data files and stored them on the hard drive (HDD) of the control PC. On storage of a new data file, the client (Manager.py) sent a copy to a free server working directory on the network (1.5 GB). The sever (Process.py) produced two files and discarded the raw data. The files, with size of some MB, were picked up by the client and stored on the evaluation PC and in an archive directory. The independent evaluation process (Evaluation.py) looked for new data files and included them to the final data evaluation. The process's output was entangling events matched to a certain interferometer phase.*

Data flow model. The introduced system had a data flow as shown in figure F.2. The measurement produced raw data files of about 1.5 GB size every 30 seconds. Those were stored on the control PC for a short period of time until being picked up by the client and copied to a server directory on the network. While waiting for the servers response, the original file was kept on the control PC, in case the server failed or didn't produce an answer.

The server started processing the file by converting the data format to the target format. A sub-process then started a C++ based parsing tool to extract the entangling event and phase readout information from the data (data file in the figure) and prepare an archived version of the data for an optional re-analysis later on (archive file). These were picked up by the client and were transferred to a storage directory for the data evaluation as well as an archive location respectively.

Event and phase information extraction

On the server a C++ tool was employed for fast parsing of photon events and extraction of entangling events with both the corresponding interferometer phase readouts and the spin state of the NV centre. The software loaded data files in 41 kB chunks to prevent overloading memory. The following parameters were sufficient for operation: the time period over which phase events were integrated (1 ms), the temporal windows for

165

photon events in the sequence and the temporal window for the spin readout event in the sequence. The output was a CSV-file, where each row contained:

```
1. Experimental cycle number
2. Relative time of the event in the sequence
3. Tomography channel of the event (D/A/R/L)
4. Number of phase readout events on D
5. Number of phase readout events on A
6. Number of phase readout events on R
7. Number of phase readout events on L
8. PSB readout to determine spin state (true/false)
```

The experimental cycle number was used to check that there wouldn't be cases with two entangling events per cycle (hinting at errors in the experiment) and to track the entangling rate over time. The uses of the other values are going to be discussed in the following sections.

The C++ program parsed the list of chronological time tags and decided based on the channel identifier in the time tag of how to act. Trigger channel events increased the experimental cycle number by one and reset the relative time in the sequence. The four tomography port events were treated according to their relative time in the sequence: If it fell into the temporal window of expected entangling photon events, a new row in the CSV-file was created. If the tomography port event wasn't from the window, it was added to the phase readout events counter. Each entangling event entry in the CSV-file got the phase readout count of all four tomography ports, for the specified integration time period, added symmetrically around the event time. Finally, the spin readout photon on the PSB channel in the respective detection window in the sequence was registered, if present as 'true', otherwise as 'false' value.

With those informations stored in the CSV-data files, the phase reconstruction process continues to be treated in appendix E.

Bibliography

[1] Aharonovich, I., Englund, D., and Toth, M. (2016). Solid-state single-photon emitters. *Nature Photonics*, 10(10):631–641. [Cited on page 16.]

[2] Alegre, T. P. M., Santori, C., Medeiros-Ribeiro, G., and Beausoleil, R. G. (2007). Polarization-selective excitation of nitrogen vacancy centers in diamond. *Physical Review B*, 76(16):165205. [Cited on page 45.]

[3] Arute, F., Arya, K., Babbush, R., Bacon, D., Bardin, J. C., Barends, R., Biswas, R., Boixo, S., Brandao, F. G., Buell, D. A., et al. (2019). Quantum supremacy using a programmable superconducting processor. *Nature*, 574(7779):505–510. [Cited on page 1.]

[4] Astner, T., Gugler, J., Angerer, A., Wald, S., Putz, S., Mauser, N. J., Trupke, M., Sumiya, H., Onoda, S., Isoya, J., Schmiedmayer, J., Mohn, P., and Majer, J. (2018). Solid-state electron spin lifetime limited by phononic vacuum modes. *Nature Materials*, 17(April). [Cited on page 62.]

[5] Atkins, P. W. and Friedman, R. S. (2011). *Molecular quantum mechanics*. Oxford university press. [Cited on page 27.]

[6] Azuma, K., Tamaki, K., and Lo, H.-K. (2015). All-photonic quantum repeaters. *Nature communications*, 6:6787. [Cited on page 10.]

[7] Balasubramanian, G., Chan, I. Y., Kolesov, R., Al-Hmoud, M., Tisler, J., Shin, C., Kim, C., Wojcik, A., Hemmer, P. R., Krueger, A., Hanke, T., Leitenstorfer, A., Bratschitsch, R., Jelezko, F., and Wrachtrup, J. (2008). Nanoscale imaging magnetometry with diamond spins under ambient conditions. *Nature*, 455(7213):648–51. [Cited on page 20.]

[8] Balasubramanian, G., Neumann, P., Twitchen, D., Markham, M., Kolesov, R., Mizuochi, N., Isoya, J., Achard, J., Beck, J., Tissler, J., Jacques, V., Hemmer, P. R., Jelezko, F., and Wrachtrup, J. (2009). Ultralong spin coherence time in isotopically engineered diamond. *Nature Materials*, 8(May):1–2. [Cited on pages 13, 19, and 62.]

[9] Barson, M. S., Peddibhotla, P., Ovartchaiyapong, P., Ganesan, K., Taylor, R. L., Gebert, M., Mielens, Z., Koslowski, B., Simpson, D. A., McGuinness, L. P., et al. (2017). Nanomechanical sensing using spins in diamond. *Nano letters*, 17(3):1496–1503. [Cited on page 20.]

[10] Bassett, L. C., Heremans, F. J., Christle, D. J., Yale, C. G., Burkard, G., Buckley, B. B., and Awschalom, D. D. (2014). Ultrafast optical control of orbital and spin dynamics in a solid-state defect. *Science (New York, N.Y.)*, 345(6202):1333–7. [Cited on pages 31, 32, 33, and 129.]

[11] Bennett, C. H., Brassard, G., Crépeau, C., Jozsa, R., Peres, A., and Wootters, W. K. (1993). Teleporting an unknown quantum state via dual classical and einstein-podolsky-rosen channels. *Physical review letters*, 70(13):1895. [Cited on page 10.]

[12] Bernien, H., Hensen, B., Pfaff, W., Koolstra, G., Blok, M. S., Robledo, L., Taminiau, T. H., Markham, M., Twitchen, D. J., Childress, L., and Hanson, R. (2013). Heralded entanglement between solid-state qubits separated by three metres. *Nature*, 497(7447):86–90. [Cited on pages 19, 75, 77, and 117.]

[13] Blinov, B. B., Moehring, D. L., Duan, L.-M., and Monroe, C. (2004). Observation of entanglement between a single trapped atom and a single photon. *Nature*, 428(6979):153–157. [Cited on page 117.]

[14] Bolef, D. (2012). *Nuclear acoustic resonance*. Academic Press. [Cited on page 98.]

[15] Browne, D. E. and Rudolph, T. (2005). Resource-efficient linear optical quantum computation. *Physical Review Letters*, 95(1):010501. [Cited on page 9.]

[16] Burnham, D. C. and Weinberg, D. L. (1970). Observation of simultaneity in parametric production of optical photon pairs. *Physical Review Letters*, 25(2):84. [Cited on page 15.]

[17] Buterakos, D., Barnes, E., and Economou, S. E. (2017). Deterministic genera-tion of all-photonic quantum repeaters from solid-state emitters. *Physical Review X*, 7(4):041023. [Cited on pages 1, 10, and 16.]

[18] Castelvecchi, D. (2018). The quantum internet has arrived (and it hasn't). *Nature*, 554(7692). [Cited on pages 1 and 19.]

[19] Chakraborty, T., Zhang, J., and Suter, D. (2017). Polarizing the electronic and nuclear spin of the nv-center in diamond in arbitrary magnetic fields: analysis of the optical pumping process. *New Journal of Physics*, 19(7):073030. [Cited on page 88.]

[20] Clevenson, H., Chen, E. H., Dolde, F., Teale, C., Englund, D., and Braje, D. (2016). Diamond-nitrogen-vacancy electronic and nuclear spin-state anticrossings under weak transverse magnetic fields. *Physical Review A*, 94(2):021401. [Cited on page 88.]

[21] Cohen-Tannoudji, C. (2010). *Quantenmechanik : 2.* de Gruyter, Berlin [u.a.], 4., durchges. u. verb. aufl.. edition. [Cited on page 28.]

[22] Degen, C. L., Reinhard, F., and Cappellaro, P. (2017). Quantum sensing. *Reviews of modern physics*, 89(3):035002. [Cited on page 1.]

[23] Dhomkar, S., Henshaw, J., Jayakumar, H., and Meriles, C. A. (2016). Long-term data storage in diamond. *Science advances*, 2(10):e1600911. [Cited on page 98.]

[24] DiVincenzo, D. P. (2000). The physical implementation of quantum computation. *Fortschritte der Physik: Progress of Physics*, 48(9-11):771–783. [Cited on page 19.]

[25] Dobrucki, J. W. and Kubitscheck, U. (2017). *Fluorescence Microscopy.* John Wiley and Sons, Ltd. [Cited on pages 41 and 42.]

[26] Doherty, M. W., Manson, N. B., Delaney, P., Jelezko, F., Wrachtrup, J., and Hollen-berg, L. C. (2013). The nitrogen-vacancy colour centre in diamond. *Physics Reports*, 528(1):1–45. [Cited on pages 13, 14, 20, 30, 31, 32, 33, 36, 37, and 54.]

[27] Dréau, a., Lesik, M., Rondin, L., Spinicelli, P., Arcizet, O., Roch, J.-F., and Jacques, V. (2011). Avoiding power broadening in optically detected magnetic resonance of single NV defects for enhanced dc magnetic field sensitivity. *Physical Review B*, 84(19):195204. [Cited on pages 43, 54, 56, 62, and 95.]

169

[28] Dutt, M. V. G., Childress, L., Jiang, L., Togan, E., Maze, J., Jelezko, F., Zibrov, a. S., Hemmer, P. R., and Lukin, M. D. (2007). Quantum register based on individual electronic and nuclear spin qubits in diamond. *Science (New York, N.Y.)*, 316(5829):1312–6. [Cited on pages 20 and 88.]

[29] Economou, S. E. and Barnes, E. (2015). Analytical approach to swift nonleaky entangling gates in superconducting qubits. *Physical Review B*, 91(16):161405. [Cited on page 80.]

[30] Fahrmeir, L., Künstler, R., Pigeot, I., and Tutz, G. (2007). Der weg zur datenanalyse. *Aufl. Heidelberg.* [Cited on page 158.]

[31] Fu, K.-M. C., Santori, C., Barclay, P. E., Rogers, L. J., Manson, N. B., and Beausoleil, R. G. (2009). Observation of the Dynamic Jahn-Teller Effect in the Excited States of Nitrogen-Vacancy Centers in Diamond. *Physical Review Letters*, 103(25):256404. [Cited on pages 45 and 67.]

[32] Gali, A., Fyta, M., and Kaxiras, E. (2008). Ab initio supercell calculations on nitrogen-vacancy center in diamond: Electronic structure and hyperfine tensors. *Physical Review B*, 77(15):155206. [Cited on pages 24, 25, and 29.]

[33] Geek3 (2019). RedPitaya STEMLab, CC BY-SA 4.0 licence. `commons.wikimedia.org/wiki/File:RedPitaya_STEMLab_FPGA_v1.1_frontview.jpg`. [Online; accessed 20-May-2020]. [Cited on page 49.]

[34] Gimeno-Segovia, M., Shadbolt, P., Browne, D. E., and Rudolph, T. (2015). From three-photon greenberger-horne-zeilinger states to ballistic universal quantum computation. *Physical review letters*, 115(2):020502. [Cited on page 10.]

[35] Gisin, N., Ribordy, G., Tittel, W., and Zbinden, H. (2002). Quantum cryptography. *Reviews of modern physics*, 74(1):145. [Cited on page 10.]

[36] Glenn, D. R., Bucher, D. B., Lee, J., Lukin, M. D., Park, H., and Walsworth, R. L. (2018). High-resolution magnetic resonance spectroscopy using a solid-state spin sensor. *Nature*, 555(7696):351–354. [Cited on page 20.]

[37] Goldman, M., Patti, T., Levonian, D., Yelin, S., and Lukin, M. (2020). Optical control of a single nuclear spin in the solid state. *Physical Review Letters*, 124(15):153203. [Cited on pages 32, 77, 88, and 91.]

[38] Goldman, M. L., Doherty, M., Sipahigil, A., Yao, N. Y., Bennett, S., Manson, N., Kubanek, A., and Lukin, M. D. (2015a). State-selective intersystem crossing in nitrogen-vacancy centers. *Physical Review B*, 91(16):165201. [Cited on pages 26 and 54.]

[39] Goldman, M. L., Sipahigil, A., Doherty, M. W., Yao, N. Y., Bennett, S. D., Markham, M., Twitchen, D. J., Manson, N. B., Kubanek, A., and Lukin, M. D. (2015b). Phonon-induced population dynamics and intersystem crossing in nitrogen-vacancy centers. *Physical Review Letters*, 114(14):1–6. [Cited on pages 37 and 122.]

[40] Grover, L. K. (1996). A fast quantum mechanical algorithm for database search. In *Proceedings of the twenty-eighth annual ACM symposium on Theory of computing*, pages 212–219. [Cited on page 1.]

[41] Hensen, B., Bernien, H., Dréau, a. E., Reiserer, a., Kalb, N., Blok, M. S., Ruitenberg, J., Vermeulen, R. F. L., Schouten, R. N., Abellán, C., Amaya, W., Pruneri, V., Mitchell, M. W., Markham, M., Twitchen, D. J., Elkouss, D., Wehner, S., Taminiau, T. H., and Hanson, R. (2015). Loophole-free Bell inequality violation using electron spins separated by 1.3 kilometres. *Nature*, 526(7575):682–686. [Cited on page 19.]

[42] Horodecki, R., Horodecki, P., Horodecki, M., and Horodecki, K. (2009). Quantum entanglement. *Reviews of modern physics*, 81(2):865. [Cited on pages 6 and 7.]

[43] Ivády, V., Abrikosov, I. A., and Gali, A. (2018). First principles calculation of spin-related quantities for point defect qubit research. *npj Computational Materials*, 4(1):1–13. [Cited on pages 27 and 29.]

[44] Jackson, J. D. (2006). *klassische Elektrodynamik*. Walter de Gruyter. [Cited on page 44.]

[45] Jacques, V., Neumann, P., Beck, J., Markham, M., Twitchen, D., Meijer, J., Kaiser, F., Balasubramanian, G., Jelezko, F., and Wrachtrup, J. (2009). Dynamic polarization of single nuclear spins by optical pumping of nitrogen-vacancy color centers in diamond at room temperature. *Physical review letters*, 102(5):057403. [Cited on page 88.]

[46] Janner, D., Tulli, D., García-Granda, M., Belmonte, M., and Pruneri, V. (2009). Micro-structured integrated electro-optic linbo3 modulators. *Laser & Photonics Reviews*, 3(3):301–313. [Cited on page 68.]

171

[47] Jenoptik (unknown). Integrated-optical modulators. `https://www.jenoptik.de/produkte/optoelektronische-systeme/lichtmodulation/integriert-optische-modulatoren-iom/phasenmodulator`. Accessed February 26, 2020. [Cited on pages 68, 69, 70, and 145.]

[48] Kalb, N., Reiserer, A. A., Humphreys, P. C., Bakermans, J. J., Kamerling, S. J., Nickerson, N. H., Benjamin, S. C., Twitchen, D. J., Markham, M., and Hanson, R. (2017). Entanglement distillation between solid-state quantum network nodes. *Science*, 356(6341):928–932. [Cited on page 88.]

[49] Kiesel, N., Schmid, C., Weber, U., Tóth, G., Gühne, O., Ursin, R., and Weinfurter, H. (2005). Experimental analysis of a four-qubit photon cluster state. *Physical Review Letters*, 95(21):210502. [Cited on page 15.]

[50] Kimble, H. J. (2008). The quantum internet. *Nature*, 453(7198):1023–1030. [Cited on pages 1 and 10.]

[51] Kimble, H. J., Dagenais, M., and Mandel, L. (1977). Photon antibunching in resonance fluorescence. *Physical Review Letters*, 39(11):691. [Cited on page 45.]

[52] King, J. P., Jeong, K., Vassiliou, C. C., Shin, C. S., Page, R. H., Avalos, C. E., Wang, H.-J., and Pines, A. (2015). Room-temperature in situ nuclear spin hyperpolarization from optically pumped nitrogen vacancy centres in diamond. *Nature communications*, 6(1):1–5. [Cited on page 20.]

[53] Kok, P. and Lovett, B. W. (2010). *Introduction to optical quantum information processing*. Cambridge University Press, Cambridge. [Cited on pages 5 and 8.]

[54] Kok, P., Munro, W. J., Nemoto, K., Ralph, T. C., Dowling, J. P., and Milburn, G. J. (2007). Linear optical quantum computing with photonic qubits. *Reviews of Modern Physics*, 79(1):135. [Cited on page 9.]

[55] Kucsko, G., Maurer, P. C., Yao, N. Y., Kubo, M., Noh, H. J., Lo, P. K., Park, H., and Lukin, M. D. (2013). Nanometre-scale thermometry in a living cell. *Nature*, 500(7460):54–58. [Cited on page 20.]

[56] Kurtsiefer, C., Mayer, S., Zarda, P., and Weinfurter, H. (2000). Stable Solid-State Source of Single Photons. *Physical Review Letters*, 85(2):290–293. [Cited on pages 44 and 45.]

[57] Kwiat, P. G., Mattle, K., Weinfurter, H., Zeilinger, A., Sergienko, A. V., and Shih, Y. (1995). New high-intensity source of polarization-entangled photon pairs. *Physical Review Letters*, 75(24):4337. [Cited on page 15.]

[58] Laferriere, L. and Taws, W. (2011). *Reference guide to fiber optic testing*. JDS Uniphase Corporation. [Cited on page 106.]

[59] Lee, J., Villa, B., Bennett, A., Stevenson, R., Ellis, D., Farrer, I., Ritchie, D., and Shields, A. (2019). A quantum dot as a source of time-bin entangled multi-photon states. *Quantum Science and Technology*, 4(2):025011. [Cited on page 17.]

[60] Lenef, A. and Rand, S. (1996). Electronic structure of the n-v center in diamond: Theory. *Physical Review B*, 53(20):13441. [Cited on page 28.]

[61] Lindner, N. and Rudolph, T. (2009). Proposal for Pulsed On-Demand Sources of Photonic Cluster State Strings. *Physical Review Letters*, 103(11):113602. [Cited on pages 1, 2, 9, 10, 11, 16, 103, and 131.]

[62] London, P., Scheuer, J., Cai, J.-M., Schwarz, I., Retzker, A., Plenio, M. B., Katagiri, M., Teraji, T., Koizumi, S., Isoya, J., et al. (2013). Detecting and polarizing nuclear spins with double resonance on a single electron spin. *Physical review letters*, 111(6):067601. [Cited on page 88.]

[63] Lu, C.-Y., Zhou, X.-Q., Gühne, O., Gao, W.-B., Zhang, J., Yuan, Z.-S., Goebel, A., Yang, T., and Pan, J.-W. (2007). Experimental entanglement of six photons in graph states. *Nature physics*, 3(2):91–95. [Cited on page 15.]

[64] Mamin, H., Kim, M., Sherwood, M., Rettner, C., Ohno, K., Awschalom, D., and Rugar, D. (2013). Nanoscale nuclear magnetic resonance with a nitrogen-vacancy spin sensor. *Science*, 339(6119):557–560. [Cited on page 20.]

[65] Mandel, L. and Wolf, E. (1995). *Optical coherence and quantum optics*. Cambridge university press. [Cited on pages 57 and 109.]

[66] Maurer, P. C., Kucsko, G., Latta, C., Jiang, L., Yao, N. Y., Bennett, S. D., Pastawski, F., Hunger, D., Chisholm, N., Markham, M., et al. (2012). Room-temperature quantum bit memory exceeding one second. *Science*, 336(6086):1283–1286. [Cited on pages 13 and 20.]

173

[67] Maze, J. R., Gali, a., Togan, E., Chu, Y., Trifonov, a., Kaxiras, E., and Lukin, M. D. (2011). Properties of nitrogen-vacancy centers in diamond: The group theoretic approach. *New Journal of Physics*, 13. [Cited on pages 23, 24, 25, 26, 28, 31, 33, 34, and 36.]

[68] Mildren, R. and Rabeau, J. (2013). *Optical engineering of diamond*. John Wiley and Sons. [Cited on pages 13, 20, and 21.]

[69] Munro, W. J., Azuma, K., Tamaki, K., and Nemoto, K. (2015). Inside quantum repeaters. *IEEE Journal of Selected Topics in Quantum Electronics*, 21(3):78–90. [Cited on page 10.]

[70] Nemoto, K., Trupke, M., Devitt, S. J., Stephens, A. M., Scharfenberger, B., Buczak, K., Nöbauer, T., Everitt, M. S., Schmiedmayer, J., and Munro, W. J. (2014). Photonic architecture for scalable quantum information processing in diamond. *Physical Review X*, 4(3):1–12. [Cited on page 13.]

[71] Neumann, P., Beck, J., Steiner, M., Rempp, F., Fedder, H., Hemmer, P. R., Wrachtrup, J., and Jelezko, F. (2010). Single-shot readout of a single nuclear spin. *Science (New York, N.Y.)*, 329(5991):542–4. [Cited on pages 47, 88, and 131.]

[72] Nielsen, M. a. (2004). Optical quantum computation using cluster states. *Physical Review Letters*, 93(4):040503–1. [Cited on page 9.]

[73] Nielsen, M. A. (2010). *Quantum computation and quantum information*. Cambridge Univ. Press, Cambridge [u.a.], 10th anniversary ed.. edition. [Cited on pages 3, 5, 6, and 117.]

[74] Pagliero, D., Laraoui, A., Henshaw, J. D., and Meriles, C. A. (2014). Recursive polarization of nuclear spins in diamond at arbitrary magnetic fields. *Applied Physics Letters*, 105(24):242402. [Cited on page 88.]

[75] Pfaff, W., Hensen, B. J., Bernien, H., van Dam, S. B., Blok, M. S., Taminiau, T. H., Tiggelman, M. J., Schouten, R. N., Markham, M., Twitchen, D. J., et al. (2014). Unconditional quantum teleportation between distant solid-state quantum bits. *Science*, 345(6196):532–535. [Cited on pages 19 and 88.]

[76] Poggiali, F., Cappellaro, P., and Fabbri, N. (2017). Measurement of the excited-state transverse hyperfine coupling in nv centers via dynamic nuclear polarization. *Physical Review B*, 95(19):195308. [Cited on pages 30, 31, 32, and 91.]

[77] Prawer, S. and Aharonovich, I. (2014). *Quantum information processing with diamond: Principles and applications.* Elsevier. [Cited on pages 20, 22, and 36.]

[78] Quantum Manifesto (2016). `http://qurope.eu/manifesto`. Accessed January 25, 2021. [Cited on page 1.]

[79] Rao, D. B., Yang, S., and Wrachtrup, J. (2015). Generation of entangled photon strings using nv centers in diamond. *Physical Review B*, 92(8):081301. [Cited on pages 16 and 131.]

[80] Raussendorf, R. and Briegel, H. J. (2001). A one-way quantum computer. *Physical Review Letters*, 86(22):5188. [Cited on page 8.]

[81] Raussendorf, R., Browne, D. E., and Briegel, H. J. (2003). Measurement-based quantum computation on cluster states. *Physical review A*, 68(2):022312. [Cited on page 9.]

[82] Reiserer, A., Kalb, N., Rempe, G., and Ritter, S. (2014). A quantum gate between a flying optical photon and a single trapped atom. *Nature*, 508(7495):237–240. [Cited on page 16.]

[83] Riedel, D., Söllner, I., Shields, B. J., Starosielec, S., Appel, P., Neu, E., Maletinsky, P., and Warburton, R. J. (2017). Deterministic enhancement of coherent photon generation from a nitrogen-vacancy center in ultrapure diamond. *Physical Review X*, 7(3):1–8. [Cited on page 130.]

[84] Robledo, L., Bernien, H., Van Weperen, I., and Hanson, R. (2010). Control and coherence of the optical transition of single nitrogen vacancy centers in diamond. *Physical review letters*, 105(17):177403. [Cited on pages 65, 83, 87, and 121.]

[85] Robledo, L., Childress, L., Bernien, H., Hensen, B., Alkemade, P. F. a., and Hanson, R. (2011). High-fidelity projective read-out of a solid-state spin quantum register. *Nature*, 477(7366):574–8. [Cited on pages 88 and 131.]

[86] Rudolph, T. (2017). Why i am optimistic about the silicon-photonic route to quantum computing. *APL Photonics*, 2(3):030901. [Cited on pages 1, 10, 15, and 16.]

175

[87] Russo, A., Barnes, E., and Economou, S. E. (2018). Photonic graph state generation from quantum dots and color centers for quantum communications. *Physical Review B*, 98(8):085303. [Cited on pages 1, 16, and 131.]

[88] Sangouard, N., Simon, C., De Riedmatten, H., and Gisin, N. (2011). Quantum repeaters based on atomic ensembles and linear optics. *Reviews of Modern Physics*, 83(1):33. [Cited on page 10.]

[89] Schön, C., Solano, E., Verstraete, F., Cirac, J. I., and Wolf, M. M. (2005). Sequential generation of entangled multiqubit states. *Physical review letters*, 95(11):110503. [Cited on page 16.]

[90] Schwartz, I., Cogan, D., Schmidgall, E. R., Don, Y., Gantz, L., Kenneth, O., Lindner, N. H., and Gershoni, D. (2016). Deterministic generation of a cluster state of entangled photons. *Science*, 354(6311):434–437. [Cited on page 16.]

[91] Shor, P. W. (1994). Algorithms for quantum computation: discrete logarithms and factoring. In *Proceedings 35th annual symposium on foundations of computer science*, pages 124–134. Ieee. [Cited on page 1.]

[92] Siyushev, P., Nesladek, M., Bourgeois, E., Gulka, M., Hruby, J., Yamamoto, T., Trupke, M., Teraji, T., Isoya, J., and Jelezko, F. (2019). Photoelectrical imaging and coherent spin-state readout of single nitrogen-vacancy centers in diamond. *Science*, 363(6428):728–731. [Cited on page 20.]

[93] Slussarenko, S. and Pryde, G. J. (2019). Photonic quantum information processing: A concise review. *Applied Physics Reviews*, 6(4):041303. [Cited on page 16.]

[94] Steck, D. A. (2007). *Quantum and Atom Optics.* available online at http://steck.us/teaching (revision 0.11.5 27 November 2016). [Cited on pages 62 and 153.]

[95] Steiner, M., Neumann, P., Beck, J., Jelezko, F., and Wrachtrup, J. (2010). Universal enhancement of the optical readout fidelity of single electron spins at nitrogen-vacancy centers in diamond. *Physical Review B*, 81(3):035205. [Cited on page 32.]

[96] Taminiau, T. H., Cramer, J., van der Sar, T., Dobrovitski, V. V., and Hanson, R. (2013). Universal control and error correction in multi-qubit spin registers in diamond. *Nature Nanotechnology*, 9(3):171–176. [Cited on pages 62 and 88.]

[97] Tanenbaum, A. S. and Van Steen, M. (2007). *Distributed systems: principles and paradigms.* Prentice-Hall. [Cited on pages 161 and 162.]

[98] Tchebotareva, A., Hermans, S. L., Humphreys, P. C., Voigt, D., Harmsma, P. J., Cheng, L. K., Verlaan, A. L., Dijkhuizen, N., De Jong, W., Dréau, A., et al. (2019). Entanglement between a diamond spin qubit and a photonic time-bin qubit at telecom wavelength. *Physical review letters*, 123(6):063601. [Cited on page 17.]

[99] Tinkham, M. (2003). *Group theory and quantum mechanics.* Courier Corporation. [Cited on pages 23, 133, 134, and 136.]

[100] Togan, E., Chu, Y., Imamoglu, a., and Lukin, M. D. (2011). Laser cooling and real-time measurement of the nuclear spin environment of a solid-state qubit. *Nature*, 478(7370):497–501. [Cited on page 88.]

[101] Togan, E., Chu, Y., Trifonov, A. S., Jiang, L., Maze, J., Childress, L., Dutt, M. G., Sørensen, A. S., Hemmer, P., Zibrov, A. S., et al. (2010). Quantum entanglement between an optical photon and a solid-state spin qubit. *Nature*, 466(7307):730–734. [Cited on pages 16 and 77.]

[102] Tohyama, M. (2018). Sinusoidal waves as random variables. In *Sound in the Time Domain*, pages 31–49. Springer. [Cited on page 156.]

[103] van Dam, S. B., Ruf, M., and Hanson, R. (2018). Optimal design of diamond-air microcavities for quantum networks using an analytical approach. *New Journal of Physics*, 20(11):115004. [Cited on page 130.]

[104] Vasconcelos, R., Reisenbauer, S., Salter, C., Wachter, G., Wirtitsch, D., Schmiedmayer, J., Walther, P., and Trupke, M. (2020). Scalable spin–photon entanglement by time-to-polarization conversion. *npj Quantum Information*, 6(1):1–5. [Cited on page 2.]

[105] Wang, X.-L., Chen, L.-K., Li, W., Huang, H.-L., Liu, C., Chen, C., Luo, Y.-H., Su, Z.-E., Wu, D., Li, Z.-D., et al. (2016). Experimental ten-photon entanglement. *Physical review letters*, 117(21):210502. [Cited on pages 15 and 129.]

[106] Wehner, S., Elkouss, D., and Hanson, R. (2018). Quantum internet: A vision for the road ahead. *Science*, 362(6412). [Cited on pages 1 and 10.]

177

[107] Weil, J. A. and Bolton, J. R. (2007). *Electron paramagnetic resonance: elementary theory and practical applications.* John Wiley & Sons. [Cited on pages 27 and 29.]

[108] Wolf, T., Neumann, P., Nakamura, K., Sumiya, H., Ohshima, T., Isoya, J., and Wrachtrup, J. (2015). Subpicotesla diamond magnetometry. *Physical Review X*, 5(4):041001. [Cited on page 20.]

[109] Wooten, E. L., Kissa, K. M., Yi-Yan, A., Murphy, E. J., Lafaw, D. A., Hallemeier, P. F., Maack, D., Attanasio, D. V., Fritz, D. J., McBrien, G. J., et al. (2000). A review of lithium niobate modulators for fiber-optic communications systems. *IEEE Journal of selected topics in Quantum Electronics*, 6(1):69–82. [Cited on page 145.]

[110] Yang, S., Wang, Y., Rao, D. D. B., Tran, T. H., Momenzadeh, A. S., Markham, M., Twitchen, D. J., Wang, P., Yang, W., Stöhr, R., Neumann, P., Kosaka, H., and Wrachtrup, J. (2016). High- fi delity transfer and storage of photon states in a single nuclear spin. *Nature Photonics*, 10(8):507–511. [Cited on page 98.]

[111] Yariv, A. (1989). *Optical electronics.* Saunders College Publ. [Cited on pages 143 and 145.]

[112] Yoran, N. and Reznik, B. (2003). Deterministic linear optics quantum computation with single photon qubits. *Physical review letters*, 91(3):037903. [Cited on page 9.]

[113] Zeilinger, A., Horne, M. A., Weinfurter, H., and Żukowski, M. (1997). Three-particle entanglements from two entangled pairs. *Physical review letters*, 78(16):3031. [Cited on page 15.]

[114] Zhang, A.-N., Lu, C.-Y., Zhou, X.-Q., Chen, Y.-A., Zhao, Z., Yang, T., and Pan, J.-W. (2006). Experimental construction of optical multiqubit cluster states from bell states. *Physical Review A*, 73(2):022330. [Cited on page 15.]

[115] Zhang, M., Feng, L.-T., Zhou, Z.-Y., Chen, Y., Wu, H., Li, M., Gao, S.-M., Guo, G.-P., Guo, G.-C., Dai, D.-X., et al. (2019). Generation of multiphoton quantum states on silicon. *Light: Science & Applications*, 8(1):1–7. [Cited on page 15.]

[116] Zhong, H.-S., Li, Y., Li, W., Peng, L.-C., Su, Z.-E., Hu, Y., He, Y.-M., Ding, X., Zhang, W., Li, H., et al. (2018). 12-photon entanglement and scalable scattershot boson sampling with optimal entangled-photon pairs from parametric down-conversion. *Physical review letters*, 121(25):250505. [Cited on pages 1 and 15.]

[117] Zhong, H.-S., Wang, H., Deng, Y.-H., Chen, M.-C., Peng, L.-C., Luo, Y.-H., Qin, J., Wu, D., Ding, X., Hu, Y., et al. (2020). Quantum computational advantage using photons. *Science*, 370(6523):1460–1463. [Cited on page 1.]

[118] Zwiller, V. and Bjork, G. (2002). Improved light extraction from emitters in high refractive index materials using solid immersion lenses. *Journal of Applied Physics*, 92(2):660. [Cited on page 44.]

List of Abbreviations